UNIVERSITY OF SOUTHAMPTON.

COMPUTER SIMULATION OF LANGMUIR-BLODGETT FILMS.

KWANG SOO KIM.

A dissertation submitted in partial fulfilment of the requirements for the degree of Doctor of Philosophy at the University of Southampton.

December 1991.

Department of Chemistry.

CONTENTS.

UNIVERSITY OF SOUTHAMPTON.

ABSTRACT.

FACULTY OF SCIENCE.

CHEMISTRY.

Doctor of Philosophy.

COMPUTER SIMULATION OF LANGMUIR-BLODGETT FILMS.

by Kwang Soo Kim.

The computer simulation has been applied to predict the structure and dynamics of a Langmuir-Blodgett film of a stearic acid with three molecular models.

The energy minimisation has been used to reveal the structure of the film at ground state(0 K). The minimum energy structure of the film is not so sentive to the molecular model for the molecular tilt but shows the big difference in the behaviour of the minimum energy as a function of molecular area. The incorporation of electrostatic interaction does not have significant effect on the minimum energy structure since Van der Waals interaction between chains dominates the overall structure of the film.

In the molecular dynamics calculation, the explicit-hydrogen model predicts that the the monolayer with A_m = 20.8Å^2 has a negligible molecular tilt and the monolayer with A_m = 21.2Å^2 has a molecular tilt of 9°. The layer has co-operative molecular motion between the molecular tilt and the azimuthal orientation of the layer because of relatively small molecular tilt. The all-atom model including electrostatic interaction predicts the molecular tilt of 18.8° for the layer with A_m = 21.2Å^2, which is more than twice the molecular tilt of the simulation using the explicit-hydrogen model. The dipolar interaction in the layer with the all-atom model has a role to determine the detailed molecular orientation of the layer. The bilayer with the all-atom model shows the strong correlation of the structures between the first layer and the second layer since there is very strong electrostatic interaction between layers.

ACKNOWLEDGEMENTS.

I would like to thank my Ph.D. supervisor, Professor Dominic J. Tildesley for his invaluable advice and encouragement throughout last three years. His encouragement and deep interest in this subject have helped me to understand this work. I would also like to thank Professor G.R. Luckhurst for the opportunity to study at Southampton.

I would like to thank Professor Nick Quirke at British Petroleum for the many invaluable suggestions, which helped to forcus to this work. He is in fact a co-supervisor with Dominic. I am also grateful to Dr. Michael A. Moller for his great help and his friendship during the first two years of this project.

I would also like to thank all the members of the Chemical Physics sub-group at Southampton for their help and friendship. Steven, Mark, Tessa, Andrew, Paul, Giulio, Ken, Steve, Martin... have all helped to make my life at Southampton happy.

I would like to thank BP and The British Council for a CASE award and for arranging the travel to Britain and support for last three years. I would also like to thank CVCP for the Overseas Research Students(ORS) Awards for the last two years.

Finally, I would like to express my sincere regard to my parents for their continual support and especially to my wife and son "Hanyoung" for their endurance and endless encouragement and love. Without their support this work would not have been possible.

To my parents, my wife and son.

이 논문을 부모님과 사랑하는
아내와 한영에게 드립니다.

"Today... I propose to tell you of a real two-dimensional world in which phenomena occur that are analogues to those described 'Flatland'. I plan to tell you about the behaviour of molecules and atoms that are held at the surface of solids and liquids."

- I. Langmuir, Science, **84**, 379 (1936).

CHAPTER ONE.

Introduction.

1. INTRODUCTION.

1.1. Langmuir-Blodgett films.

A simple fatty acid such as stearic acid ($C_{17}H_{35}COOH$) or arachidic acid ($C_{19}H_{40}COOH$) consists of a linear, saturated, alkyl chain (C_nH_{2n+1}) terminated by a carboxylic acid group. Under fixed conditions the carboxylic acid group (-COOH) of the amphiphile is hydrophilic. Alkyl groups are known to be hydrophobic, and normally hydrophilicity of such amphiphilic molecules decreases with the increasing chain length. Amphiphilic molecules containing more than 13 carbon atoms in an alkyl chain of molecule can be spread to form a stable monolayer spontaneously at the air/water (or oil/water) interface, minimising the thermodynamic free energy of the system.

It was Benjamin Franklin who made a first attempt to place the subject of monolayer on a scientific basis. Franklin observed the spreading of a drop of oil on Clapham pond in 1774[1]. He also showed that oil had a big influence on the surface of the pond even when the layer of oil could only be a few nanometers thick. The first scientific observation of monolayer was made by Agnes Pockels in 1893[2]. She developed a simple apparatus which became the model for what is called a Langmuir trough. She carried out many quantitative studies of monolayers by spreading the amphiphile, stearic acid on water and she obtained the first pressure-area isotherms, so familiar in monolayer research. She obtained results which predict a monolayer thickness of 2.3 nm which is very close to the value for the length of stearic acid, 2.5 nm.

It was, however, Irving Langmuir[3] who carried out systematic studies of monolayers of amphiphilic compounds at the air/water interface and thus gave his name to the subject. For his measurements of the spreading pressure of films on water, he developed a number of new techniques including the surface film balance which is now called the Langmuir trough. Langmuir confirmed that films on a water

surface had approximately the thickness of a single molecular length and that the molecules were arranged at the water surface with the polar functional group immersed in the water and the nonpolar chain directed nearly vertically to the surface [4]. Katharine Blodgett who was Langmuir's research collegue at the General Electric Company was able to transfer the fatty acid monolayer from the air/water interface to a solid support such as a glass slide[5]. She also studied systematically the multilayers of carboxylic acid transfered layer by layer from the air/water interface to a solid substrate[6]. Mono- or multilayers on solid substrate which are transfered from the air/water interface are now called Langmuir-Blodgett(LB) films as distinct from Langmuir films which refer to the floating monolayer film at the air/water interface.

The Langmuir monolayers are the insoluble assemblies of amphiphilic molecules such as surface active agents, fatty acids or lipids at the air/water interface. An important indicator of the monolayer properties is a plot of surface pressure as a function of the surface area at constant temperature, the surface pressure-area isotherm. Figure 1.1 is a sketch of a typical surface pressure-molecular area isotherm of stearic acid monolayer film on water. There are a number of transitions in the diagram as a function of the surface area per molecule. These changes are quasi-2-dimensional phase transitions in the Langmuir monolayer which occurs during the compression of the film[7]. At very low surface pressures (« 1 mN m^{-1}) the concentration of amphiphilic molecules on water is very low and the monolayer is thought to be in a gaseous state. In this state the area available to one molecule is much larger than the area of the hydrophilic head group and it is generally assumed that the alkyl chain extends along the air/water interface (Figure 1.2(a)). With an increase in the surface pressure on compresson of the monolayer, a gas-liquid transition occurs. This gas-liquid transition in monolayer has been studied in great detail using carefully measured surface pressure-area isotherm. Due to the

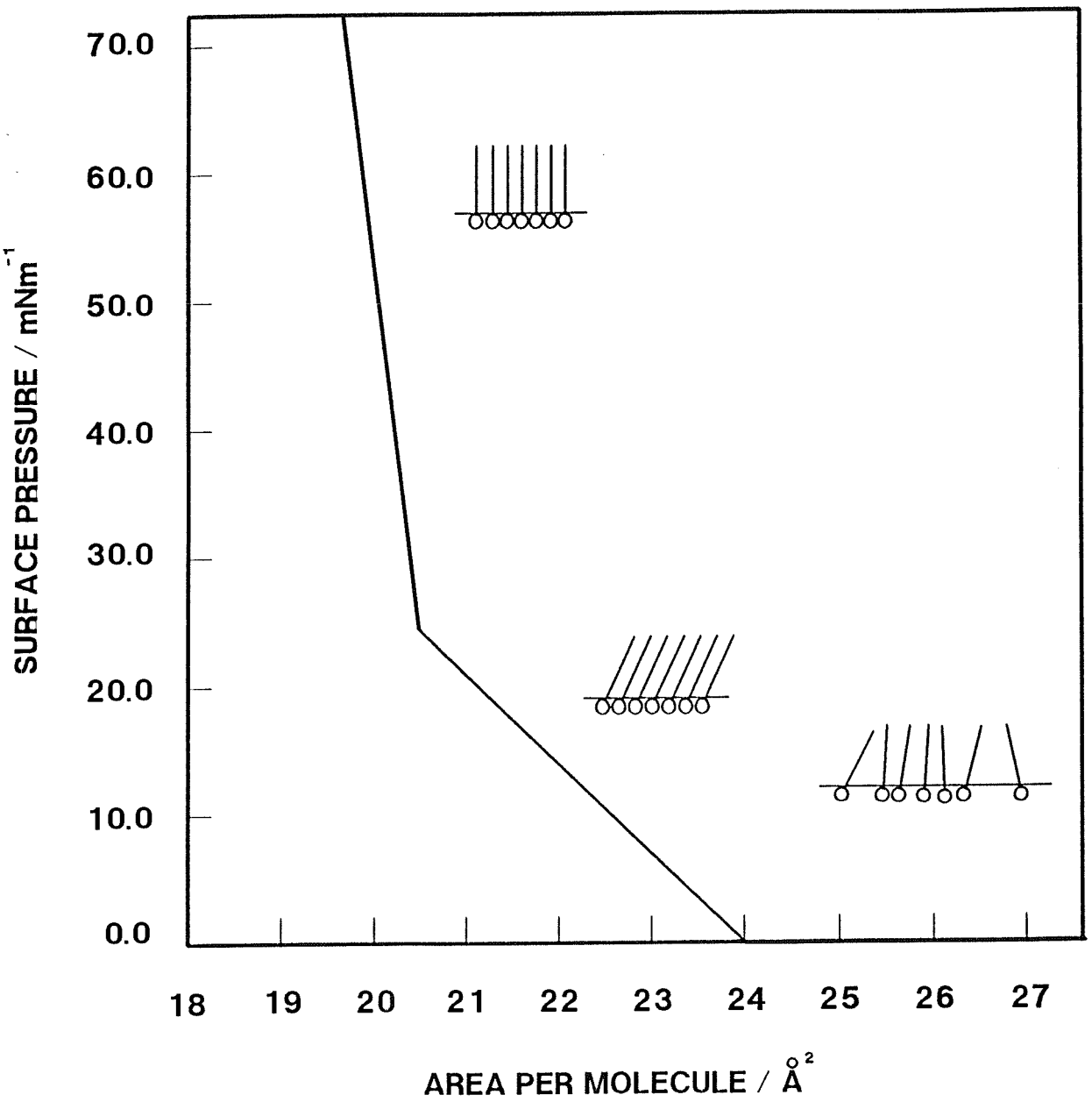

Figure 1.1. A surface pressure-molecular area isotherm for a stearic acid monolayer film on water.

decreasing distance between headgroups (i.e. decrease in the area per molecule), the alkyl tails of molecules are not oriented along the interface but have a tendency to align perpendicular to the surface(Figure 1.2(b)). For many long amphiphiles there is a kink in the liquid regime of the surface pressure-area isotherm. This kink divides the liquid phase regime into two phases: so called a liquid-expanded phase at lower surface pressure regime and a liquid-condensed phase at higher surface pressure regime [p.178 in Ref. 7]. Further increase in the surface pressure induces a liquid-solid phase transition at an area of approximately 20 $Å^2$ per molecule. This transition is due to a closely packed ordered solid-like arrangement of the quasi-two-dimensional array (Figure 1.2(c)). The compressibility of the monolayer ($-1/A(\partial A/\partial \Pi)_T$) in this region is approximately constant and close to zero.

1.2. The structure of Langmuir-Blodgett films.

The Langmuir film floating on water surface can be transferred onto a solid substrate such as glass slide or PTFE (poly(tetrafluoro-ethylene)) plate under appropriate conditions (pH, temperature, surface pressure, etc..) by passing the solid substrate through a Langmuir film of amphiphilic molecules that exists as a monolayer at the air/water interface. This procedure which is called the Langmuir-Blodgett technique, forms the Langmuir-Blodgett(LB) film on the solid surface. This transfer process of Langmuir monolayer is illustrated in Figure 1.3 schematically. Multilayer LB films can be constructed by successive dipping, in which each pass of solid substrate adds one layer onto the pre-existing LB film. Well-ordered LB films can be deposited onto a solid substrate if the conditions for the transfer such as the spreading pressure are kept constant during monolayer transfer onto the solid substrate. Recently, highly-ordered thin organic films in the range of one molecular layer to sub-micron thickness layer have been successfully deposited on a solid substrate using the Langmuir-Blodgett technique[8].

The modes of deposition of the multi-layered LB films are largely dependent

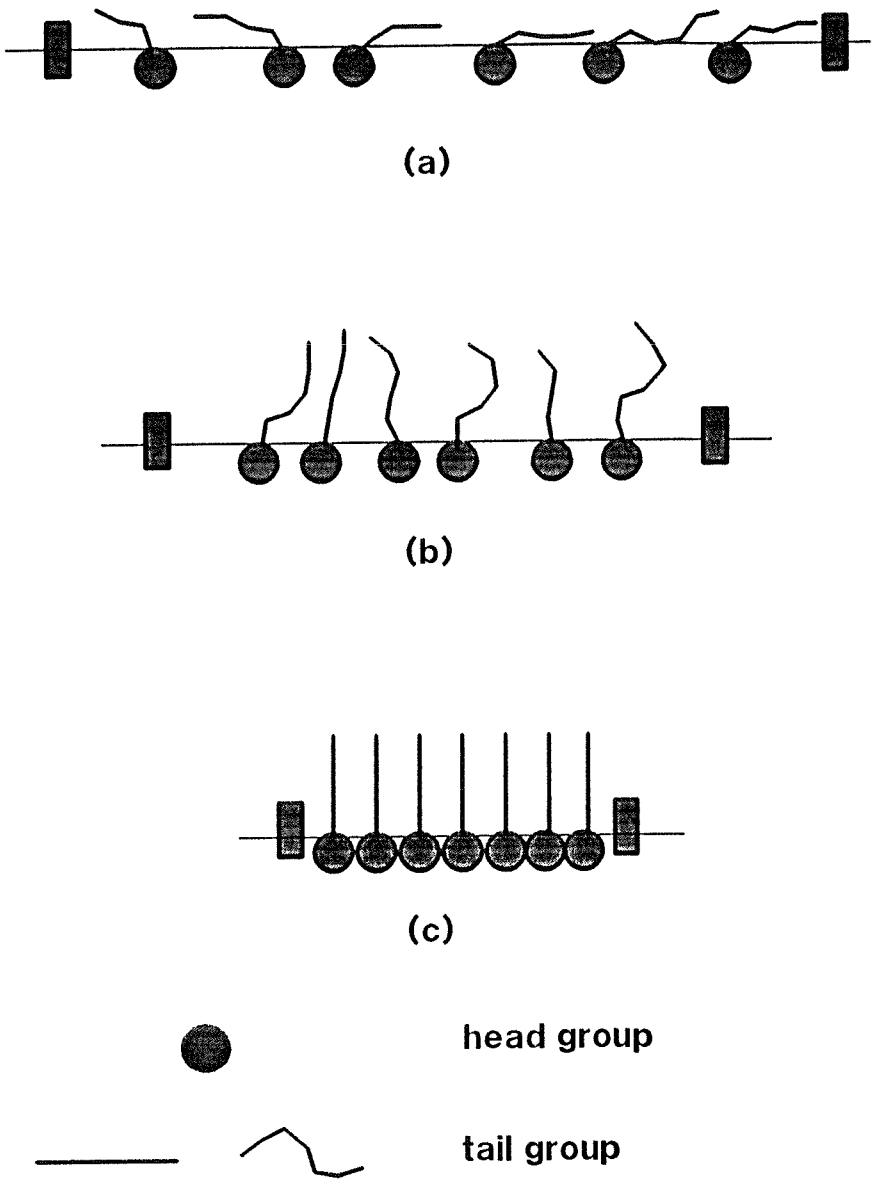

Figure 1.2. The orientation and packing of the amphiphiles on water: (a) very low surface pressure(«1 mN m^{-1}); (b) high surface pressure(< 10 mN m^{-1}); (c) very high surface pressure(> 20 mN m^{-1}).

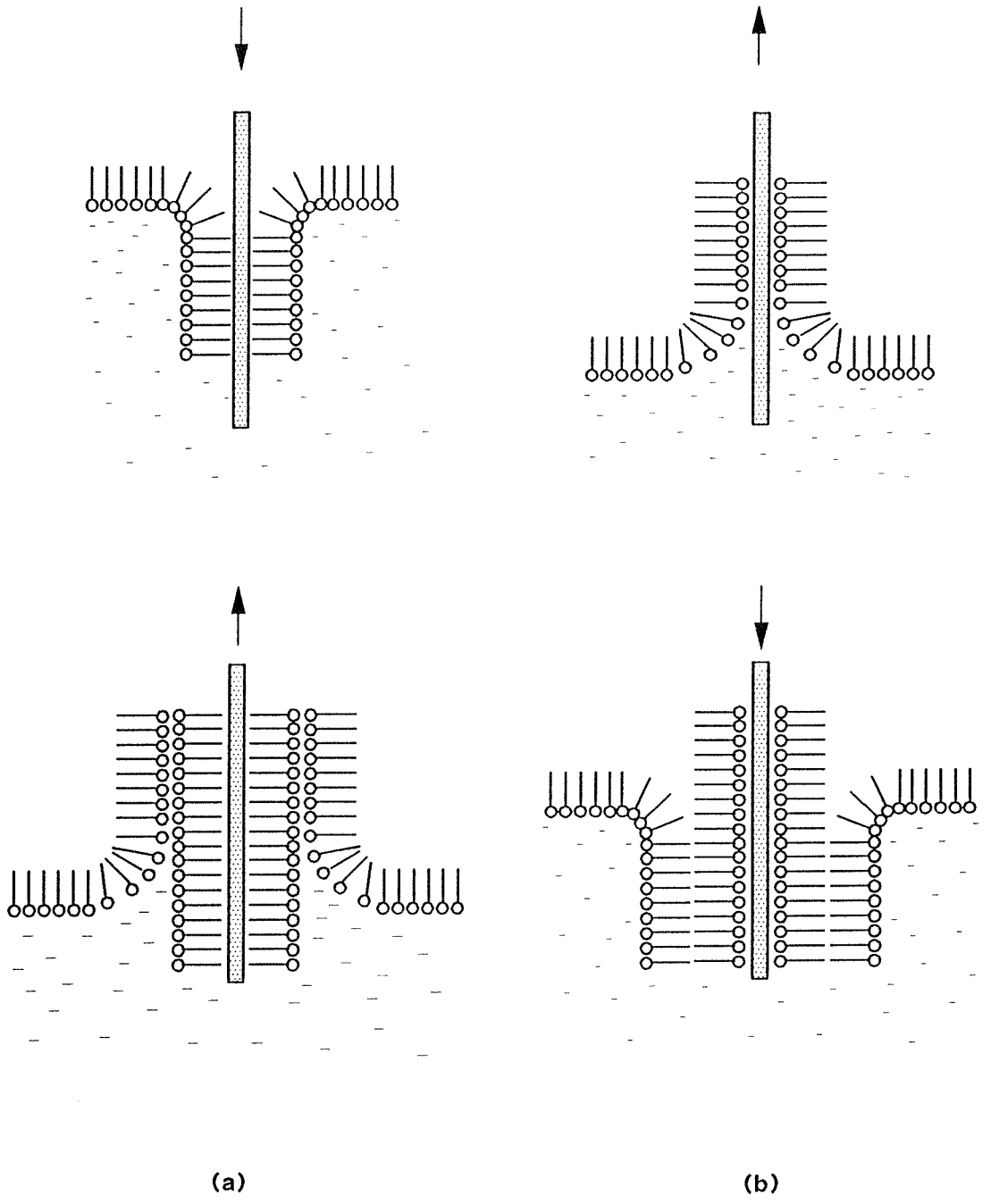

Figure 1.3. Schemetic representation of the deposition of a Langmuir film: (a) a hydrophobic surface; (b) a hydrophilic surface.

on the hydrophilicity of constituent molecules and the dipping method of solid substrate. The most common deposition mode is Y-type deposition in which the amphiphilic molecules are arranged with head-to-head and tail-to-tail on the substrate as illustated in Figure 1.4(b). Although Y-type layers are the most easily produced multi-layers, monolayers can be deposited by only inserting the solid substrate into the subphase or by only lifting up the solid substrate from the subphase. These deposition mode are referred to as X-type and Z-type mode respectively. Schematic diagrams for X- and Z-types of layers are shown in Figure 1.4(a) and (c) respectively. Fatty acid monolayers are normally deposited as Y-type layers. However, X-type deposition is possible as well by a suitable change in the dipping conditions e.g. a high pH value [5,7,9,10]. There are a number of reports of Z-type deposition. Most of these concern aromatic materials with relatively short alkyl chain or no carbon atoms, for instance substituted anthracene derivatives, porphyrins, azobenzene derivatives and polymers[11,12,13,14,15]. There has been considerable interest in the properties of these films but at present there is not a complete understanding of the method of deposition or the structure of the deposited film.

1.3. Experiments on Langmuir-Blodgett films.

The understanding of the relationships between the molecular structure of amphiphiles and their organisation on different surfaces is a fundamental requirement in an application of Langmuir-Blodgett films. The packing and orientation of amphiphiles affect the surface chemistry of the films and play an important role in the phenomena of lubrication, corrosion control, adhesion and catalysis[98].

Information on the structure of the monolayer and multilayer films can be obtained by a number of experimental methods, such as X-ray diffraction[16-32], electron diffraction[33-37], infra-red[38-47], raman[48] spectroscopy, neutron diffraction[49], and fluorescence depolarization[50-53]. In addition a number of surface analysis techniques such as surface second harmonic generation(SHG)[54], low energy helium

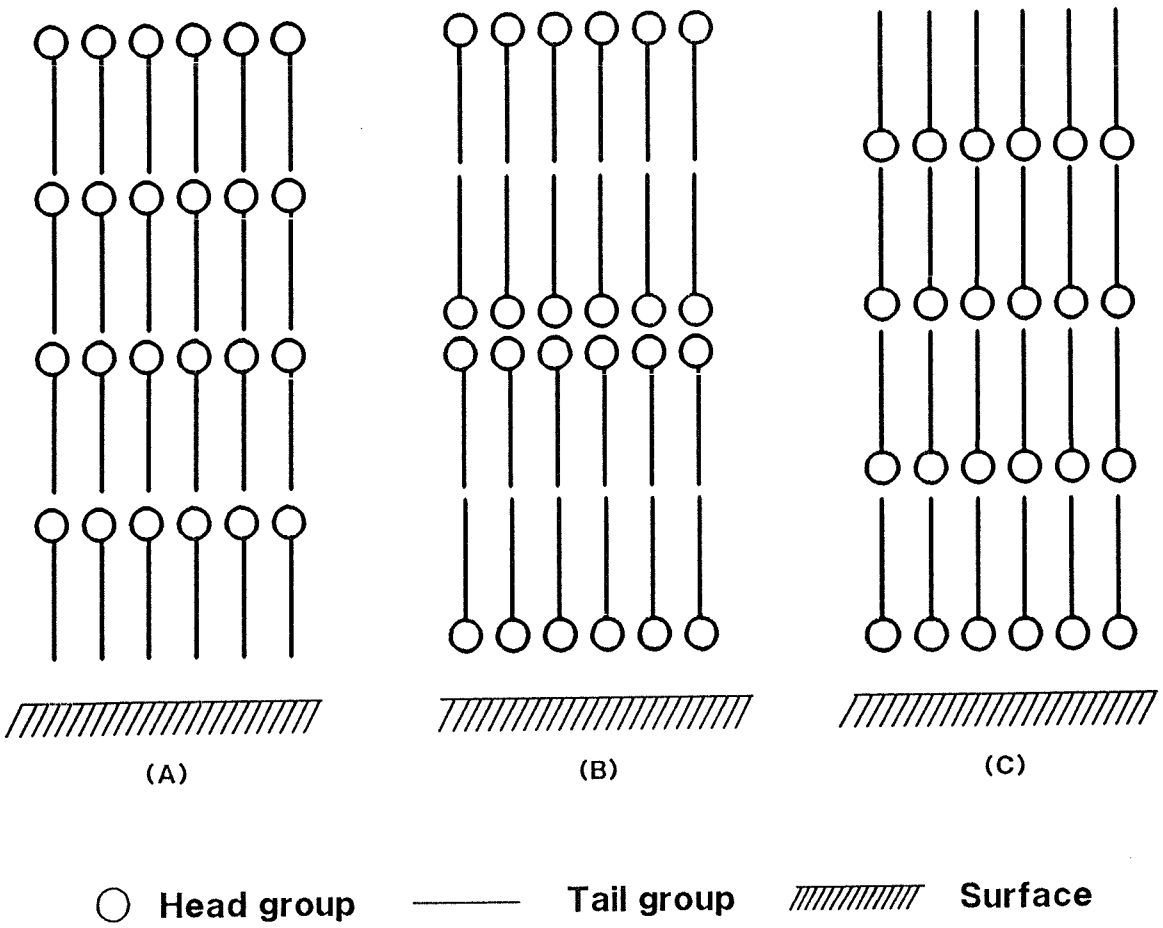

Figure 1.4. The deposition mode of Langmuir-Blodgett film on surface: (a) X-type; (b) Y-type; (c) Z-type.

diffraction[55], scanning electron microscopy[56], auger electron spectroscopy[57-60], secondary-ion mass spectroscopy(SIMS)[61], electron spin resonance[62,63], scanning tunnelling microscopy[64], and quite recently atomic force microscopy[65,66] have been utilized in LB film characterizations. The major focus in these experimental studies of LB films is the orientational and translational orientation of the layer.

1.3.1. Theoretical background of the Langmuir-Blodgett film experiment.

X-ray scattering is one of the major experimental techniques to reveal the structure of the Langmuir or Langmuir-Blodgett films. The out-of-plane scattering reflectivity $R(Q_z)$, as a function of the perpendicular scattering vector $Q_z = 4\pi/\lambda$, is related to the vertical electron density $\rho(z)$ by

$$\frac{R(Q_z)}{R_F(Q_z)} = \left| \frac{1}{\rho_w} \int \frac{d\rho}{dz} \exp(iQ_z \cdot z)\, dz \right|^2 , \qquad (1.1)$$

where R_F is the "Frensel" reflectivity expected for an interface where the electron density,$\rho(z)$, changes abruptly from zero to the density of the surface(See Figure 1.5). To analyze the X-ray data, we need a model of the layer, such as two slab model used to describe the reflectivity for several phospholipid and fatty acid monolayers[24,67]. For this case there is an approximate relation between film thickness and Q_{min}, the value of the scattering vector Q_z at the first minimum of the normalized reflective curve:

$$Q_{min}(l_T + \frac{1}{2}l_H) \simeq \frac{3}{2}\pi , \qquad (1.2)$$

where l_T is the thickness of the upper slab, representing alkyl tail and l_H is the thickness of the lower slab of the head group.

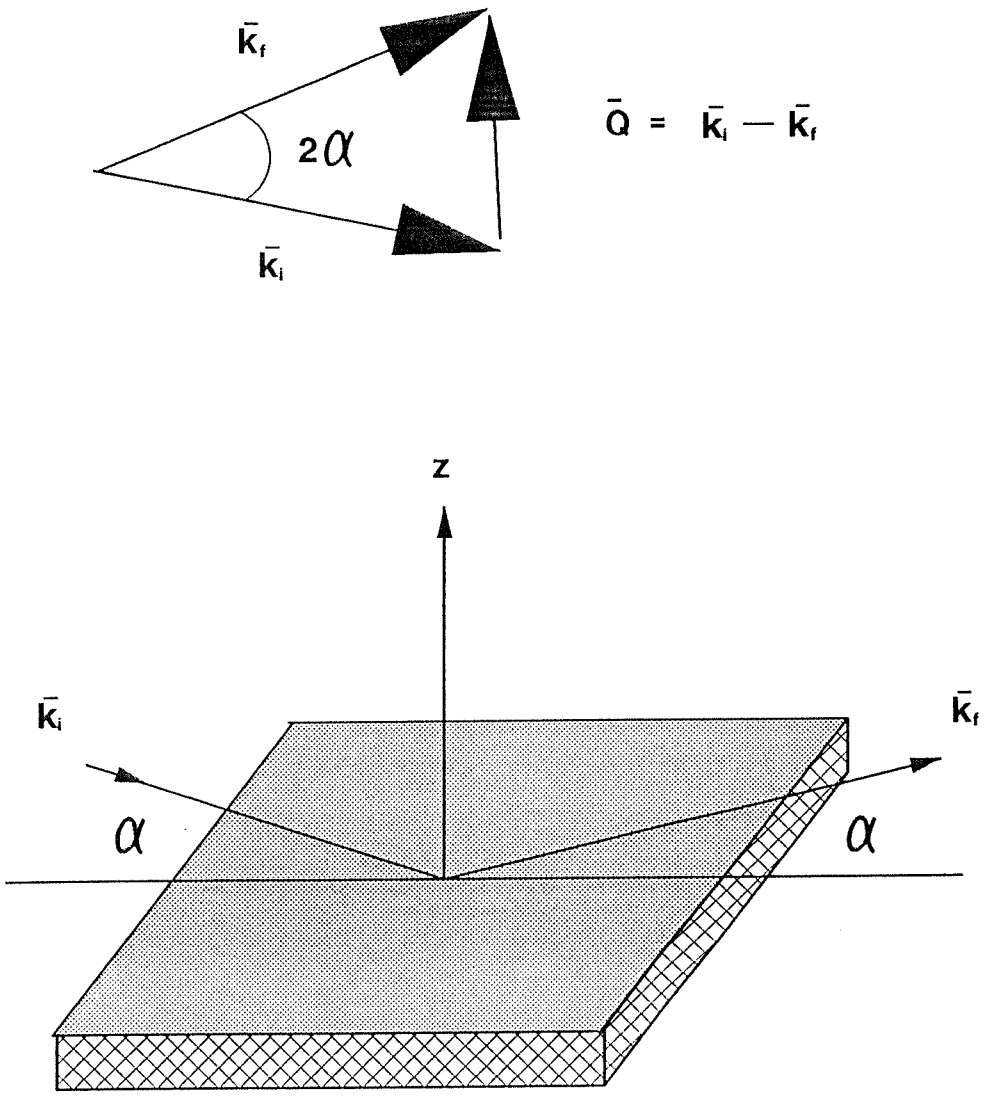

Figure 1.5. A X-ray scattering geometry for the out-of-plane mode at the sample surface.

The molecular tilt, θ, can be obtained from the comparison of the projected tail length, l_T, with the length of fully extended alkyl chain tail, l_T^o, according to

$$\cos\theta = l_T / l_T^o \quad . \tag{1.3}$$

1.3.2. The translational structure of Langmuir and Langmuir-Blodgett films.

After the pioneering work of Holley and Bernstein[68] there have been a large number of studies on the structure of a number of fatty acids on a variety of surfaces. The in-plane structure of LB film, such as lattice symmetry and lattice spacing, has normally been examined by X-ray diffraction and electron diffraction. X-ray diffraction methods have been extensively used to obtain the layer thickness of LB films. Most of the studies have been focused on the long alkyl chain fatty acids. Lesslauer *et al.*[69] studied the structure of barium stearate multilayers with between 4 and 120 layers. Lesslauer[70] extended this study to include the multilayer of myristrate and magnesium stearate. The X-ray d-spacings obtained for the long-chain fatty acid LB films are generally found to correspond to the results from crystalline modifications and these values have good agreement with those from optical techniques, such as interferometric measurements, within experimental error. Recently, Kjaer *et al.*[29] examined the structure of arachidic acid and cadmium arachidate monolayers on the water surface by using synchrotron X-ray diffraction and reflection. They confirmed that the structure of monolayer existing at a surface pressure between 1 and 25.6 mN m^{-1}, which region is known to be a liquid region in surface pressure-area isotherm, is an ordered phase with long range positional correlation (a correlation length, $\xi \approx 150$Å) and the alkyl tails are uniformly tilted away from the surface normal and the tilt angle decreases continuously from 33° to 0°. They also established the structural model from the combination of reflection and diffraction data, where the alkyl chains of the arachidic acids form a hexagonal lattice

and molecules are tilted toward a nearest neighbour chain.

In order to understand the structure of LB film of a material such as an alkanoic acid it is essential to examine the packing of aliphatic tail groups in the film. Electron diffraction is particularly useful in examining the in-plane structure of LB films, such as packing of C_2H_4 sub-units in an alkyl chain. In earlier studies, Germer and Storks[71] studied the electron diffraction from the LB films of stearic acid and the metal salts of the acid. They found that the hydrocarbon tails of barium stearate molecules form hexagonal arrays with their axes normal to the supporting surface with a nearest neighbour separation of 4.85Å and the stearic acid molecules form a close packed structure with the tails normal to the surface. Russell *et al.*[72] reported the results of a RHEED experiment on cadmimum stearate LB films deposited onto single crystal of InP, which revealed an orthorombic packing. Vogel and Wöll [73] characterized the single fatty acid monolayers deposited onto noble metal single crystals (Cu, Ag, Au) by low-energy-electron diffraction (LEED). They characterized the structure of a deposited monolayer by a lattice constant (i.e. the inter-chain distance) and found that the interchain distance of the deposited fatty acid monolayer is 4.9 ± 0.1Å. The interchain distance of 4.9Å from this experiment is in good agreement with that from another electron diffraction experiment on Cd stearate monolayer by Garoff *et al.* [34]. Garoff *et al.* studied the bond-orientational order by electron diffraction and confirmed that a cadmium stearate monolayer forms a fully hexagonally close-packed ordered structure. They also calculated a lattice spacing between alkyl chains of 4.89Å from the $<100>$ d-spacing of 4.20 ± 0.01Å. This lattice spacing between chains indicates an area per molecule of 21Å^2 on the assumption of triangular lattice structure in the plane of the surface. There have been a number of electron diffraction studies on the tricosenoic acid($C_{22}H_{45}COOH$) LB film and the details of these results, which are not central to thesis, can be found in [74].

1.3.3. Orientational ordering of LB film.

Another important structural property of the LB film is the orientational ordering of the constituent molecules. Infra-red (IR) spectroscopy is a particularly powerful tool for investigating the orientation of the alkyl chain component of molecules in an LB film relative to the substrate surface. Following Chollet's theoretical treatment[75] of the absorption of polarized IR radiation by organic monolayers, it is possible to obtain an estimate of the tilt of the molecules. Especially the absorption of the IR radiation depends on the relative orientation of the infra-red electric field and the dipole transition moment. Even with the use of FT-IR methods, Fransis and Ellison [76] and Takenaka *et al.*[77] needed to develop special techniques to accumulate the weak signal from LB film which results from the small amount of adsorbants (i.e. less than 10^{16} molecules).

Takenaka *et al.*[77] examined the structure of a stearic acid LB film on a germanium plate by IR attenuated total reflection(ATR) spectroscopy. They estimated that the stearic acid molecules in LB film are tilted away from the normal to surface at the angle from 24° to 35°. Onishi *et al.*[17] studied the mono- and multi-layer films of cadmium arachidate deposited on a glass plate using the same technique. They found that the films have a regular perpendicular alignment of the alkyl chain of arachidate molecules to the glass surface and that there is a strong interaction between the carboxylate group of arachidate molecule and the glass in monolayer. Allara *et al.*[39,40] also monitored the orientation of cadmium arachidate deposited onto silver with from 1 to 10 monolayers. They estimated that the alkyl chains of the arachidate molecules aligned nearly normal to the surface with a small tilt (less than 5° from the surface normal). They [43] also applied infra-red reflection spectroscopy to determine the structures of adsorbed monolayer films of n-alkanoic acids (n=16~22) on oxidized aluminium substrate. They found that monolayer films formed close-packed assemblies with extended alkyl tails oriented with their chain axes tilted away from the surface normal with an angle of ca. 10°. Bonnerot *et al.*

[33] studied the structures of docosanoic and ω-tricosanoic acids transferred onto carbon and aluminium substrates. They observed a structural transition with the increase of thickness of films from 1 to more than 7 layers. There was a change of the structure of the unit cell from hexagonal to orthorombic and axis of molecular chains from perpendicular to the substrate surface for the first layer to the tilt angle of 18°~23°. They also confirmed this structure by electron diffraction. Kimura *et al.*[78] studied the structure of a stearic acid LB film with upto 9 monolayers on a germanium plate by IR-ATR spectroscopy. From the analysis of CH_2 scissoring band they found that the hydrocarbon chain of stearic acid in the first monolayer is in a hexagonal or pseudo-hexagonal subcell packing where each hydrocarbon chain rotates freely around its long axis which is oriented nearly perpendicular to the surface. In the multilayer, the molecules in upper layers crystallize with the monoclinic form where the hydrocarbon chains are packed alternately and tilted away from the surface normal at the angle of about 30°. Recently, Dote and Mowery [44] examined the effect of substrate on the orientation and bonding of LB monolayers of stearic acid deposited on a polycrystalline gold and an oxidized aluminium surface by infra-red reflectance-absorption spectroscopy (IRRAS). They found that the stearic acid molecules on aluminium form a metal-carboxylate structure with a canted orientation with respect to the substrate surface in order to accommodate the nearly perpendicular configuration of the alkyl chains. However, they found that on gold the carboxylate group is primarily symmetrically bonded to the substrate with the alkyl chains tilted away from the surface normal. They also observed a molecular rearrangement as the films age. In a number of studies on the orientation of fatty acid molecules in LB monolayer films using polarized infra-red spectroscopy the alkyl chains of the fatty acids have found to be tilted away from the normal to the substrate surface at an angle of between 8° and 25°. On the other hand , the molecules in the multilayers of fatty acid salts have been found to be almost perpendicular to the substrate [33].

X-ray and electron diffraction techniques have also been utilized to estimate the orientational properties of the molecules in the LB films. Outka *et al.* [16] used the near-edge x-ray absorption techniques (NEXAFS) to determine the orientation of the arachidic acid molecule and its salt in a monolayers on a Si(1,1,1) surface. In their study, the hydrocarbon chains of the cadmium arachidate monolayer is estimated to lie within 15° from the surface normal, the hydrocarbon chains of the calcium arachidate monolayer is estimated to be tilted by $33 \pm 5°$ from the surface normal, but the arachidic acid molecules in the monolayer do not form any ordered phase at all. Fromherz *et al.*[20] also utilized the X-ray scattering to characterize the orientation of cadmium salt of fatty acids from myristate($n=14$) to lignocerate($n=24$). They obtained film thickness from model calculations of the scattering intensity and estimated the molecular tilt of about 16° and 17° for cadmium stearate and cadmium arachidate respectively. Garoff *et al.*[34] estimated the orientation of a cadmium stearate monolayer on a SiO surface from their transmission electron diffraction results. They estimated that the long axes of the molecules are tilted away from the surface normal by 8° but the direction of tilt(the azimuthal angle) is not ordered. Recently, Robinson *et al.*[79] analyzed the in-plane structures of fatty acids in LB films by RHEED. They concluded that the saturated fatty acid molecules in the LB films are tilted with a tilt angle of 17°~36° but the molecular tilt is essentially independent of the deposition pressure. Table 1.1 summarizes some results of molecular tilts of saturated fatty acids measured by experiment.

Table 1.1. Summary of molecular tilt from experiments.

Sysytem	Tilt/°	Experimental method	Ref.
Stearic acid/Ge	24-35	IR	77
Stearic acid/Ge	30	IR	78
Cd stearate/SiO	8	electron diffraction	34
Cd stearate/glass	16	X-ray scattering	20
Stearic acid	10	IR	43
Cd stearate/Silica	0	Fluorescence anisotropy	50
Arachidic acid	10	IR	43
Cd arachidate/Si	15	NEXAFS	16
Ca arachidate/Si	33	NEXAFS	16
Cd arachidate	17	X-ray scattering	20
Cd arachidate/glass	0	IR	17
Cd arachidate/silver	<5	IR	39,40

1.4. Application of Langmuir-Blodgett films.

There has been considerable activity in Langmuir-Blodgett film research to develop various applications for the film[80]. According to recent reviews[8] on the applications of Langmuir-Blodgett films, most effort is being applied to develop various materials for use in the electronics industry. The long term objective of this may be the possible development of super-molecular assemblies for large memory storage, molecular switching and superconducting devices, where the LB films form an essential part of the structure. The factors which govern the applicability of the LB films are the precise control over the thickness of the film down to nanometers, the orientation and architecture of the molecules and the uniformity of the films. Other promissing applications of the LB films are non-linear applications, such as acoustic surface wave devices[81], infra-red detectors and optoelectronics devices[80] where materials with non-centrosymmetric structures are required. Another promising application may be the enhanced device processing. In integrated circuit technology the demand for faster speeds and larger memory has led to a continuous improvement of microlithographic techniques for fabricating ever decreasing circuit elements. This requires sub-micron resolution and has necessitated a move away from conventional photo-lithography to more sophisticated technology such as X-ray or electron beam lithography. LB films have been already tested as sensitive positive and negative resists in producing structures using ultra-high resolution electron beams[83,84]. Another potential application is the molecular sieves and filters, for example LB films as synthetic membraines for ultra filtration, gas separation and reverse osmosis [85,86,87].

1.5. Computer simulations of Langmuir and Langmuir-Blodgett films.

It may be worth reviewing other works on the modeling of Langmuir, Langmuir-Blodgett films and related materials using computer simulation before discussing the results of our work. Van der Ploeg and Berendsen published one of

the papers on molecular dynamics simulation of a bilayer lipid membrane in 1982[88]. In the study they built a system with a bilayer membrane of 16 decane molecules ($C_{10}H_{22}$) composed of a chain of the pseudo-atoms representing CH_2 groups in an alkyl chain. They constrained the bond length of the molecules by the SHAKE method [89,90] and performed the simulation using Verlet algorithm[91] with a periodic boundary condition in two-dimensions(x,y). They used a molecular area of 25Å^2 per molecule. They modeled the interaction using Lennard-Jones potential for all intramolecular and intermolecular pairs and dihedral potential function based on the that of Ryckaert and Bellemans[92,93]. Their results have a good agreement between bond orientational order parameter, S_{CD}, determined from deuterium NMR data and that from the calculation. Cardini *et al.*[94] performed molecular dynamics for the caracterization of LB monolayer. They used 90 molecules of 20 pseudo-atoms in a triangular lattice with interchain separation of 4.9Å. They observed molecular tilt angle of 40° directing to nearest neighbour molecule. Another important result of the calculation is power spectra for the dynamics of arachidate monolayer. The frequencies calculated(0 - 500 cm^{-1}) are in the far infra-red spectral region. Baremann *et al.*[95] carried out another molecular dynamics calculation on the same system with same starting condition mentioned above with different molecular area, 21, 26 and 35Å^2. Harris and Rice[96] carried out a molecular dynamics simulation of a Langmuir monolayer of pentadecanoic acid($C_{14}H_{29}COOH$) on water. They represented the effect of water by an effective surface 9-3 potential without explicit electrostatic interactions. Hautman and Klein[97] performed molecular dynamics simulations of hexadecanethiol ($CH_3(CH_2)_{15}SH$) chains on a gold(111) surface. In this study, the molecules consisted of spherical pseudo-atoms connected by rigid bond(d_{cc} = 1.53Å, d_{cs} = 1.82Å). They observed the effect of C-S bond orientation against the surface on the molecular orientation by constraining the angle between C-S bond and the surface normal. They carried out the simulation at 300K using 90 molecules with interchain separation of 4.97Å. They found the different molecular

tilts in the model with and without the constraint on the C-S bond of 28° and 19.6° respectively.

1.5. An overview of the later chapters.

We begin with a brief discussion about the basic concepts of statistical mechanics useful for the computer simulation and the molecular and potential model for the simulation in chapter 2. In chapter 3 we discuss the results of molecular dynamics simulation of Langmuir-Blodgett monolayer of stearic acid using the explicit-hydrogen model, including the results of energy minimisation using the explicit-hydrogen and the united-atom models. In chapter 4 we present the result of molecular dynamics simulation of a stearic acid monolayer on hydrophilic surface using the all-atom model as well as the potential model for the all-atom head group. In chapter 5 we discuss the result of molecular dynamics simulation of stearic acid bilayer using the all-atom model where we are discussing the modification of interaction model in the system. Finally we summarize the results from this work in chapter 6.

References.

[1] G.G. Roberts(Ed.), *Langmuir-Blodgett Films*, Plenum Press, New York 1990.

[2] A. Pockels, Nature(London), **48**, 152 (1893).

[3] I. Langmuir, J. Am. Chem. Soc., **37**, 1139 (1915); **38**, 2221 (1916); **40**, 1361 (1918); I. Langmuir, J. Am. Chem. Soc., **39**, 1848 (1917).

[4] I. Langmuir, Trans. Faraday Soc., **15**, 62 (1920).

[5] K.B. Blodgett, J. Am. Chem. Soc., **57**, 1007 (1935).

[6] K.B. Blodgett, Phys. Rev., **51**, 964 (1937).

[7] G.L. Gaines. Jr., *Insoluble Monolayers at Liquid-gas Interfaces,* Wiley, New York 1966.

[8] G.G. Roberts, Adv. Phys., **34**, 475 (1985); R.M. Nicklow, M. Pomerantz, and A. Semuller, Phys. Rev, **68**, 77 (1980).

[9] A.E. Alexander, J. Chem. Soc., London, **1**, 778 (1939).

[10] Y.K. Levine, A.I. Bailey and M.H.F. Wilkins, Nature, **220**, 577 (1968).

[11] P.S. Vincent, W.A. Barlow, F.F. Boyle, J.A. Finney and G.G. Roberts, Thin Solid Films, **60**, 265 (1979).

[12] R. Jones, R.H. Tregold and P. Hodge, Thin Solid Films, **99**, 25 (1983).

[13] R. Jones, R.H. Tregold, A. Hoorfar and R.A. Allen, Thin Solid Films, **134**, 57 (1985).

[14] S.J. Mumby, J.F. Rabolt and J.D. Swalen, Thin Solid Films, **133**, 161 (1985).

[15] Y. Nishikata, M. Katimoto, A. Marikawa, and Y. Imai, Thin Solid Films, **160**, 15 (1988).

[16] D.A. Outka, J. Stor, J.P. Rabe and J.D. Swalen, J. Chem. Phys., **88**(6), 4076 (1988).

[17] T. Ohnish, A. Ishitani, H. Ishda, N. Yamamoto and H. Tsubomura, J. Phys. Chem., **82**, 1989 (1978).

[18] S.W. Barton, B.N. Thomas, E.B. Flom and S.A. Rice, J. Chem. Phys., **89**, 2257 (1988).

[19] V. Skida, M. Filipkowski, A.F. Garito and J. Kent Blasie, Phys. Rev., B, **34**, 5826 (1986).

[20] P. Fromherz, U. Oelschlagel and W. Wilke, Thin Solid Films, **159**, 421 (1988).

[21] V. Skita, W. Richardson, M. Filipkowski, A. Garito and J.K. Blasie, J. Phys.(Paris), **47**, 1849 (1986).

[22] L.B. Hazell, A.A. Rizvi, I.S. Brown and S. Ainsworth, Spectrochemica Acta, **40B**(5/6), 739 (1985).

[23] M.R. Buhaenko, M.J. Grundy, R.M. Richardson and S.J. Roser, Thin Solid Films, **159**, 253 (1988).

[24] K. Kjaer, J. Als-Nielsen, C.A. Helm, P. Tippmann-Krayer and H. Mohwald, Thin Solid Films, **159**, 17 (1988).

[25] K. Kjaer, J. Als-Nielsen, C.A. Helm, L.A. Laxhuber and H. Mowald, Phys. Rev. Letters, **58**, 2224 (1987).

[26] P. Dutta, J.B. Peng, B. Lin, J.B. Ketterson, M. Prakash, P. Georgopoulos and S. Ehrlich, Phys. Rev. Letters, **58**, 2228 (1987).

[27] B. Lin, J.B. Peng, J.B. Ketterson, P. Dutta, B.N. Thomas, J. Buontempo and S.A. Rice, J. Chem. Phys., **90**, 2393 (1989).

[28] S.G. Wolf, M. Deutsch, E.M. Landau, M. Lahav, L.Leiserowitz, K. Kjaer and J. Als-Nielsen, Science, **242**, 1286 (1988).

[29] K. Kjaer, J. Als-Nielsen. C.A. Helm, P. Tippman-Krayer and H. Mohwald, J. Phys. Chem., **93**, 3200 (1989).

[30] L.B. Hazell, I.S. Brown and F. Freisinger, Surface and Interface Analysis, **8**, 25 (1986).

[31] K. Kobayashi, K. Takaoka and Ochiai, Thin Solid Films, **159**, 267 (1988).

[32] J.P. Rabe, J.D. Swalen, D.A. Outka and J. Stohr, Thin Solid Films, **159**, 275 (1988).

[33] A. Bonnerot, P.A. Chollet, H. Frisby and M. Hoclet, Chem. Phys., **97**, 365

(1985).

[34] S. Garoff, H.W. Deckman, J.H. Dunsmuir, M.S. Alvarez and J.M. Bloch, J. Phys. (Paris), **47**, 701 (1986).

[35] J.A. Champman and D. Tabor, Proc. Roy. Soc. A, **242**, 96 (1957).

[36] G. Bolbach, R. Beavis, S. Della Negra, C. Deprun, W. Ens, Y. Lebeyec, D.E. Main, B. Schueler and K.G. Standing, Nuclear Instruments and Methods in Physics Research, **B30**, 74 (1988).

[37] A. Fischer and E. Sackmann, J. Phys. (Paris), **45**, 517 (1984).

[38] S. Palacin, P. Leiseur, I. Stefanelli and A. Barraud, Thin Solid Films, **159**, 83 (1988).

[39] D.L. Allara and R.G. Nuzzo, Langmuir, **1**, 45 (1985).

[40] D.L. Allara and R.G. Nuzzo, Langmuir, **1**, 52 (1985).

[41] M.C.Porter, T.B. Bright, D.L. Allara and C.E.D. Chidsey, J. Am. Chem. Soc., **109**, 3559 (1987).

[42] D.D. Saperstein, J. Phys. Chem., **90**, 1408 (1986).

[43] D.L. Allara and J.D. Swalen, J. Phys. Chem., **86**, 2700 (1982).

[44] J.L. Dote and R.L. Mowery, J. Phys. Chem., **92**, 1571 (1988).

[45] M. Vandevyver, Thin Solid Films, **159**, 243 (1988).

[46] C.A. Jones, M.C. Petty, G.G. Roberts, G. Davies, J. Yarwood, N.M. Ratcliffe and J.W. Barton, Thin Solid Films, **155**, 187 (1987).

[47] H.G. Braun, H.Fuchs and W.Schrepp, Thin Solid Films, **159**, 301 (1988).

[48] S.B. Dierker, C.A. Murray, J.D. LeGrange and N.E. Schlotter, Chem. Phys. Letters, **137**, 453 (1987).

[49] R.R. Highfield, R.K. Thomas, P. Cummings, D. Gregory and J. Mingis, Thin Solid Films, **99**, 165 (1983).

[50] J.D. LeGrange, H.E. Riegler, W.P. Zurawsky and S.F. Scarlata, J. Chem. Phys., **90**, 3838 (1989) .

[51] J.E. Riegler and J.D. LeGrange, Phys. Rev. Lett., **61**, 2492 (1988).

[52] B. Moore, C.M. Knobler, D. Broseta and F. Rondelez, J. Chem. Soc., Faraday Trans.2, **82**, 1753 (1986).

[53] D.J. Keller, H.M. McConnell, V.T. Moy, J. Phys. Chem., **90**, 2311 (1986).

[54] M.W. Kim, S.-N. Liu, Am. Inst. Phys. Conf. Proc. **172**, 477 (1986).

[55] C.E.D. Chidsey, G.-Y. Liu, P. Rowntree, G. Scoles, J. Chem. Phys., **91**, 4421 (1989).

[56] P. Fromherz, C. Kemper, E. Maass, Thin Solid Films, **159**, 405 (1988).

[57] C. Mori, H. Noguchi, M. Mizuno and T. Wadanabe, Jpn J. Appl. Phys., **19**, 725 (1980).

[58] A. Barraud, C. Rosilio and A. Ruaudel-Teixier, Thin Solid Films, **68**, 7 (1980).

[59] T. Smith, J. Appl. Phys., **43**, 2964 (1972).

[60] J.M. Green and L.R. Falkner, J. Am. Chem. Soc., **105**, 2950 (1983).

[61] F. Toyakawa, H. Abe, K. Furoya and T. Kikuchi, Surf. Sci., **133**, L429 (1983).

[62] S.-I. Kuroda, K. Ikegami, K. Saito, M. Saito and M. Sugi, Thin Solid Films, **159**, 285 (1988).

[63] J. Richard, M. Vandevyver, P. Leseiur, A. Ruaudel-Teixier, A. Barraud, R. Bozio and C. Pecile, J. Chem. Phys., **86**, 2428 (1987).

[64] J.H. Coombs, J.B. Pethica and M.E. Welland, Thin Solid Films, **159**, 293 (1988).

[65] A.L. Weisenhorn, M. Egger, F. Ohnesorage, S.A.C. Gould, S.-P. Heyn, H.G. Hansma, R.L. Sinsheimer, H.E. Gaub and P.K. Hansma, Langmuir, **7**, 8 (1991).

[66] H.G. Hansma, S.A.C. Gould, P.K. Hansma, H.E. Gaub, M.L. Longo and J.A.N. Zasadzinski, Langmuir, **7**, 1051 (1991).

[67] C.A. Helm, H. Mohwald, K. Kjaer, J. Als-Nielsen, Europhys. Lett., **4**, 697 (1987).

[68] C. Holly and C. Bernstein, Phys. Rev., **49**, 403 (1936): **52**, 525 (1937).

[69] W. Lesslauer and J.K. Blasie, Biophys.J., **12**, 175 (1972).

[70] W. Lesslauer, Acta Crystallogr.B **30**, 1927 (1974).

[71] L.H. Germer and K.H. Storks, J. Chem. Phys., **6**, 280 (1938).

[72] G.J. Russell, M.C. Petty, I.R. Peterson, G.G. Roberts, J.P. Lloyd and K.K. Kan, J. Mater. Sci., **3**, 25 (1984).

[73] V. Vogel and C. Woll, Thin Solid Films, **159**, 429 (1988).

[74] I.R. Peterson, G.J. Russell and G.G. Roberts, Thin Solid Films, **109**, 371 (1983); I.R. Peterson and G.J. Russell, Br. Polym. J., **17**, 364 (1985); I.R. Peterson and G.J. Russell, Thin Solid Films, **134**, 143 (1985).

[75] P.A. Chollet, Thin Solid Films, **68**, 13 (1980).

[76] S.A. Francis and A.H. Ellison, J. Optical Soc. Am., **49**, 131 (1959).

[77] T. Takenaka, K. Nogami, H. Gotoh and R. Gotoh, J. Colloid Interface Sci., **35**, 395 (1971).

[78] F. Kimura, J. Umemura and T. Takenaka, Langmuir, **2**, 96 (1986).

[79] I. Robinson, D.J. Jarvis and J.R. Sambles, J. Phys. D: Appl. Phys., **24**, 347 (1991).

[80] G.G. Roberts and C.W. Pitt, *Langmuir-Blodgett Films, 1982*, Elesevier Scientific Publishing Co. 1983.

[81] J.D. Maines and E.G.S. Paige, IEE Rev., **120**, 1078 (1973).

[82] S. Kowel, Thin Solid Films, **152**, 377 (1987).

[83] A. Banerjie and J.B. Lando, Thin Solid Films, **68**, 67 (1980).

[84] G. Fariss, J. Lando and S. Rickert, J. Mater. Sci., **18**, 2603 (1983).

[85] T.R. Chern, W.J. Koros, H.B. Hopfenberg and V.T. Starrett, *Material Science of Synthetic Membranes*, ACS Symp. Ser., **269**, Washington, p.25 (1985).

[86] G.D. Ross and J.A. Quinn, Science, **159**, 636 (1967).

[87] O. Albrecht, A. Laschewsky and H. Ringsdorf, J. Membrane Sci., **22**, 187 (1985).

[88] P. van der Ploeg and H.J.C. Berendsen, J. Chem. Phys., **76**, 3271 (1982).

[89] J.P. Ryckaert, G. Ciccotti and H.J.C. Berendsen, J. Comput. Sci., **23**, 327 (1977).

[90] W.F. van Gunsteren and H.J.C. Berendsen, Mol. Phys., **34**, 1311 (1977).

[91] L. Verlet, Phys. Rev., **159**, 98 (1967).

[92] J.P. Ryckaert and A. Bellemans, Faraday Discuss. Chem. Soc., **64**, 95 (1978).

[93] J.P. Ryckaert and A. Bellemans, Chem. Phys. Lett., **30**, 123 (1975).

[94] G. Cardini, J.P. Bareman and M.L. Klein, Chem. Phys. Lett., **145**, 493 (1988).

[95] J.P. Bareman, G. Cardini and M.L. Klein, Phys. Rev. Lett., **60**, 2152 (1988).

[96] J. Harris and S.A. Rice, J. Chem. Phys., **89**, 5898 (1988).

[97] J. Hautman and M.L. Klein, J. Chem. Phys., **91**, 4994 (1989).

[98] A.W. Adamson, *Physical Chemistry of Surfaces.*, Wiley, New York (1976).

CHAPTER TWO.

Computer Simulation.

2. COMPUTER SIMULATION.

Computer simulation is an important and valuable tool in statistical mechanics because they provide essentially exact results for the properties of many-body systems where the partition function can not be solved analytically. Using computer simulation, we can test the results of approximate statistical mechanical theories, adjust models of intermolecular and intramolecular interactions so that observable properties agree with experiment and obtain a detailed picture of the structure and dynamics at a molecular level.

Although computer simulation has many advantage there are a number of difficulties which need to be mentioned. Probably the weakest aspect of the method is that they normally can deal with only a very small number of molecules, compared with typically 10^{23} molecules in a macroscopic system. Recently, there have been a number of studies using parallel algorithms and computer architectures which consider more than 10^6 molecules[1,2], but most simulations consider between a hundred and a thousand atoms and use periodic boundary conditions to minimise surface effect.

In this chapter we will discuss the basic statistical mechanical concepts used in computer simulation, and the methods of computer simulation. We will also describe the potential models and method of constraint in molecular dynamics used in this work.

2.1. Statistical mechanical concepts in computer simulation.

The behaviour and properties of a macroscopic system which is composed of a large number of particles ($>10^{23}$) can be defined by a few parameters such as pressure, volume and temperature. The relationships between these macroscopic properties are the subject of thermodynamics. Although macroscopic measurements show that the thermodynamic properties of an experimental system (its temperature, pressure, composition, etc...) remain the same in the absence of an external stimulus,

the microscopic structure of the system will be continuously changing, due to the redistribution of the available energy between one particle and another as the result of intermolecular collisions.

To specify the microscopic state of a system made up of N molecules it is necessary to specify 3N positions and 3N momenta(the position may include the orientation and the conformation of the molecule). These variables evolve according to Hamilton's equations:

$$\dot{\mathbf{r}}_i = \frac{\partial H}{\partial \mathbf{p}_i} \tag{2.1}$$

$$\dot{\mathbf{p}}_i = -\frac{\partial H}{\partial \mathbf{r}_i} \tag{2.2}$$

where i = 1,...,N.

If we wait for a long time to measure some macroscopic property, the system will eventually flow through all the possible microscopic states consistent with the constraint imposed to control the system. For a system of N particles some property A at a particular point in its phase space Γ is denoted as $A(\Gamma)$. With the evolution of time $A(\Gamma)$ will change. We can reasonably assume that macroscopic property A_{obs} observed experimentally is the time average of $A(\Gamma)$ taken over a long time interval:

$$\begin{aligned} A_{obs} &= \langle A \rangle_{time} = \langle A(\Gamma(t)) \rangle_{time} \\ &= \lim_{t \to \infty} \frac{1}{t} \int_0^t A(\Gamma(t))\, dt \end{aligned} \tag{2.3}$$

2.1.1. Ensembles.

In the late ninteenth century it was not possible to solve these 6N coupled equations for interesting systems and the discipline of statistical mechanics was developed to avoid the problem of calculating a time average. The fundamental axiom of statistical mechanics is that during an observation of an isolated system, every microscopic state occurs with equal probability. When we consider a system with N molecules there will be a large number of microscopic states of the system corresponding to the same macroscopic state. The concept of an ensemble, first introduced by Gibbs[3], is a collection of such microscopic states of the system, all with the same macroscopic properties. A typical ensemble is the canonical ensemble where the systems are closed to molecular transport and are of fixed volume, but are separated from their neighbours by diathermal walls so that heat energy can be transfered between the systems. The systems are in thermal equilibrium and are at constant temperature. This canonical ensemble is a constant-N,V,T ensemble. The fundamental axiom of statistical mechanics can be used to show that a state i with energy E_i occurs with a probability

$$p(E_i) = \frac{\exp(-\beta E_i)}{Q_{NVT}} \qquad (2.4)$$

where Q_{NVT} is the canonical partition function, $\beta = 1/k_BT$, and k_B is Boltzmann's constant. The partition function is the sum of the Boltzmann factors over all possible states of the ensemble

$$Q_{NVT} = \sum_i \exp(-\beta E_i) \; . \qquad (2.5)$$

For a classical liquid of N atoms

$$Q_{NVT} = \frac{1}{\Lambda^{3N} N!} \int dr^{(N)} \exp(-\beta V(r^{(N)})) \qquad (2.6)$$

where $\Lambda = (h^2/2\pi mkT)^{1/2}$ is the de Broglie thermal wavelength of an atom of mass m, which comes from the integration over the 3N momenta and $V(r^{(N)})$ is the total potential energy of the N atoms at position $r^{(N)}$. Q_{NVT} is central to the calculation of the thermodynamic and structural properties of canonical ensemble and is related to the Helmholtz free energy, A, by

$$A = -k_B T \ln Q_{NVT} \; . \qquad (2.7)$$

The volume dependence of A is one route to the pressure e.g.

$$p = -\left(\frac{\partial A}{\partial V}\right)_{TN} = \frac{kT}{Q_{NVT}} \left(\frac{\partial Q_{NVT}}{\partial V}\right)_{TN} \; . \qquad (2.8)$$

Some straight forward manupulation leads to the virial equation for a fluid with a pair-additive intermolecular potential

$$p = \rho k_B T - \frac{1}{3V} \langle W \rangle_{NVT} \qquad (2.9)$$

where $<W>_{NVT}$ is the virial and is a sum over distinct pair interactions

$$W = \sum_{i<j} \sum \mathbf{r}_{ij} \cdot \nabla_{r_{ij}} V(r^{(N)}) \; . \qquad (2.10)$$

A microcanonical ensemble is a collection of systems which have the same number of particles, N, the same volumes, V, and same energies, E.

The state of the system can be characterized by the microcanonical partition function, Ω_{NVE}, which has the form

$$\Omega_{NVE} = \sum_{\Gamma} \delta(H(\Gamma)-E) \qquad (2.11)$$

where δ is the Kronecker-delta function for the case of discrete energies and is the Dirac delta function for the continuous energy states. $\delta(H(\Gamma)-E)$ is a weight function for the microcanonical ensemble and Ω_{NVE} is the number of microscopic states with fixed N, V and energy lying between E and $E+\delta E$.

The entropy in the canonical ensemble is related to the microcanonical partition function by

$$S = k_B \ln Q_{NVT} \cdot \qquad (2.12)$$

The entropy is a measure of the area of the constant energy hypersurface in this phace space.

The method of molecular dynamics approximately generates states in the microcanonical ensemble since the solution of the equation of momenta conserves energy. The calculation of the configurational integral is the central problem of classical statistical mechanics and the Monte Carlo simulation technique is a computational method of evaluating this integral.

Expansion for ensemble averages, such as virial W, are independent of the choice of ensemble as the thermodynamic limit ($N \to \infty$, $V \to \infty$, $N/V \to \infty$) is approached. Expansions relating fluctuations to thermodynamic observables are ensemble dependent. For example the specific heat C_v for N atoms is

$$C_v = \frac{3}{2}Nk_B + \frac{1}{k_BT}\langle(\delta V)^2\rangle_{NVT} \qquad (2.13)$$

or

$$C_V = \frac{3}{2}Nk_B\left[1 - \frac{2}{3Nk_B^2T^2}\langle(\delta V)^2\rangle_{NVE}\right]^{-1} \qquad (2.14)$$

where $<(\delta A)^2>_{ens} = <(A-<A>_{ens})^2>_{ens}$.

Equation (2.13) relates the specific heat C_v to variables observable in the canonical ensemble and (2.14) relates C_v to variables observable in the microcanonical ensemble.

2.2. Structural properties.

2.2.1. Distribution functions.

The microscopic structure of simple fluids or liquids can be characterized by a set of equilibrium probability densities and distribution functions for the positions of the molecules. These set of functions provide a quantitative measure of the correlations between the positions of different molecules.

In the canonical ensemble, the normalized probability of finding a system of N identical molecules in positions, $\mathbf{r}^{(N)}$, with momenta, $\mathbf{p}^{(N)}$, is

$$f^{(N)}(\mathbf{r}^{(N)},\mathbf{p}^{(N)}) = \frac{\exp[-\beta H(\mathbf{r}^{(N)},\mathbf{p}^{(N)})]}{N!\,h^{3N}Q_{NVT}} \; . \qquad (2.15)$$

The N-body probability density $P^{(N)}(\mathbf{r}^{(N)})$ with respect to the coordinates of the N particles can be obtained by integrating equation (2.15) over all momenta

$$P^{(N)}(\mathbf{r}^{(N)}) = \int \cdots \int d\mathbf{p}^{(N)}\, f^{(N)}(\mathbf{r}^{(N)}, \mathbf{p}^{(N)}) \quad . \tag{2.16}$$

Then $P^{(N)}(\mathbf{r}^{(N)})$ is just the probability of finding identical particles at position $\mathbf{r}^{(N)}$ in the volume element $d\mathbf{r}^{(N)}$ regardless of the values of their momenta and is given by

$$P^{(N)}(\mathbf{r}^{(N)}) = \frac{\exp(-\beta V(\mathbf{r}^{(N)}))}{Z_{NVT}} \quad . \tag{2.17}$$

This probability density function is still of little practical value since it can not be measured. The probability of finding particle 1 in $d\mathbf{r}_1$ at $\mathbf{r}_1$, particle 2 in $d\mathbf{r}_2$ at $\mathbf{r}_2$, ..., particle n in $d\mathbf{r}_n$ at $\mathbf{r}_n$, irrespective of the positions of the remaining (N-n) particles is obtained by integrating equation (2.17) over the coordinates of remaining (N-n) particles:

$$\begin{aligned} P^{(n)}(\mathbf{r}_1, \ldots, \mathbf{r}_n) &= \frac{1}{Z_{NVT}} \int \cdots \int \exp\left(\frac{-V(\mathbf{r}^{(N)})}{kT}\right) d\mathbf{r}_{n+1} \cdots d\mathbf{r}_N \\ &= \int \cdots \int P^{(N)}(\mathbf{r}^{(N)})\, d\mathbf{r}_{n+1} \cdots d\mathbf{r}_N \quad . \end{aligned} \tag{2.18}$$

The most important distribution functions for understanding the structure of a condensed phase are the single-particle density distribution function $P^{(1)}$ and the pair or two-particle density distribution function $P^{(2)}$.

The single particle density function is obtained by integrating the probability density function, $P^{(N)}(\mathbf{r}^{(N)})$ over all coordinates except for $\mathbf{r}_1$ and multiplying N, which is the way of choosing one particle from N identical particles:

$$P^{(1)}(\mathbf{r}_1) = \frac{N}{Z_{NVT}} \int \cdots \int \exp\left(\frac{-V(\mathbf{r}^{(N)})}{kT}\right) d\mathbf{r}_2 \cdots d\mathbf{r}_N \quad . \tag{2.19}$$

For a homogeneous isotropic fluid of N identical atoms this reduces to

$$P^{(1)}(\mathbf{r}_1) = \frac{N}{V} = \rho \,. \tag{2.20}$$

The two particle density distribution function $P^{(2)}(\mathbf{r}_1,\mathbf{r}_2)$ can be obtained by integrating $P^{(N)}(\mathbf{r}^{(N)})$ over the particle coordinates $\mathbf{r}_3$, ... , $\mathbf{r}_N$ and by multiplying by the number of ways choosing two particles from N, N!/(N-2)! :

$$P^{(2)}(\mathbf{r}_1,\mathbf{r}_2) = \frac{N!}{(N-2)!}\frac{1}{Z_{NVT}}\int\cdots\int \exp\left(\frac{-V(\mathbf{r}^{(N)})}{kT}\right) d\mathbf{r}_3 \cdots d\mathbf{r}_N \,. \tag{2.21}$$

This function is usually normalized to a form defined by

$$g^{(2)}(\mathbf{r}_1,\mathbf{r}_2) = \frac{P^{(2)}(\mathbf{r}_1,\mathbf{r}_2)}{P^{(1)}(\mathbf{r}_1)\,P^{(1)}(\mathbf{r}_2)} \,. \tag{2.22}$$

This function is a pair correlation function for two particles at $\mathbf{r}_1$ and $\mathbf{r}_2$. For a homogeneous and isotropic fluid of spherical particles $P^{(2)}(\mathbf{r}_1,\mathbf{r}_2)$ depends only upon the separation between the two particles.

$$g^{(2)}(r_{12}) = \frac{P^{(2)}(r_{12})}{P^{(1)}(\mathbf{r}_1)P^{(1)}(\mathbf{r}_2)} \tag{2.23}$$

where $r_{12} = |\mathbf{r}_1 - \mathbf{r}_2|$.

From equation (2.20) $P^{(1)}(\mathbf{r}_1) = P^{(1)}(\mathbf{r}_2) = \rho$ so

$$g^{(2)}(r_{12}) = \frac{N(N-1)}{\rho^2 Z_{NVT}} \int \cdots \int dr^{(N-2)} \exp(-\beta V(r^{(N)})) \quad . \qquad (2.24)$$

This function is usually referred to as the radial distribution function. The radial distribution function measures the probability of finding a particle at a given distance from an atom fixed at the origin. At large distances

$$\lim_{r_{12} \to \infty} g^{(2)}(r_{12}) = 1 \quad . \qquad (2.25)$$

The radial distribution function is quite important in the study of condensed phases because this quantity can be related to the thermodynamic properties of the phase and experimentally we can measure the radial distribution function from radiation scattering experiments such as X-ray or neutron scattering.

2.3. Computer simulation methods.

2.3.1. Energy minimisation.

From a computational point of view, the minimisation of energy falls into the general area of non-linear optimisation [4]. Given a set of independent variables $\mathbf{x} = (x_1, x_2, \ldots, x_n)$ and an objective function $V = V(\mathbf{x})$, energy minimisation finds the set of values for the independent variables, $\mathbf{x}$, for which the objective function V has its minimum value (Figure 2.1(a)). Energy minimisations in molecular system are normally restricted to the prediction of static structures and of those properties which can be described within an harmonic dynamical approximation since there is no explicit consideration of motion of atoms in energy minimisation. However, a real difficultiy with this technique is that most potentials have many local minima in their potential surface as shown in Figure 2.1(b) and in this case it is difficult to find the

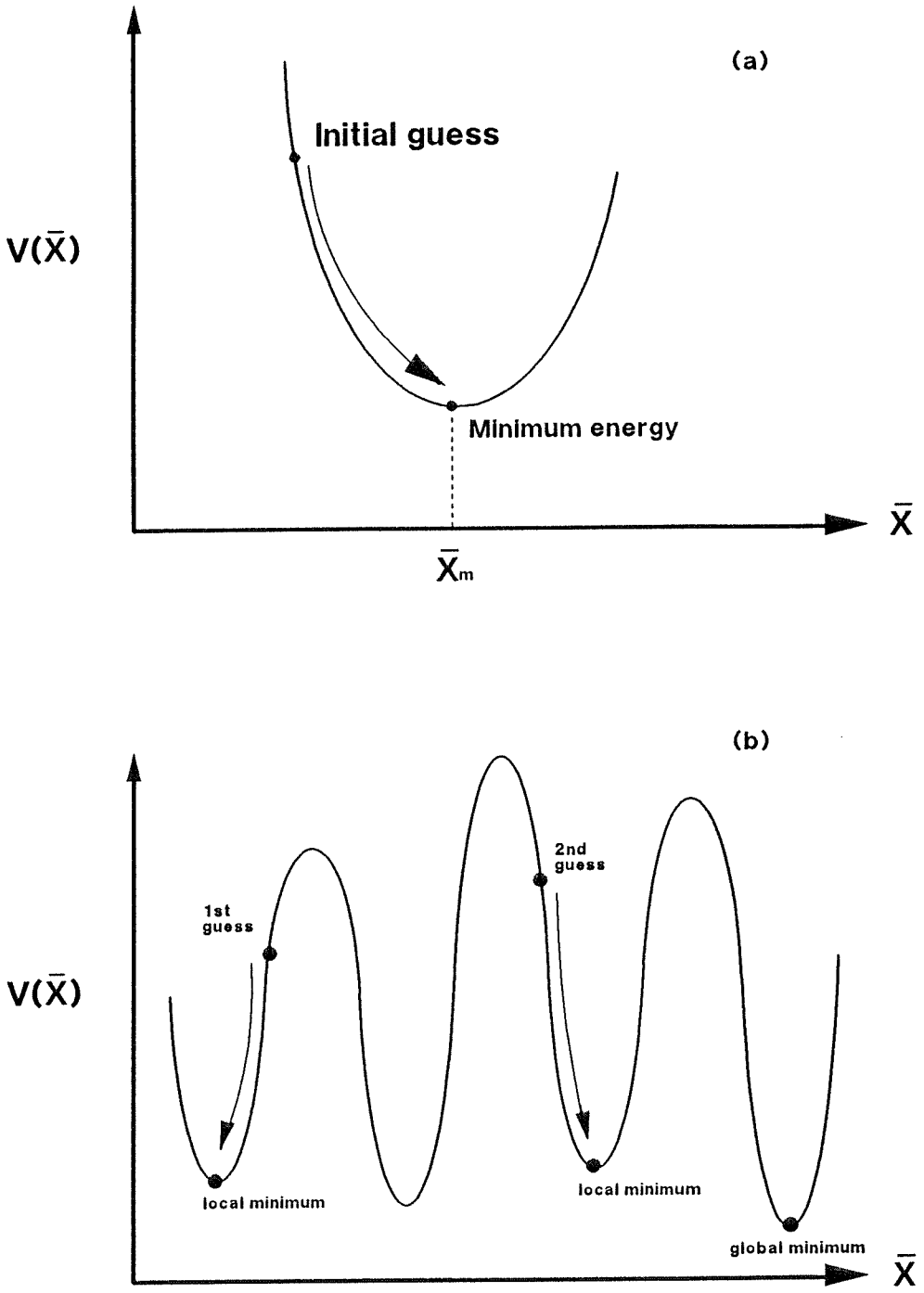

Figure 2.1. Schematic representation of minimisation process.

global minimum.

A number of minimisation algorithms have been developed to find the global minimum from local minima on the potential surface[4]. We may classify the minimisation algorithms according to the type of derivative which is used to choose the search direction for the minimum. The simplest methods use only the potential energy function value and search randomly over configuration space until it reaches its minimum. This method, however, is only suitable for the simplest problems. Greater efficiency is obtained using gradient methods in which the derivatives of the potential function, $\partial V/\partial x_i$, $\partial^2 V/\partial x_i^2$, are calculated with respect to all the independent structural variables x_i . The most widely used gradient methods are

1) steepest descent method, in this method the direction of the minimisation is simply determined by the gradients of the object function $V(\mathbf{x})$ between iterations, and their calculation involves only first-order differentials of this function i.e. the value of the independent variable $x_i^{(k+1)}$ in the $(k+1)^{th}$ iteraction are determined by

$$\mathbf{x}^{k+1} = \mathbf{x}^k + \alpha^{(k)}\mathbf{s}^{(k)} \tag{2.26}$$

where $\mathbf{s}^{(k)} = -\mathbf{g}^{(k)}$ with $g_i^{(k)} = (\partial V/\partial x_i)^{(k)}$ and $\alpha^{(k)}$ is a numerical constant to optimise the efficiency of the iteration.

2) conjugate gradients method, this method uses an orthogonalization process to generate the conjugate descent direction. The displacement vector $\mathbf{s}^{(k)}$ deciding the direction and magnitude of displacement is calculated from the information based on the previous values of the gradients to speed up the convergence of the process.

$$\mathbf{s}^{(k)} = -\mathbf{g}^{(k-1)} + \beta^{(k)}\mathbf{s}^{(k-1)} , \tag{2.27}$$

where

$$\beta^{(k)} = \frac{\mathbf{g}^{T(k-1)} \cdot \mathbf{g}^{(k-1)}}{\mathbf{g}^{T(k-2)} \cdot \mathbf{g}^{(k-2)}} , \qquad (2.28)$$

where $\mathbf{g}^{(k)}$ are the vectors whose components are the derivatives with respective to individual coordinates and the superscript, T, means the transpose of the vector. When we use the second derivatives to guide the direction of the process we get more rapid convergence as in Newton methods. In this method the variables $(k+1)^{th}$ iteration is determined by

$$\mathbf{x}^{(k+1)} = \mathbf{x}^{(k)} - \mathbf{H}^{(k)} \cdot \mathbf{g}^{(k)} \qquad (2.29)$$

where the matrix **H** has the element of the second derivatives $(\partial^2 V/\partial x_i \partial x_j)$.

The Newton-Raphson method of solving nonlinear simultaneous equation is the basic idea behind the NAG library routine which we used for the energy minimisation in this work. If F(x) is the nonlinear function having a minimum value at x^* the improved estimate $x^{(2)}$ can be determined from initial estimate $x^{(1)}$ by drawing the tangent to F(x) at the point $x^{(1)}$ and finding the point $x^{(2)}$ from the intersection of this line with the abscissa. This process can be expressed by:

$$F(x^{(1)}) = -\left(\frac{dF}{dx}\right)_{x=x^{(1)}} (x^{(2)} - x^{(1)}) . \qquad (2.30)$$

The generalization of this process to a set of N functions $F_i(x_j)$ of N variables x_j is straightforward. The initial estimate $x_j^{(1)}$ gives the improved estimate $x_j^{(2)}$ according to

$$F_i^{(1)} = -\sum_j J_{ij}\left(x_j^{(2)} - x_j^{(1)}\right), \qquad (2.31)$$

where $J_{ij} = \partial F_i/\partial x_j$ evaluated at the initial estimate.

One of the most important properties of the Newton-Raphson method is that of 'quadratic convergence'.

2.3.2. The molecular dynamics method.

The molecular dynamics method is concerned with the evolution of the properties of a system with time. Each molecule in a system is considered to be a point mass whose motion is determined by the forces exerted on it through the interactions with all the other molecules in the system. The motion of the molecules is described by the classical Newtonian equations of motion.

In a system of N particles the momentum of the i^{th} particle $\mathbf{p}_i$ is related to its position by

$$\mathbf{p}_i = m_i \frac{d\mathbf{r}_i}{dt} \qquad (2.32)$$

where m_i is a mass of particle i and vector $\mathbf{r}_i$ is the position of the particle. Then the force acting on the particle at time t is

$$\mathbf{F}_i = \frac{d\mathbf{p}_i}{dt} . \qquad (2.33)$$

This force is given by the negative gradient of the N-particle potential function with respect to the position of the i^{th} particle

$$\mathbf{F}_i = m\ddot{\mathbf{r}}_i = -\nabla_i V(\mathbf{r}_1, \cdots, \mathbf{r}_N) . \tag{2.34}$$

Combining (2.32) and (2.33) we obtain a set of coupled second order differential equations which can be solved numerically to give the position $\mathbf{r}_i$ and momenta $\mathbf{p}_i$ as a function of time. The numerical integration method used to solve the coupled differential equations usually involves a finite difference method. For example, the method of Verlet [6] is based on a Taylor expansion of the position coordinates up to second order term with respect to time t,

$$\mathbf{r}_i(t+\Delta t) = \mathbf{r}_i(t) + \mathbf{v}_i(t)\,\Delta t + \frac{1}{2}\mathbf{a}_i(t)\,\Delta t^2 \tag{2.35}$$

$$\mathbf{r}_i(t+\Delta t) = \mathbf{r}_i(t) - \mathbf{v}_i(t)\,\Delta t + \frac{1}{2}\mathbf{a}_i(t)\,\Delta t^2 , \tag{2.36}$$

where $\mathbf{v}_i$ and $\mathbf{a}_i$ are the velocity and acceleration of molecule i. Adding (2.35) and (2.36) we obtain

$$\mathbf{r}_i(t+\Delta t) = 2\mathbf{r}_i - \mathbf{r}_i(t-\Delta t) + \Delta t^2\left(\frac{\mathbf{F}_i}{m_i}\right). \tag{2.37}$$

The velocity of the particle is calculated from the formula

$$\mathbf{v}_i(t) = \frac{\mathbf{r}_i(t+\Delta t) - \mathbf{r}_i(t-\Delta t)}{2\Delta t} . \tag{2.38}$$

The method of molecular dynamics is more powerful than the Monte Carlo method as it can be used to calculate both equilibrium and time dependent properties of a fluid. This method was first proposed by Alder and Wainwright [7] to simulate the hard-disc and hard-sphere liquids.

2.4. Molecular models and potentials.

The initial step in computer simulation is the construction of a model of the intermolecular forces between the atoms in the system. The accuracy of the molecular model determines the reliability of the prediction of experimental behaviour. In this section we will discuss the molecular models used to describe the stearic acid molecule. We concentrate on the aspects common to all the models discussed in this thesis. We will discuss the some of the aspects, such as electrostatic interaction and dihedral potential arising by the rotation of bond of headgroup, in the appropriate chapter.

2.4.1. Molecular models.

The stearic acid molecule is composed of a methyl group (CH_3-) and 16 methylene groups (-CH_2-) and a carboxylic acid group (-COOH). Two different models have been used to represent the alkyl chains.

The united-atom model.

The simpler model for the alkyl chain, based on the work of Ryckaert and Bellemans [8], is called the united-atom model(UA).

In this model the hydrogen atoms in methyl and methylene units are considered as the part of the carbon atom so that the methyl and methylene groups are considered as single Lennard-Jones sites. The carboxylic acid headgroup (-COOH) in the stearic acid molecule is modelled as a single site following van der Ploeg and Berendsen [9,10]. This molecular model has been used widely in the simulation of liquid butane and decane [11,12], in the MD simulation of lipid-bilayers [9,10] and in the MD simulation of Langmuir-Blodgett films [13,14,15].

The explicit-hydrogen model.

In the explicit-hydrogen model(EH) the hydrogen atoms in the methylene

groups are considered explicitly and models them as individual Lennard-Jones atoms. This model recognises that the detailed structure of the hydrocarbon backbone plays an important role in determining the structure of n-alkane assemblies in dense phases. For example, the packing of hydrogen atoms were found to play an important part in stabilizing the crystal structure of tricosane [16]. In this model the methyl terminal group and carboxylic acid groups are treated as single Lennard-Jones sites as in the UA model. Both the UA and EH model ignore the electrostatic interactions between the polar headgroups.

The all-atom model.

The all-atom model(AA) is identical to the EH model except for the explicit consideration of the atoms in the carboxylic acid group. The four atoms of the headgroup are considered as individual Lennard-Jones sites with additional partial charges to represent the molecular dipole moment. The three molecular models are represented schematically in Figure 2.2.

2.4.2. Potentials.

The total potential energy is the sum of intramolecular and intermolecular interactions. The intramolecular potential is the sum of three terms, u_b the bond-stretching energy, u_θ the bond angle deformation energy and u_ϕ the dihedral or torsional energy. The intermolecular energy is the sum of two terms u_{vdW} the dispersion-repulsion energy and u_{el} the electrostatic energy.

$$U_{total} = \sum_i u_b(b_i) + \sum_j u_\theta(\theta_j) + \sum_k u_\phi(\phi_k) + \sum_{m<n} u_{vdW}(r_{mn}) + \sum_{a<b} u_{el}(r_{ab}) \qquad (2.39)$$

where b_i, θ_j, ϕ_k, r_{mn} and r_{ab} represent the bond length, the bond angle, the dihedral

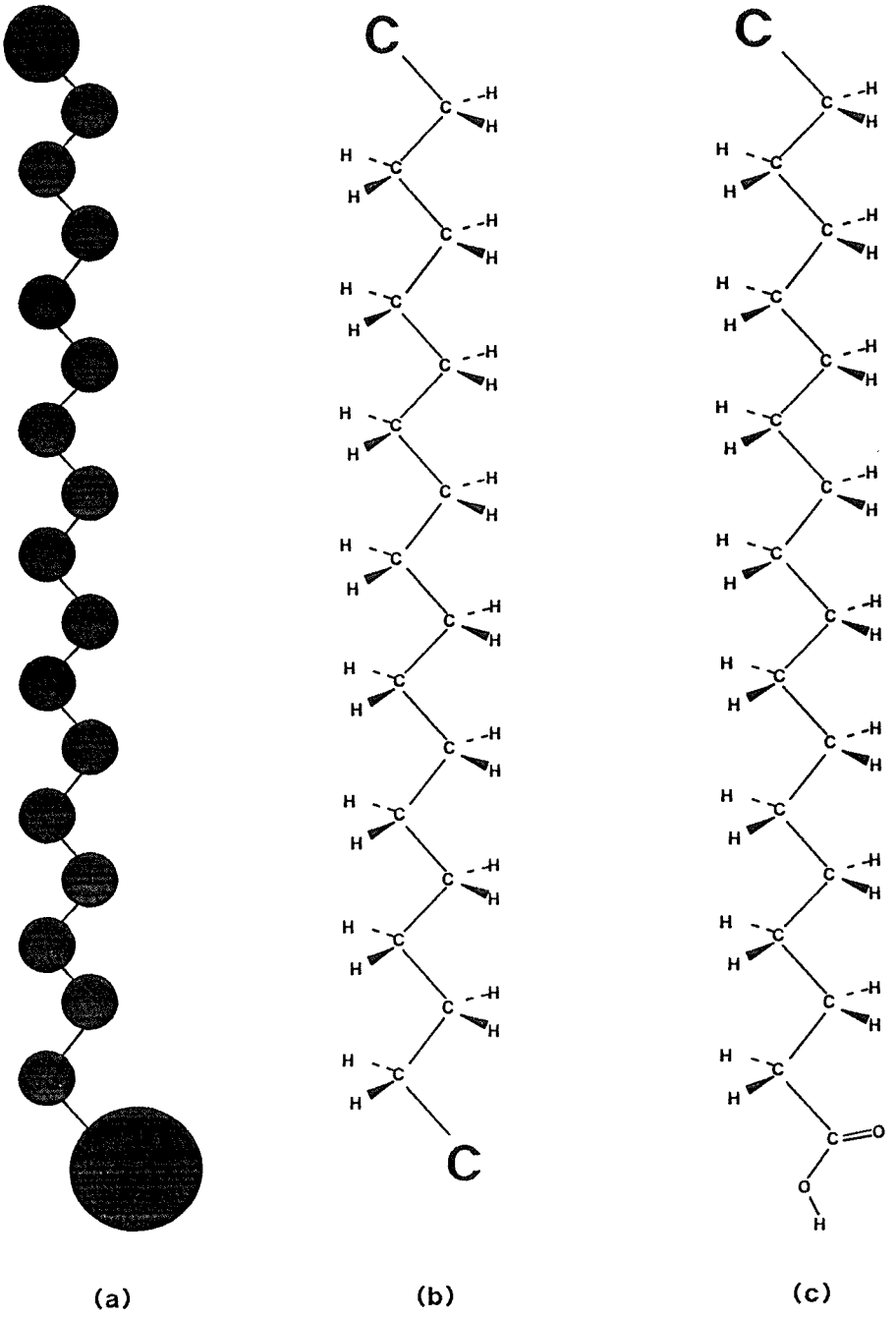

Figure 2.2. Molecular models used in this work; (a) the united-atom model, (b) the explicit-hydrogen model and (c) the all-atom model. A united atom is represented by a filled circle in figure 2.2(a) and C in figure 2.2(b) and (c).

angle, distance between interaction site and the distance between charges respectively.

The bond stretching potential.

Each bond in the molecule is treated as a spring with a characteristic force constant, k_b, and equilibrium bond length b_{eq}. The potential function for bond stretching is given by

$$U(b) = \frac{1}{2} k_b (b - b_{eq})^2 . \qquad (2.40)$$

where b_{eq} is the equilibrium bond-length. Fixing the bond-length at their equilibrium value is a reasonable approximation which does not change the nature of the problem[17] and which allows for the use of a longer time step in molecular dynamics. The constraint technique is described in section 2.5.

The bond angle deformation potential.

The second term in (2.37) accounts for the deformation energy of changing the valence angles between adjacent covalent bonds. It is normally taken as a harmonic function of the displacement.

$$u_\theta(\theta) = \tfrac{1}{2} k_\theta (\theta - \theta_{eq})^2 , \qquad (2.41)$$

which is approximated in this study by

$$u_\theta(\theta) = k_\theta [1 - \cos(\theta - \theta_{eq})] . \qquad (2.42)$$

This change of functional form generates simpler expressions for derivatives used in the calculation of the force. The force constant k_θ and equilibrium bond angle θ_{eq}

are given in Table 2.1.

Dihedral potential.

The third term in (2.37) represents the change on rotation of part of a molecule about an axes through the covalently bonded atoms. This potential has contribution from the non-bonded interactions between atoms belonging to the same molecule and from the distortion of the bond electron orbitals. The dihedral potential for the rotation about the C-C bond of the n-alkane can be approximated as[8]

$$u_{\phi}(\phi_i) = \sum_{n=0}^{5} c_n (\cos \phi_i)^n \ . \qquad (2.43)$$

The dihedral potential for n-butane is shown in Figure 2.3 with the definition of dihedral angle and the potential parameters are summarized in Table 2.1.

Non-bonded potential.

The non-bonded potential represented as the fourth term in equation (2.36) is the interaction potential corresponding to the exchange-repulsion and attractive dispersion between interaction sites in different molecules and for pairs of sites in the same chain which are separated by more than 3 methylene groups.

For the non-bonded dispersion interaction we have used the Lennard-Jones potential given by

$$u_{VdW}(r) = 4\epsilon \left[\left(\frac{\sigma}{r} \right)^{12} - \left(\frac{\sigma}{r} \right)^{6} \right] . \qquad (2.44)$$

ϵ is the well-depth, which is the magnitude of $u_{VdW}(r)$ at its minimum, $r_m = 2^{1/6}\sigma$.

σ is the distance between two interaction sites when the potential is equal to zero.

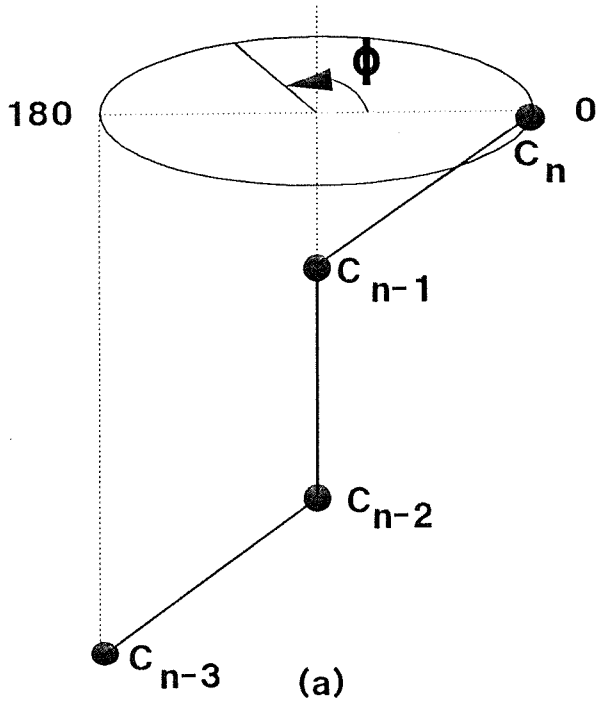

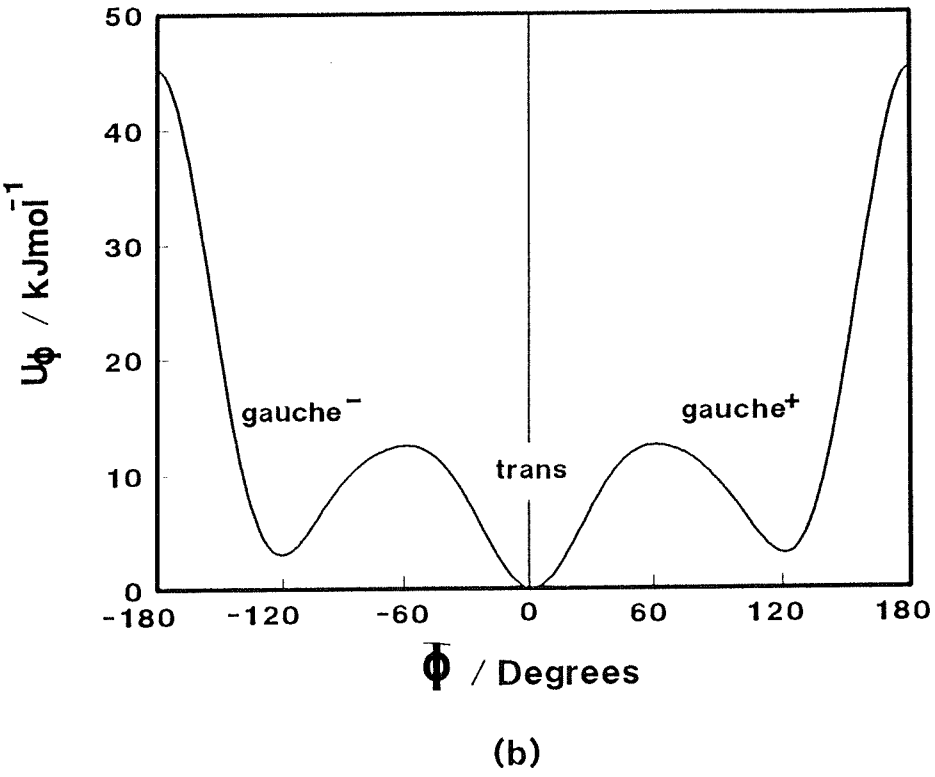

Figure 2.3. Dihedral potential of n-butane from (2.43) and the definition of the dihedral angle.

The Lennard-Jones potential parameters for UA model were taken from the lipid bilayer simulations by van der Ploeg and Berendsen [9,10], where the parameters for carboxylic acid headgroup (-COOH) and tail group ($-CH_3$) were derived from the polarizabilities and van der Waals radii of COO^- and CH_3 groups.
Those potential parameters have successfully reproduced the trends of experimental NMR order parameters of lipid bilayer measured for various methylene group along the chain.

The potential parameters for the explicit-hydrogen model were taken from exp-6 potential parameters used by Williams [18]. He derived these parameters from least square fits to the crystal structures (lattice constants and molecular orientations) and heats of sublimation of a number of aliphatic hydrocarbons. These potential parameters were converted from their original exp-6 form to Lennard-Jones potential form to be used in our calculations by fitting the well depth and location of the potential minimum. We have used the parameter set group VII of exp-6 equation [18] for this parameter conversion. This fitting produced a potential which is very similar to the original exp-6 potential near the potential well. The Lennard-Jones and exp-6 potentials around the potential well for carbon-carbon interaction are shown in Figure 2.4. The Lennard-Jones potentials for carbon-carbon, carbon-hydrogen, and hydrogen-hydrogen interactions for the explicit-hydrogen model are shown in Figure 2.5. Potential parameters for the interaction between unlike atoms in different molecules can be obtained by using the mixing rules based on the parameters for like atoms. The most widely used approximations are the Lorentz-Berthelot rules, in which the collision diameter is taken to be the arithmetic mean and the well-depth to be the geometric mean of those of the pure species:

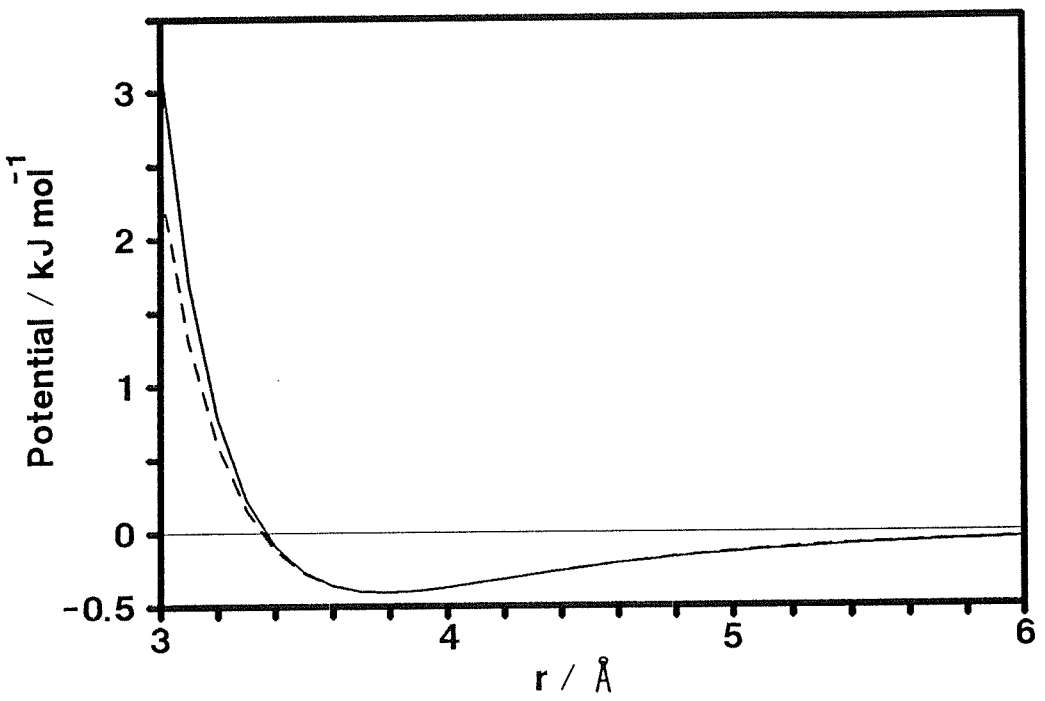

Figure 2.4. The Lennard-Jones potential(solid line) and exp-6 potential(dashed line) for carbon-carbon interaction around potential well.

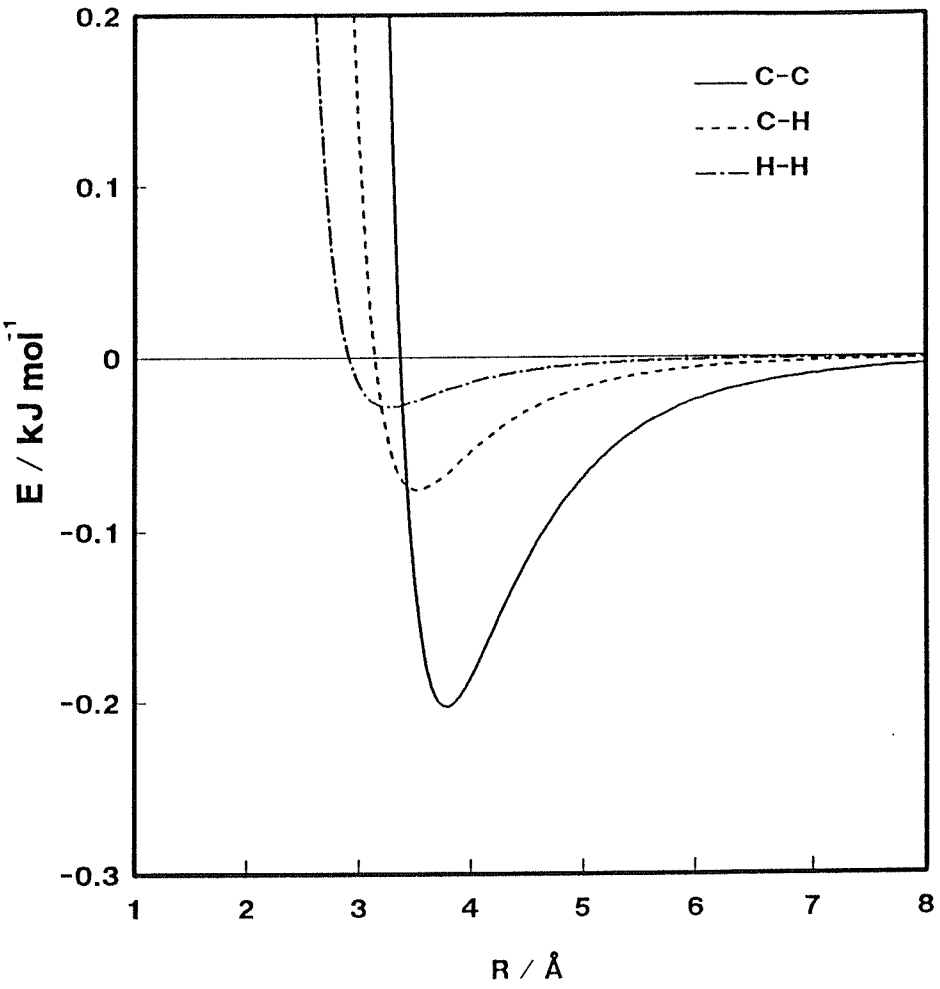

Figure 2.5. Lennard-Jones potentials for C-C, C-H and H-H interaction of EH model.

$$\sigma_{AB} = \frac{1}{2}(\sigma_A + \sigma_B) \tag{2.45}$$

$$\epsilon_{AB} = (\epsilon_A \cdot \epsilon_B)^{\frac{1}{2}} \tag{2.46}$$

The potential parameters for the Lennard-Jones potential are summarized in Table 2.1.

The electrostatic interactions between partial charges in the headgroups is described in chapter 4.

Surface potential.

The interaction between molecules in the LB layer and surface provides significant portion of the structural energy in Langmuir-Blodgett films.

Consider an atom over a solid(i.e. graphite) surface as shown in Figure 2.6.

The distance, r, of the atom from the atom on the surface is $r^2 = X^2 + Y^2 + (z+Z)^2$.

According to the Lennard-Jones potential, the interaction of an atom with a solid surface can be expressed by

$$V(z) = 4\,\epsilon_{gs}\,\hat{n} \int_{X=-\infty}^{\infty} \int_{Y=-\infty}^{\infty} \int_{0}^{\infty} \left[\frac{\sigma_{gs}^{12}}{[(z+Z)^2 + X^2 + Y^2]^6} - \frac{\sigma_{gs}^{9}}{[(z+Z)^2 + X^2 + Y^2]^3} \right] dX\,dY\,dZ \tag{2.47}$$

where $\hat{n}$ is the number density of atoms in solid.

Changing variables by

$$s^2 = X^2 + Y^2$$

$$dX\,dY = s\,ds\,d\phi$$

$$= 2\pi\, s\,ds$$

we get

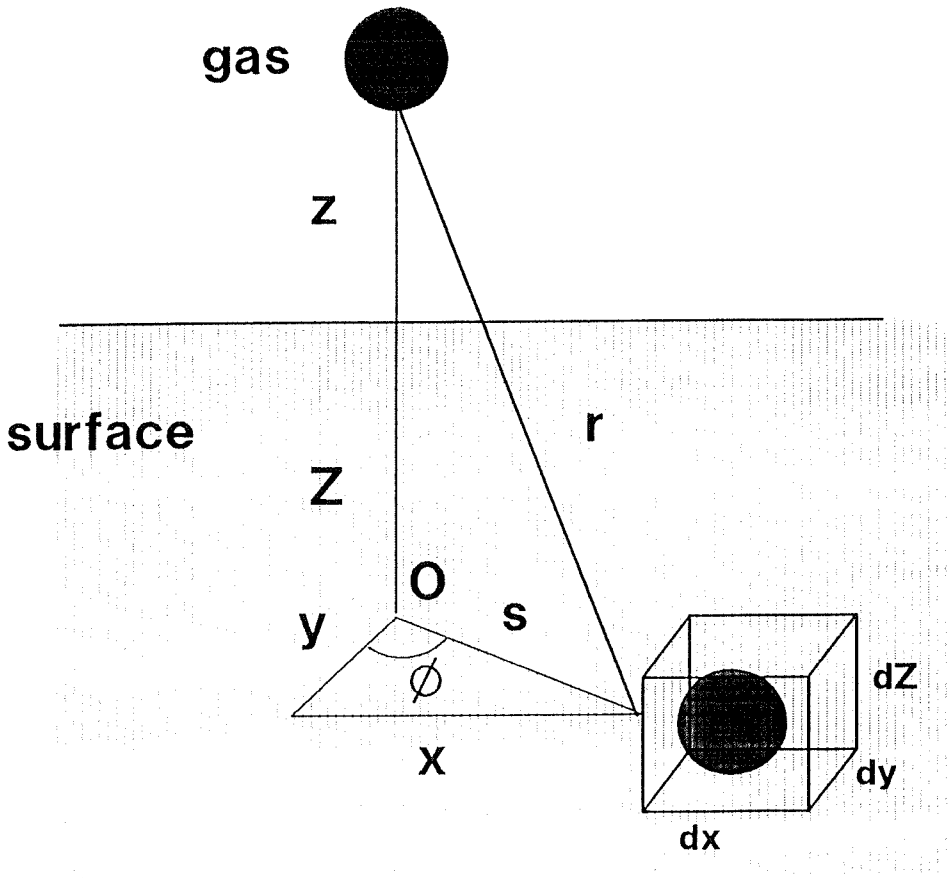

Figure 2.6. A gas atoms on the solid surface.

$$V(z) = 4\epsilon_{gs}\hat{n}\int_{\phi=0}^{2\pi}\int_{s=0}^{\infty}\int_{Z=0}^{\infty}\left\{\frac{2\pi\sigma_{gs}^{12}s}{[(z+Z)^2+s^2]^6} - \frac{2\pi\sigma_{gs}^{6}s}{[(z+Z)^2+s^2]^3}\right\}dZ\,ds\,d\phi \qquad (2.48)$$

Integrating over s and ϕ we obtain

$$V(z) = 2\pi\hat{n}\epsilon_{gs}\int_{Z=0}^{\infty}\left[\frac{2\sigma_{gs}^{12}}{5(z+Z)^{10}} - \frac{\sigma_{gs}^{6}}{(z+Z)^4}\right]dZ \qquad (2.49)$$

Another integration over Z gives us

$$V(z) = \frac{2\pi\hat{n}\epsilon_{gs}\sigma_{gs}^3}{3}\left[\frac{2}{15}\left(\frac{\sigma_{gs}}{z}\right)^9 - \left(\frac{\sigma_{gs}}{z}\right)^3\right] \qquad (2.50)$$

The parameters for the surface interaction are summarized in Table 2.1.

Table 2.1. Potential parameters for the stearic acid molecule.

Bond angle deformation potential		
k_θ		520.0 kJ mol^{-1}
θ_{eq}		109.47°
Dihedral potential		
		c_n/kJ mol^{-1}
c_0		9.2789
c_1		12.1557
c_2		-13.1207
c_3		-3.0597
c_4		26.2403
c_5		-31.4950
Lennard-Jones potential		
site	ϵ/K	σ/Å
Tail[a)]	77.250	3.740
Chain[b)]	72.00	3.923
Head[a)]	110.688	4.220
Carbon[c)]	48.784	3.367
Hydrogen[c)]	6.835	2.908
surface potential.		
ϵ_s		28.0 K
σ_s		3.4Å
$\hat{n}$		0.114 $Å^{-3}$

a) parameter set for UA and EH models.

b) parameter set for UA model.

c) parameter set for EH model.

2.5. Constraints in molecular dynamics simulation.

In the simulation of a flexible molecule such as an n-alkane there are a number of independent motions which have characteristic times which are well-separated from one another[20]. The bond-stretching motion has a characteristic time of 10^{-16} sec and can be separated from the overal rotational motion of the chain(10^{-9} sec). The fast internal motions can be usefully frozen using constraint dynamics.

2.5.1. Geometric contraints of n-alkane chain.

In this study of molecular dynamics of a Langmuir-Blodgett film, a number of geometrical constraints have been imposed on the constituent stearic acid molecules. The first constraint is on the C-C bond lengths between adjacent carbon atoms. These are fixed at their average distance, d_{cc}, by (n-1) rigid bond constraints:

$$|\mathbf{r}_{i+1} - \mathbf{r}_i|^2 - d_{CC}^2 = 0 \quad , i = 1 \ldots . n-1 \; . \tag{2.51}$$

The second constraint is the bond length constraint on carbon-hydrogen bond in methylene ($-CH_2-$) group in which the C-H bond lengths are fixed at their equilibrium bond length, d_{CH}, by

$$|\mathbf{r}_i - \mathbf{r}_H|^2 - d_{CH}^2 = 0 \tag{2.52}$$

where $\mathbf{r}_i - \mathbf{r}_H$ denotes the vector from hydrogen atom attached directly to the i^{th} carbon atom. Bond orientational constraint is achieved by making the mid-point of the line joining the two hydrogen atoms in the methylene group of the carbon atom i lie along $\mathbf{b}_i$, the bisector of the bond angle (β) for C_{i-1}-C_i-C_{i+1} at a distance $d_{CH}\cos(\alpha/2)$ from the carbon atom

$$\frac{1}{2}(\mathbf{r}_H + \mathbf{r}_{H'}) - \mathbf{r}_i - d_{CH}\frac{\mathbf{b}_i}{|\mathbf{b}_i|}\cos\left(\frac{\beta}{2}\right) = 0 \tag{2.53}$$

where $\mathbf{b}_i = 2\mathbf{r}_i - \mathbf{r}_{i+1} - \mathbf{r}_i$.

Finally the planes containing the HCH' atoms and C_{i-1} C_i C_{i+1} atoms are constrained to be mutually perpendicular

$$(\mathbf{r}_H - \mathbf{r}_{H'})\cdot(\mathbf{r}_{i+1} - \mathbf{r}_{i-1}) = 0 . \tag{2.54}$$

The geometries of an alkane chain and a methylene group are illustrated in Figure 2.7.

2.5.2. Method of constraint.

The constraints imposed on the molecular system of N-atoms of the n-alkane chains belong to the class of sclernomous (time independent) holonomic constraints of the form [21]

$$\sigma_k(\mathbf{r}_1,\ldots,\mathbf{r}_N) = 0, \quad k = 1,\ldots,l . \tag{2.55}$$

Now, the problem is to solve 3N Newtonian equations of motion satisfying the l constraints. This is achieved by applying Lagrange's method of undetermined multipliers which includes the constraints

$$m_i \frac{\partial^2 \mathbf{r}_i}{\partial t^2} = -\nabla_i\Big(V + \sum_{k=1}^{l} \lambda_k \sigma_k \Big) . \tag{2.56}$$

This adds a zero term to the intermolecular potential energy V, while satisfying the constraints at all times by solving for λ_k. We can rewrite equation (2.56) as

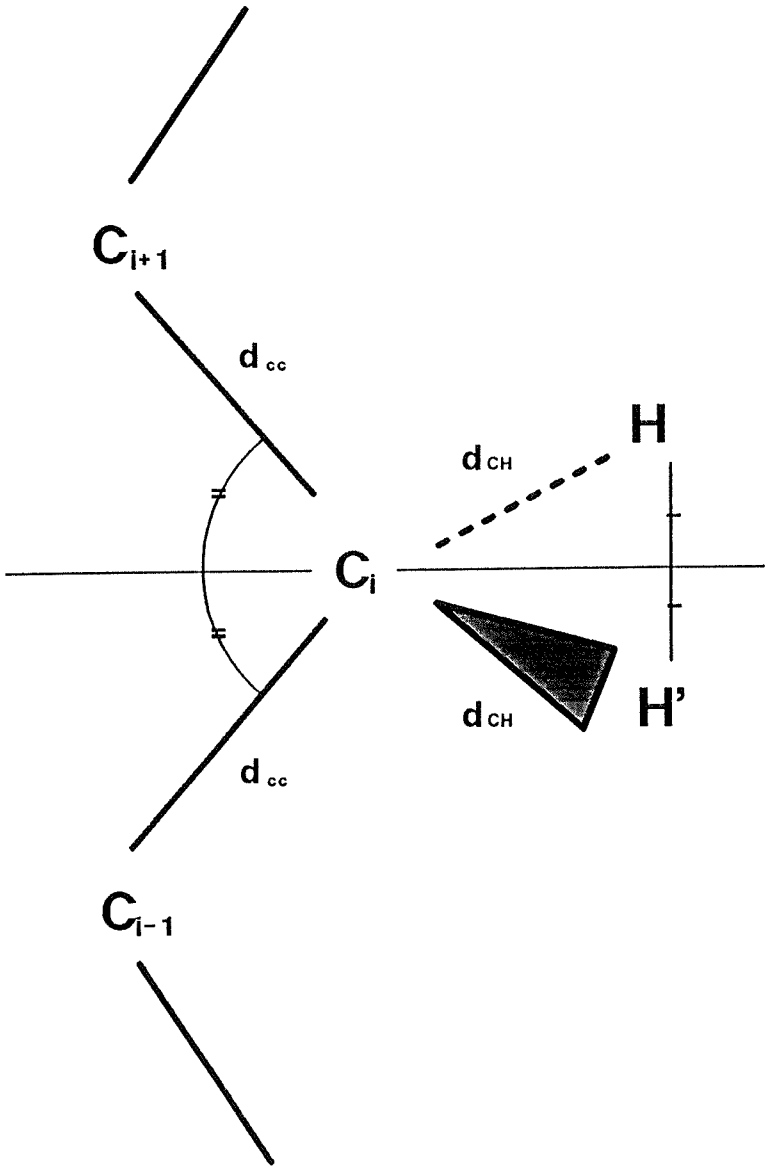

Figure 2.7. Geometrical constraints imposed on the alkane chain and methylene group.

$$m_i \frac{\partial^2 \mathbf{r}_i}{\partial t^2} = \mathbf{F}_i + \mathbf{G}_i \tag{2.57}$$

$$\mathbf{F}_i = -\nabla_i V \tag{2.58}$$

$$\mathbf{G}_i = -\sum_{k=1}^{l} \lambda_k \nabla_i \sigma_k \ , \tag{2.59}$$

where $\mathbf{F}_i$ is the total force from pair interactions without any constraints and $\mathbf{G}_i$ is the force from constraints to compensate the $\mathbf{F}$ along the directions of the constraints.

In the Verlet algorithm, the position of particle i at time $t+\delta t$, including constraint force, will be:

$$\mathbf{r}_i(t+\delta t) = 2\mathbf{r}_i(t) - \mathbf{r}_i(t-\delta t) + \frac{\mathbf{F}_i(t) + \mathbf{G}_i(t)}{m_i}(\delta t)^2 \tag{2.60}$$

or

$$\mathbf{r}_i(t+\delta t) = \mathbf{r}_i' + \delta \mathbf{r}_i \tag{2.61}$$

where

$$\mathbf{r}_i' = 2\mathbf{r}_i(t) - \mathbf{r}_i(t-\delta t) + \frac{\mathbf{F}_i(t)}{m_i}(\delta t)^2 \tag{2.62}$$

and

$$\delta \mathbf{r}_i = \frac{\mathbf{G}_i(t)}{m_i}(\delta t)^2 \ . \tag{2.63}$$

Here $\mathbf{r}'_i$ is the coordinates after a normal molecular dynamics step without applying constraints and $\delta \mathbf{r}_i$ is the correction to be made by the constraints. $\mathbf{r}_i(t+\delta t)$ is the coordinates after a constraint step. Using (2.55), (2.59) and (2.60), the constraint conditions can be written as

$$\delta \mathbf{r}_i = -\frac{(\delta t)^2}{m_i} \sum_{k=1}^{l} \lambda_k \nabla_i \sigma_k(\mathbf{r}_1(t),...,\mathbf{r}_N(t)) \,. \tag{2.64}$$

Let us consider a methylene(CH_2) unit in an alkane chain. We need to consider two constraint conditions: the H-C-H bond angle constraint and the bond length constraint to maintain the geometry of the methylene unit. To achieve bond angle constraint we may put in a fictitious bond between two hydrogen atoms in the methylene unit. For three atoms in a methylene unit we can write the equation of motion including constraint forces:

$$\begin{aligned} m_1 \ddot{\mathbf{r}}_1 &= \mathbf{f}_1 + \mathbf{g}_1 \\ m_2 \ddot{\mathbf{r}}_2 &= \mathbf{f}_2 + \mathbf{g}_2 \\ m_3 \ddot{\mathbf{r}}_3 &= \mathbf{f}_3 + \mathbf{g}_3 \end{aligned} \tag{2.65}$$

Here $\mathbf{f}_1$, $\mathbf{f}_2$, and $\mathbf{f}_3$ are the forces acting on the carbon and two hydrogen atoms respectively due to the interaction and $\mathbf{g}_1$, $\mathbf{g}_2$ and $\mathbf{g}_3$ are the forces of constraint to keep the desired bond lengths constant:

$$\begin{aligned} |\mathbf{r}_{12}(t)|^2 - d_{12}^2 &= 0 \\ |\mathbf{r}_{23}(t)|^2 - d_{23}^2 &= 0 \\ |\mathbf{r}_{13}(t)|^2 - d_{12}^2 &= 0 \end{aligned} \tag{2.66}$$

The forces of constraint on the three atoms can be written in the form with confirming Newton's third law:

$$\begin{aligned} \mathbf{g}_1 &= \lambda_{12}\mathbf{r}_{12} - \lambda_{13}\mathbf{r}_{13} \\ \mathbf{g}_2 &= \lambda_{23}\mathbf{r}_{23} - \lambda_{12}\mathbf{r}_{12} \\ \mathbf{g}_3 &= \lambda_{13}\mathbf{r}_{13} - \lambda_{23}\mathbf{r}_{23} \end{aligned} \tag{2.67}$$

where λ_{ij} is the undetermined Lagrangian multiplier.

From eq.(2.61) we can write three equations for the Verlet algorithm:

$$\mathbf{r}_1(t+\delta t) = \mathbf{r}_1'(t+\delta t) + \left(\frac{\delta t^2}{m_1}\right)\lambda_{12}\mathbf{r}_{12}(t) - \left(\frac{\delta t^2}{m_1}\right)\lambda_{13}\mathbf{r}_{13}(t) \tag{2.68}$$

$$\mathbf{r}_2(t+\delta t) = \mathbf{r}_2'(t+\delta t) - \left(\frac{\delta t^2}{m_2}\right)\lambda_{12}\mathbf{r}_{12}(t) + \left(\frac{\delta t^2}{m_2}\right)\lambda_{23}\mathbf{r}_{23}(t) \tag{2.69}$$

$$\mathbf{r}_3(t+\delta t) = \mathbf{r}_3'(t+\delta t) + \left(\frac{\delta t^2}{m_3}\right)\lambda_{13}\mathbf{r}_{13}(t) - \left(\frac{\delta t^2}{m_3}\right)\lambda_{23}\mathbf{r}_{23}(t)\ . \tag{2.70}$$

The distances between two atoms will be

$$\mathbf{r}_{12}(t+\delta t) = \mathbf{r}'_{12}(t+\delta t) + \delta t^2\left(\frac{1}{m_1}+\frac{1}{m_2}\right)\lambda_{12}\mathbf{r}_{12}(t) - \left(\frac{\delta t^2}{m_1}\right)\lambda_{13}\mathbf{r}_{13}(t) - \left(\frac{\delta t^2}{m_2}\right)\lambda_{23}\mathbf{r}_{23}(t) \tag{2.71}$$

$$\mathbf{r}_{23}(t+\delta t) = \mathbf{r}'_{23}(t+\delta t) + \delta t^2\left(\frac{1}{m_2}+\frac{1}{m_3}\right)\lambda_{23}\mathbf{r}_{23}(t) - \left(\frac{\delta t^2}{m_2}\right)\lambda_{12}\mathbf{r}_{12}(t) - \left(\frac{\delta t^2}{m_3}\right)\lambda_{13}\mathbf{r}_{13}(t) \tag{2.72}$$

$$\mathbf{r}_{13}(t+\delta t) = \mathbf{r}'_{13}(t+\delta t) - \delta t^2\left(\frac{1}{m_1}+\frac{1}{m_3}\right)\lambda_{13}\mathbf{r}_{13}(t) + \left(\frac{\delta t^2}{m_1}\right)\lambda_{12}\mathbf{r}_{12}(t) - \left(\frac{\delta t^2}{m_3}\right)\lambda_{23}\mathbf{r}_{23}(t) \tag{2.73}$$

By taking the square modulus of both sides of equations (2.72) and (2.73) and applying desired constraints to match the constraints in eq.(2.66) we obtain quadratic equations in δt^2. The quadratic term proportional to $(\delta t^2)^2$ are dropped and the remaining linear equation in δt^2 are solved for λ_{12}, λ_{23} and λ_{13}, which gives us

improved estimates of λ_{12}, λ_{23} and λ_{13}. The improved estimates are substituted into the quadratic equations to give new linear equations. This process is repeated iteratively. For a very small molecule, the constraint equations can be solved by straightforward method such as matrix inversion. However, for large polyatomic molecules with many constraints of n we are required to solve a matrix of n x n components. This would be very time consuming for a large molecules. An alternative way, which is suggested by Ryckaert *et al.* [22], is to solve linear equations for all constraints, treating all constraints in succession, iteratively, until all constraints are satisfied to within a specified tolerance.

References.

[1] W.C. Swope and H.C. Andersen, Preprint for publication.

[2] M. Pinches, D.J. Tildesley, and W. Smith, Molec. Simul., **6**, 51 (1991).

[3] J.W Gibbs, *Elementary Principles of Statistical Mechanics*, 1902, Yale University Press.

[4] S.L.S Jacoby, J.S. Kowalski, and J.T. Pizzo, *Iterative Methods for Nonlinear Optimisation Problems*, Prentice-Hall, Inc. (1972); W.H. Press, B.P. Flannery, S.A. Teukolsky and W.T. Vetterling in *Numerical Recipes, The Art of Scientific Computing*, Cambridge University Press, Cambridge (1986).

[5] N. Metropolis, A.W. Rosenbluth, M.N. Rosenbluth, A.H. Teller, and E. Teller, J. Chem. Phys., **21**, 1087 (1953).

[6] L. Verlet, Phys. Rev., **159**, 98 (1967).

[7] B.J. Alder and T.E. Wainwright, J. Chem. Phys., **27**, 1208 (1957).

[8] J.-P. Ryckaert and A. Bellemans, Faraday Dis. Chem. Soc., **66**, 95 (1978).

[9] P. van der Ploeg and H.J.C. Berendsen, J. Chem. Phys., **76**, 3271 (1982).

[10] P. van der Ploeg and H.J.C. Berendsen, Mol. Phys., **49**, 233 (1983).

[11] J.-P. Ryckaert and A. Bellemans, Chem. Phys. Lett. **30**, 123 (1975).

[12] S. Leggetter and D.J. Tildesley, Mol. Phys., **68**, 519 (1989).

[13] G. Cardini, J.P. Baremann and M.L. Klein, Chem. Phys. Lett., **145**, 493 (1988).

[14] J.P. Bareman, G. Cardini and M.L. Klein, Phys. Rev. Letters, **60**, 2152 (1988).

[15] J. Harris and S.A. Rice, J. Chem. Phys., **89**, 5898 (1988).

[16] J.-P. Ryckaert, I.R. McDonald and M.L. Klein, Mol. Phys., **67**, 957 (1989).

[17] W.F. van Gunsteren, Mol. Phys., **40**, 1015 (1980).

[18] D.E. Williams, J. Chem. Phys., **47**, 4680 (1967).

[19] W.A. Steele, Surf. Sci., **36**, 317 (1973).

[20] M. Bixon, A. Rev. Phys. Chem., **27**, 65 (1976).

[21] H. Goldstein, *Classical Mechanics.*, Chapter 1, (1950), Addison-Wesley.

[22] J.-P. Ryckaert, G. Ciccotti and H.J.C. Berendsen, J. Comput. Phys., **23**, 327 (1977).

CHAPTER THREE.

A Langmuir-Blodgett Monolayer with the Explicit-Hydrogen Model.

3. A LANGMUIR-BLODGETT MONOLAYER WITH THE EXPLICIT-HYDROGEN MODEL.

3.1. Introduction.

The united-atom model has been extensively used to examine the structure and properties of alkanes[1,2,3,4], lipid layers[5,6] and Langmuir[7,8] and Langmuir-Blodgett films[9,10]. Recently, Ryckaert *et al.* [11,12] used the explicit-hydrogen model in their molecular dynamics simulation of an n-alkane bilayer. They claimed that the explicit consideration of hydrogen atoms in an alkyl chain is important in the investigation of the structure of long chain alkanes in the solid phase or similar phases. In this chapter we discuss the energy minimisation calculations of a Langmuir-Blodgett monolayer of stearic acid on a structureless surface using both the united-atom and the explicit-hydrogen models. Molecular dynamics calculations with the explicit-hydrogen model are presented.

3.2. Models.

The details of the molecular models and potentials used in this study have been discussed in chapter 2. We will now present some additional information on the potential models which discussed in this chapter.

The united-atom(UA) model for the hydrocarbon backbone of stearic acid was based on that of Ryckaert and Bellemans [1], as used in their lipid bilayer simulations [5]. The CH_3 (tail) and CH_2 groups were treated as single interaction centres. The non-bonded interactions were modelled using Lennard-Jones interactions

$$u(r) = 4\epsilon\left\{\left(\frac{\sigma}{r}\right)^{12} - \left(\frac{\sigma}{r}\right)^{6}\right\} \qquad (3.1)$$

for all intermolecular pairs and for all intramolecular pairs separated by at least 3

methylene groups. For crossed interactions, the Lorentz-Berthelot mixing rules were used. Internal motions of the chain were approximated by bond-bending and torsional potentials taken from previous simulations of flexible chain systems[1,3,5,6]. The bending potential was modelled using

$$V(\theta) = k_b[1 - \cos(\theta - \theta_0)] \tag{3.2}$$

with k_b = 520 kJ mol^{-1}, θ_0 = 109.5°. This change in the functional form results in simpler expressions for the forces. The dihedral potential for the alkane chain was modelled with the potential form given in Eq.(2.41) and the potential parameters are summarized in Table 2.1. We have assumed that the dihedral potentials for bonds at the end of the chain are the same as for those in the middle of the chain. The COOH (head) groups were also modelled as single force centres, with potential parameters taken from the lipid bilayer simulation[5]. These potential parameters are also listed in Table 2.1. They were derived from the polarizabilities and van der Waals radii of COO^- and CH_3, and were successful in reproducing the experimentally observed NMR orientational order parameters of a lipid bilayer.

In the explicit-hydrogen model, the CH_2 groups were split into individual C and H atom force sites. The parameters for these sites were taken from Williams[13]. The potential parameters were converted from their original exp-6 form to the Lennard-Jones form used in our calculations. This conversion was discussed in chapter 2.

We employed the minimum image convention over molecular centres of mass in two dimension(x,y), without a distance cutoff, in the calculation of the total intermolecular energy of each molecule. We also performed a number of calculations with a cylindrical cut-off of 17Å. This cut-off had a negligible effect on the results for the minimum energy structure and increased the computational time. As in the original Williams potential, no long-range corrections were applied in the

calculations.

In the explicit-hydrogen model, single force centres were also used to represent the head and tail groups. The dipole moment of the head group has not been included in the model. We recognize that the head group potential is a crude representation of the interaction between two carboxylic acid groups, or between a carboxylic acid group and the surface, but our principal concern in the work which will be discussed in this chapter will be the effects of the detailed geometry of the hydrocarbon tails on the properties of the films. The effect of the structure of the headgroup will be discussed in chapter 4.

The surface is supposed to be a general hydrophilic surface on which the head groups are physisorbed, and no attempt has been made to model its structural details. The surface was approximated by a continuum solid occupying the region of space below the film. This continuum approximation results in a 9-3 Lennard-Jones potential of the form:

$$u(z) = \frac{2\pi\rho\epsilon\sigma^3}{3}\left\{\frac{2}{15}\left(\frac{\sigma}{z}\right)^9 - \left(\frac{\sigma}{z}\right)^3\right\}. \qquad (3.3)$$

The details of the surface potential were discussed in chapter 2.

The potential parameters, presented in Table 2.1, were taken from a commonly used graphite potential[14,15]. The parameter ρ is the number density of graphite atoms, namely 0.114Å^{-3}. Our head groups are held to the surface by a dispersion interaction with a well-depth of 6.44 kJ mol^{-1}. This value can vary considerably, depending on the composition of the substrate, and in previous published simulations of arachidic acid, a well-depth of about 5.76 kJ mol^{-1} was used [9,10].

3.3. Energy minimisation.

We have performed a number of energy minimisation calculations for monolayer films at different densities with both the united-atom and the explicit-hydrogen models. Since Langmuir-Blodgett monolayers of fatty acids with more than 12 carbon atoms form close-packed triangular arrays[14,15,16,17], the head groups of the stearic acid molecules were fixed in a triangular lattice on the surface at each particular head group area per molecule A_m. The molecules were fixed in an all-trans configuration at their equilibrium bond angles. Minimisations were performed using one molecule per unit cell and two molecules per unit cell where the energy is a function of the three Euler angles θ (tilt), ϕ (azimuth), ψ (twist) and z_H (position of head group over surface). The angles θ and ϕ are defined with respect to a vector passing the centres of the bonds between the carbon atoms of the chains, where θ is defined as the tilt of the molecular axis away from the surface normal, ϕ is the angle between the space-fixed x-axis and the projection of this vector onto the space-fixed x-y plane, and $\psi=0$ when the plane of the carbon atoms (1-18) lies in the space-fixed x-z plane which is shown in Figure 3.1. In calculating the energy of a molecule at a head group area A_m, we included all the interactions with neighbouring molecules within a rectangle of side $a_x=8(2A_m/\sqrt{3})^{1/2}$ and $a_y=8(\sqrt{3}/2A_m)^{1/2}$ centred on the molecule: the normal minimum image convention is used with periodic boundary conditions. The sum of the intermolecular energy and molecule-surface energy, E, can be calculated as a function of the molecular orientation(ϕ,θ,ψ,z_H). In energy minimisation we did not include the non-bonded intramolecular energy, the bond-angle energy and the dihedral energy since they are unchanged during the minimisation at fixed trans-configuration. $E(\phi,\theta,\psi,z_H)$ was minimised using the NAG library routine E04JBF for $0\le\theta\le\pi/2$, $0\le\phi\le2\pi$, $0\le\psi\le2\pi$ and $z_H>0$. The minimum value of the energy of one molecule per unit cell system, E_{min}, is shown as a function of A_m for the two models in Figure 3.2. Results for some representative head group areas are given in Table 3.1 and Table 3.2.

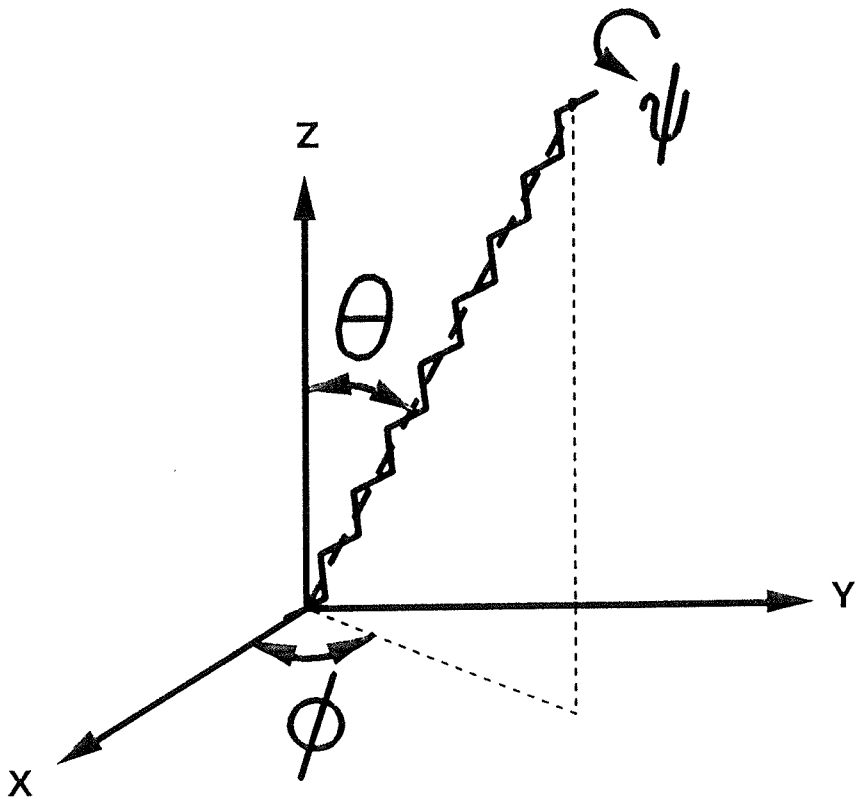

Figure 3.1. The orientation of a stearic acid molecule in a space fixed frame.

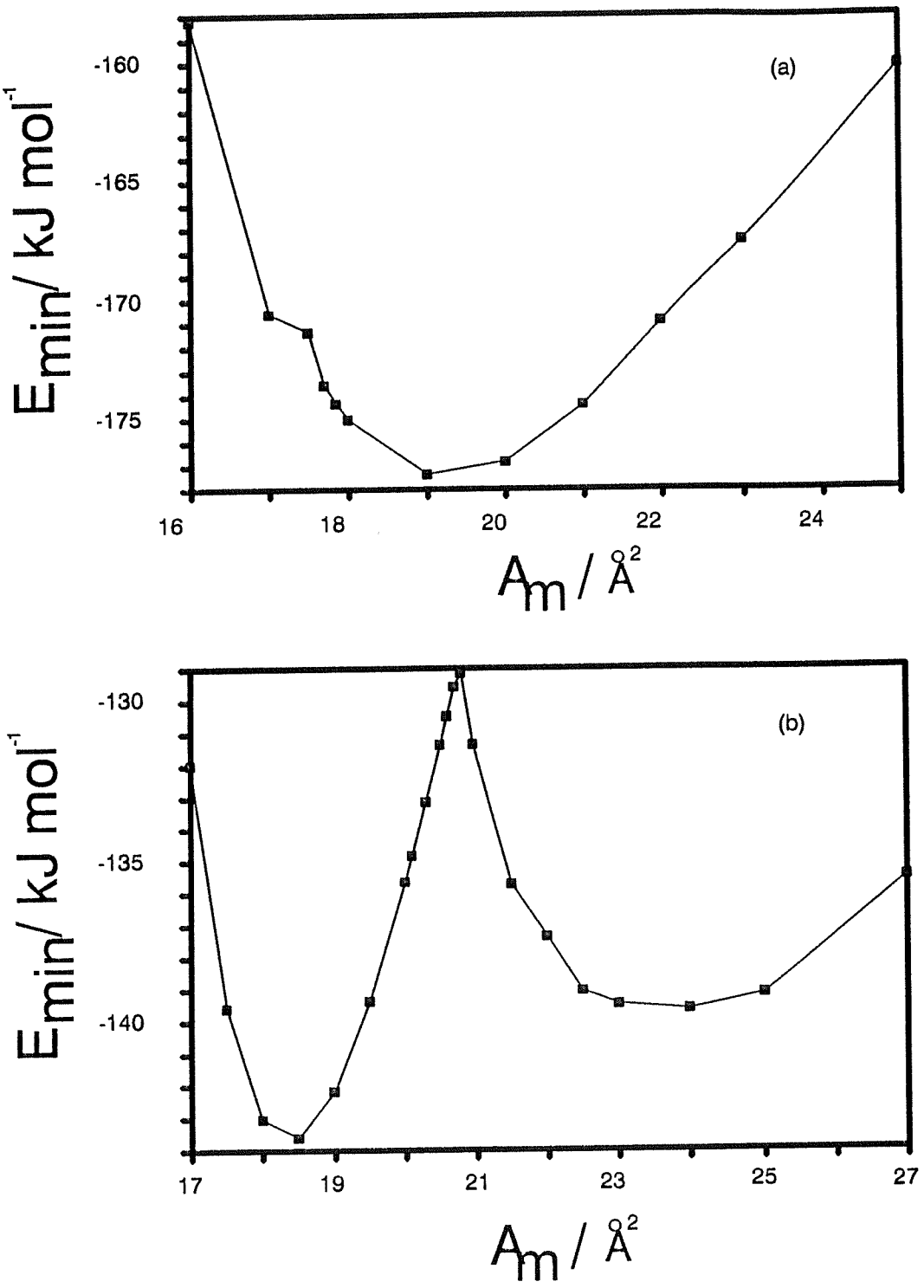

Figure 3.2. The minimum energy E_{min} as a function of A_m: (a) the united-atom model; (b) the explicit-hydrogen model.

The most striking feature of these results is the comparison in the behaviour of the two models. For the united-atom model, the minimum energy decreases smoothly with decreasing head group area to a minimum at $A_m = 19Å^2$. As the layer is further compressed, the repulsive forces between the united-atom groups increase and E_{min} increases monotonically, but with a small cusp near $A_m = 17.5Å^2$. For the explicit-hydrogen model, there is a maximum in E_{min} as a function of A_m at $20.9Å^2$. The plot of tilt angle at minimum energy, θ_{min}, as a function of A_m in Figure 3.3 shows that the cusp and the maximum are associated with a sudden tilt of the layer from 0° to 19° for the united-atom model and from 0° to 30° for the explicit-hydrogen model. This tilting is accompanied by a change in the azimuthal angle, ϕ_{min}, by 27° and 25° for the united-atom and explicit-hydrogen models respectively, and a change in the twist angle ψ_{min} by 56° and 221°. The plots of θ_{min} vs. A_m are comparable to recent x-ray diffraction results for arachidic acid Langmuir layers, where the onset of tilting occurs near $A_m = 19.8Å^2$ [20]. The similarity in the results for the two models suggests that the explicit-hydrogen model could be approximated by a united-atom model with a larger value of σ for the CH_2 groups. Accordingly, we have performed energy minimisation calculations for the united atom model for the σ values 4.22Å, 4.3Å and 4.5Å. Figure 3.4 shows the molecular tilt behaviours in the monolayer as a function of headgroup area (A_m) for three different σ values. The results are very similar to each other, while the molecular tilt occurs at the A_m = $20Å^2$, $20.5Å^2$ and $22.0Å^2$ for σ = 4.22Å, 4.3Å and 4.5Å respectively. This results imply that rescaling the size of the united-atom methylene group can reproduce the moleculat tilt behaviour of the explicit-hydrogen model. However, rescaling united-atom size did not reproduce the minimum energy behaviour of the explicit-hydrogen model as a function of headgroup area.

A recent one-sublattice energy minimisation study of a 3×3 patch of docosane thiol ($CH_3(CH_2)_{11}SH$) on Au(111) has also shown how the molecular tilt in a monolayer of long-chain hydrocarbons is controlled by the close-packing arrangement

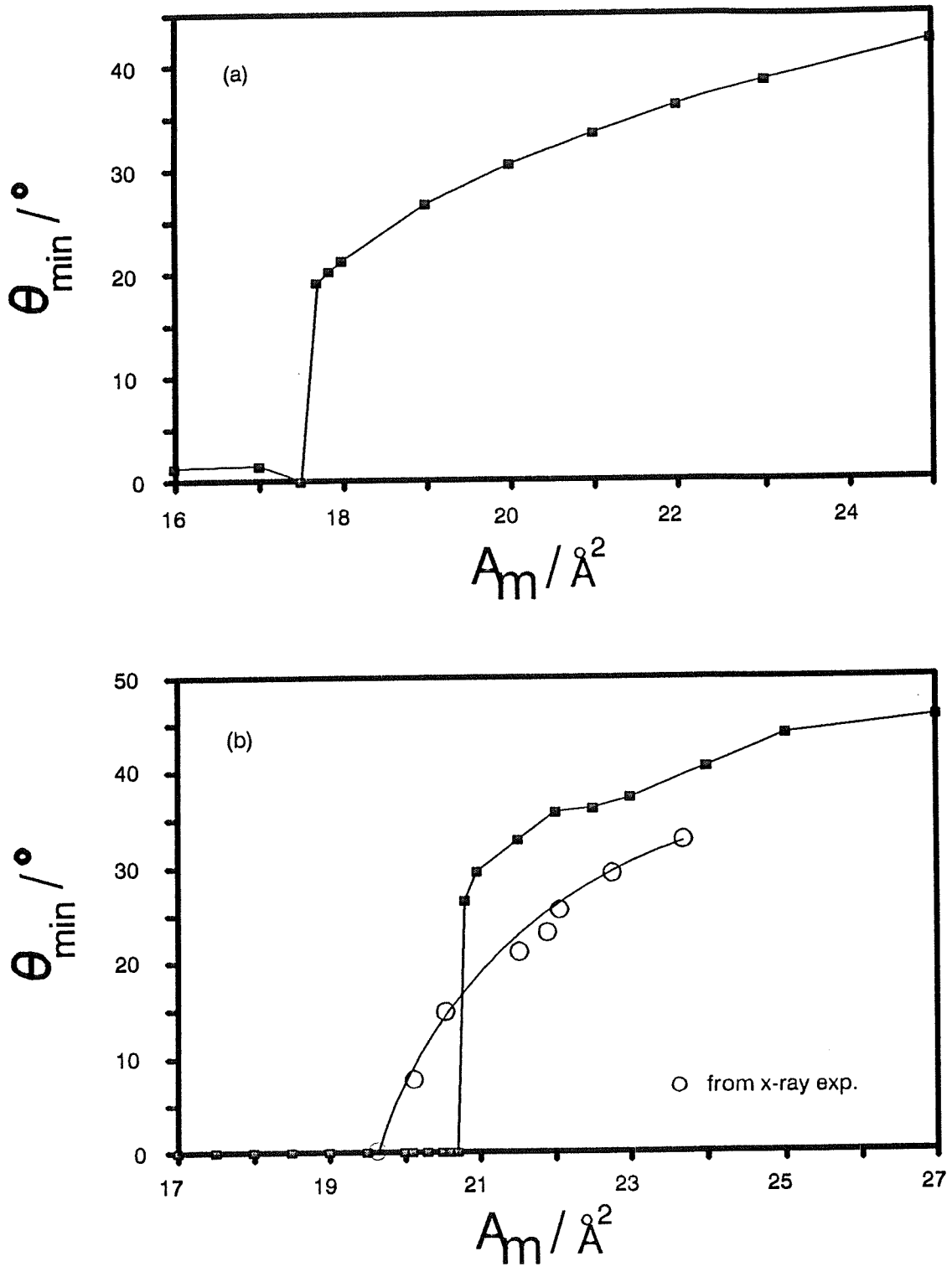

Figure 3.3. Molecular tilt at minimum energy θ_{min} as a function of A_m: (a) the united-atom model; (b) the explicit-hydrogen model. Open circles denote the data from [20].

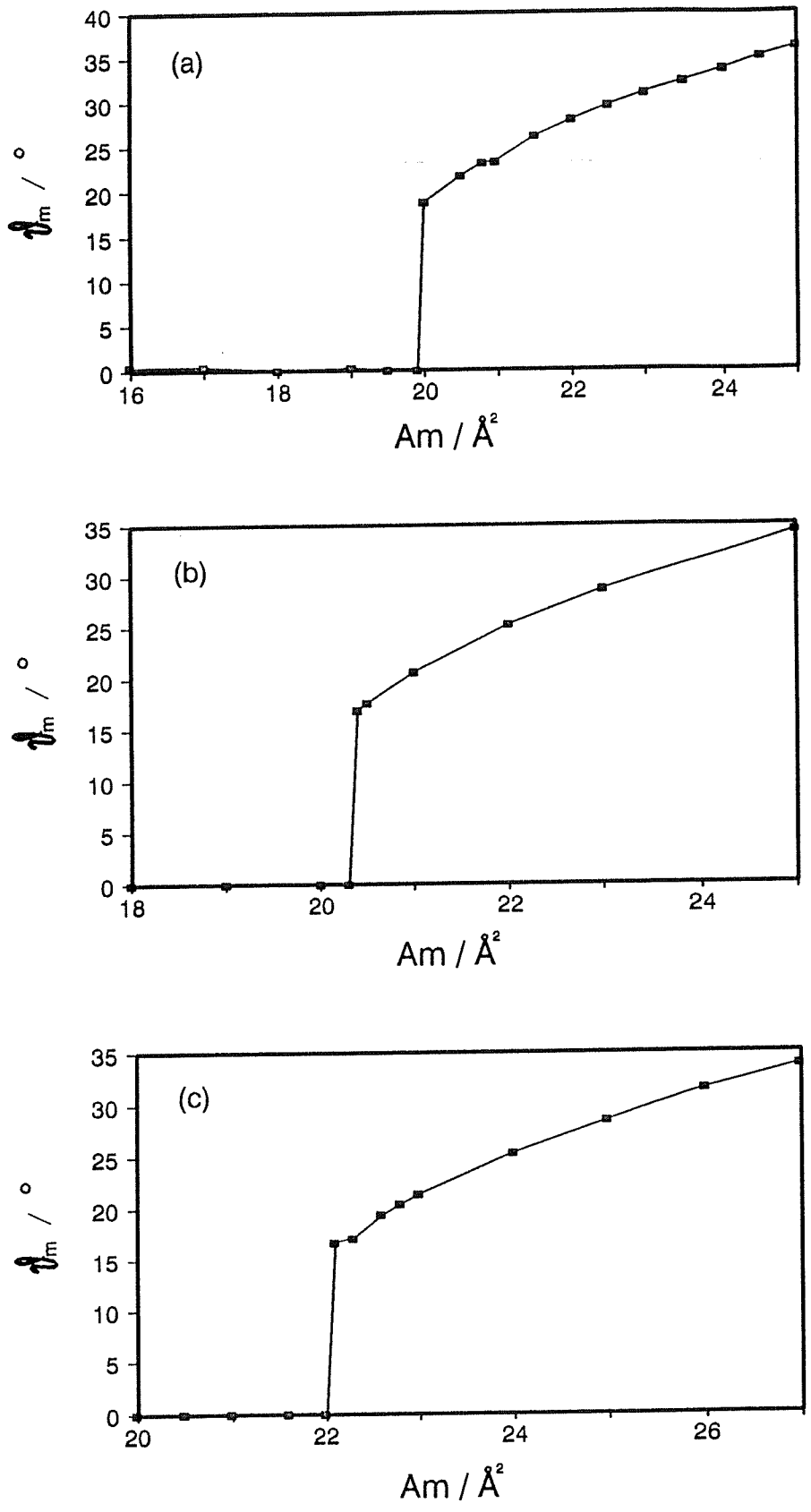

Figure 3.4. The molecular tilt behaviours of the monolayer at minimum energy using the united-atom model with various σ : (a) σ = 4.22Å, (b) σ = 4.3Å and (c) σ = 4.5Å.

Table 3.1. Energy minimisation results for the monolayer of the united-atom model.

Head Group Area A_m /Å^2	The United-Atom Model ϕ_{min} /°	θ_{min} /°	ψ_{min} /°	E_{min} /kJ mol^{-1}
16	0.00	1.35	149.99	-158.20
17	0.00	1.49	149.93	-170.58
18	27.45	21.29	93.86	-175.02
19	28.16	26.66	92.69	-177.35
20	28.75	30.50	91.92	-176.82
21	28.90	33.49	91.43	-174.41
22	17.76	36.20	88.61	-170.91
23	12.97	38.58	84.37	-162.52
25	14.91	42.38	78.17	-160.13

Table 3.2. Energy minimisation results for the monolayer of the explicit-hydrogen model.

Head Group Area A_m /Å^2	The Explicit-Hydrogen Model ϕ_{min} /°	θ_{min} /°	ψ_{min} /°	E_{min} /kJ mol^{-1}
17	0.00	0.00	0.00	-131.97
18	0.00	0.00	0.00	-143.04
19	0.00	0.00	0.00	-142.17
20	0.00	0.00	0.00	-135.66
21	24.58	29.55	223.69	-131.36
22	23.35	35.69	226.63	-137.36
23	21.14	37.26	228.63	-139.47
25	16.04	43.96	242.32	-139.14

of the hydrogen atoms of the methylene groups[21]. In that system, a plot of E_{min} vs. lattice spacing was similar to our Figure 3.2(b), with two energy minima corresponding to molecular tilts of 0° and 38°. This phenomenon is also seen in the crystal structures of solid lipids, including stearic acid, where there are several crystal variations, tilted at the angles which produce the close-packing arrangement of hydrogen atoms on neighbouring chains. This behaviour is much reduced in the united-atom model, where there are no hydrogen atoms to interlock, but only CH_2 'pseudo-atoms'. Since the head group area per molecule of Langmuir-Blodgett films of molecules containing long chain hydrocarbons is usually close to 21Å^2[16,17,18,22], it is essential to study the more detailed explicit-hydrogen model to obtain reliable results on the structure of the monolayer.

The second interesting feature of these results is the sharpness of the tilting transition with density. Clearly for a perfectly ordered monolayer at 21Å^2 and 0K, the layer would be tilted, but at room temperature, entropic effects, such as conformational disordering and lateral motions of the chains around their lattice points can decrease the effective head group area of the stearic acid molecules. A small decrease in the effective A_m could cause the layer to stand upright. An estimate of the height of the barrier between the tilted and non-tilted forms, of about 1300 K molecule^{-1} is seen in Figure 3.2(b). The precise molecular tilt will be determined by entropic and energetic considerations which are finely balanced at typical experimental values of A_m. The above minimum energy structures can also be compared with the crystal structures of stearic acid which are shown in Figure 3.5. In the B and C forms of the bulk crystals, the head groups lie in a plane, and the angle between this plane (defined by the **a** and **b** crystal axes) and the crystal **c** axis, is a measure of the tilt of the chains in the crystal. The short axes of the chains are oriented in a two-sublattice herringbone structure. The rare, low-temperature A form of the bulk crystal has not been completely characterised[23]. For the B structure, the tilt of the chains is 27.5° from the normal to the plane of the head groups, at an

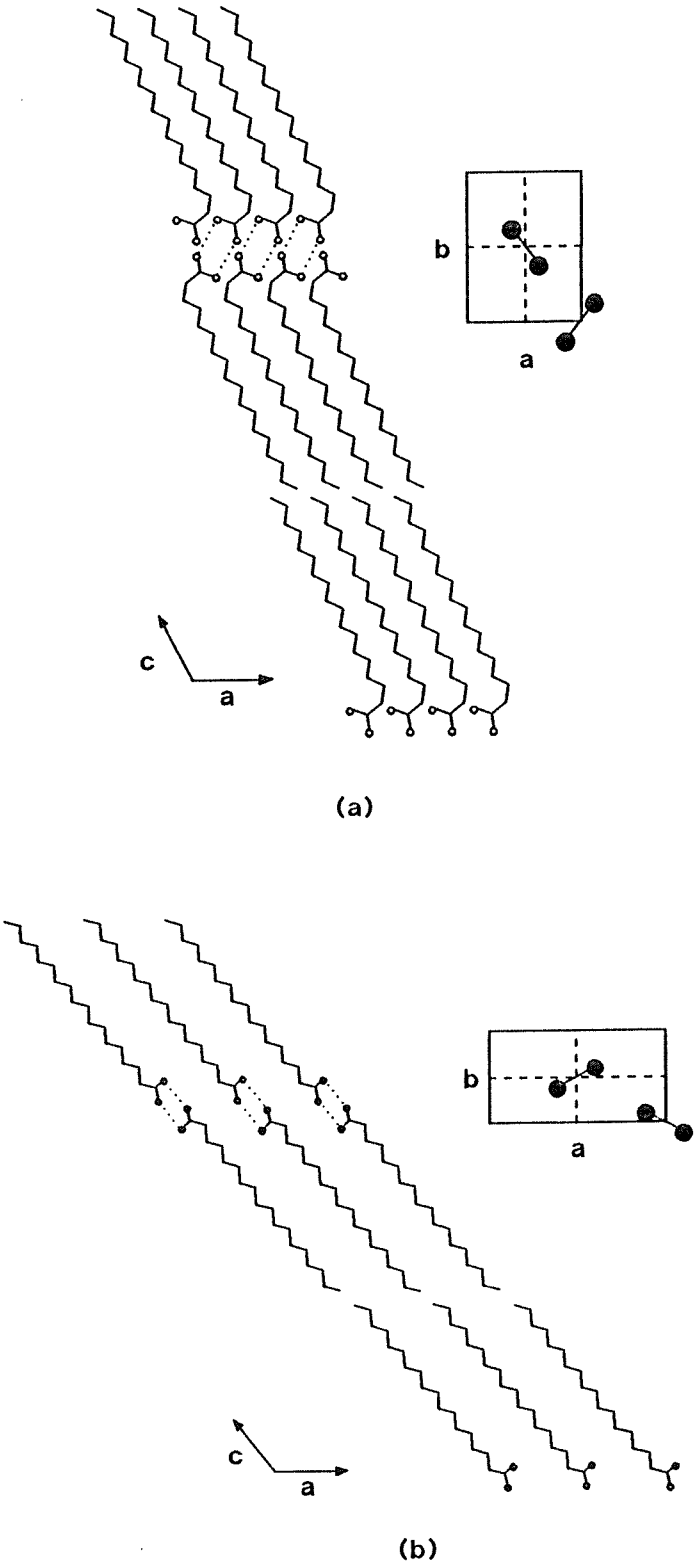

Figure 3.5. The structures of a stearic acid crystal: (a) B-form; (b) C-form.[23,24]

effective A_m of 20.7Å^2 in this plane[24]. The C structure has a chain tilt of 38° at an effective A_m of 23.2Å^2[23]. Neither of these structures is triangular in the plane of the head groups, as is the case for the Langmuir-Blodgett films. The C form has a 4.95 × 9.36Å unit cell, compared to a 5.18 × 8.96Å unit cell for the corresponding triangular array at A_m=23.2Å^2, while the B form has a 5.587 × 7.386Å unit cell, compared to 4.89 × 8.47Å for the corresponding triangular array at A_m=20.7Å^2.

We have calculated the configurational energy of a monolayer of stearic acid on a structureless surface, set up as a single layer of either the B or C bulk crystal structures of stearic acid, using the explicit-hydrogen model. The resulting energies were -117.89 and -116.88 kJ mol^{-1} for the B and C phases respectively. The experimental crystal structure of the B form includes a gauche bond at the hydrophillic end of the chain. Without this gauche bond, our model gave an energy of -137.42 kJ mol^{-1}.

Energy minimisations starting from the B and C structures resulted only in small structural changes. The all-trans B form transformed from a tilt of 27.4° to 26.7°, with E_{min} = -143.15 kJ mol^{-1}. The tilt of the molecules starting in the C form went from 38.3° to 37.1°, with E_{min} = -137.29 kJ mol^{-1}. These results can be compared with the energy minimisations performed on the triangular lattice. At A_m=20.7Å^2, the energy minimised triangular lattice had a tilt of 0°, and energy E_{min} = -129.6 kJ mol^{-1}. At A_m=23.2Å^2, the triangular lattice had a tilt of 38° and an energy E_{min} = -139.4 kJ mol^{-1}. These results suggest that, within our model, at 0K, the orientation of the hydrocarbon chains is strongly dependent on the choice of the unit cell. In addition we performed the energy minimisation calculations with two molecules per unit cell on the triangular lattice structure used for the calculation with one molecule per unit cell. Figure 3.6 represents the minimum energy behaviour as a function of headgroup area. The result tells us that the monolayers with two molecules per unit cell structure are energetically more stable than the monolayer with one molecule per unit cell structure in the range of A_m of less than 22Å^2.

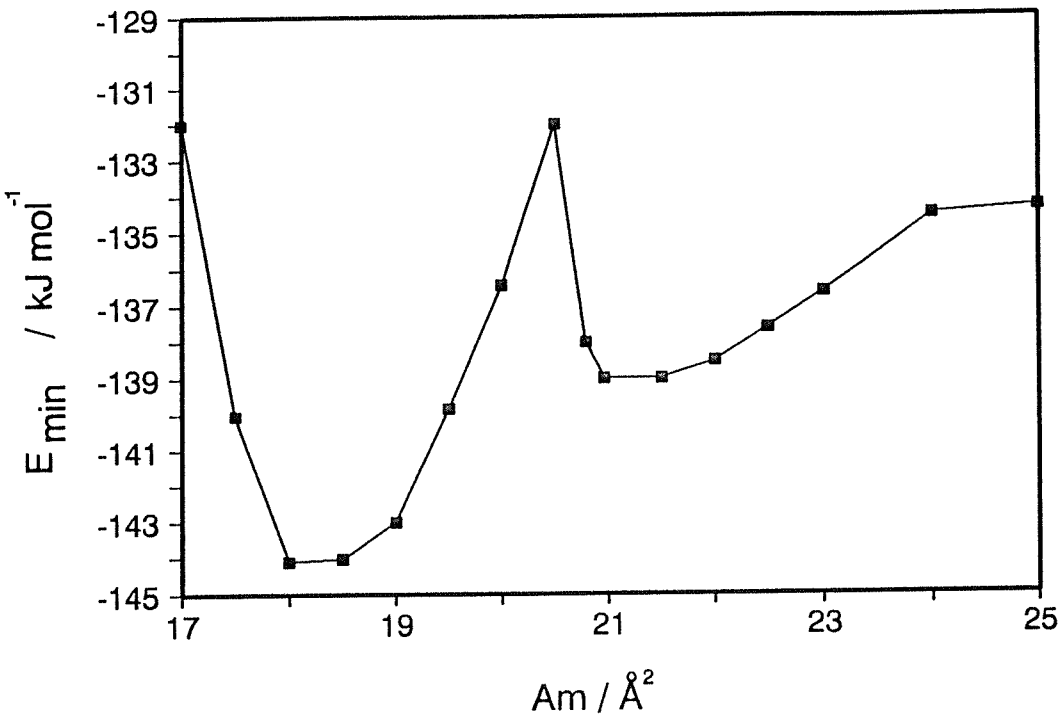

Figure 3.6. Minimum energy E_{min} behaviour as a function of A_m for the explicit-hydrogen model with two molecules per unit cell structure.

In conclusion, the energy minimised structures of monolayers with surface below and vacuum above are relaxed forms of the bulk crystal structure and the size and shape and occupancy of the unit cell play an important rôle in stabilizing the structure of the layer. The explicit-hydrogen model is more realistic than the united-atom model with the original Ryckaert and Bellemans potentials for predicting the molecular tilt of the layer. Scaling the size of the united-atom model can improve the agreement with the tilting transition observed experimentally, but the details of the energy as a function of headgroup area are quite different for the two models.

3.4. Molecular dynamics.

3.4.1. Simiulation method.

In the molecular dynamics simulations of the monolayer, the trajectories of the stearic acid molecules were generated using Verlet algorithm [25]. The bond lengths of the molecule were constrained to their equilibrium values using the SHAKE algorithm[26,27]. A further scalar constraint was added to the molecules to keep the plane of the hydrogen atoms of each CH_2 group normal to the plane of the three nearest carbon atoms. Finally, a vector passing through a carbon atom and the H-H bisector was constrained to be co-linear with a vector passing through the carbon atom and the bisector of a line joining the two neighbouring carbon atoms. This vector constraint was applied using the method developed by Ryckaert[27].

A single layer of 64 molecules was set up on a triangular array with all of the molecules in the all-trans conformation. The molecules were set up in a one-sublattice structure with their long axes normal to the surface, and with their molecular planes parallel to the box x-axis, corresponding to initial orientational angles $(\phi,\theta,\psi) = (0,0,0)$. The triangular array was oriented such that the box x-axis was aligned along a direction of nearest neighbours.

Two simulations were performed: one on either side of the change in tilt observed in the energy minimisations. Headgroup areas of A_m=20.79Å^2 and 21.2Å^2, correspond to head group separations of 4.90Å and 4.94Å. Both simulations were started at 298K. The simulation at A_m=20.79Å^2 was run for an equilibration phase of 25000 steps of 2fs, in which the molecular velocities were scaled to 298K every step, followed by a production phase of 25000 steps. The simulation at A_m=21.2Å^2 had a 50000 step equilibration and a 150000 step production. The results reported in this work are averages taken over the production phases of the simulations, which gave phase space trajectories over 50ps and 300ps respectively. The criterion for convergence of the constraints was set at 10^{-8} Å^2.

Table 3.3 lists the energies, surface pressure and tilt angle of the films at the two densities. The total energy was conserved to 1 part in 10^4, with a value of the standard deviation of the total energy to the standard deviation of the kinetic energy of 0.0027. Careful monitoring of the properties throughout the simulation showed that equilibrium had been achieved. We note that in the time scale of these simulations there can be some exchange of energy between various modes, resulting in fluctuations with lifetimes which are significant fractions of the length of the simulation.

In calculating the surface pressure, we have used the definition of Steele[28]:

$$\phi A = \int_{V_s} \left\{ \frac{1}{2}\left[p_{XX}(\mathbf{r}) + p_{YY}(\mathbf{r})\right] - p_{ZZ}(\mathbf{r}) \right\} \mathbf{dr} \qquad (3.4)$$

or equivalently in terms of the molecular virials:

$$\phi A = \frac{1}{2}\left[V_m^X + V_m^Y\right] - V_m^Z - V_s^Z \ , \qquad (3.5)$$

where

$$V_m^Z = \frac{1}{2}\sum_i \sum_{j \neq i} \langle z_{ij} f_{ij}^Z \rangle \qquad (3.6)$$

and

$$V_s^Z = \sum_i \langle z_i f_j^Z \rangle \ , \qquad (3.7)$$

where the summations are over molecular centres of mass. Here f_{ij}^Z is the Z component of the intermolecular force between molecule i and molecule j and f_j^Z is the Z component of the molecule-surface force. A 50,000 step equilibration run with the united-atom model gave an unrealistically low surface pressure of -500 ± 200 mN m^{-1} at A_m=20.79Å^2. As a result, subsequent simulations concentrated on the explicit-hydrogen model, and the results quoted in the remainder of this chapter are from the explicit-hydrogen model. The calculated surface pressure was about 0 mN m^{-1} for the explicit-hydrogen model systems at both A_m=20.79Å^2 and 21.2Å^2, when the large fluctuations are taken into account. The calculation of the pressure involves steeply varying integrals, since the potential varies rapidly with **r** in a solid, and this is the origin of the large fluctuations. As the fluctuations are much larger in magnitude than the result itself, it is difficult to make a meaningful comparison with experiment. However, in contrast to the united-atom model, the explicit-hydrogen model systems were not under significant expansion.

Table 3.3. Results for the molecular dynamics simulation of stearic acid monolayer LB film with the explicit-hydrogen model.

Property\molecular area	20.79Å^2	21.2Å^2
Temperature / K	300 ± 6	290 ± 8
Non-Bonded Energy / kJ mol^{-1}	-112.6 ± 0.6	-111.3 ± 0.9
Bond Bending Energy / kJ mol^{-1}	18.0 ± 0.8	17.6 ± 0.8
Dihedral Energy / kJ mol^{-1}	14.6 ± 0.7	14.8 ± 0.7
Surface Energy / kJ mol^{-1}	-9.7 ± 0.2	-9.2 ± 0.2
Surface Pressure / mN m^{-1}	-44 ± 128	-24 ± 122
Most Probable Tilt / ° (momemt of inertia)	0.0	8.9
Most Probable Tilt / ° (end-to-end vector)	0.0	7.8
Average Tilt / °	2.6 ± 0.5	10.2 ± 2.5
$<P_1>$	0.999 ± 0.000	0.983 ± 0.008
$<P_2>$	0.997 ± 0.001	0.950 ± 0.022
$<P_4>$	0.989 ± 0.004	0.840 ± 0.070

3.4.2. Translational ordering in LB monolayers.

Figure 3.7 shows the radial distribution function for molecular centres of mass, averaged over the length of the production phase of the simulation at 21.2Å^2. This figure corresponds to a triangular solid with a nearest neighbour spacing of 4.9Å. We have also calculated the hexagonal order parameter exp(i6θ)/6, where θ is the angle between three nearest neighbour centres of mass projected onto the surface plane. The hexagonal order parameter was originally developed to study the hexatic phase on an adsorbed xenon film [29]. Figure 3.8 shows the value of the order parameter as a function of time. The large value of 0.77 indicates that the system has on average an hexagonal symmetry which is maintained throughout the simulation. The average rms displacement (in three dimensions) of the molecular centres of mass was followed as a function of time, and it showed a solid-like behaviour, reaching a plateau at about $[<\Delta r^2>]^{1/2}$ = 1.6Å. These results may be influenced by the starting configuration and the use of periodic boundary conditions. In order to simulate an infinite system, we have used the periodic boundary conditions, which means that the system must start with a certain degree of translational ordering. We have chosen a starting configuration which fits the experimental observation: a triangular lattice. This starting configuration gave reasonable results for the spreading pressure and tilting angle.

3.4.3. Orientational ordering in LB monolayer.

Molecular tilt and azimuthal angles.

To compare with the energy minimisation calculations, the distribution of molecular tilts in the system was calculated as a running average throughout the simulations. The long-axis of the flexible amphiphile can be defined approximately in two different ways. In the first method we use the end-end (C_1-C_{18}) vector from the head-group to the methyl group of a molecule. In the second method the moment of inertia tensor of the amphiphile is diagonalised. This tensor is defined

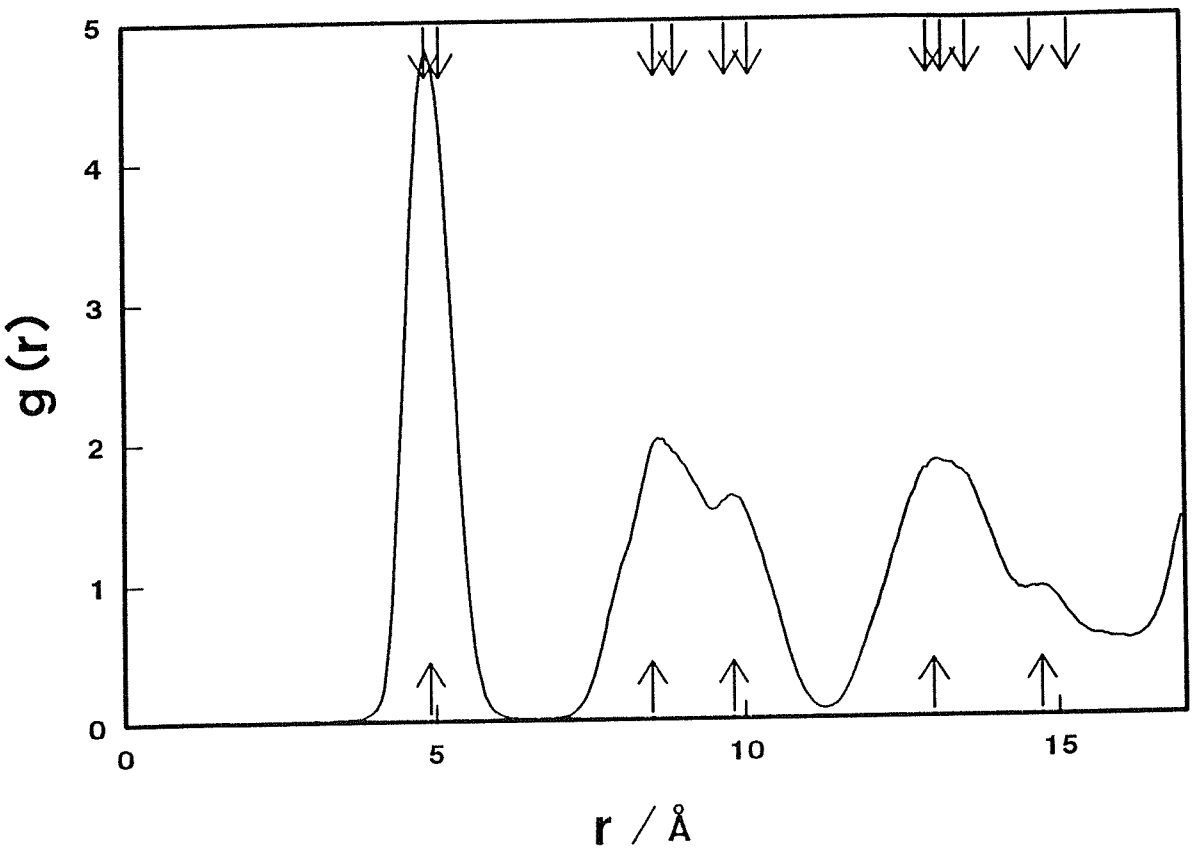

Figure 3.7. Radial distribution of the molecular centres of mass for A_m = 21.2Å^2. The upper arrows indicate the expected peak positions for a triangular 4.9x8.49Å lattice and lower arrows for a rectangular 4.85x8.9Å lattice.

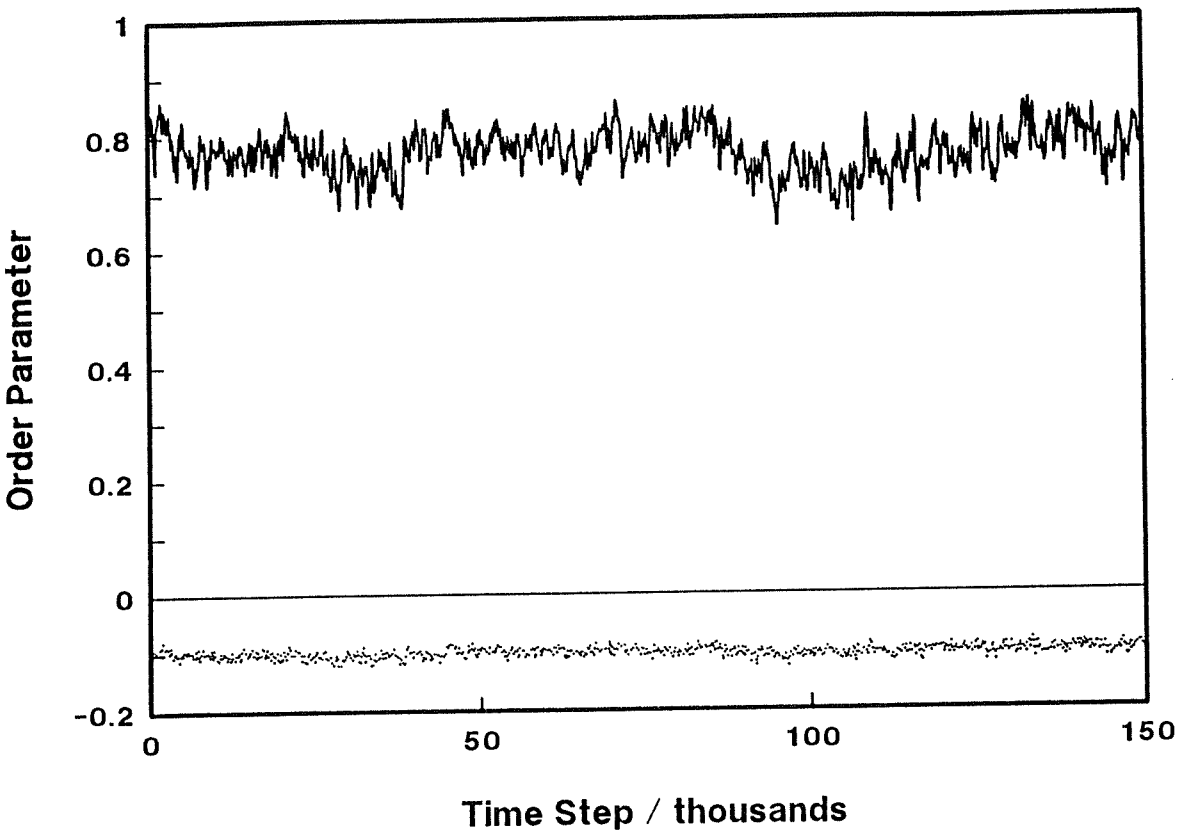

Figure 3.8. The hexagonal order parameter $\exp(i6\theta)/6$ as a function of time for A_m = 21.2Å^2: the real part(solid line) and the imaginary part(dot line).

as

$$\mathbf{I} = \sum_{i=1}^{n} m_i(r_i^2 \mathbf{1} - \mathbf{r}_i\mathbf{r}_i) \tag{3.8}$$

where $\mathbf{r}_i$ is the position of atom i from the molecular centre of mass and the sum is over all atoms in the molecule. The eigenvector corresponding to the smallest eigenvalue is the longest principal axis of the inertia tensor. The tilt angle, θ, of a molecule is defined as the angle between the long axis of the molecule and the surface normal. The most probable tilt, defined as the tilt corresponding to the maximum in $g(\cos\theta)$ shown in Figure 3.9, for each method is shown in Table 3.3, along with the average values of $<\cos\theta>$. In this table, the tilt is measured in degrees away from the surface normal as shown in Figure 3.1. In general, the tilt calculated from the direction of the molecular end-end vector was not significantly different from the tilt from the moment of inertia tensor. The distribution of the cosines of the molecular tilts is presented in Figure 3.9. This plot is not symmetric about 1, as is the case for N_2/graphite[30], since the molecules could not flip end-over-end in such a dense system.

Table 3.4 summarizes the tilt values found in the energy minimisations and MD simulations, along with recent experimental results for stearic acid LB films. The simulation at A_m=20.79Å^2 had a most probable tilt of 0°, while the simulation at 21.2Å^2 had the most probable tilt of 9°, supporting the finding of the energy minimisation calculations that the structure changes from upright to tilted near the head group area 21Å^2.

Figure 3.10(a) shows the instantaneous average tilt (not the most probable tilt) of the layer as a function of time. The average tilt of the layer was defined as the inverse cosine of the average of the cosines of the tilts of all the molecules, that is: $\cos^{-1}<\cos\theta>$. The large fluctuations in the average tilt were associated with large-

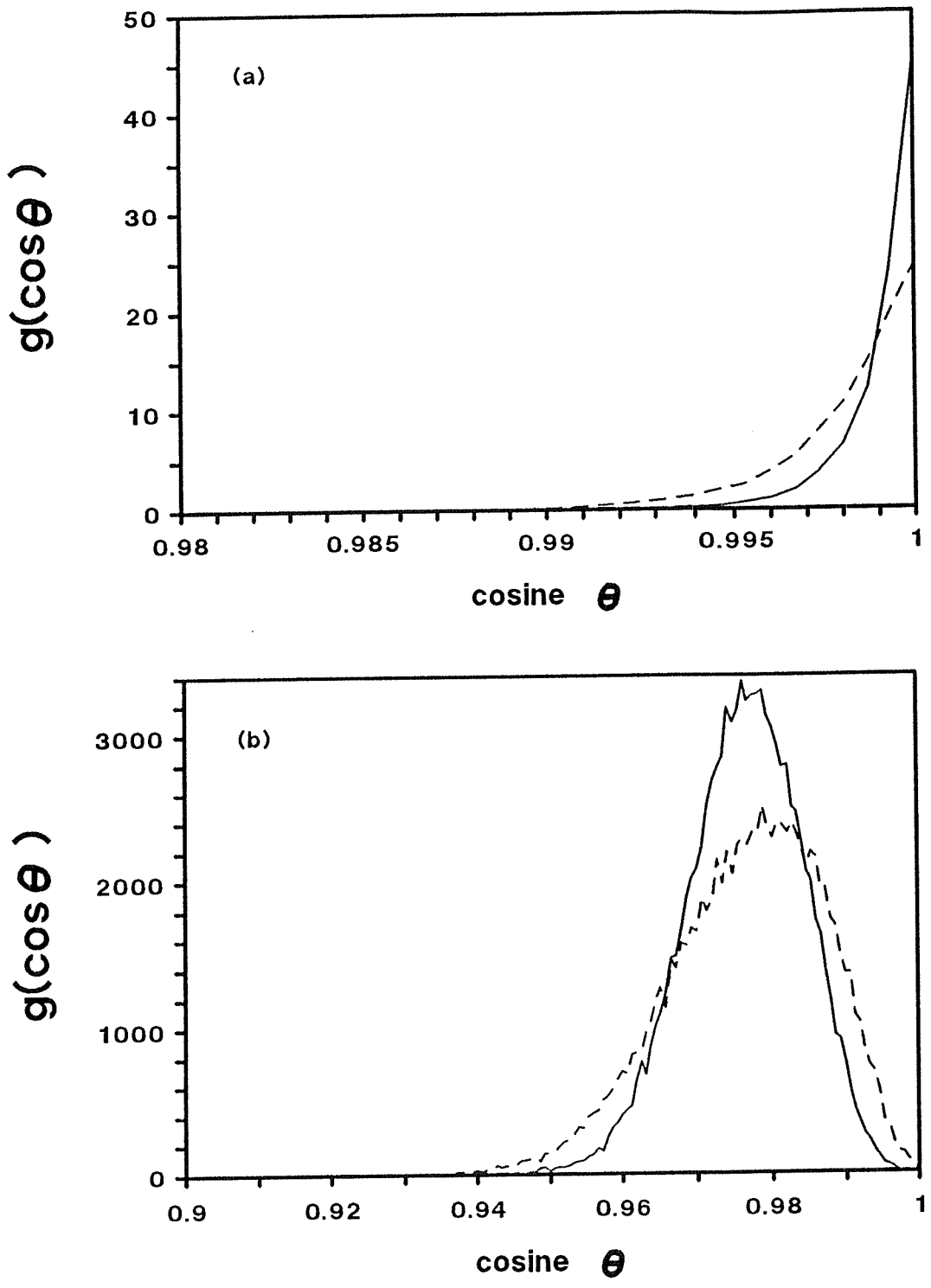

Figure 3.9. Distribution of the cosine of the molecular tilts for: (a) Am = 20.79Å^2, (b) Am = 21.2Å^2. The solid line represent tilt from moment of inertia and dashed line from the end-end vectors of the molecules.

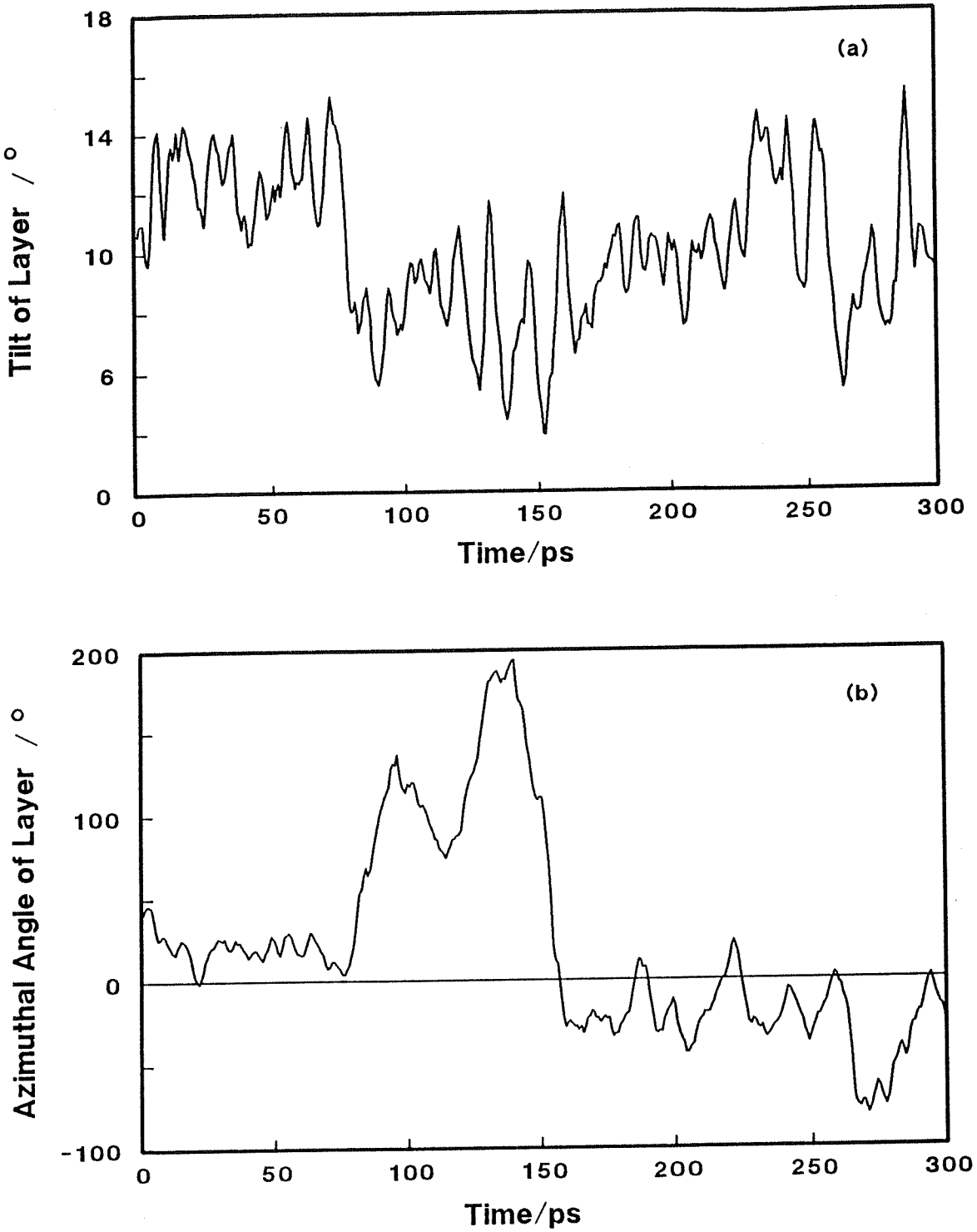

Figure 3.10. (a) The average molecular tilt taken from $\cos^{-1}(\langle P_1 \rangle)$ and (b) the average azimuthal angle of the layer with time for A_m = 21.2Å^2.

scale cooperative motions of the layer. Figure 3.10(b) shows the time variation of the average azimuthal angle of the layer, defined as the angle between the projection of the molecular axis, determined from the moment of inertia tensor, onto the plane of the surface, and the x-axis, averaged over all the molecules of the layer. This angle tended to stay near $+25°$ and $-25°$, very nearly the value of $\pm 30°$ expected if the molecules were pointing towards their next-nearest neighbours. However, the system also went through two 'excursions' during the 300ps, during which the molecules precessed by $180°$ and $-70°$ respectively. These changes in azimuthal angle were preceded by changes in the tilt angle.

Table 3.4. Comparison of Molecular Tilts from Experiment and Simulation.

System	Molec. Area ($Å^2$)	Tilt (°)	Experimental Technique	Ref.
Stearic acid/gr[a]	20.8	0	energy minimisation	b
Stearic acid/gr	21.2	30	energy minimisation	b
Stearic acid/gr	20.8	0	MD simulation	b
Stearic acid/gr	21.2	8	MD simulation	b
Stearic acid B	20.7	27	X-ray diffraction	24
Stearic acid C	23.2	38	X-ray diffraction	23
Cd Stearate/Silica	-	0	fluorescence anisotropy	31
Cd Stearate/Silica	20.7	8	electron diffraction	16
Stearic acid/Al	-	12	IR	32
Stearic acid/Ge	-	0	FTIR	33
Arachidic acid/gr	20.8	40	MD simulation, UA model	9
Cd arachidate/Si	-	15	NEXAFS	34,35
Ca arachidate/Si	-	33	NEXAFS	34,35

[a] gr = graphite

[b] This work.

As the tilt angle decreases, it is easier for molecules to precess. These excursions make it difficult to assign an average tilt for the simulated system, but we estimate it to be about 9°, in good agreement with experimental results for stearic acid LB films (Table 3.4).

The average tilt is much smaller than the value from the minimum energy configuration. One possible explanation is that this was due to the presence of gauche bonds near the surface, decreasing the effective head group area. Accordingly, we performed a simulation of all-trans molecules, whose dihedral potential was approximated by a simple harmonic potential, with the same form as the bond bending potential:

$$V(\phi) = \frac{1}{2} k_d (\phi - \phi_0)^2 \tag{3.9}$$

approximated as

$$V(\phi) = k_d \{1 - \cos(\phi - \phi_0)\}, \tag{3.10}$$

with k_d = 65 kJ mol^{-1}, ϕ_0 = 0°.

The parameter k_d was chosen so that the potential would be a good approximation to the full dihedral potential near the trans well. However, after 12,000 simulation steps, the average tilt in the system was only 9°: similar to the original model. A calculation of the variation of configurational energy with tilt showed that there is no energy barrier to tilting, when the other two angles are kept fixed in their values from the minimum energy configuration. This meant that the low value of the tilt angle was not due to the system being locked into a nearly upright structure by an energy barrier, but to some other mechanism.

In order to test out a different possible explanation for the low tilt angle, a further simulation was performed with the original dihedral potential, but starting from the minimum energy configuration $(\phi,\theta,\psi) = (0°, -30°, \pm 69°)$ of a two-sublattice

energy minimisation at $A_m = 21.2\text{Å}^2$. Figure 3.11 shows the average tilt (taken from $\cos^{-1}\langle\cos\theta\rangle$) as a function of time for this system. This shows that the smaller tilt in the system is not due to the formation of gauche defects. It may instead be due to thermal motions of the molecules, including the translational motion of the chains, the translational motion of the head groups normal to the surface, and the vibrational motions of the dihedral angles of the chains.

Therefore, at a fixed density, as the temperature is increased, the molecules will become more and more upright. However, our results show that the tilt is apparently not sensitive to the presence of a small number of gauche bonds. The larger tilt found in the simulations of arachidate chains[9,10] is apparently due to their use of the united-atom model, where the effective density of the layer will be less than for the explicit-hydrogen model. Values of the orientational order parameters $\langle P_2\rangle$ and $\langle P_4\rangle$ have also been measured by fluorescence anisotropy. For Cd stearate on fused silica, the values were $\langle P_2\rangle = 0.33$ and $\langle P_4\rangle = 0.02$ [31]. These values are much smaller than the simulation results, possibly indicating a greater level of orientational disorder in the experimental system. It is also possible that this low order is due to the probe molecules upsetting the local order when placed in the film.

Molecular twist angle.

We have also examined the orientation ψ(twist angle) of the molecules in the plane of the surface. The twist angle, ψ, of the molecule is the angle between local x-axes and vector **R** defined by

$$\mathbf{R} = (-1)^n \left(\mathbf{r}^n - \frac{1}{2}(\mathbf{r}_{n-1} + \mathbf{r}_{n+1})\right) \qquad (3.11)$$

which is the vector connecting the carbon atom C_n to the bisector of the vector joining

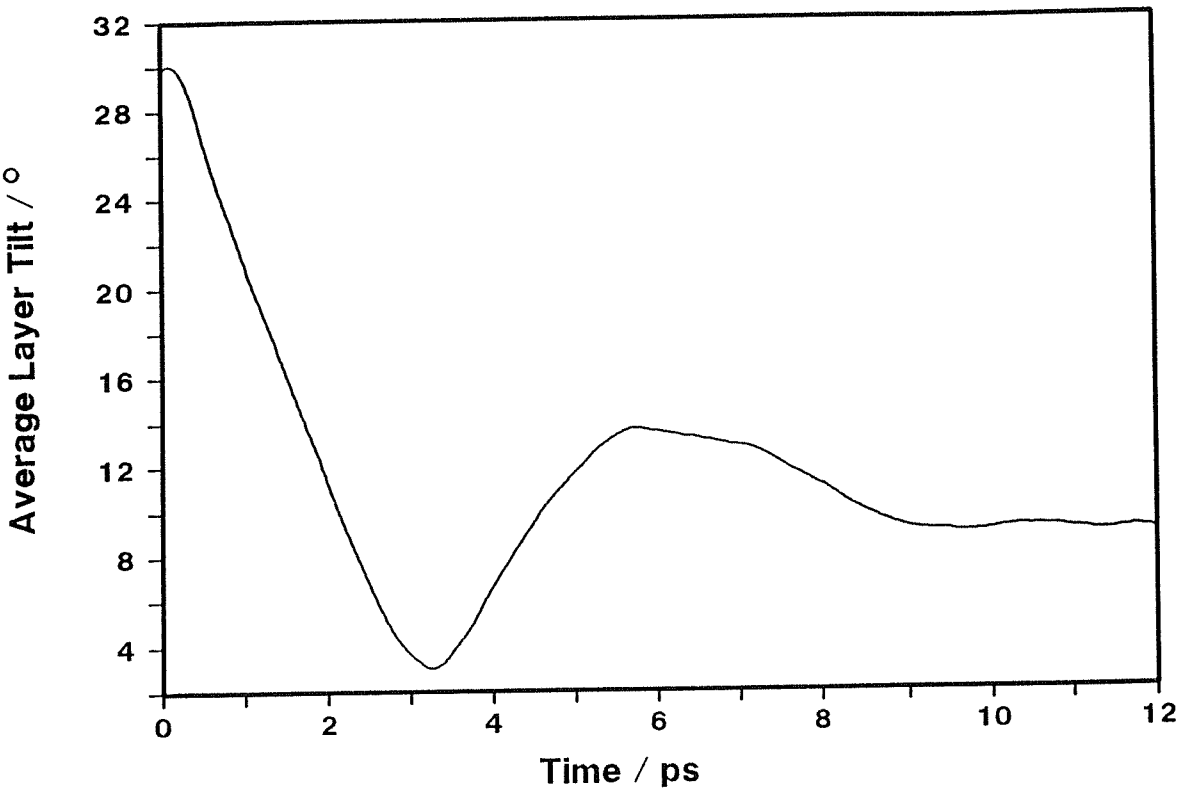

Figure 3.11. The time dependency of the average molecular tilt taken from $\cos^{-1}(<P_1>)$ at A_m = 21.2Å^2. The simulation started from the minimum energy structure obtained from the energy minimisation.

the carbon atoms C_{n-1} and C_{n+1}. This is the rotation of the molecule about its own long axes. The twist angle of the molecule is only meaningful for molecules in the all-trans conformation and we have only calculated this twist angle for these molecules. The vector representing the in-plane orientation is illustrated in Figure 3.12. Figure 3.13 shows the distribution of ψ angles for both simulations. In each case, the molecules formed a two-sublattice structure with the axes perpendicular. This is reminiscent of the herringbone structure, which is common for small non-spherical molecules adsorbed on surfaces, and for the crystal structures, where the angle between two molecules of differing sublattices is not 90°. However, there is little evidence in our system for orientational ordering into a precise herringbone with axes at 90°. Instead, the molecules form a system with two preferred orientations at random locations. Molecules flipped between sub-lattices, apparently at random. We have also calculated the value of ψ measured from the direction of tilt ϕ. The result was the same two-sublattice behaviour found when measured with respect to the x-axis.

The ψ angle distribution of Figure 3.13 is inconsistent with the symmetry of the triangular lattice, where one would expect to observe three roughly equivalent sublattices at $\psi = 0°$, 60° and 120°. Indeed, a calculation of the intermolecular energy of a layer of 16 all-trans rigid molecules at (ϕ,θ,ψ) = (0,10,0), as the value of ψ for the central molecule was varied from 0° to 360°, showed this type of symmetry (see Figure 3.14(a)). The molecule had preferred orientations 60° apart, where the plane of the carbon atoms was oriented along a line of nearest neighbours. As a result, we have examined the average distances of the six nearest neighbours of each molecule in the second sublattice, and found that the local crystal field is rectangular rather than triangular at these points.

The barrier to rotation about ψ for a perfect static lattice, from Figure 3.14(a), is about 30 kJ mol^{-1} (3600 K), which is large enough prevent any molecules from entering the other sublattices. The barrier encountered by simulation molecules is

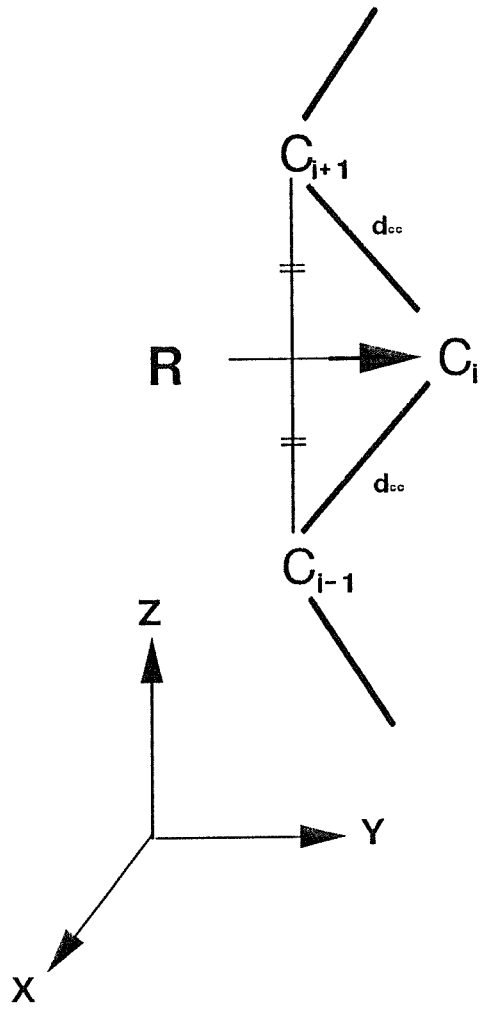

Figure 3.12. The vector representating the in-plane orientation of the CH_2 group in the alkyl chain of a stearic acid molecule.

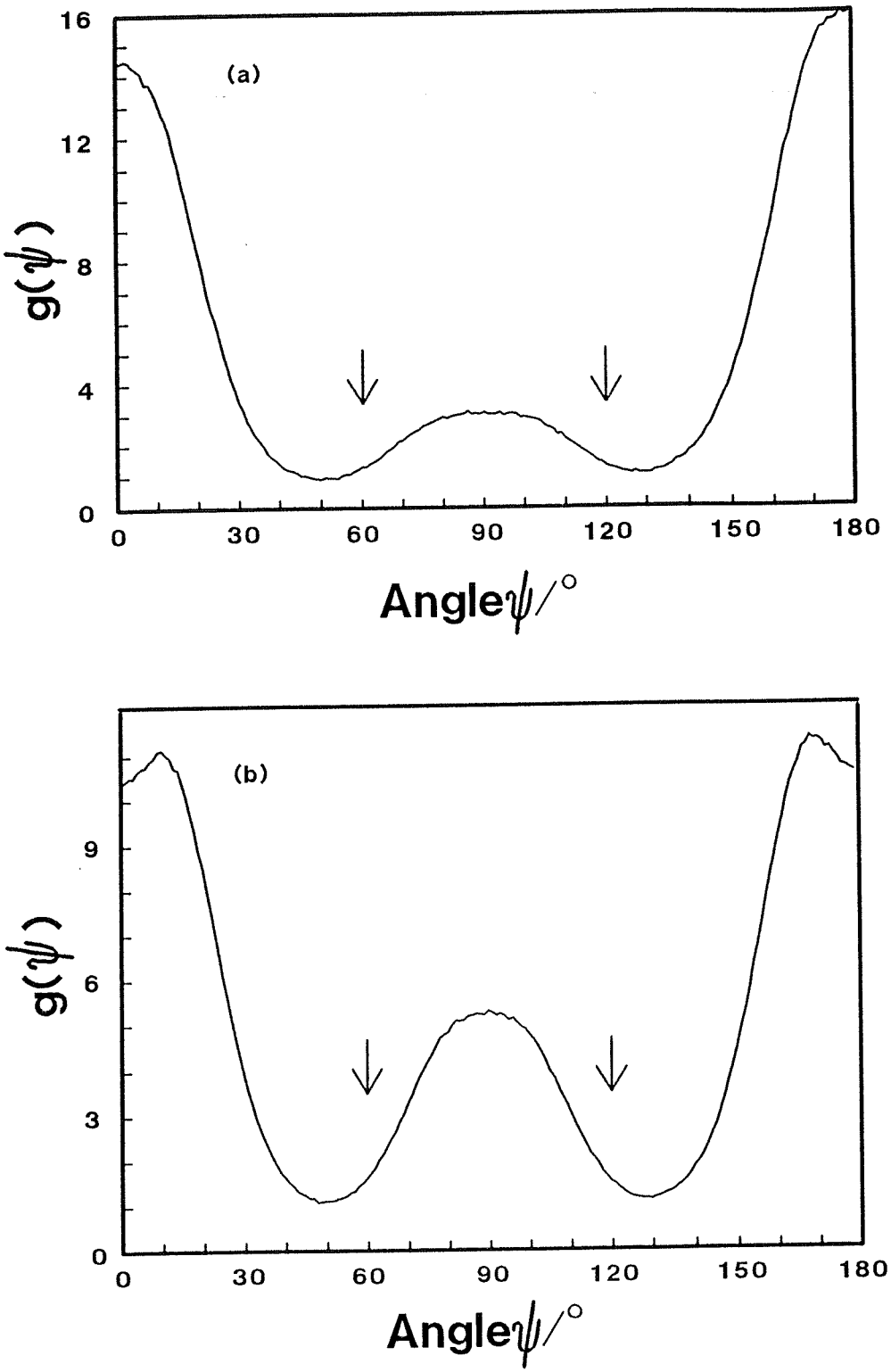

Figure 3.13. Distribution of twist angles for the CH_2 groups of the molecules: (a) A_m = 20.79Å^2; (b) A_m = 21.2Å^2. The arrows indicate the expected position for a triangular lattice.

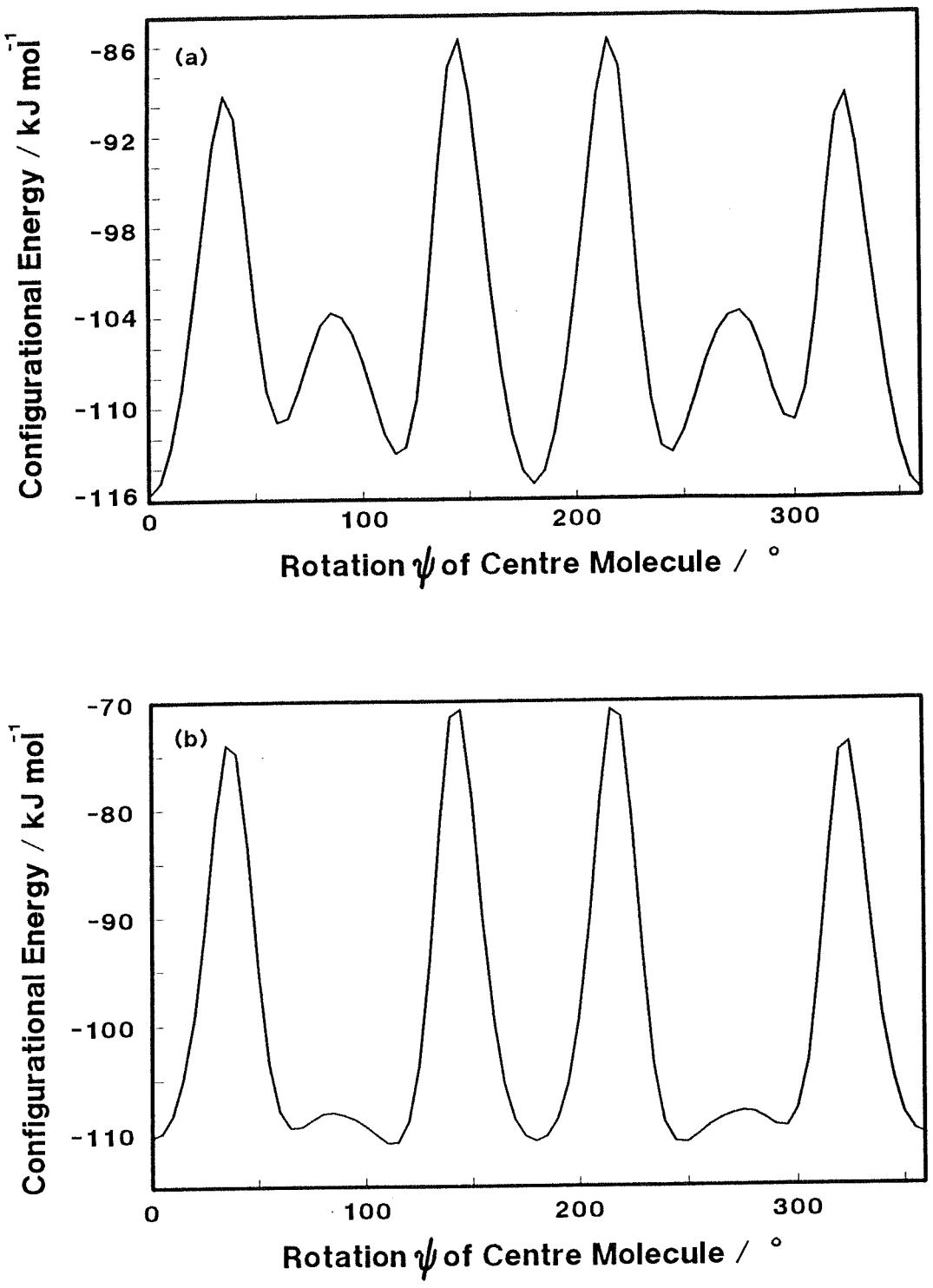

Figure 3.14. Configurational energy of a 4x4 molecular layer with all-trans configuration at (ϕ,θ) = (0,10) with the rotation ψ of the molecule at centre about its long axis: (a) a triangular 4.9x8.49 lattice; (b) a rectangular 4.85x8.9 lattice.

expected to be lower, since the simulated system has more degrees of freedom, and thus one would expect to see three equivalent sublattices.

However, we do not see any population of sublattices at 60° and 120° because the rotation about ψ is accompanied by a distortion of the nearest neighbour crystal field from triangular 4.9 × 8.49Å to rectangular 4.86 × 8.89Å (±0.1Å). A calculation of the intermolecular energy as a function of ψ for the central molecule in this rectangular structure is shown in Figure 3.14(b). In this structure, there is a broad energy minimum centred at $\psi = 90°$. The small energy maximum near $\psi = 80°$ would be expected to lead to a double peak in $g(\psi)$. The single peak obtained in Figure 3.13 suggests that thermal motion smears out the locations of these two minima, so that the molecules do not see a maximum. In conclusion, the crossing of the rotational barrier about ψ is accompanied by a distortion of the local crystal field which stabilizes the orientation of 90° in the second sublattice instead of 60° and 120°, so we see molecules only at $\psi = 0°$ and $\psi = 90°$. This can be expected if the relaxation time for a molecule in the second sublattice to return to the first sublattice is much less than the relaxation time for the local crystal field to return to triangular while the central molecule remains in the second sublattice. Figure 3.14(b) shows that the second sublattice is about 4 kJ mol^{-1} (480 K) less favourable in energy than $\psi = 0°$ in a perfect triangular crystal field. This value is likely to be similar for the simulated system, thus accounting for the lower population in the second sublattice.

The peak in Figure 3.13(b) associated with the first sublattice, with maxima near $\psi = 0°$ and $\psi = 180°$ is split. The molecules in the simulation at $A_m = 21.2Å^2$ tended to orient slightly away from their nearest neighbours. This is likely due to the fact that the potential between two neighbouring molecules is highly anisotropic. As thermal motion brings two molecules together, they will tend to slightly orient away from each other because the potential is softer in this direction.

The time evolution of the fraction of molecules contained in each sublattice was followed for the system at $A_m = 21.2Å^2$. The system appeared to reach

equilibrium, with an average population of 0.72 in the sublattice with molecular planes oriented parallel to the box x-axis, and an average population of 0.28 in the sublattice oriented normal to the x-axis. For the system at $A_m = 20.8Å^2$, the average populations were 0.80 and 0.20. There were no global "excursions" in ψ, as there were for the tilt and azimuthal angles: the molecular planes always tended to lie either parallel or perpendicular to the x-axis.

3.4.4. Conformational defects in LB monolayer.

We have also examined the occurrence of conformational defects in the simulated monolayers. We define a gauche-plus (g^+) defect as a C-C-C-C dihedral angle between 60° and 180° and a gauche-minus (g^-) defect as a dihedral angle between -60° and -180°. A dihedral angle from +60° to -60° denotes a trans conformation and an angle of 180° denotes an eclipsed conformation. On average, the number of all-trans molecules was 94% in the system at $A_m = 20.79Å^2$, and 87% in the system at $21.2Å^2$. These values are much higher than those found in lipid bilayer simulations, due to the larger head group areas ($25Å^2$/molecule) in the lipid bilayers[6].

Figure 3.15 shows the distribution $g_D(z)$ of gauche bonds normal to the surface plane, along with the distribution of carbon atoms $g_C(z)$. For both models, the distributions are solid-like and did not change with time. There are 18 peaks in $g_C(z)$, corresponding to the head group, sixteen carbon atoms, and the tail group. The defect distributions show that they tend to cluster at the tops of the chains. However, there is a large number of gauche defects at bottom of the chains (nearest the head group) in the simulation at $A_m = 21.2Å^2$. There are also shoulders on the high z side of the two main peaks in $g_D(z)$, which correspond to a single molecule which moved upwards during the course of the run, until several segments of its chain were above the tail groups of the other molecules.

Figure 3.16 shows the radial distribution function for gauche defects. As the

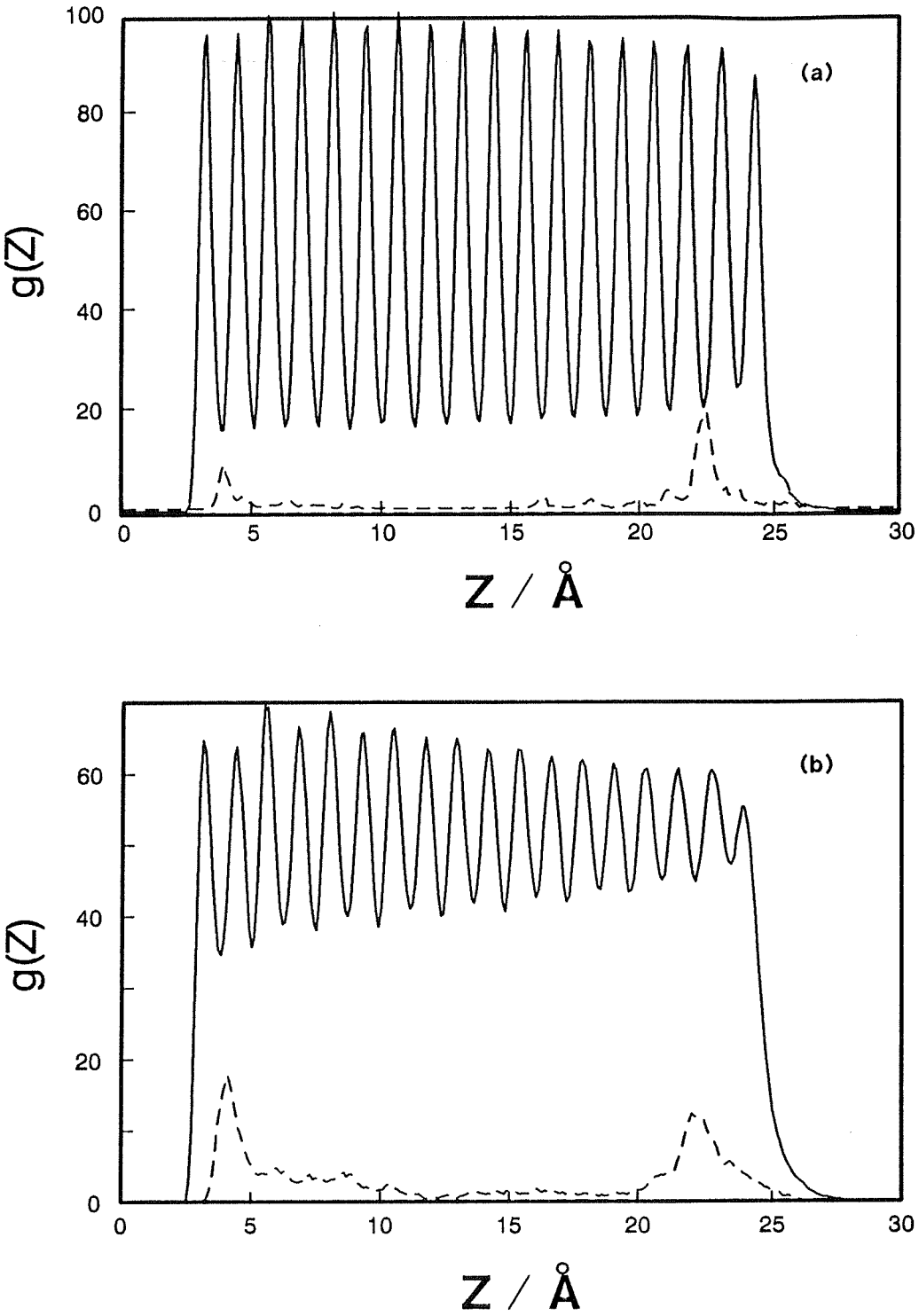

Figure 3.15. Distribution of carbon atoms (solid line) and gauche defects (dashed line) along z from the surface at (a) A_m = 20.79Å^2 and (b) A_m = 21.2Å^2. The dashed lines indicate 5 x g(Z).

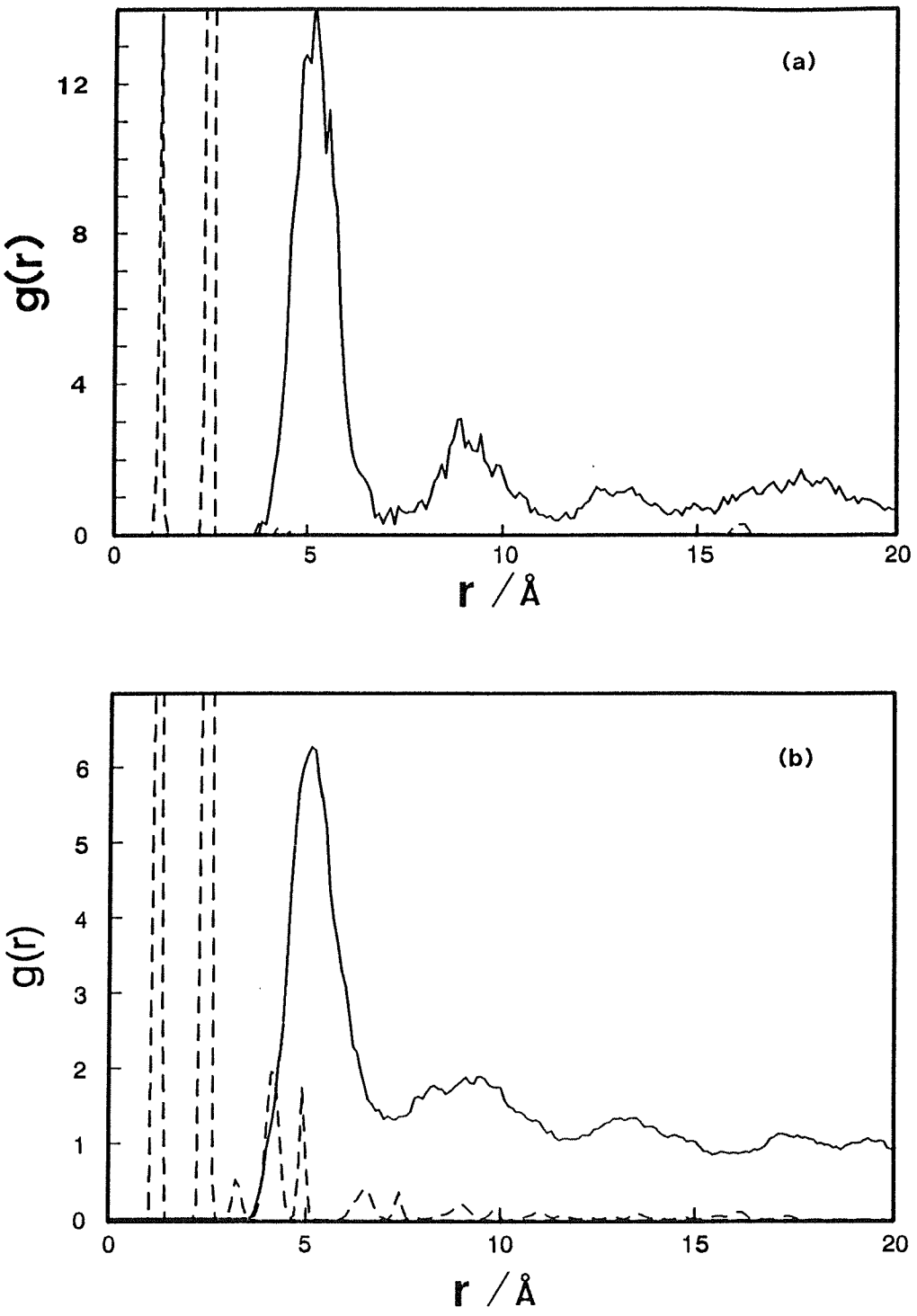

Figure 3.16. Radial distribution of gauche defects in separate molecules(solid line) and within molecule(dashed line) at (a) A_m = 20.79Å^2 and (b) A_m = 21.2Å^2.

number of defects is not conserved, this function has been normalized to the average density of defects during the course of the simulation. This is analogous to the radial distribution function calculated in a grand canonical Monte Carlo simulation. The distribution of defects in our system is liquid-like. Its non-random nature indicates how the presence of a gauche bond can promote the formation of a another one nearby, either in the same chain or in a neighbouring chain.

There are other types of conformational defects present in the chains. The most important is the combination of two gauche bonds tg^+tg^-t (t=trans), known as a kink or crankshaft. Kinks are energetically preferred over other combinations of gauche defects, because they preserve the overall direction of the chain. Others, such as g^+g^-, g^+g^+ or an isolated gauche bond, cause large changes of direction in the molecular chains, and therefore most often occur near the ends of the molecules.

Table 3.5 lists the average numbers of these defects found in the simulated system. The kink defects occurred mainly at the ends of the molecules, and no movement of kinks along the chains was observed.

Langmuir-Blodgett films are permeable to small gas molecules such as hydrogen and nitrogen. The mechanism is unknown, but may involve kink defects. We have calculated the free volume near one of the kinks in the simulation by performing 1,000,000 test insertions each of atoms of various sizes in random locations near a kink defect chosen from the molecular dynamics simulation at $A_m=21.2Å^2$. The largest atom successfully inserted had a radius of only 1.2Å (see Figure 3.17). However, this result will depend on system size, as larger local fluctuations in density are possible in a larger system. It is only possible to state that the diffusion of gas molecules through a Langmuir-Blodgett film may require a greater structural deformation than the formation of a single isolated kink.

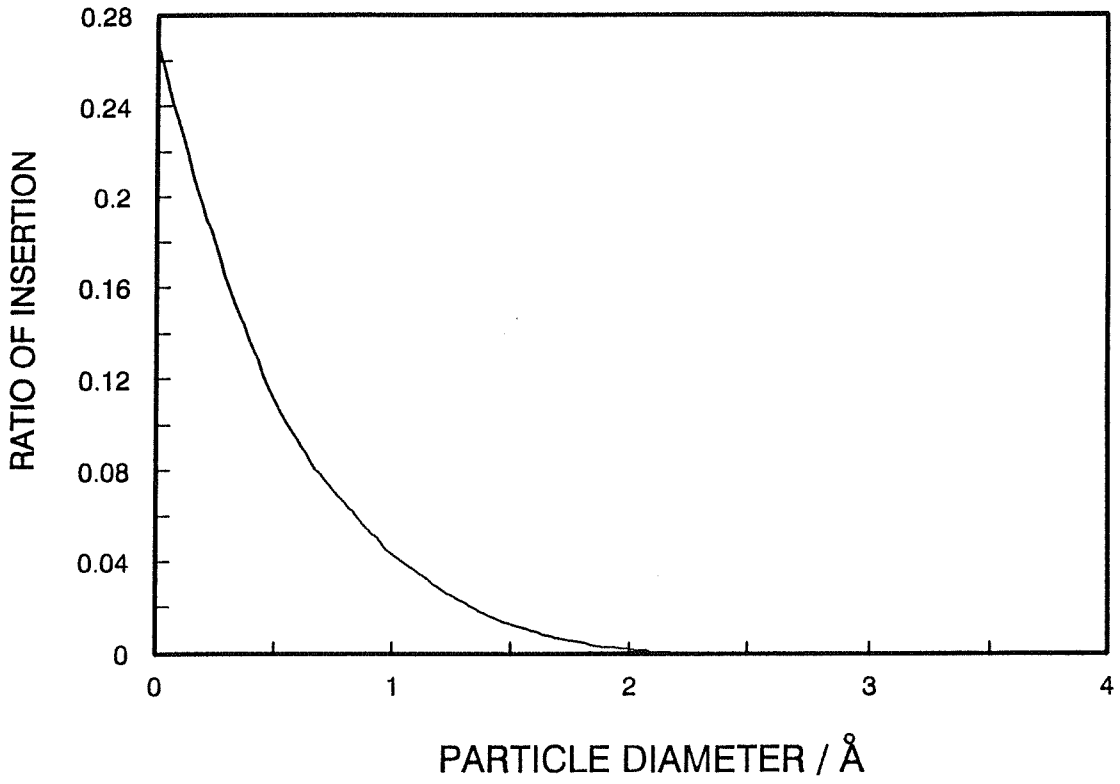

Figure 3.17. Probability of inserting particle into LB film monolayer, A_m = 21.2Å^2.

Table 3.5. Conformational Defects - Average Number per Molecule.

Defect type\molecular area	20.79Å^2	21.2Å^2
gauche	0.10 ± 0.03	0.23 ± 0.08
gauche plus	0.05 ± 0.02	0.13 ± 0.05
gauche minus	0.05 ± 0.02	0.10 ± 0.05
double gauche	0.000	0.004
kink	0.003	0.033

3.4.5. NMR order parameters.

Deuterium nuclear magnetic resonance (NMR) can, in principle, be used to characterize the orientational ordering of the C-H (or C-D) bonds of the Langmuir-Blodgett film molecules. These experiments measure the order parameter S_{CD}, a measure of the anisotropy of the C-D bond direction with respect to the surface normal. Although these experiments have not yet been performed on Langmuir-Blodgett films, data is available from lipid bilayers[32]. The order parameter tensor S_{ij} is defined as

$$S_{ij} = \frac{1}{2}(3\cos\theta_i \cos\theta_j - \delta_{ij}) , \qquad (3.12)$$

where θ_i is the angle between axis i and the surface normal. We have labelled the axes in the following manner:

x : H-H vector

y : bisectrix of HC_iH angle

z : vector from C_{i-1} to C_{i+1}.

The order parameter is averaged over all CH_2 groups and over time. The geometry of the molecule gives an expression for the C-D order parameter: $S_{CD} = 2/3\ S_{xx} + 1/3\ S_{yy}$. For the C-C bond order parameter, one has: $S_{CC} = 1/3\ S_{yy} + \cos(70°32')S_{yz} + 2/3\ S_{zz}$. The range of the order parameters is from +1 (fully ordered parallel to surface normal) to -½ (fully ordered perpendicular to surface normal). The results are shown in Figure 3.18. For both models, S_{zz} was near unity, indicating that the chains are highly ordered and near parallel to the surface normal. The result $S_{zz} = -2S_{xx}$ meant that there was rotation of the chains only about the z-axis. The order parameters in the system at $A_m = 21.2Å^2$ decrease near both ends of the chain, due to the presence of defects. Experimental results from lecithin bilayers show a slightly

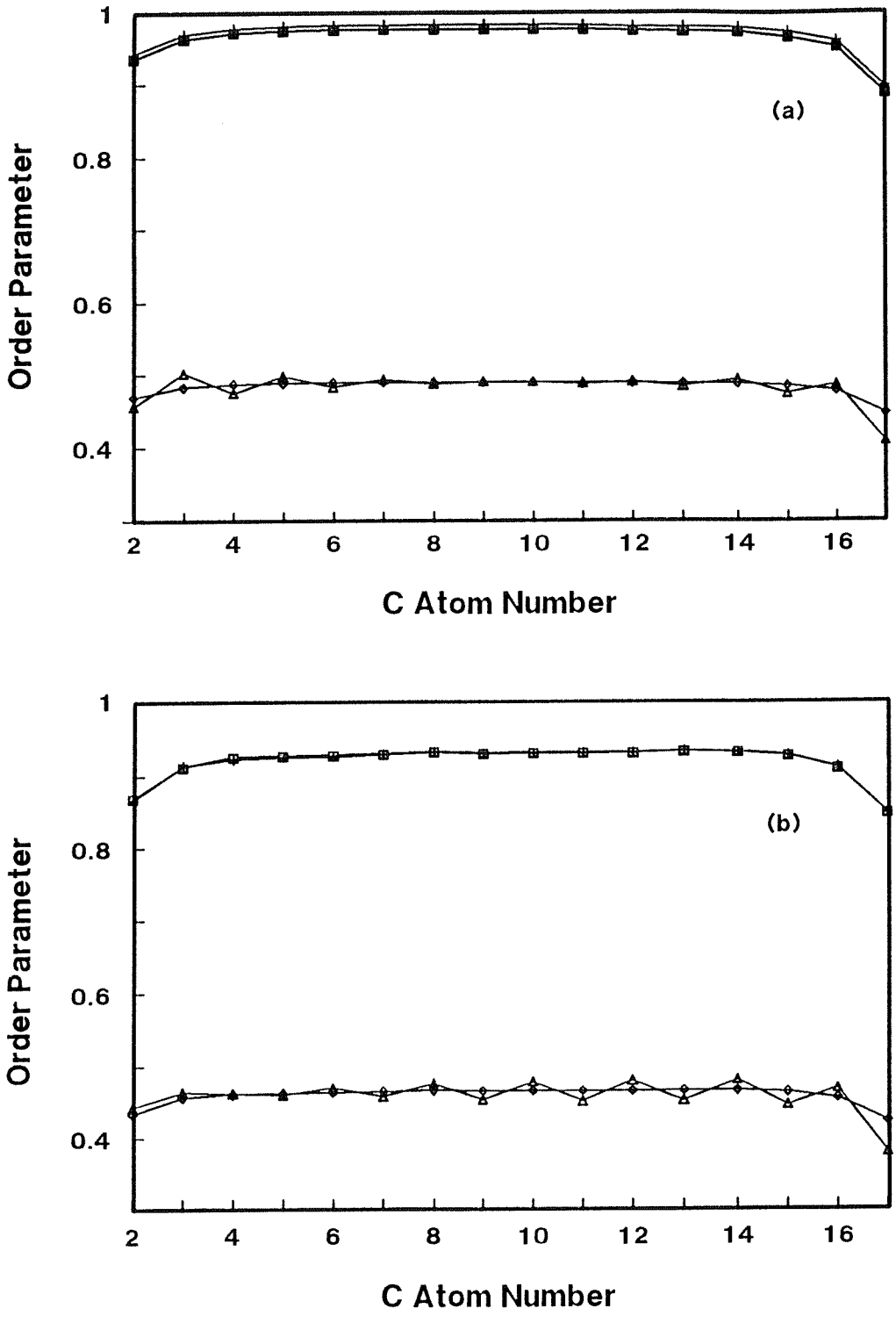

Figure 3.18. NMR order parameters of the layer with (a) A_m = 20.79Å^2 and (b) A_m = 21.2Å^2.

different pattern. The order parameter decreases only at the tail end of the chain, and its value is much less than our molecular dynamics result. This is in part due to the much larger head group area in these systems: about 25Å^2 per molecule.

3.4.6. Dynamics of LB monolayers.

The dynamics of the Langmuir-Blodgett film was examined through the calculation of the velocity auto-correlation function for carbon atom motions. Figure 3.19 shows the Fourier transform of this function, for velocity components parallel and perpendicular to the surface plane. This plot is very similar to the molecular dynamics result for arachidate chains[9]. To identify the various modes, the velocity auto-correlation function of a single molecule was also calculated, both in vacuum and on the surface. This showed that the high frequency peaks at 380-480 cm^{-1} are due to bond bending and torsional motions, and the broad feature near 50-200 cm^{-1} is due to translational motions of the chains in the plane of the surface.

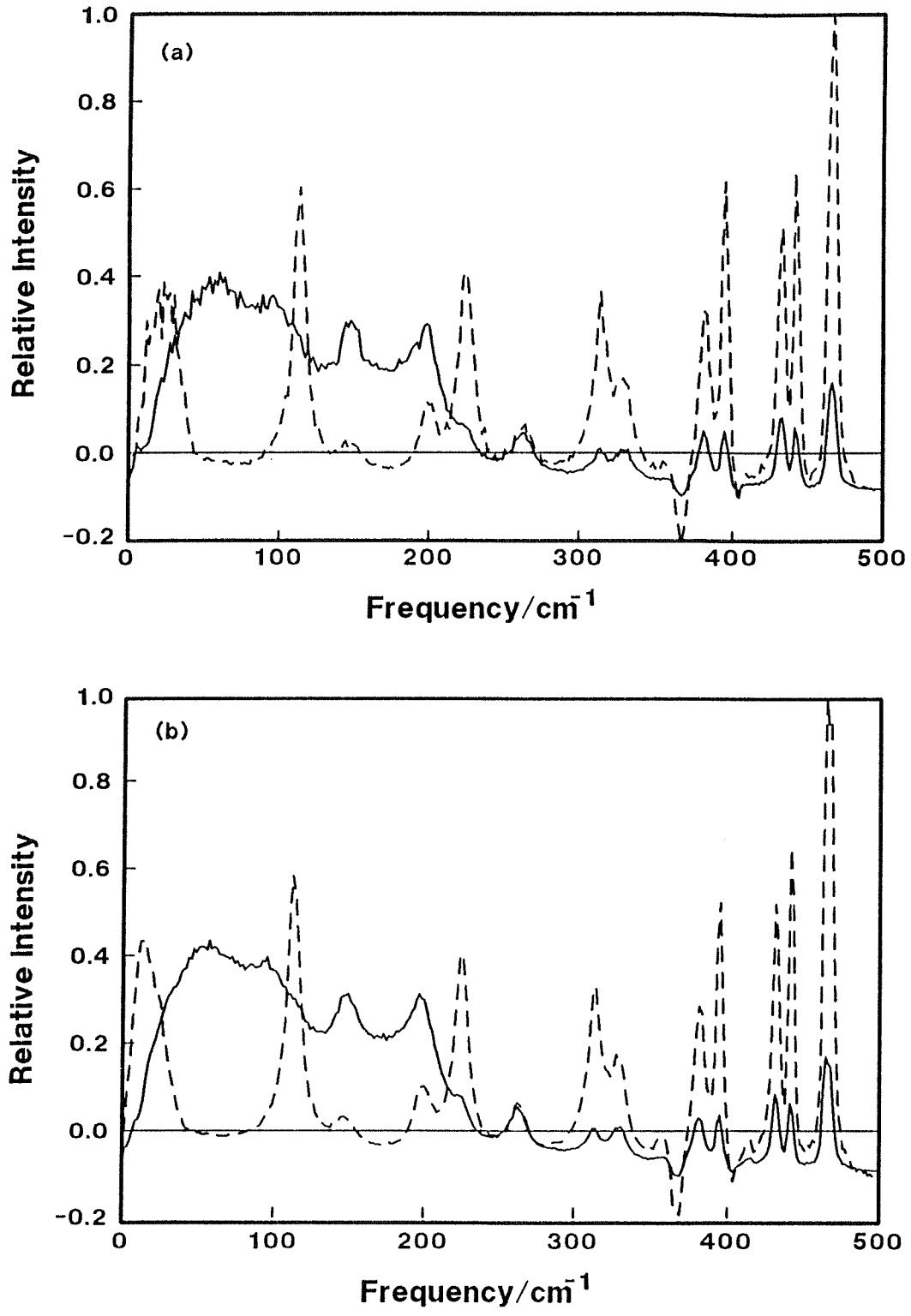

Figure 3.19. Power spectrum of molecular motions, in-plane (solid line) and out of plane (dashed line) for (a) A_m = 20.79Å^2 and (b) A_m = 21.2Å^2.

3.5. Conclusions.

Molecular simulation predicts a significant structural change in supported stearic acid monolayers at densities close to those observed experimentally for Langmuir-Blodgett films. At a head group area per molecule close to 21Å^2 the tilt of the long axis of the molecules with respect to the surface normal suddenly changes from a finite value depending on temperature (32° at 0K, 9° at 300K) to zero. This tilting transition is caused by the packing of the hydrogen atoms belonging to methylene groups on neighbouring molecules. It can not be reproduced in a satisfactory manner by models that we have examined in which the methylene groups are represented by united atoms. As the temperature is raised from 0K to room temperature the tilt angle in the monolayer just prior to the transition falls from 32° to approximately 9°. The predominant cause of the reduction being an increase in the effective density of the layer due to lateral thermal vibrations of the molecules.

The simulations have been performed at densities which are usually labelled "liquid" in the diagram of the surface pressure-area isotherm of Langmuir stearic acid films, though there has as yet been no experimental determination of its diffusion constant. This phase is predicted by our energy minimisation and molecular dynamics studies to be solid and to show a continuous change, as the density is varied, between tilt angles which are similar to those of the B and C forms of bulk stearic acid crystals. The change in tilt angle is accompanied by a change in the number of conformational defects. This suggests that this phase may not be liquid, but a solid, changing in orientational and conformational order rather than in translational order, in agreement with recent grazing incidence x-ray scattering results.

At the lower head group areas our results are not sensitive to the model of the methylene groups. The stearic acid monolayer displays a non-negligible fraction of conformational defects at 300K however (due to the increased density) there are far less than have been reported for simulations of lipid bilayers. The defects cluster at the top and bottom of the layer and are highly correlated both within and between

molecules. The presence of conformational defects does not open up any significant free volume within the layer.

The layer displayed long lived (100ps) co-operative motions involving simultaneous changes in tilt angle and a precession. These motions can be interpreted as attempted excursions of the layer as a whole between equivalent symmetry positions of the crystalline structure. While similar excursions may take place in small domains of a laboratory stearic acid monolayer, for larger arrays of molecules such excursions are probably suppressed.

We are aware of the weakness of our current head group model, in that it does not include the head group structure or dipolar interactions. The proximity of the head groups to each other means that these interactions may have an effect on the structure and dynamics. Also, it is possible that the glass surfaces on which these films are usually deposited will be hydrated. There may be hydrogen bonding between the head groups and the surface. Alternatively, the head groups may be chemically bonded to the surface. We will extend our model to be able to improve this weakness in next chapter.

The results presented above demonstrate the importance of the packing of hydrogen atoms along the backbone of neighbouring amphiphillic molecules in determining the structure of a simple Langmuir-Blodgett film. They also illustrate the role of entropic effects in modifying the quantitative predictions of energy minimisation calculations.

References.

[1] J.-P. Ryckaert and A. Bellemans, Faraday Disc. Chem. Soc. **66**, 95 (1978); Chem. Phys. Lett. **30**, 123 (1975).

[2] S. Toxavaerd, J. Chem. Phys., **89**(6), 3808 (1988)

[3] J.-P. Ryckaert and A. Bellemans, Chem. Phys. Lett., **36**, 123 (1975).

[4] J.H.R. Clarke and D. Brown, Mol. Phys., **58**, 815 (1986).

[5] P. van der Ploeg and H.J.C. Berendsen, J. Chem. Phys., **76**(6), 3271 (1982).

[6] P. van der Ploeg and H.J.C. Berendsen, Mol. Phys., **49**(1), 233 (1983).

[7] R.W. Pastor, R.M. Venable and M. Karplus, J. Chem. Phys., **89**(2), 1112 (1988).

[8] J. Harris and S.A. Rice, J. Chem. Phys., **89**(9), 5898 (1988).

[9] G. Cardini, J.P. Bareman and M.L. Klein, Chem. Phys. Lett., **145**(6), 493 (1988).

[10] J.P. Bareman, G. Cardini and M.L. Klein, Phys. Rev. Lett., **60**(21), 2152 (1988).

[11] J.-P. Ryckaert, M.L. Klein and I.R. McDonald, Phys. Rev. Lett., **58**, 698 (1987).

[12] J.-P. Ryckaert, I.R. McDonald and M.L. Klein, Mol. Phys., **67**, 957 (1989).

[13] D.E. Williams, J. Chem. Phys., **47**, 4680 (1967).

[14] W.A. Steele, J. Phys.(Paris), **38**, C4-61 (1977).

[15] J. Talbot, D.J. Tildesley and W.A. Steele, Mol. Phys., **51**, 1331 (1984).

[16] S. Garoff, H.W. Deckman, J.H. Dunsmuir, M.S. Alvarez and J.M. Bloch, J. Phys.(Paris), **47**, 701 (1986).

[17] V. Vogel and C. Wöll, Thin Solid Films, **159**, 429 (1988).

[18] A. Bonnerot, P.A. Chollet, H. Frisby and M. Hoclet, Chem. Phys., **97**, 365 (1985).

[19] S.W. Barton, B.N. Thomas, E.B. Flom, S.A. Rice, B.Lin, J.B. Peng, J.B. Ketterson and P. Dutta, J. Chem. Phys., **89**, 2257 (1988).

[20] K. Kjaer, J. Als-Nielsen, C.A. Helm, P. Tippman-Krayer and H. Möhwald, J. Phys. Chem., **93**, 3200 (1989).

[21] A. Ulman, J.E. Eilers and N. Tillman, Langmuir, **5**, 1147 (1989).

[22] N.E. Schlotter, M.D. Porter, T.B. Bright and D.L. Allara, Chem. Phys. Lett., **132**, 93 (1986).

[23] V. Malta, G. Cellotti, R. Zannetti and A.F. Martelli, J. Chem. Soc., **B3**, 548 (1971).

[24] M. Goto and E. Asada, Bull. Chem. Soc. Jpn., **51**, 2456 (1978).

[25] L. Verlet, Phys. Rev., **159**, 98 (1967).

[26] J.-P. Ryckaert, G. Ciccotti, and H.J.C. Berendsen, J. Comput. Phys., **23**, 327 (1977).

[27] J.-P. Ryckaert, Mol. Phys., **55**, 549 (1985).

[28] W.A. Steele, *The Interaction of Gases with Solid Surfaces*(Permagon, Oxford, 1974).

[29] J. Tobochinik and G.V. Chester, Phys. Rev., **B25**, 6778 (1982).

[30] J. Talbot, D.J. Tildesley and W.A. Steele, Faraday Discuss. Chem. Soc., **80**, 91 (1985).

[31] J.D. LeGrange, H.E. Riegler, W.P. Zurawsky and S.F. Scarlator, J. Chem. Phys., **90**, 3838 (1989).

[32] J. Seelig and W. Niederberger, Biochemistry, **13**, 1585 (1974).

[33] F. Kimura, J. Umemura, and T. Takenaka, Langmuir, **2**, 96 (1987).

[34] D.A. Outka, J. Stöhr, J.P.Rabe, J.D. Swalen, and H.H. Rotermund, Phys. Rev. Lett., **59**, 1321 (1987).

[35] J.P. Rabe, J.D. Swalen, D.A. Outka, and J. Stöhr, Thin Solid Films, **159**, 275 (1988).

CHAPTER FOUR.

A Langmuir-Blodgett Monolayer with the All-Atom Model.

4. A LANGMUIR-BLODGETT MONOLAYER WITH THE ALL-ATOM MODEL.

4.1. Introduction.

In this chapter we will discuss the results of the energy minimisation and molecular dynamics calculations for the monolayer of stearic acid using the all-atom representation of the carboxylic acid headgroup. The representation of the alkyl chain in the all-atom model is same as that of the chain in the explicit-hydrogen model. As mentioned in chapter 3, although the explicit-hydrogen model established the importance of including a realistic representation of the hydrocarbon chain, the united-atom representation of the carboxylic acid headgroup is a poor representation of the interaction between the headgroups and between the headgroup and surface because there are no dipole-dipole, or partial charge interactions between the polar carboxylic acid groups. A number of workers [1,2,3] have simply ignored the headgroup to concentrate on the structure induced by the packing of the hydrocarbon chains. Others[4,5,6] have represented the repulsion-dispersion interaction between headgroups as a united-atom Lennard-Jones potential. In these studies the electrostatic interaction between headgroups and between headgroup and surface has been ignored. A number of studies of the adsorbed alkanethiols($C_nH_{2n+1}SH$) on the Au(111) surface[7,8] have recognised that the sulphur headgroups are chemically adsorbed at fixed sites on the surface. In these studies the sulphur-sulphur lateral interaction is represented by a Lennard-Jones interaction with the σ parameter chosen to be sufficiently large to lock the molecules into the triangular commensurate lattice. There have been two studies which have explicitly attempted to handle the dipolar interactions between the molecules. Egbert and Berendsen[9] have studied a sodium-decanoate/decanol/water system. The chains in these molecules are treated as united-atoms but the hydrophilic groups are treated explicitly. Hautman *et al.* [10] have studied adsorbed alkanthiols with polar tail-groups (i.e. $HS(CH)_nX$ with X=-OH or -CN).

In this chapter we attempt to model completed monolayers of stearic acid molecules on a structureless surface. It is a systematic extension of the work presented in chapter 3 in which we extend the explicit-hydrogen representation of the chain include a realistic representation of the headgroup. The all-atom representation of the carboxylic acid headgroup includes a dipole-dipole interaction modelled using partial charges. Torsional potentials are used to control the relative orientation of the plane of the backbone and the plane of the headgroup. The hydrophilic interaction between the headgroup and the surface is represented using an attractive dispersion interaction and an image charge interaction between the dipole and the underlying dielectric medium. The aim of the work is to understand the effect of the headgroup on the structure of the film by a careful comparison with the results of the explicit-hydrogen model discussed in chapter 3.

4.2. Molecular model and potentials.

In this section we discuss the additional potentials required for the all-atom headgroup. In this model we have represented the four atoms of carboxylic acid headgroup explicitly as dispersion-repulsion force centres and we have modelled the dipole-dipole interaction by including the partial charges on the four atoms of the headgroup. The detailed structure of headgroup is shown in Figure 4.1 and potential and geometric parameters are given in Table 4.1 and Table 4.2 respectively.

4.2.1. The electrostatic interaction.

The electrostatic interctions between partial charges in headgroups are the most significant improvement over the explicit-hydrogen model discussed in chapter 3.
We have used a cylindrical cut-off for the electrostatic interaction between partial charges. This cut-off was set to half the shortest side of the simulation box.

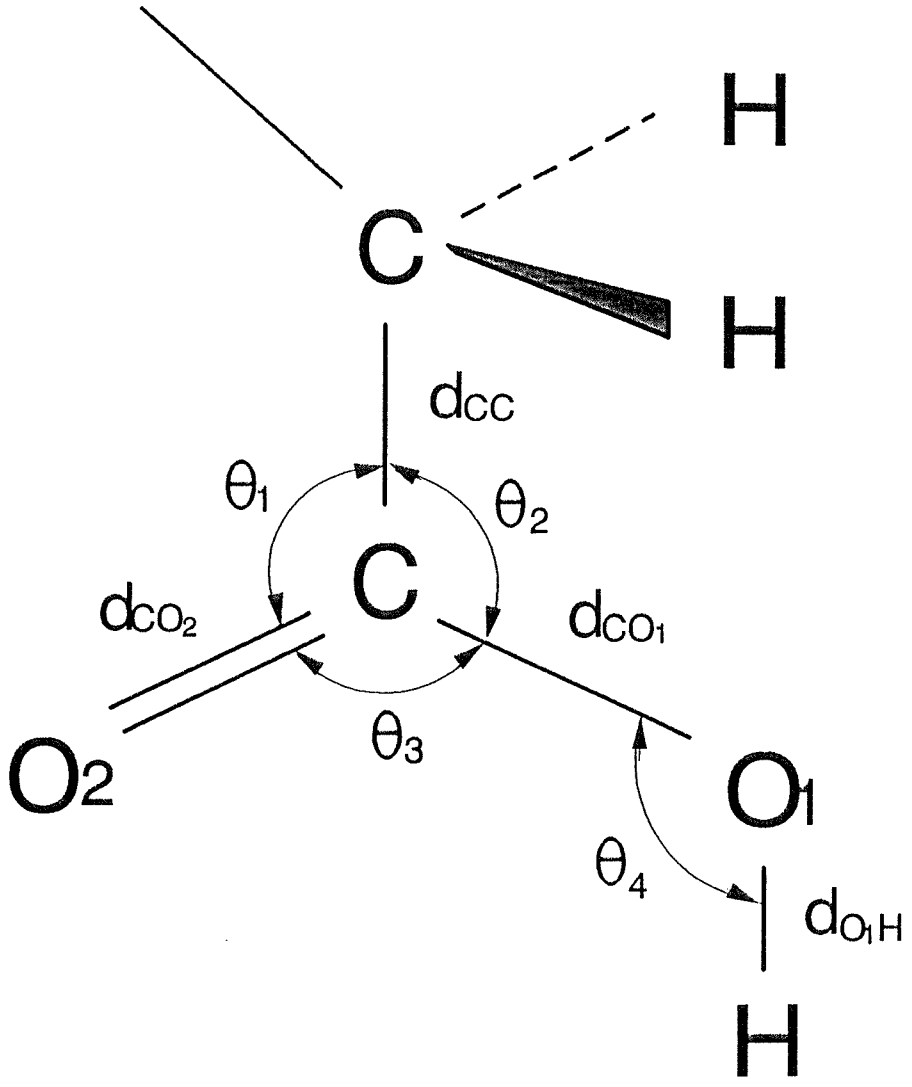

Figure 4.1. Structure of a carboxylic acid headgroup for the all-atom model.

Table 4.1. Potential parameters for the all-atom headgroup.

Site	ϵ / kJ mol^{-1}	σ / Å	Mass / amu	Charge / |e|
C[a]	0.50209	3.296	12.011	0.575
O[b]	0.62760	2.940	16.000	-0.350
O[c]	0.83681	2.850	16.000	-0.450
H[d]	0.08368	1.782	2.016	0.225

a) carbon atom in the headgroup.

b) oxygen atom of hydroxyl group.

c) oxygen atom of carbonyl group

d) hydrogen atom of hydroxyl group.

Table 4.2. Geometric parameters for the all-atom headgroup.

bond	bond length
d_{CO1}	1.364 Å
d_{CO2}	1.250 Å
d_{O1H}	0.960 Å

If the distance from the carbon atom of the headgroup of a molecule to the carbon atom of the headgroup of a neighbour is less than the cut-off distance all the charges of both headgroups are included in the calculation of the dipole-dipole interaction. For instance, in Figure 4.2 the headgroup carbon atom of molecule A is inside the cylinder with a radius r_c although its oxygen and hydrogen atom are outside. In this case we include all the interactions between charges in molecules 1 and A. The hydrogen and oxygen atoms of the headgroup of molecule B are inside the cut-off but we do not include molecule B in the calculation because the carbon atom of the headgroup of molecule B lies outside the cylinder. We maintain the electrical neutrality within the cut-off. To study the question of system size dependence we performed energy minimisation calculations with three different system size, 6x6, 8x8 and 10x10 molecules. In the calculation we modelled the electrostatic interaction as;

$$V_{el}(r_{\alpha\beta}) = \sum_{\alpha}\sum_{\beta} \frac{Q_\alpha Q_\beta}{4\pi\epsilon_0 r_{\alpha\beta}}, \qquad (4.1)$$

where Q_α and Q_β are charges in electron charge unit, $4\pi\epsilon_0 = 1.11265\text{x}10^{-10}\ J^{-1}C^2m^{-1}$ and $r_{\alpha\beta}$ is the distance between charges. The charges for the atoms of headgroup are taken from AMBER force field [11] and listed in Table 4.1. The results of the energy minimisation are summarized in Table 4.3. As one might expect increasing the system size increases the magnitude of the electrostatic interaction; the total change in the electrostatic interaction in increasing from a 6x6 molecular system to 10x10 molecular system is 0.5% of the total configurational energy. The molecular tilt predicted by energy minimisation studies of the monolayer changes by less than 2% in moving from an 8x8 to a 10x10 system. We have used an 8x8 system with a cylindrical cut-off for the partial charge interactions.

Another important electrostatic interaction in this system is the potential between charges on the atoms of head group and the image charges in the hydrophilic surface

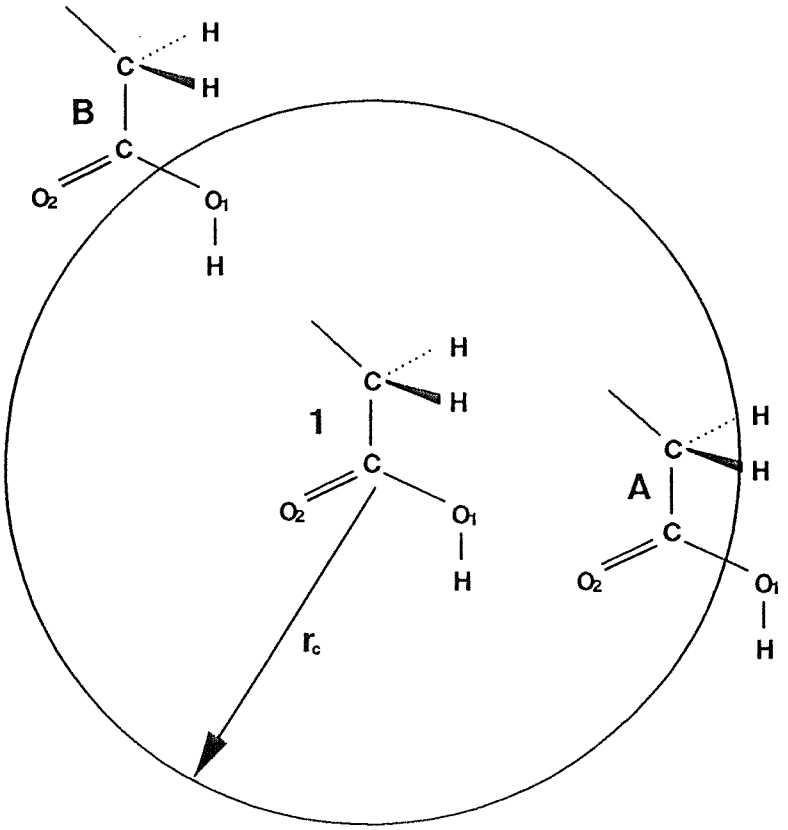

Figure 4.2. Schematic representation of the idea maintaining the electrical neutrality within a cylinder with cut-off r_c in the calculation of electrostatic interaction.

induced by these charges on the headgroup atoms. The surface in this study was supposed to be hydrophilic with relative permitivity $\epsilon'/\epsilon_0 = 4.0$ of quartz [12]. In a continuum model the image plane is located at the point where the relative permitivity changes discontinuously from ϵ' (relative permitivity of the surface) to ϵ (relative permitivity above the surface). The position of the image plane for an atomic surface is uncertain and we have followed the normal way of locating the plane at $Z_{ip} = \sigma_{ss}/2$ [13,14]. The position of image charge is defined by

$$Z_i = -(Z_c - Z_{ip}) , \tag{4.2}$$

where Z_c is the perpendicular distance from the surface to the partial charge and σ_{ss} is the interplanar spacing in the surface crystal, 3.37Å [15]. The electrostatic interaction between charge and image charge was modelled by[16]

$$v_{IC} = \sum_{\alpha}\sum_{\beta} \frac{Q_\alpha Q_\beta^i}{8\pi\epsilon_0(Z_c - Z_i)} , \tag{4.3}$$

where Q_α and Q_β^i are the magnitude of charge α and the magnitude of the image charge of a charge β respectively. The image charge is defined as

$$q^i = \frac{(\epsilon - \epsilon')}{(\epsilon + \epsilon')} q , \tag{4.4}$$

The polarizability $\alpha=(\epsilon-\epsilon')/(\epsilon+\epsilon')$ has a value of -0.6 in this system. A charge interacts with its own image and with images of other charges. There is no interaction between image charges.

Table 4.3. Effect of system size on the electrostatic interaction(kJ mol^{-1}).

system size	A_m = 20.6 $Å^2$	A_m = 21.2 $Å^2$
6 x 6	-3.230(0.0[a])	-3.001(30.61)
8 x 8	-3.329(0.0)	-3.092(30.43)
10 x 10	-3.385(0.12)	-3.174(30.38)

a) Numbers in bracket indicate the molecular tilt at the minimum energy.

4.2.2. The dihedral potentials.

There are 8 dihedral potentials for the carboxylic acid headgroup, which are listed in Table 4.4 (The identification of the atoms is shown in Figure 4.1.). The dihedral potential parameters were taken from MM2 force field [19]. The potentials have the functional form

$$E = \frac{1}{2}V_1(1+\cos\phi) + \frac{1}{2}V_2(1-\cos 2\phi) + \frac{1}{2}V_3(1+\cos 3\phi),\ 0<\phi<2\pi\ . \qquad (4.5)$$

We converted the dihedral potentials in the form shown above to the potential form used by Ryckaert and Bellemans[20], which are used in our molecular dynamics simulation;

$$U(\phi) = (\frac{1}{2}V_1 + V_2 + \frac{1}{2}V_3) + \frac{1}{2}(V_1 - 3V_3)\cos\phi - V_2\cos^2\phi + 2V_3\cos^3\phi \qquad (4.6)$$

In our model the eight dihedral potentials can be simplified to four. The potentials O1C1C2H1 and O1C1C2H2 are combined with the potential O1C1C2C3 and the potentials O2C1C2H1 and O2C1C2H2 are combined with the potential O2C1C2C3. This is possible because the methylene group is rigid. The two effective dihedral potential equations for O1C1C2C3 and O2C1C2C3 are

$$U_I = U_{O1C1C2C3}(\phi) + U_{O1C1C2H1}(\phi - 120) + U_{O1C1C2H2}(\phi + 120) \qquad (4.7)$$

$$U_{II} = U_{O2C1C2C3}(\phi) + U_{O2C1C2H1}(\phi - 120) + U_{O2C1C2H2}(\phi + 120)\ . \qquad (4.8)$$

The other two dihedral potentials are the potentials for HO1C1C2 and HO1C1O2. We summarize the parameters for the 4 dihedral potential in Table 4.5.

Figure 4.3 and Figure 4.4 show the dihedral potentials as a function of dihedral rotation

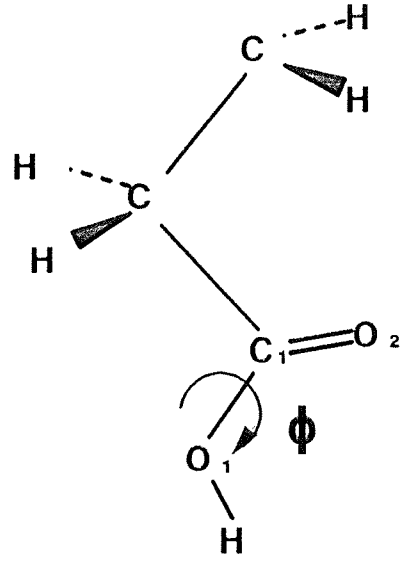

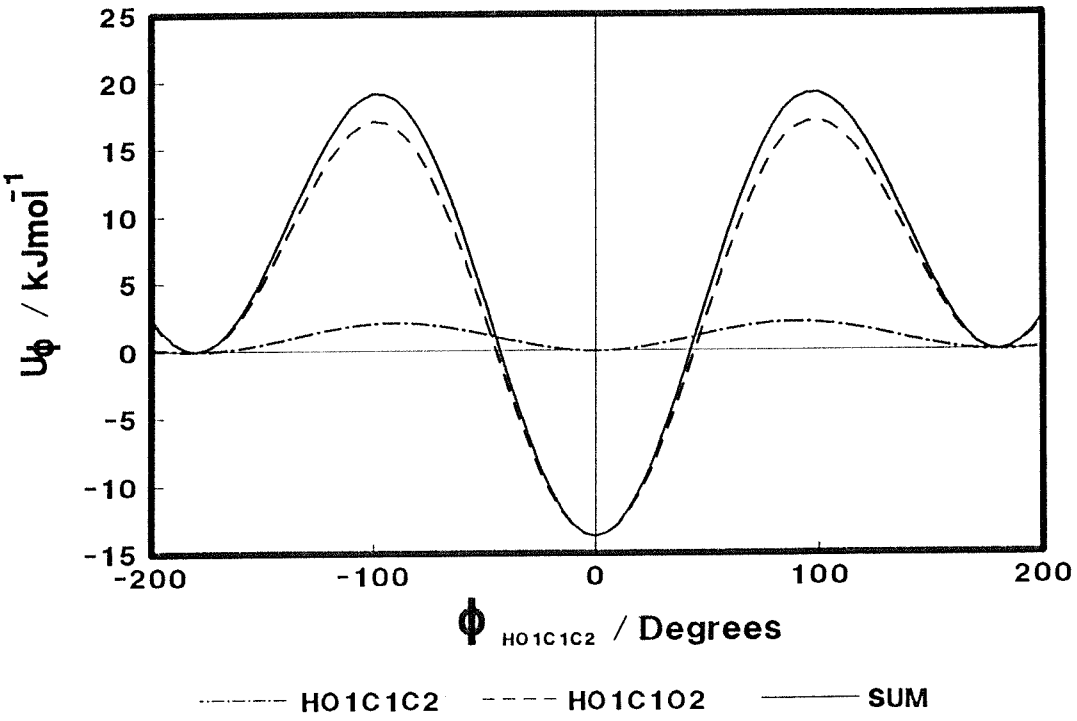

Figure 4.3. Dihedral potentials of headgroup combining to give the dihedral rotation around the C_1-O_1 bond.

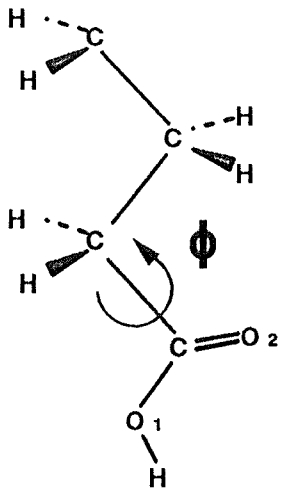

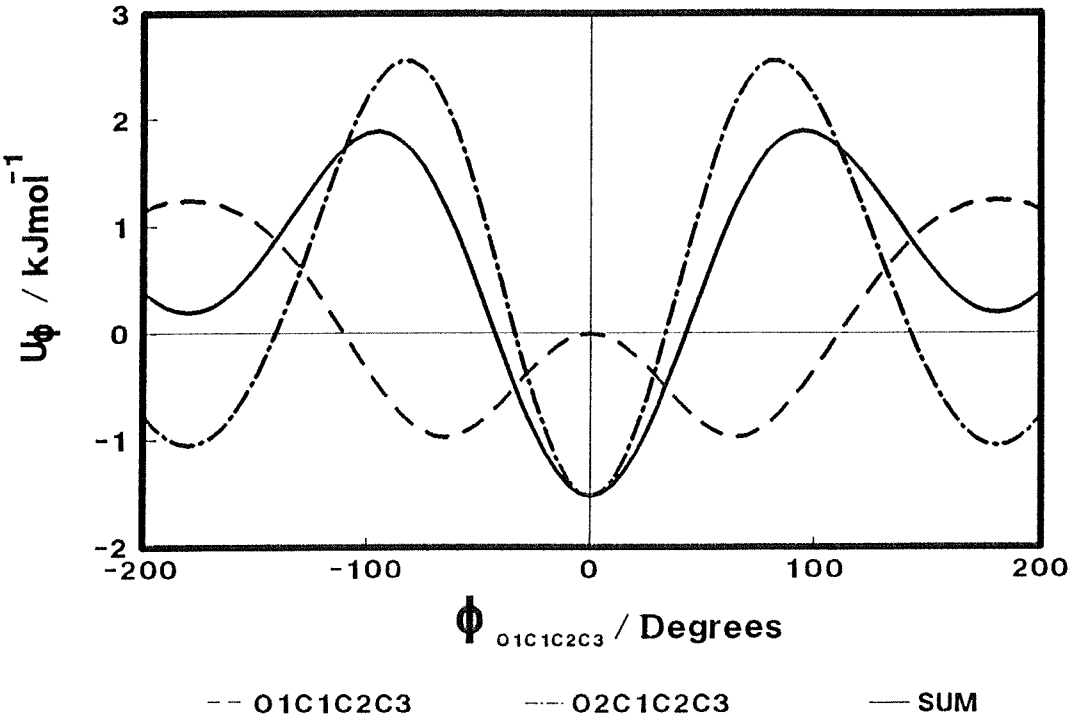

Figure 4.4. Dihedral potentials of headgroup combining to give the dihedral rotation around the C_1-C_2 bond.

along the C1-O1 bond and C1-C2 bond respectively. The trans H-O1-C1-C2 configuration and cis H-O1-C1-O2 configuration are energetically the most favorable structure.

4.2.3. The bond-bending potentials.

There are four bond-bending potentials in the carboxylic acid headgroup; H-O1-C1, O1-C1-O2, O1-C1-C2 and O2-C1-C2. We have used same potential form for the bond-bending of alkane chain. The potential parameters and equilibrium bond angles are listed in Table 4.6, which were taken from Amber force field[19].

4.2.4. Additional potentials.

Two more potentials are implemented in the all-atom model, They are an intramolecular electrostatic interaction and a Van der Waals repulsion-dispersion interaction between H and O2 in the same headgroup. The non-bonded Van der Waals interaction was modelled as a potential of the form[19]:

$$E_v = A \exp(-B r_{HO_2}) - C/r^6_{HO_2} , \qquad (4.9)$$

where $A/k_B = 7.12 \times 10^6$ K

$B = 4.252$ Å^{-1}

$C/k_b = 3.566 \times 10^4$ KÅ^6

r_{HO2} = distance between H and O_2.

The parameters were taken from MM2 force field[19].

Table 4.4. Dihedral potential parameters from MM2 force field for the all-atom headgroup [17].

atom set	V_1/kJ mol^{-1}	V_2/kJ mol^{-1}	V_3/kJ mol^{-1}
O1-C1-C2-C3	1.676	-1.257	-0.293
O1-C1-C2-H1	0.0	0.0	-0.067
O1-C1-C2-H2	0.0	0.0	-0.067
O2-C1-C2-C3	-0.545	3.788	0.210
O2-C1-C2-H1	-0.670	0.0	-0.419
O2-C1-C2-H2	-0.670	0.0	-0.419
H-O1-C1-C2	0.0	2.095	0.0
H-O1-C1-O2	-13.764	23.464	0.0

Table 4.5. Dihedral potential parameters for the all-atom headgroup.

atom set	C_0/kJ mol$_{-1}$	C_1/kJ mol^{-1}	C_2/kJ mol^{-1}	C_3/kJ mol^{-1}
O1-C1-C2-C3	-0.633	-1.479	1.257	0.855
O2-C1-C2-C3	2.501	-1.020	-3.788	1.257
H-O1-C1-C2	2.095	0.0	-2.095	0.0
H-O1-C1-O2	16.582	6.882	-23.464	0.0

Table 4.6. Bond-bending potential parameters for the all-atom headgroup[11].

bond angle [a)]	K_b / kJ mol^{-1}	θ_0 / °
θ_1	335.20	125.0
θ_2	335.20	109.0
θ_3	335.20	124.0
θ_4	146.65	113.0

a) See Figure 4.1 for the identification of bond angle.

4.3. Energy minimisation.

We have performed the energy minimisation calculations for the monolayer of 8x8 molecules at various headgroup areas(A_m) for the all-atom model. The carbon atom of the head groups of stearic acid molecules were positioned on a triangular lattice at a lattice spacing chosen to produce a particular value of A_m. All the carbon atoms of the alkyl tail group and the atoms of the headgroup of a stearic acid molecule are in the same plane.

In the energy minimisation we calculated the total energy of the system using minimum image convention. The total energy of the system including intermolecular and molecule-surface interaction was minimised using the NAG library routine E04JBF as discussed in chapter 3. The minimisation was carried out using both one molecule per unit cell and two molecules per unit cell. The minimum energy structures were calculated with and without the electrostatic interactions between partial charges in head groups to examine the effect of electrostatic interaction on the structure of the layer. Figure 4.6 and Figure 4.7 shows the minimum energy E_{min} and molecular tilt at minimum energy θ_{min} as a function of headgroup area A_m for the monolayers with and without the electrostatic interaction. The results are summarized in Table 4.7 and Table 4.8 respectively.

The minimum energy structures from the energy minimisation with and without the electrostatic interactions are very similar to each other as shown in Figure 4.6 and Figure 4.7. The structures of monolayers with the all-atom model are also very similar to the minimum energy structures of monolayers with the explicit-hydrogen model where the carboxylic acid head group was considered as a single interaction site without electrostatic interactions. The molecular tilt occurs at A_m = 20.7Å^2 in the monolayer with the all-atom model but the molecules start to tilt at A_m = 20.8Å^2 in the monolayer with the explicit-hydrogen model(see Figures 3.2, 3.3 and 3.5). This difference in the value of A_m at which the molecular tilt begins reflects the difference in the effective head group area of the all-atom model and in which carboxylic acid headgroup is considered

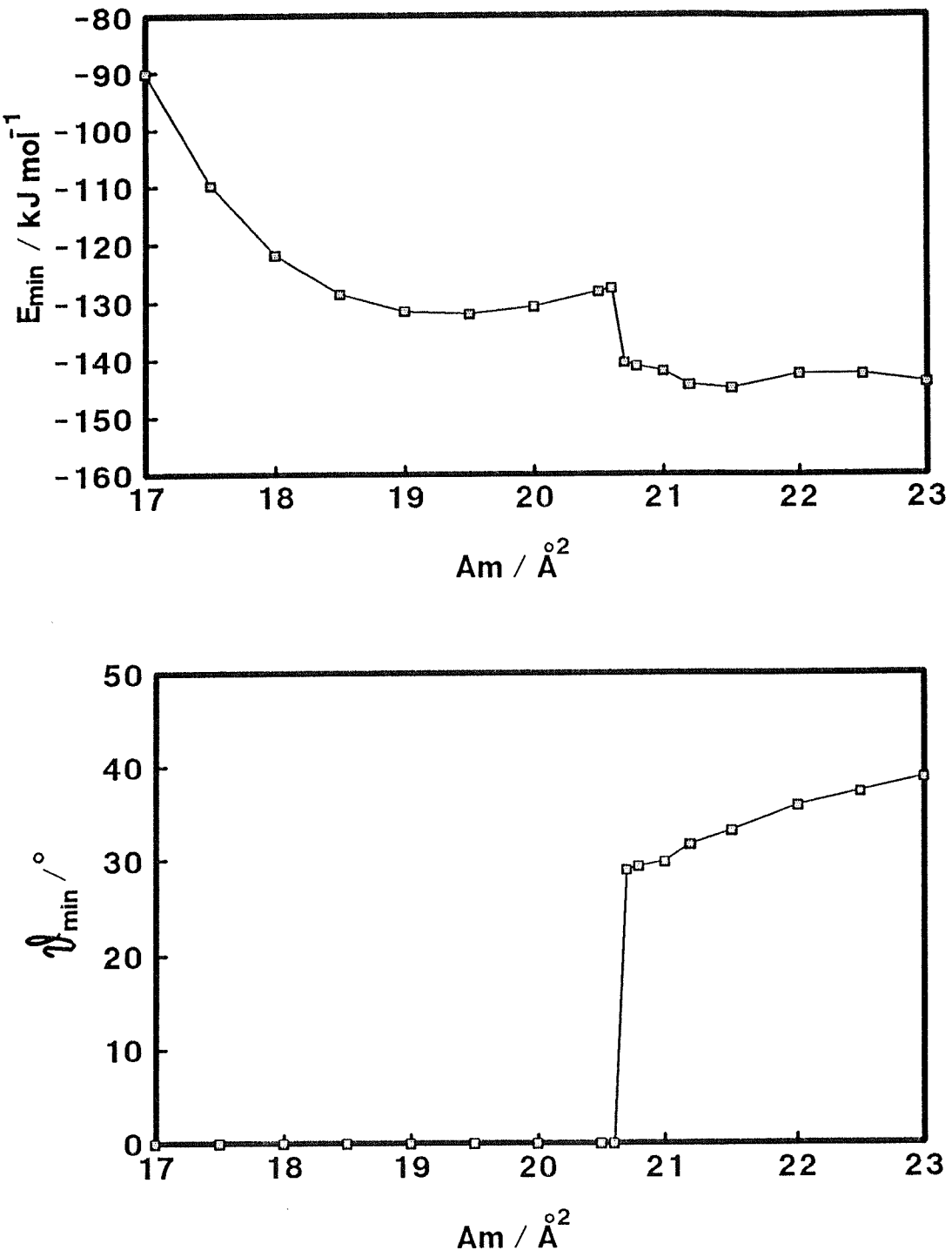

Figure 4.5. Minimum energy E_{min} and molecular tilt θ_{min} at E_{min} of monolayer with the all-atom model without electrostatic interaction as a function of headgroup area A_m.

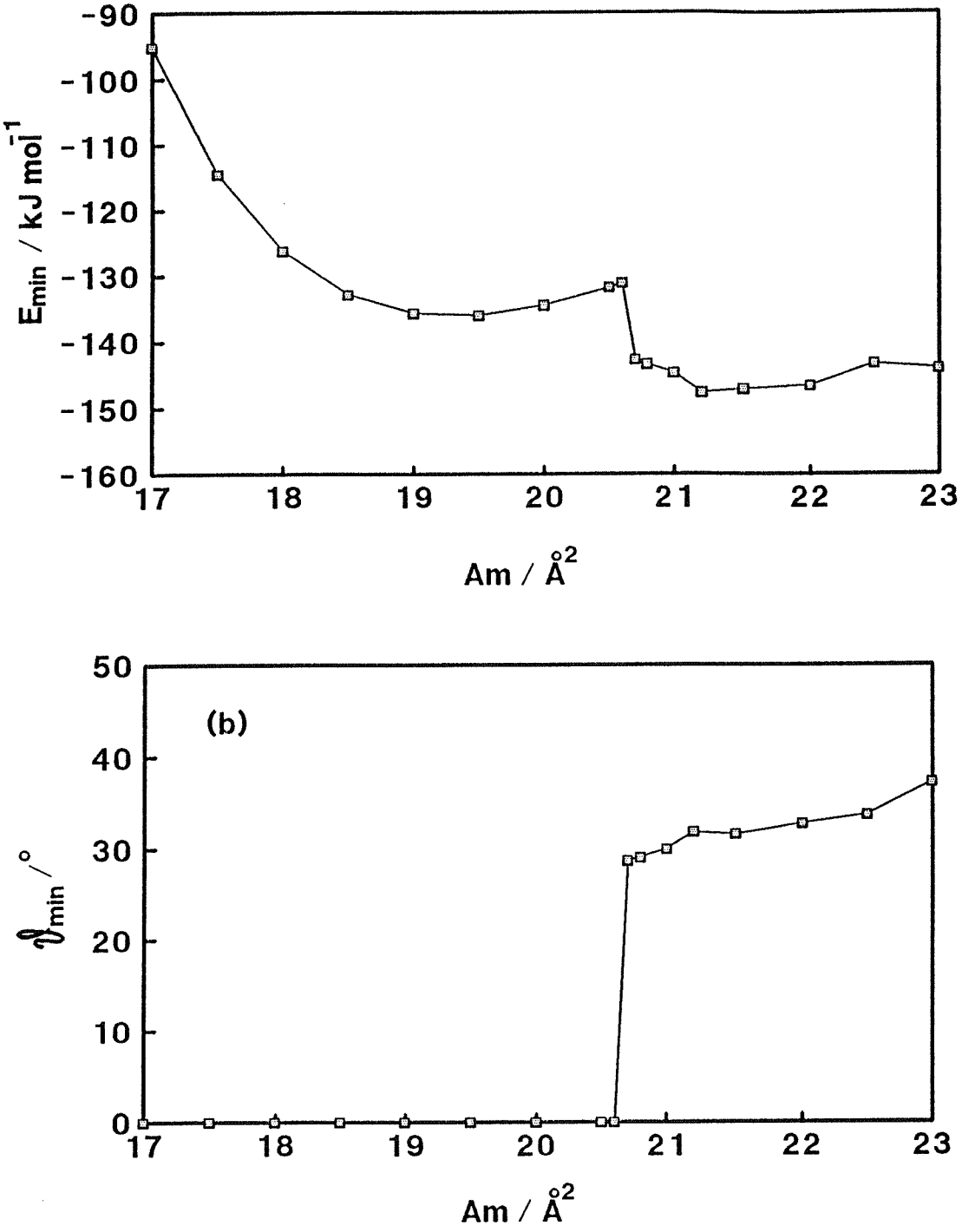

Figure 4.6. Minimum energy E_{min} and molecular tilt θ_{min} at E_{min} of the monolayer with the all-atom model with electrostatic interaction as a function of headgroup area A_m.

as a single spherical pseudo-atom. The minimum energy structures have one molecule per unit cell in the region of $A_m < 20.7Å^2$, $A_m \geq 23Å^2$ but the monolayer has two molecules per unit cell structure in the region $20.7Å^2 \leq A_m < 23Å^2$ as shown in Table 4.9. The behaviour of lattice structure is similar to that of the explicit-hydrogen model monolayer. The electrostatic interaction between head groups has a small effect on the static minimum energy structure at 0 K since the electrostatic energy of the layer is less than 5% of the total energy of the layer. The major component controlling the global structure is the intermolecular interaction between alkyl chain of the stearic acid molecules and the intermolecular interaction is mainly governed by the in-plane packing and out-of-plane inter-locking of the alkyl chain of the molecules as discussed in chapter 3. However in reaching this conclusion, we recall that the headgroup of all the molecules are fixed rigidly with respect to the hydrocarbon backbones. This constraint is relaxed in the molecular dynamics calculation.

Table 4.9. Results of energy minimisation using the all-atom model without the electrostatic interaction.

Headgroup Area/Å^2	ϕ_{min} /°	θ_{min} /°	$\psi_{min,1}$ /°	$\psi_{min,2}$ /°	E_{min}/kJ mol^{-1}
17	0.0	0.0	0.0	0.0	-90.207
18	0.0	0.0	0.0	0.0	-121.770
19	0.0	0.0	0.0	0.0	-131.597
20	0.0	0.0	0.0	0.0	-130.767
20.7	89.9	28.9	136.1	224.1	-140.487
22	90.8	33.1	135.7	222.3	-145.028
23	78.6	37.3	233.6	233.6	-142.602

Table 4.10. Results of energy minimisation using the all-atom model with the electrostatic interaction.

Headgroup Area/Å^2	ϕ_{min} /°	θ_{min} /°	$\psi_{min,1}$ /°	$\psi_{min,2}$ /°	E_{min}/kJ mol^{-1}
17	0.0	0.0	0.0	0.0	-95.207
18	0.0	0.0	0.0	0.0	-126.286
19	0.0	0.0	0.0	0.0	-132.899
20	0.0	0.0	0.0	0.0	-134.518
20.7	89.9	28.7	135.8	224.3	-142.670
22	90.1	32.8	136.7	223.1	-146.595
23	79.7	37.4	230.9	230.9	-143.996

4.4. Molecular dynamics.

The molecular dynamics simulations of 8x8 molecules have been carried out with Verlet algorithm[21] discussed in chapter 2. During the simulation the bond lengths of the molecules were constrained to their equilibrium values using the SHAKE algorithm [22] and the plane containing 3 atoms of methylene (-CH_2-) group is constrained to be normal to the plane of the three nearest carbon atoms of alkyl chain of molecules and finally the vector dividing the bond angle of H-C-H is constrained to be co-linear with the vector connecting the carbon atom and the bisector of the line joining neighbouring two carbon atoms as implemented in the molecular dynamics simulation using the explicit-hydrogen model discussed in chapter 3. The carbon, O1 and O2 atoms of the headgroups are constrained to be coplanar and the three bond lengths, d_{CO1}, d_{CO2}, and d_{O1H} are constrained to their experimental values. A monolayer of 64 stearic acid molecules of the all-trans configuration was positioned on the hydrophilic surface in a triangular lattice corresponding to the minimum energy structure. Two molecular dynamics simulations were carried out with two different head group areas (A_m=20.6 Å^2 and A_m=21.2 Å^2) on either side of the change of tilt observed in the energy minimisation calculations. We performed the 30,000(60ps) equilibriation and 35,000 production(70 ps) steps for system of A_m = 20.6 Å^2 and 39,000(78ps) equilibration and 49,000(98ps) production steps for the system A_m = 21.2 Å^2 with a time step of $2x10^{-15}$ sec. Both simulations were started at a temperature of 298 K.

The instantaneous structures of the stearic acid monolayers viewed along the three orthogonal directions for the monolayers with A_m = 20.6Å^2 and A_m = 21.2Å^2 are presented in Figure 4.7.

4.4.1. The translational ordering of the monolayers.

The distribution of molecular centres of mass..

Figure 4.8 shows the trajectories of the molecular centres of mass during production period for the monolayers with A_m = 20.6Å^2 and A_m = 21.2Å^2 respectively.

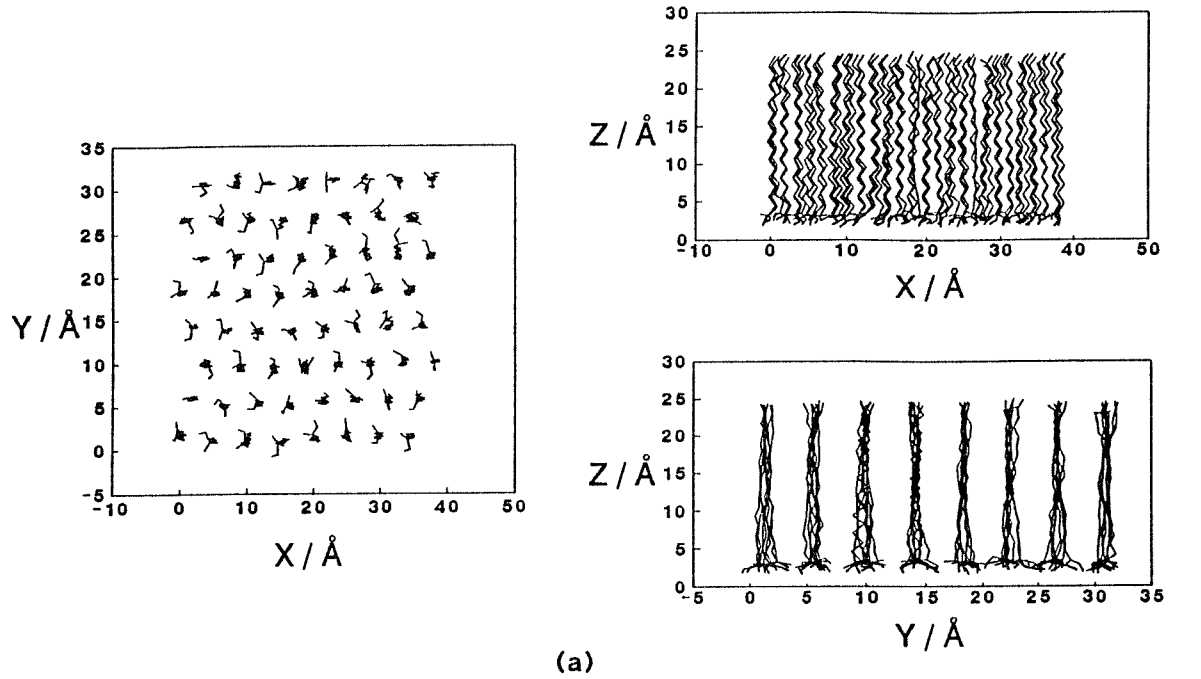

(a)

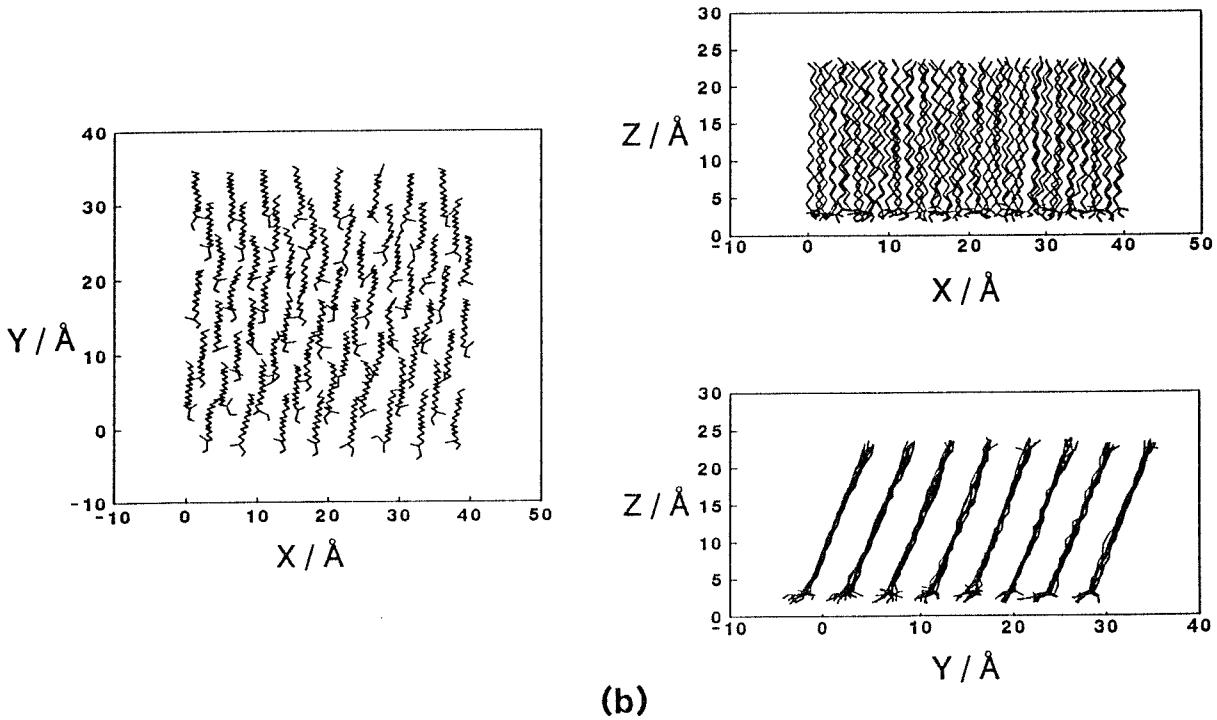

(b)

Figure 4.7. Snapshot of the structure of the monolayer during the simulations for the (a) A_m = 20.6Å^2 and (a) A_m = 21.2Å^2 form the x-, y-, and z-directions.

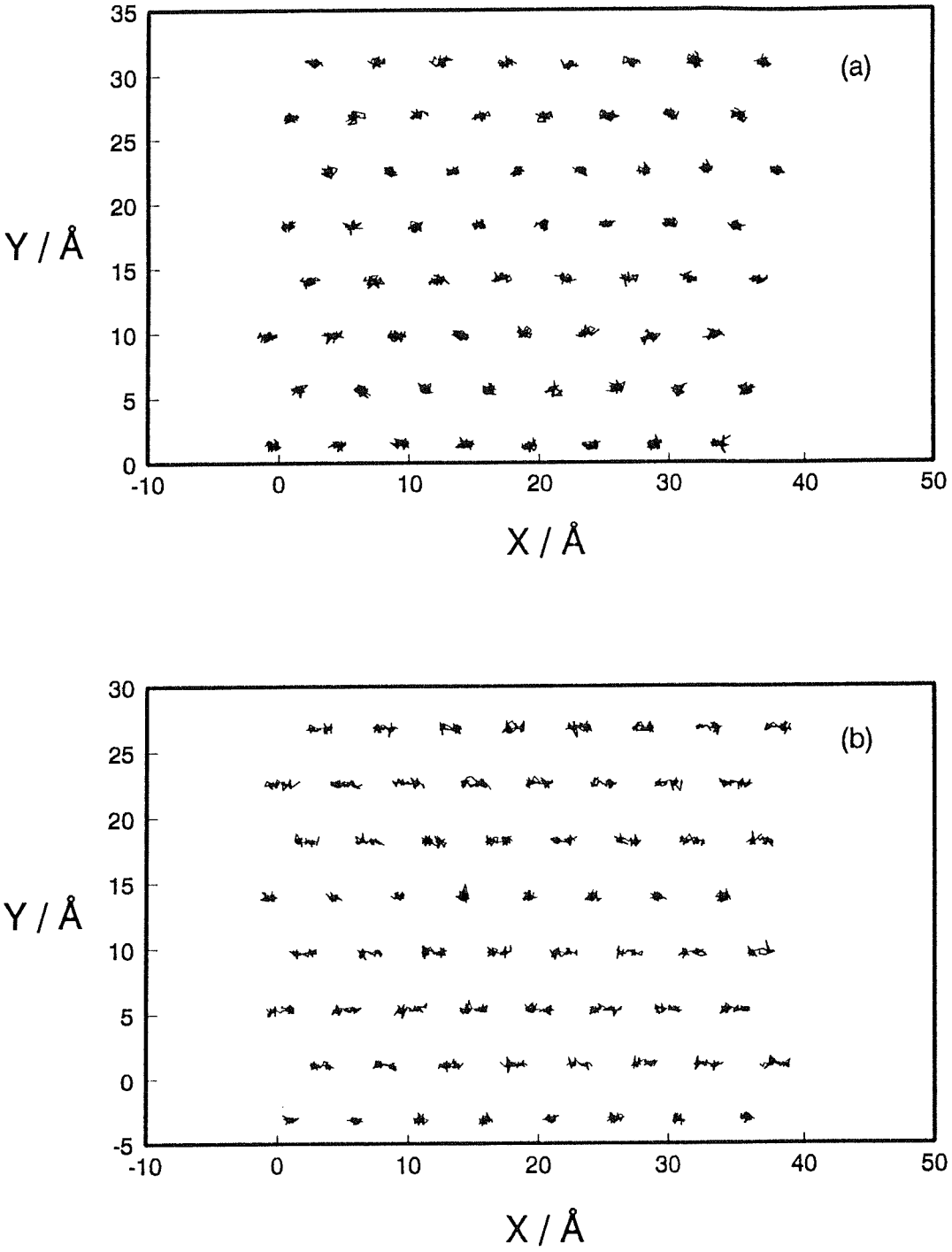

Figure 4.8. Trajectories of the molecular centres of mass during the production period for (a) A_m = 20.6Å^2(70 ps) and (b) A_m = 21.2Å^2(98 ps).

To examine the equilibrium structures we calculated the in-plane radial distribution functions of the molecular centres of mass for the layers, g(r). Figure 4.9 shows the g(r) for the molecular centres of mass for A_m=20.6Å^2 and A_m=21.2Å^2. The two figures are typical of the radial distribution function of a solid showing strong first peak representating the first shell of lattice. To evaluate the quantitative measure of in-plane lattice structure we calculated the hexagonal order parameter(OP6) as a function of time. OP6 is defined as

$$OP6 = \frac{1}{6}\sum_{j=1}^{6} \exp(i6\theta_j) \qquad (4.10)$$

where θ_j is the angle between the molecular centres of mass of two adjacent nearest neighbour molecules and molecular centre of mass of central molecule (inset in Figure 4.10). Figure 4.10 represents the OP6 for both layers. OP6 shows a relatively high value of 0.8±0.02 throughout the simulation which means that the monolayers have well-defined hexagonal structure during the simulation.

The distribution of conformational defects.

As discussed in the previous chapter we defined the gauche plus(g+) and the gauche minus(g-) defect for the dihedral angle between 60° and 180° and between -60° and -180° respectively(see Figure 2.4). The average number of all-trans molecules was 97.7% in the monolayer with A_m=20.6Å^2, and 66.9% in the monolayer with A_m=21.2Å^2. Figure 4.11 shows the distribution of gauche defects and carbon atom g(z) along the direction normal to the surface for the layer. For both layers the distribution is solid-like. The distributions of gauche defects for both layers show that gauche defects are distributed at the both ends of a chain (near head and tail groups) but a large number of defects are localized near head group of the chain. To understand this distribution we analyzed the distribution of dihedral angle of the bonds close to the headgroup.

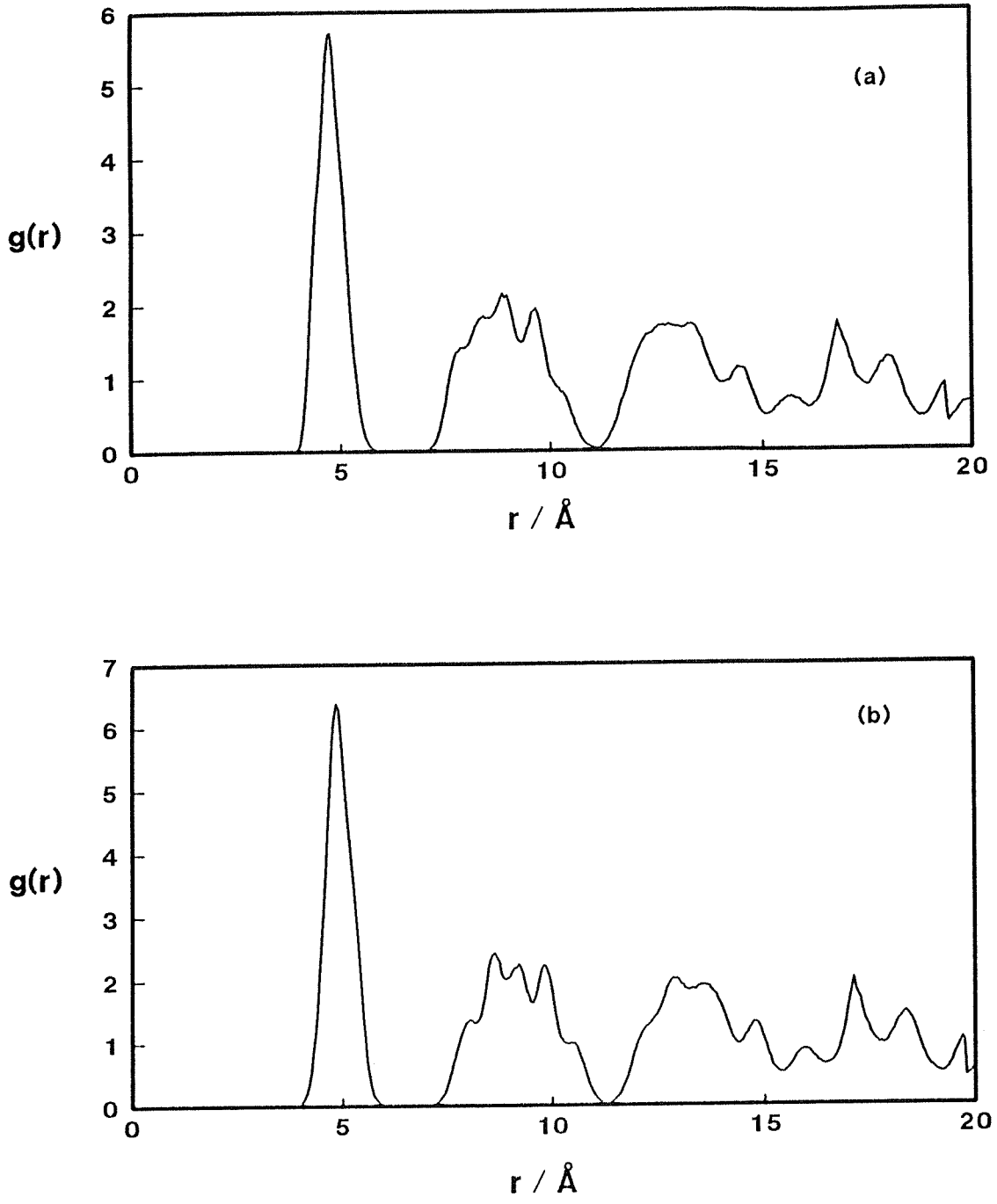

Figure 4.9. Radial distribution functions of molecular centres of mass for (a) A_m = 20.6Å^2 and (b) A_m = 21.2Å.

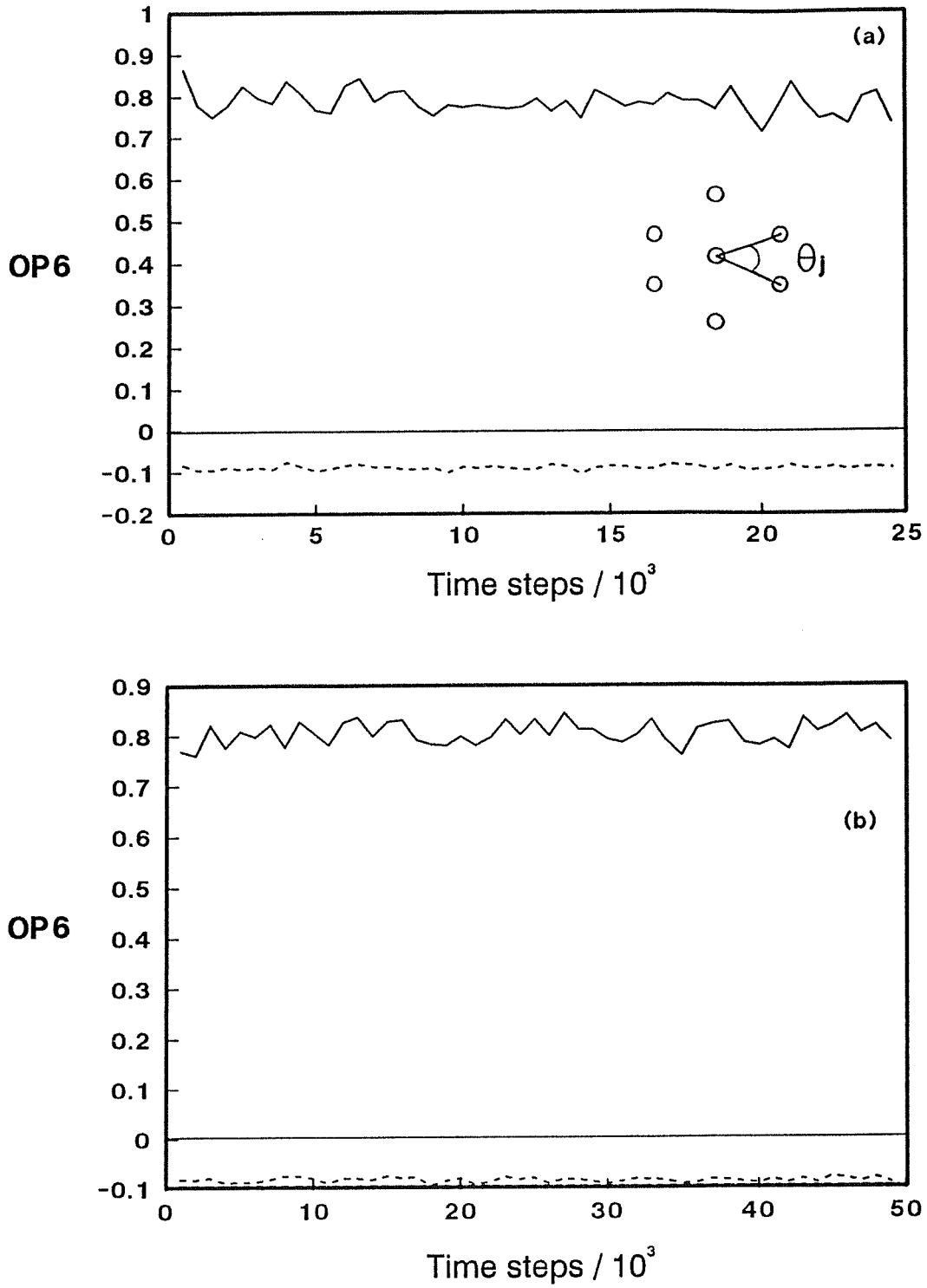

Figure 4.10. Hexagonal order parameters for (a) A_m = 20.6Å^2 and (b) A_m = 21.2Å^2 during the simulation.

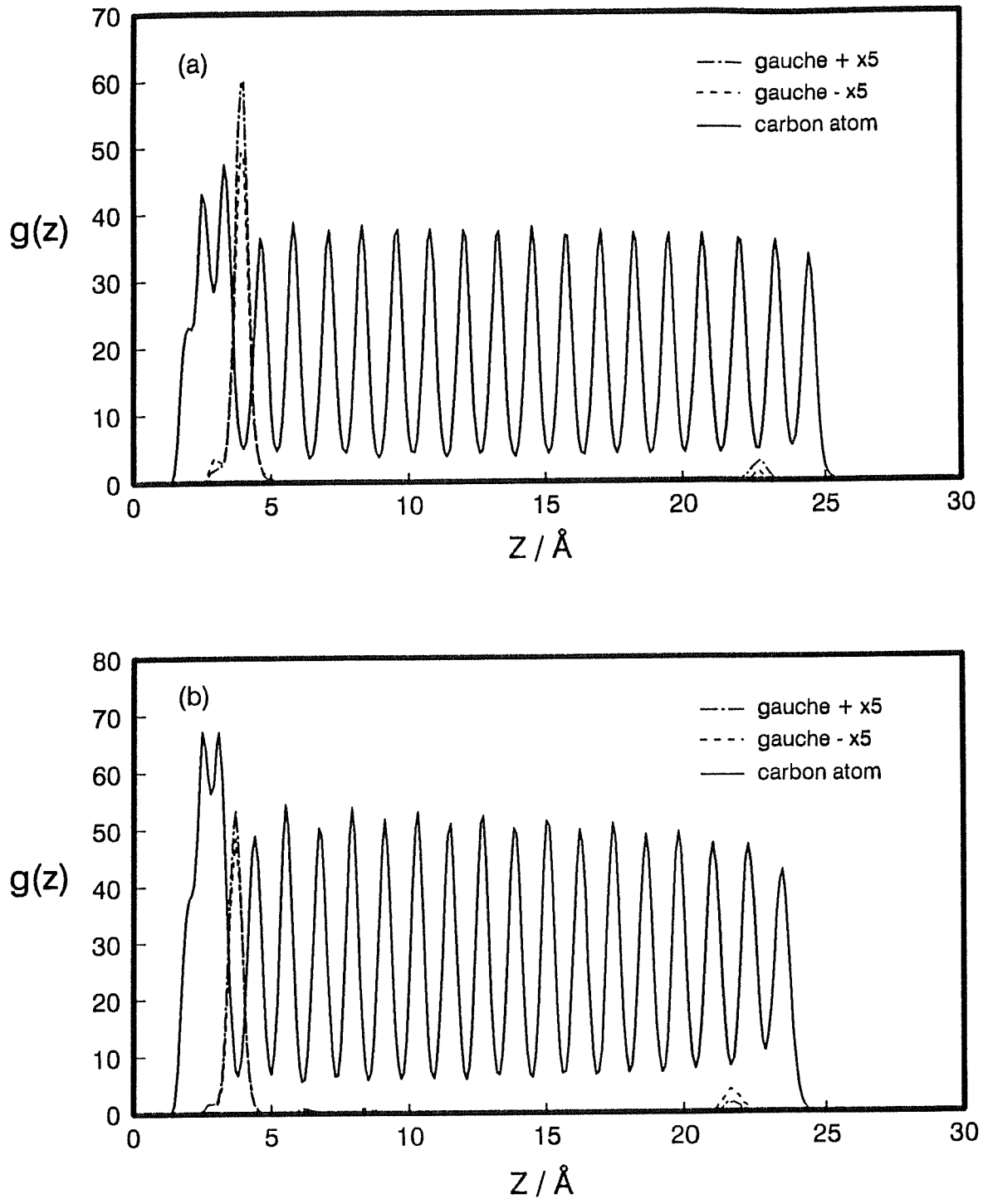

Figure 4.11. Distribution of gauche defects and carbon atom along the normal to surfacefor the layer of (a) A_m = 20.6Å^2 and (b) A_m = 21.2Å^2.

Figure 4.12(a) shows the distribution of the dihedral angle of the bonds near to head group for the monolayer with A_m = 20.6Å^2. In an alkane chain the gauche defect is defined as a bond which has a dihedral angle(ϕ) of $60<\phi<180$ or $-60<\phi<-180$. In this thesis a gauche defect has this geometric definition based on the simpler usage common in discussing the alkane chain structure. Figure 4.12(b) compares the dihedral potentials by the rotation of the headgroup about C1-C2 and that of n-butane. The dihedral potential for the headgroup rotation is quite different to that of the n-butane. The dihedral potential of the headgroup about C1-C2 bond is flatter than corresponding figure for n-butane($\Delta E_{n\text{-butane}} = E_{(\phi=120)} - E_{(\phi=0)}$ = 2.93 kJ mol^{-1}, $\Delta E_{head} = E_{(\phi=180)} - E_{(\phi=0)}$ = 1.8 kJ mol^{-1}) and the corresponding distribution of dihedral angle around the headgroup is quite broad. Most of the gauche defects are located at the bond between carbon atom of the head group and the first carbon atom of the alkyl chain. Interestingly there is a gauche defect at same position in a stearic acid molecule of crystal structure B, which has a very similar molecular area (A_m = 20.7Å^2) to the headgroup area of the layer(A_m = 20.6Å^2)[21]. The in-plane radial distribution of gauche defects is shown in Figure 4.13 for the both systems. The distribution of gauche defects are liquid-like while the distributions of molecular centres of mass are solid-like as previously discussed.

We also calculated the in-plane distribution and hexagonal order parameters for the head and the tail groups in both systems. Figure 4.14 shows the distributions of head and tail groups. The figure shows that the distribution is liquid-like and that the distribution of the head group is very similar to that of the tail group in the layer with A_m = 20.6Å^2 but the distribution of the tail group is more liquid-like than that of the head group for the layer with A_m = 21.2Å^2. Figure 4.15 shows the hexagonal order parameters of the head and tail groups during the simulations for the both system. The order parameters for the head and the tail groups are 0.51 ± 0.05 and 0.43 ± 0.06 for the layer with A_m=20.6Å^2 and 0.48 ± 0.1 and 0.22 ± 0.1 for the layer with A_m=21.2Å^2 respectively. This indicates the tail group and the head group are more hexagonally

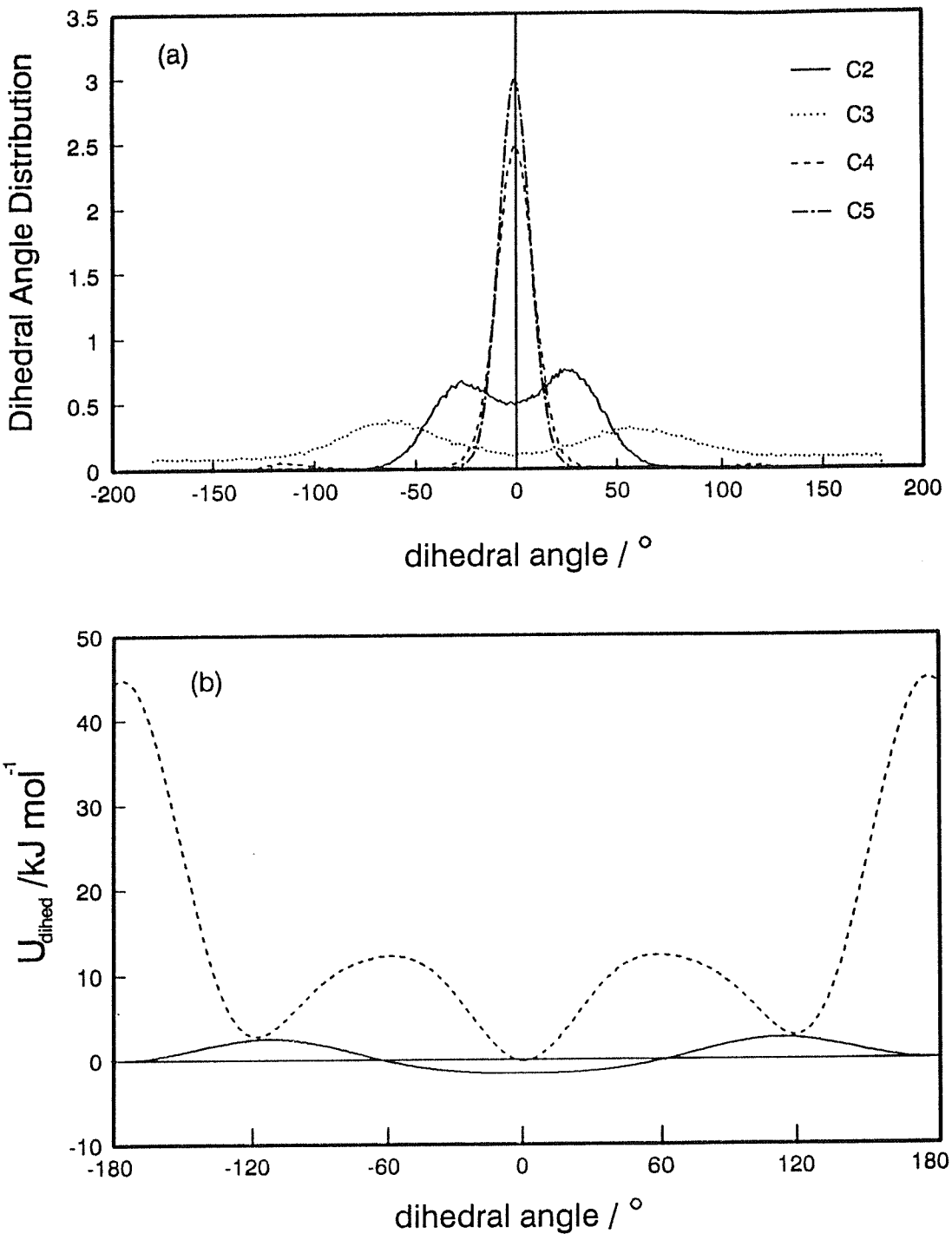

Figure 4.12. (a) the distribution of dihedral angles of the bonds near to head group for the A_m = 20.6Å^2; (b) the comparison between dihedral potential about C1-C2(solid line) and that of n-butane(dashed line).

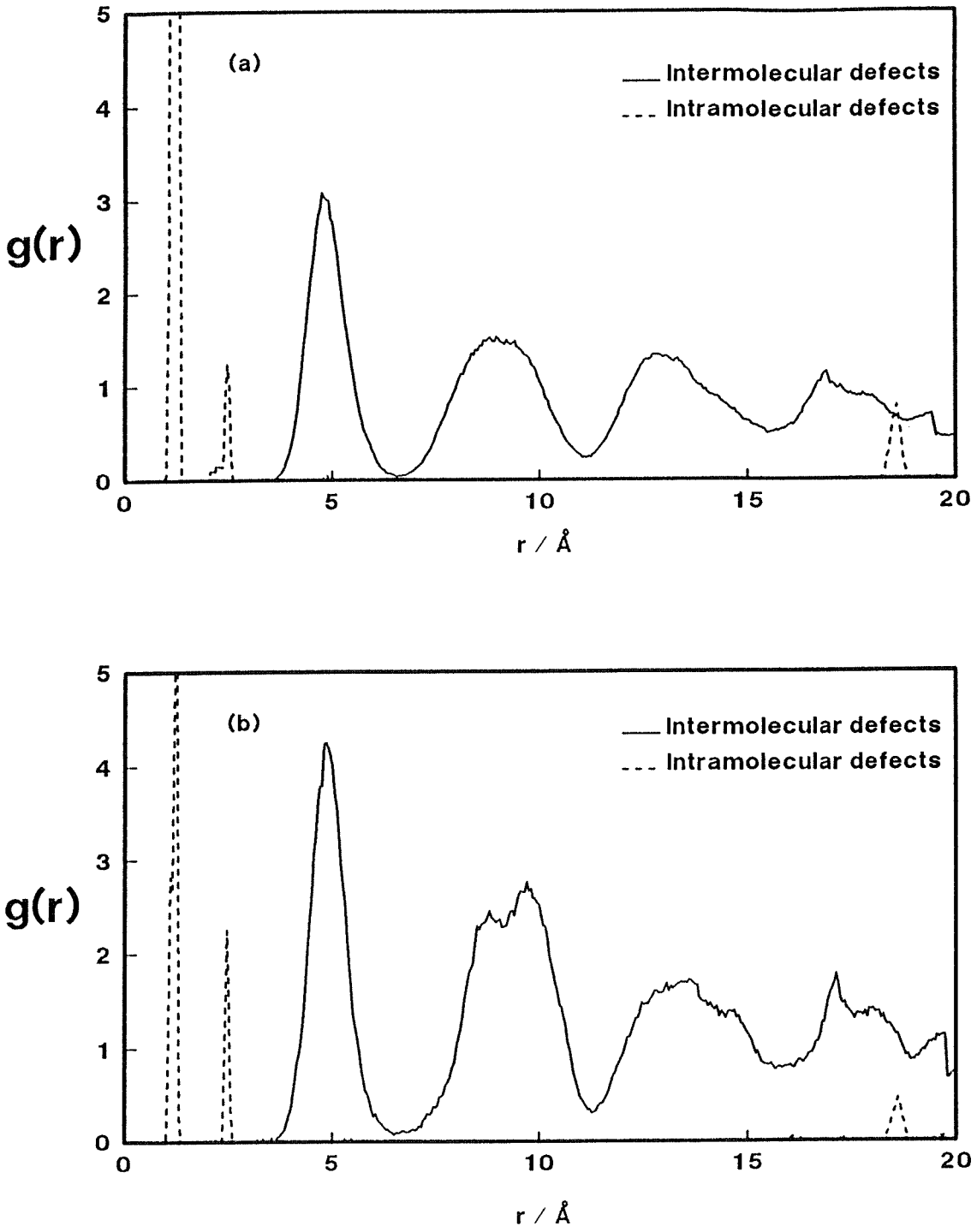

Figure 4.13. Radial distribution of gauche defects for the layer of (a) A_m = 20.6Å^2 and (b) A_m = 21.2Å^2.

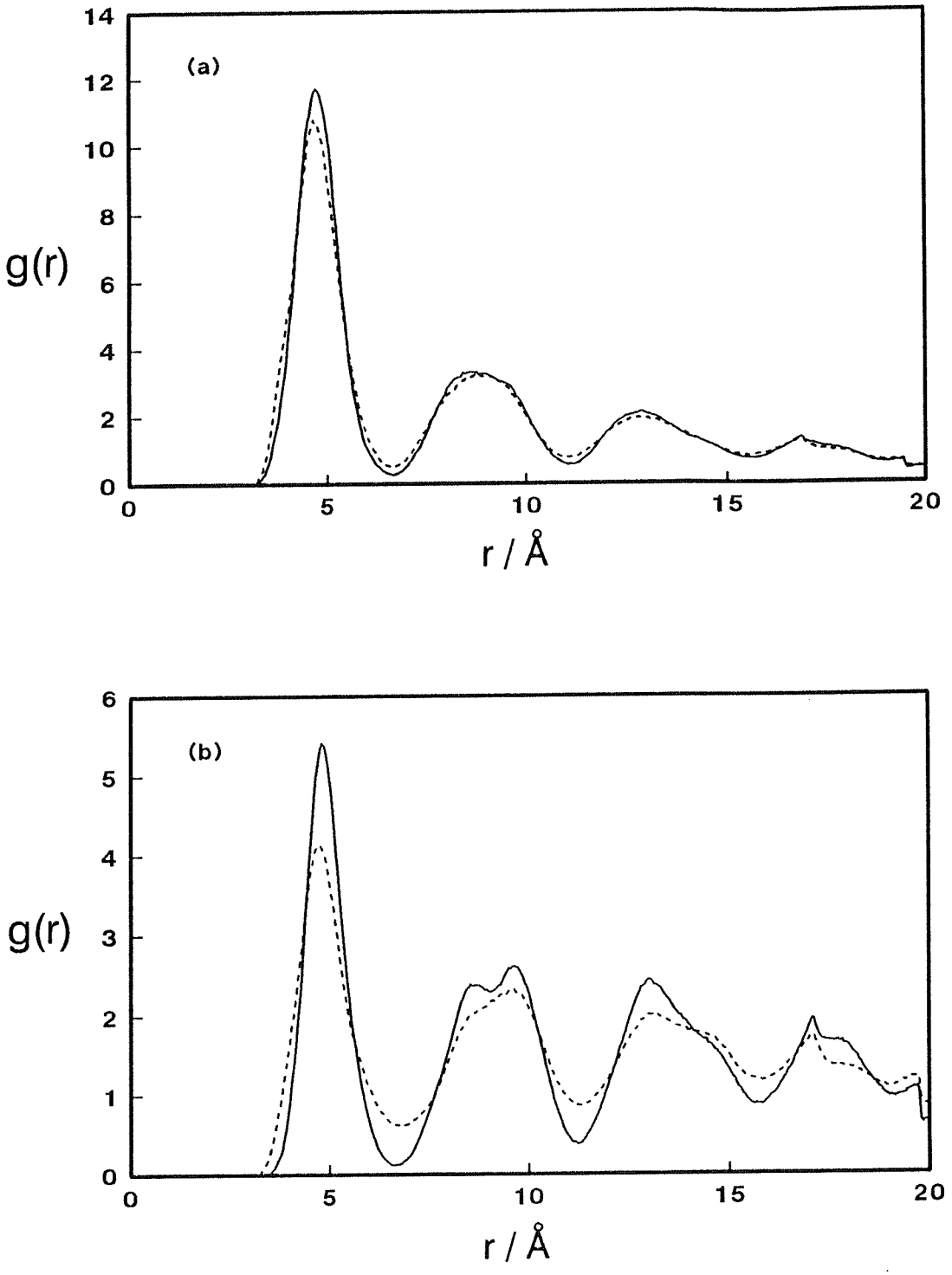

Figure 4.14. Radial distribution function of head group (solid line) and tail group (dashed line) for (a) A_m = 20.6Å^2 and (b) A_m = 21.2Å^2.

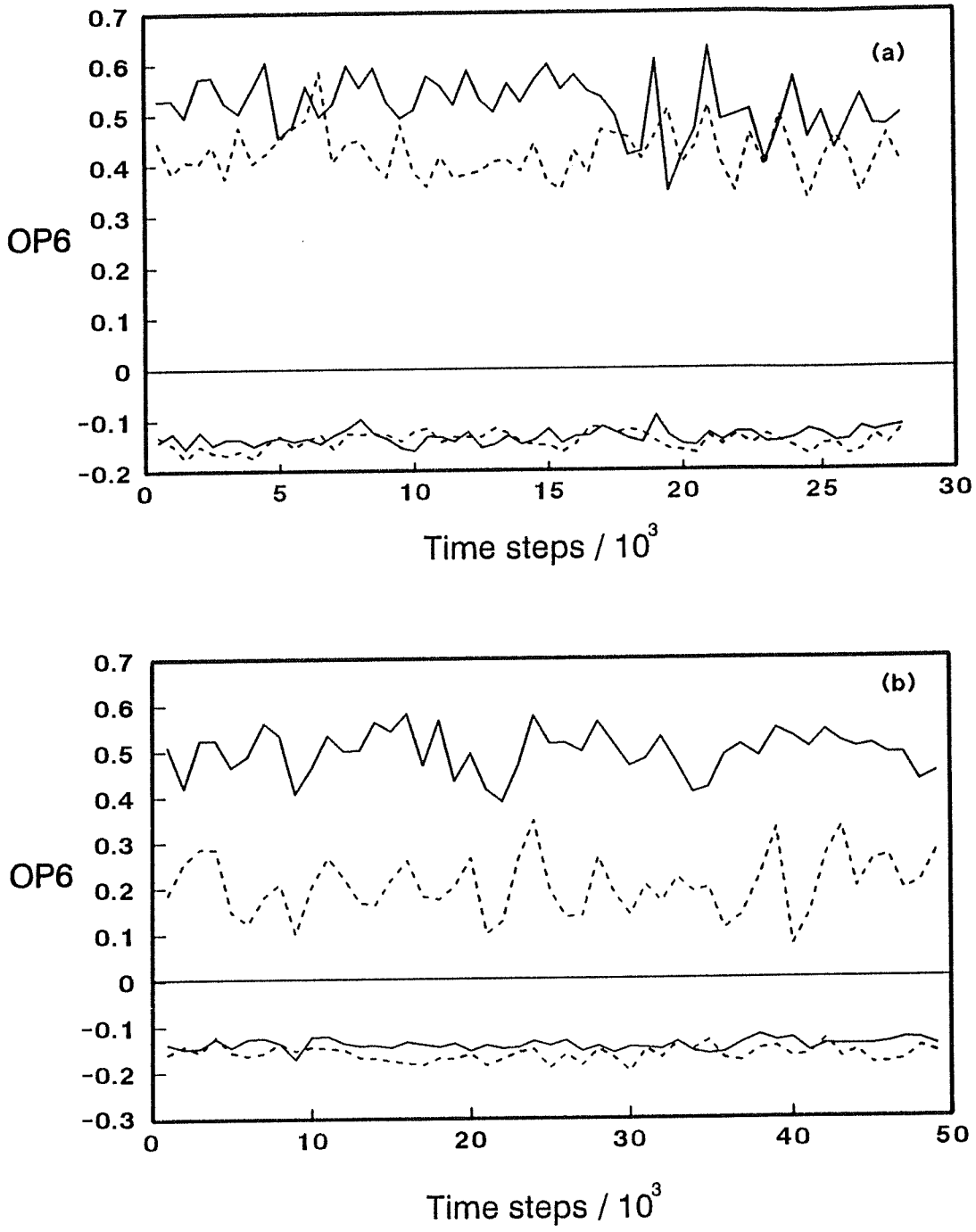

Figure 4.15. Hexagonal order parameters of the head and tail groups of the monolayer: (a) A_m = 20.6Å^2; (b) A_m = 21.2Å^2.

disordered than the molecular centres of mass (see Figure 4.10, where OP6=0.8±0.02 for the molecular centres of mass) and that the head and the tail groups in the monolayer with A_m=20.6Å^2 have hexagonally similar structures while the tail groups in the layer with A_m=21.2Å^2 are hexagonally more disordered than the headgroups. The likely reason for the differences in the radial distrubution function and the hexagonal order of the head and the tail groups is the gauche defects in the chain.

4.4.2. The orientational ordering of the monolayers.

Figure 4.7 indicated that the layers are strongly orientationally ordered structures. The molecules in the monolayer with A_m=20.6Å^2 are aligned nearly parallel to the surface normal while the molecules in the monolayer with A_m=21.2Å^2 are tilted away from the surface normal. To obtain quantitative measure of the orientational ordering of the monolayer we calculated the average values of the three Euler angles(ϕ,θ,ψ) for the both monolayers.

Figure 4.16 shows the distribution of g(cos(θ)) as a function of cos(θ), where θ is the tilt angle of the molecule. The most probable tilt angle is the angle corresponding to the the maximum in g(cos(θ)). The most probable molecular tilts are 2.4° and 18.8° for A_m = 20.6Å^2 and 21.2Å^2 respectively. The average tilt angle(θ) for the monolayer with A_m = 21.2Å^2 is much larger than that of the layer of the explicit-hydrogen model with same headgroup area(θ = 9°) discussed in chapter 3.

We calculated the in-plane molecular orientation for the both layers. Figure 4.17 shows the average azimuthal angle and its distribution for the layer with A_m = 21.2Å^2 during the complete simulation. The average azimuthal angle has the value of 91±5°, which means that the molecules in the layer are directed towards their next-nearest neighbour molecules throughout the simulation. In constrast to the simulation with the explicit-hydrogen model the azimuthal angle remains essentially constant with time. The system does not attempt to explore the six degenerate ground states in which the molecules point towards the next-nearest neighbour molecules in the triangular

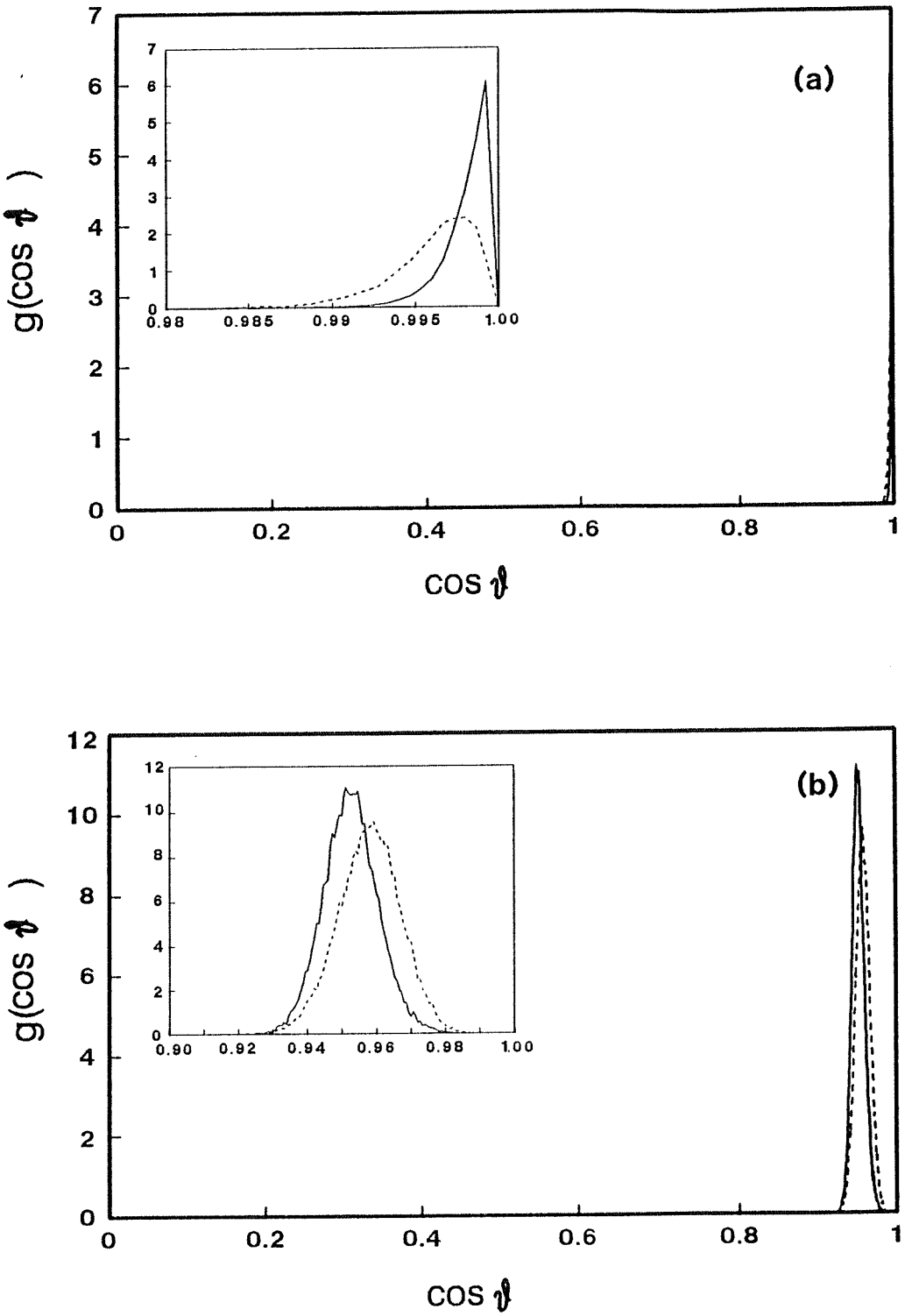

Figure 4.16. Distribution of the cosine of molecular tilt angles of the layer of (a) A_m = 20.6Å^2 and (b) A_m = 21.2^2.

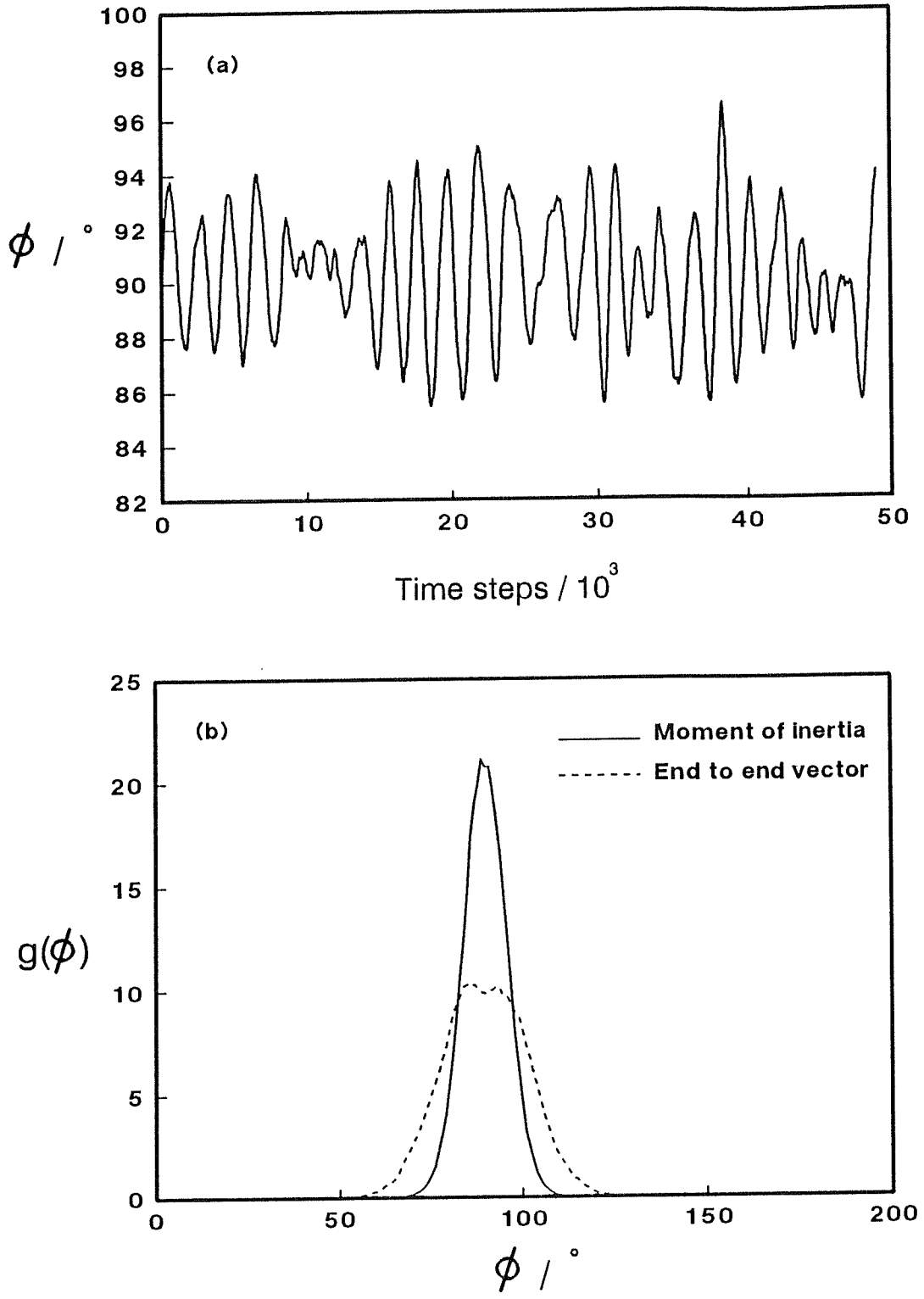

Figure 4.17. The average molecular azimuthal angle(a) and its distribution(b) of the layer of A_m = 21.2Å^2.

lattice. The more realistic headgroup interactions of the all-atom headgroup lock the molecules into one azimuthal direction on the timescale of the simulation. The larger molecular tilt angle found in the simulation of the all-atom model also inhibit the azimuthal rotation. Interestingly the simulations with the united-atom methylene groups predict a nearest neighbour molecular tilt[3,8]. Our MD simulation results are supported by the energy minimisation calculations of the all-atom model which also predicted a next-nearest neighbour orientation. We also calculated the distribution of the molecular twist angle, $g(\psi)$, which measures the orientation of the short axis of the hydrocarbon chain for the all-trans molecules. Figure 4.18 shows the distribution of molecular twist angle of the layer with A_m = 21.2Å^2. The monolayer has a lattice structure of two molecules per unit cell. The two molecules in a unit cell have anti-parallel orientation. One of the molecules has a molecular twist angle(ψ) of 0° and the other has $\psi = 180°$ measured with respect to the x-axis of the simulation box. In the monolayer with the explicit-hydrogen model at same density, a small fraction of the molecules have a molecular twist angle(ψ) of 90°. This difference results from the dipolar orientation between the headgroups in the monolayer in the all-atom model which strongly favours the anti-parallel orientation. Dipolar orientation will be discussed later in this chapter.

4.4.3. X-ray structure factor, S(**k**).

If the particle i is at $\mathbf{r}_i$ in a system of N particles, the density of particles at a point **r** is defined as

$$\rho(\mathbf{r}) = \sum_{i=1}^{N} \delta(\mathbf{r} - \mathbf{r}_i) \ . \qquad (4.11)$$

The Fourier transform of the particle density is

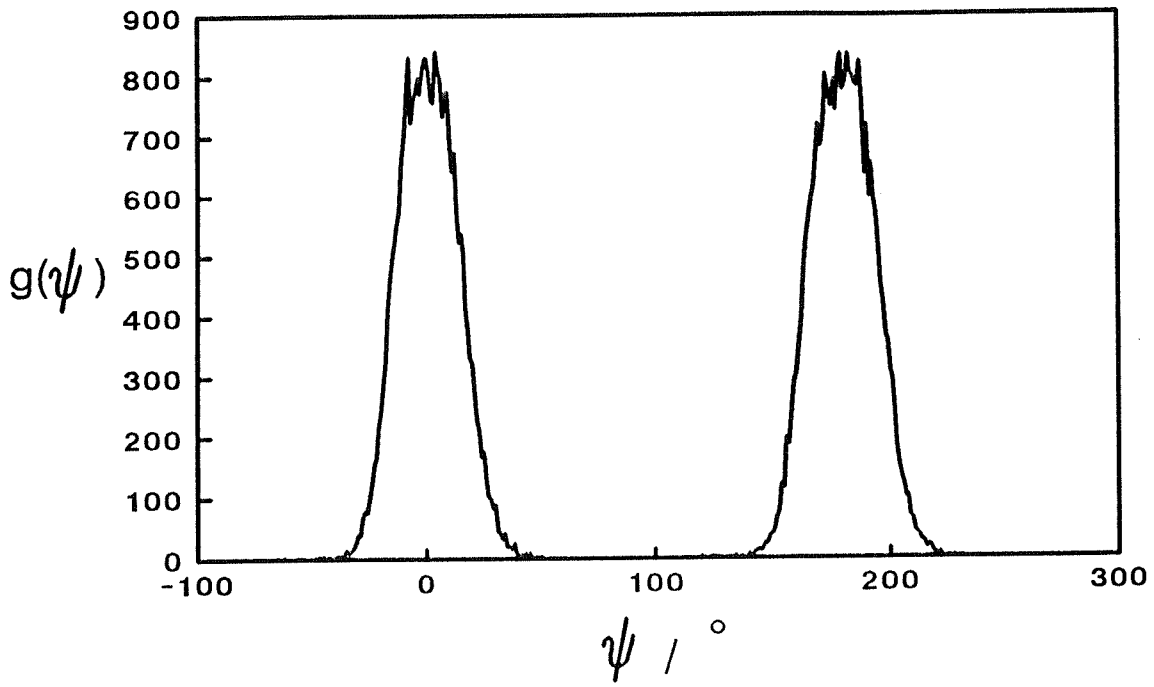

Figure 4.18. Distribution of molecular twist angle about molecular long axes of the layer of A_m = 21.2Å^2.

$$\rho_{\mathbf{k}} = \int \exp(-i\mathbf{k}\cdot\mathbf{r})\,\rho(\mathbf{r})\,d\mathbf{r}$$
$$= \sum_{i=1}^{N} \exp(-i\mathbf{k}\cdot\mathbf{r}_i) \ . \qquad (4.12)$$

The structure factor S(**k**) is the auto-correlation function of the Fourier components of the particle density, $\rho_{\mathbf{k}}$:

$$S(\mathbf{k}) = \frac{1}{N}\langle \rho_{\mathbf{k}} \cdot \rho_{-\mathbf{k}} \rangle \ . \qquad (4.13)$$

The structure factor for a set of N molecules containing m scattering centres is

$$S(\mathbf{k}) = \frac{1}{N}\langle \rho_{\mathbf{k}} \cdot \rho_{-\mathbf{k}} \rangle \qquad (4.14)$$

where

$$\rho_{\mathbf{k}} = \sum_{i=1}^{N} \sum_{\alpha=1}^{m} b_{\alpha}(k)\, e^{-i\mathbf{k}\cdot\mathbf{r}_{i\alpha}}$$

and $b_{\alpha}(k)$ is the X-ray scattering length of the atom which depends on $|\mathbf{k}|$.

In the calculation of the structure factor we summed over all the atoms in the system using Eq. (4.14), for various values of **k**. k_x and k_y can only take restricted values within the periodic boundary condition, namely $k_x = 2\pi n/L_x$ and $k_y = 2\pi m/L_y$, where L_x and L_y are periodic box length in x and y direction respectively and n and m are integers. Figure 4.19 shows the structure factors for the monolayers with $A_m = 20.6\text{Å}^2$ and $A_m = 21.2\text{Å}^2$. They show the six peaks characteristic of a triangular structure. For the monolayer with $A_m = 20.6\text{Å}^2$ there are two strong peaks and four weak peaks. For

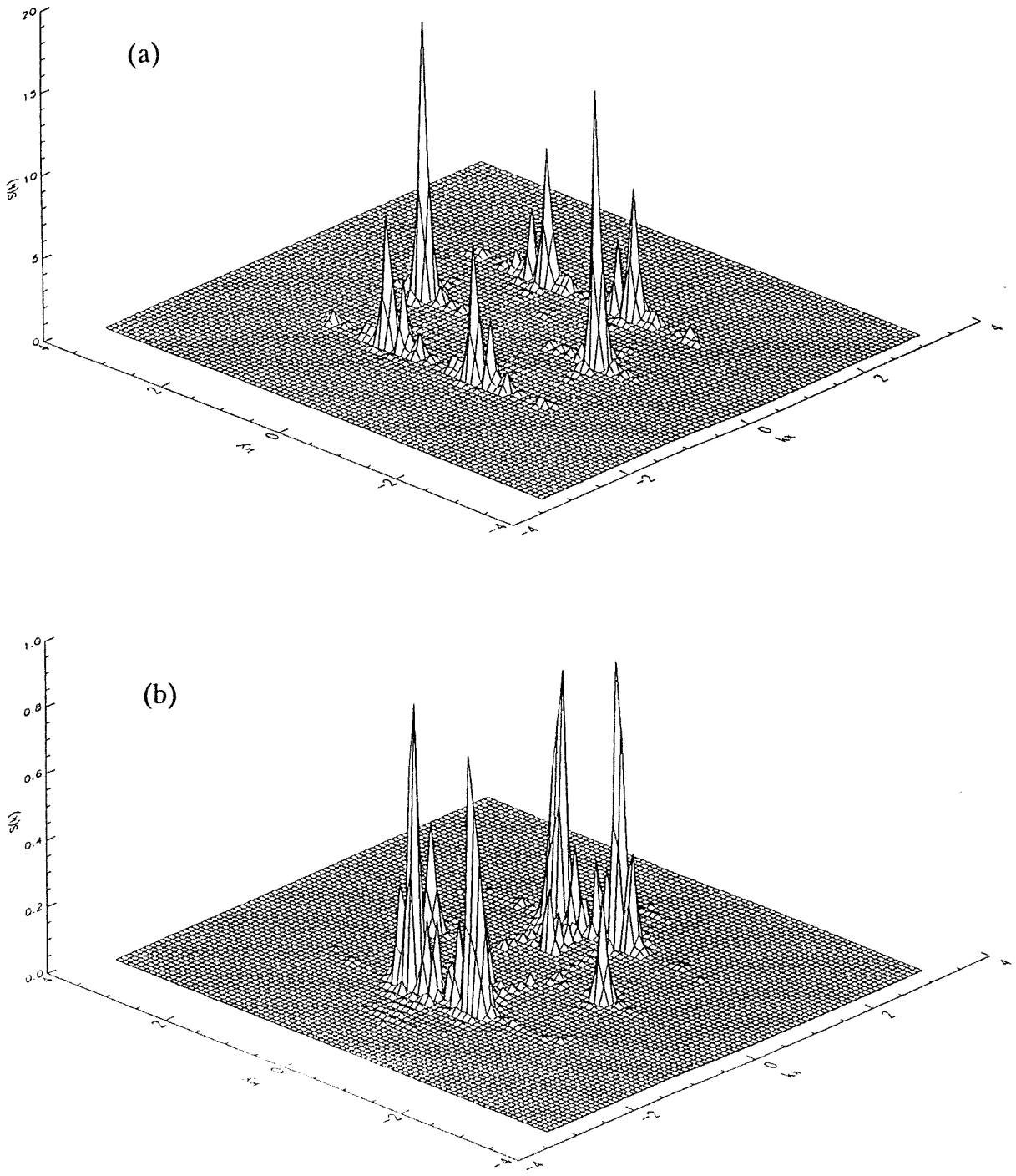

Figure 4.19. The structure factor, S(**k**) for the monolayer with (a) A_m = 20.6Å^2 and (b) A_m = 21.2Å^2.

the monolayer with A_m = 21.2Å^2 there are four strong and two weak peaks. To understand these modulations in intensity we generated several idealized monolayer structures with different azimuthal orientations and tilt angles and calculated the corresponding structure factors of these single configurations. The results are summarized in Table 4.11. This shows that the structure factor depends on the molecular tilt and the azimuthal orientation of the molecules and also depends on the lattice structure of the layer. For example, the monolayer which has the molecular tilt towards the next-nearest-neighbours with θ=20° shows the structure factor with four strong and two weak peaks. This is the pattern which corresponds to the structure factor for the monolayer with A_m = 21.2Å^2 calculated in its MD simulation. The monolayer without molecular tilt shows a structure factor with two strong and four weak peaks, which corresponds to the structure factor from the MD simulation of the monolayer with A_m = 20.6Å^2. The monolayer with herring-bone structure(two molecules per unit cell structure) shows the structure factor with six strong peaks with equal intensities. The intensity of the weak peak in the structure factor is dependent on the degree of the rotational freedom of the molecules about their long axes. The structure factors from the MD simulation of arachidic acid[1,2] show two strong and four weak peaks. The layers of arachidic acid are tilted towards the nearest-neighbour. Experimentally Garoff *et al.*[23] measured the electron diffraction pattern from stearic acid monolayer on Aluminium surface. They obtained the six peaks with similar intensities. As they discussed, the stearic acid molecules in the monolayer have significant rotational motion about their long axes and the layer has a small tilt, of approximately 8°, and the layer could be supposed to be a mixture of the domains with two-sublattice structure and with one-sublattice structure.

Table 4.11. Summary of the structure factors from the idealized monolayer structures.

ϕ/°	θ/°	ψ/°	S(k)
0.0	0.0	0.0	2s, 4w
0.0	0.0	0.0/90.0	6s
0.0	20.0	0.0	2s, 4vw
0.0	20.0	0.0/90.0	2s, 4vw
90.0	20.0	0.0	4s, 2w
90.0	20.0	0.0/90.0	4s, 2w
90.0	20.0	0.0/90.0	4s, 2w

s: strong peak

w: weak peak

vw: very weak peak

4.4.4. NMR order parameters.

As discussed in chapter 3, deuterium nuclear magnetic resonance spectroscopy can be used to characterize the orientation of C-H bond of the molecules in Langmuir-Blodgett film. We calculated the NMR order parameters using Eq.(3.12). The S_{CD} is the measure of the anisotropy of C-D bond in a chain of molecule to surface normal. Figure 4.20 shows the NMR order parameters of each carbon atoms along the chain for both systems. S_{zz} are nearly unity throughout the chain except the carbon atom near to the headgroup for the monolayer with A_m = 20.6Å^2, which means that the alkyl tails of the molecules are nearly parallel to the z-axes. However, S_{zz} for the monolayer with A_m = 21.2Å^2 is less than 0.9 all along the chain which means that the alkyl tails of the molecules in the layer are tilted away from the z-axis. For the monolayers with the explicit-hydrogen model S_{zz} for the monolayer with A_m = 21.2Å^2 was nearly unity because the average tilt of the layer was relatively small (ca. 9°). From the reason for the symmetry, order parameter tensor S is diagonal except for the S_{yz} of small value and the sum of the diagonal components of S is zero. If the molecular rotation about the molecular z-axis is isotropic $S_{zz} = -2S_{xx} = -2S_{yy}$. From this relationship we can investigate the anisotropy of the rotation about the molecular z-axis by comparing S_{zz} with $-2S_{xx}$. Figure 4.20(b) shows that S_{zz} is not equal to $-2S_{xx}$ in the monolayer with A_m = 21.2Å^2. This indicates that there is an anisotropy in the rotation of molecule about its long axes[5,9].

4.4.5. Dipolar orientation of the monolayers.

The most significant improvement of the all-atom model over the explicit-hydrogen model discussed in chapter 3 is the inclusion of the dipolar interactions in the layer. As discussed earlier in this chapter we have obtained a different in-plane lattice structure compare to that of the explicit-hydrogen model due to this interaction (compare Figure 3.12 and Figure 4.18). We analyzed the distribution of the in-plane dipolar orientations for both monolayers. The vector representating the dipole in a molecule

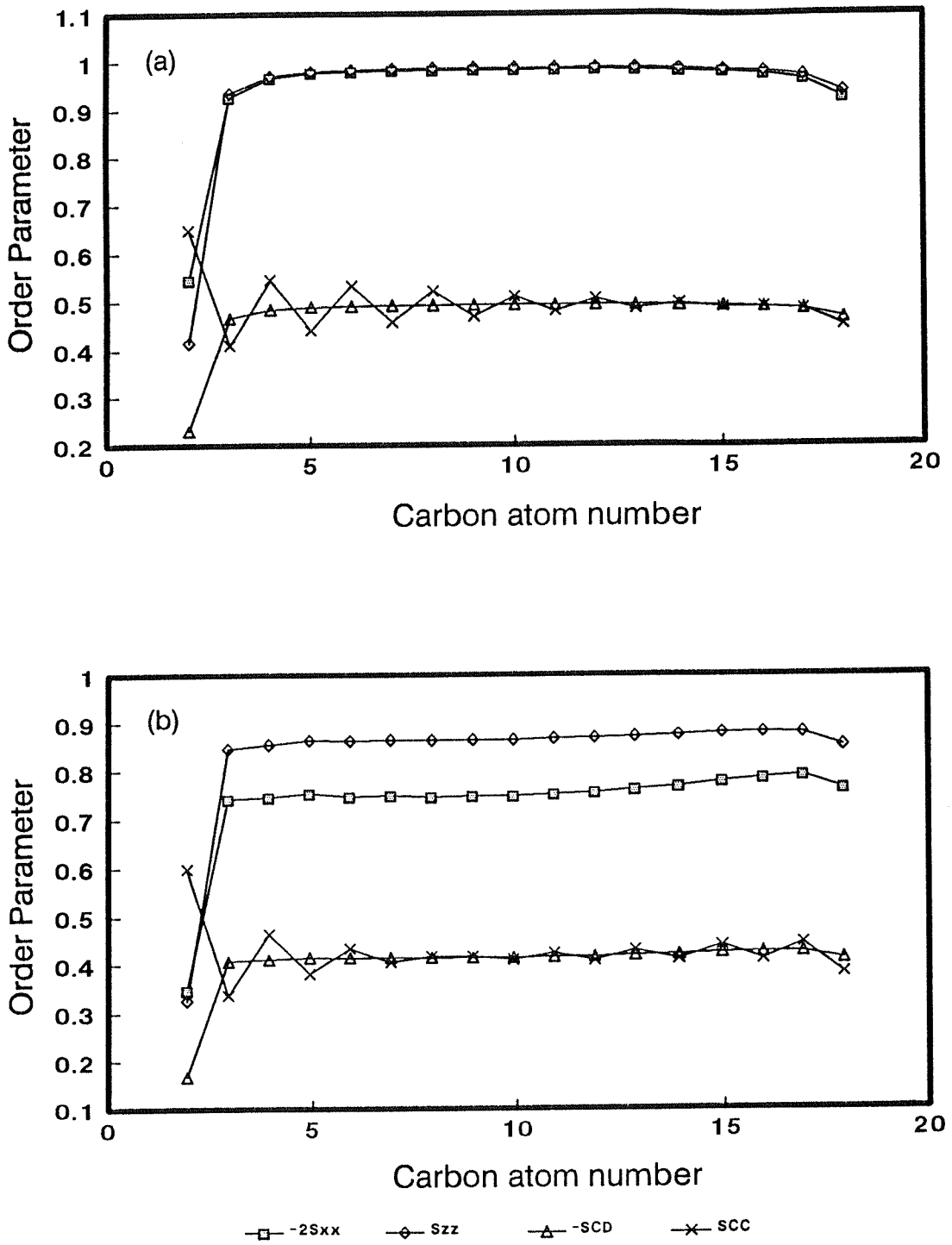

Figure 4.20. NMR order parameters of stearic acid monolayer using the all-atom model for (a) A_m = 20.6Å^2 and (b) A_m = 21.2Å^2.

is defined as

$$\mu = \sum_{i=1}^{4} q_i r_i \qquad (4.15)$$

where the origin is taken to be the carbon atom of the headgroup.

The dipolar vector is nearly parallel to the C=O bond with the magnitude of 1.79D (1D=3.33564x10^{-30} Cm) and points from the oxygen atom to the carbon atom in the headgroup. Figure 4.21 and Figure 4.22 show the distribution of dipolar tilt(θ_μ) and azimuthal(ϕ_μ) angles for both systems. Figure 4.21 shows that the dipoles in the layer are nearly parallel to the surface. This ensures a strong attractive interaction with image charges on the surface. The movement of the dipoles on the headgroup of a stearic acid molecule is strongly related to the dihedral rotation about the bond H-O1-C1-C2 and O1-C1-C2-C3. Equally strong dipolar interaction can also restrict the dihedral rotation about these two bonds. The distributions of dipolar azimuthal angles shown in Figure 4.22 shows the dipoles aligned in a one sub-lattice structure with a relatively broad distribution for the layer with A_m=20.6Å^2 and a two sub-lattice alignment with an anti-parallel orientation for the layer with A_m=21.2Å^2. The broad distribution of dipolar azimuthal angle at A_m=20.6Å^2 is connected with the idea that there is significant rotational freedom about the long axes of the molecules which is approximately parallel to z-axis (surface normal) and the dipolar motion is strongly coupled with the motion of the backbone of the chain. In the monolayer with A_m = 21.2Å^2 there are two molecules per unit cell structure with anti-parallel orientations and the molecules are tilted away from the surface normal. The rotation of dipole about the long axis of the molecule means that the dipole is tilted away from the parallel orientation to the surface, which is the most favorable orientation for the dipolar interaction and non-bonded interaction of head group with surface. In both case the dipole are aligned in a head-to-tail configuration in the layer.

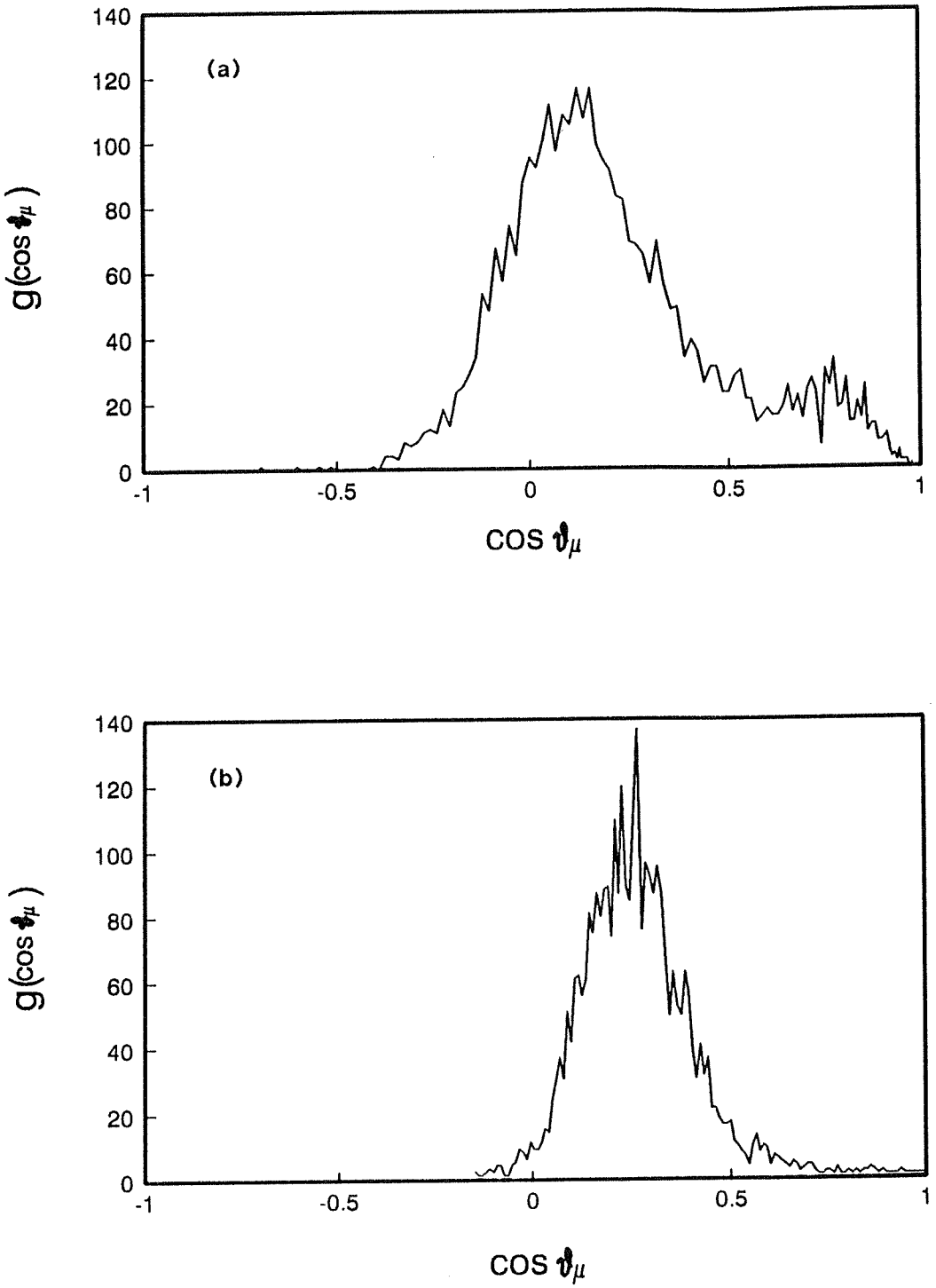

Figure 4.21. Distribution of dipolar tilt angle for the monolayer with (a) A_m = 20.6Å^2 and (b) A_m = 21.2Å^2.

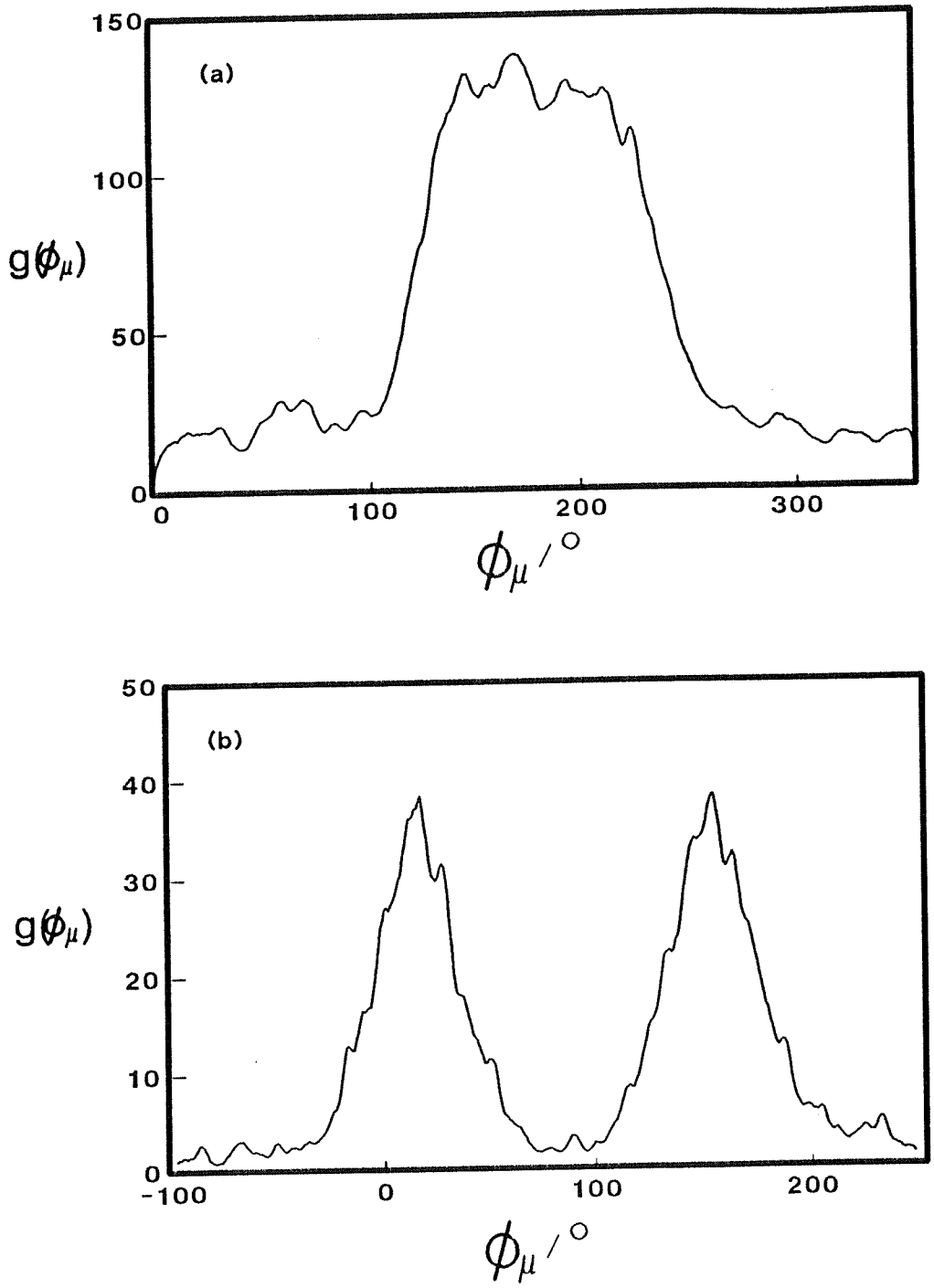

Figure 4.22. Distribution of dipolar azimuthal angle of the monolayer with (a) A_m = 20.6Å^2 and (a) A_m = 21.2Å^2.

4.4.6. Dynamics of the monolayer.

The dynamics of the Langmuir-Blodgett film was examined by calculating the velocity auto-correlation functions for the carbon atoms in the chain. The power spectrum of the layer is the Fourier transform of velocity auto-correlation function:

$$\hat{C}(\omega) = 2\int_0^{\infty} dt\, C(t) \cos \omega t \,, \tag{4.16}$$

where C(t) is the velocity auto-correlation function defined by:

$$C(t) = \frac{\langle v(0)\cdot v(t)\rangle}{\langle v(0)\cdot v(0)\rangle} \tag{4.17}$$

where v(t) is the velocity of an atom in the chain at time t. Figure 4.23 shows the power spectrums for the both layer. These spectra are very similar to the spectra for the layer of the explicit-hydrogen model and other molecular dynamics result for the arachidic acid molecules[2]. The power spectra in Figure 4.23 indicate that the carbon atom motion is a combination of various motions with different time scales. To identify the motion we analyzed the various modes of the carbon atom motion separately. The translational motion of the molecular centres of mass is very slow and produced peaks in the region of $0 < \omega < 100$ cm^{-1}. These correspond to the motion of molecular centres of mass. The in-plane motion corresponds to the azimuthal motion and the out-of-plane motion corresponds to the molecular tilt motion. The fast motion in the region of $350 < \omega < 490$ cm^{-1} is mainly due to the bond angle distortion. Figure 4.24 and Figure 4.25 show the correlation functions and power spectra for the in-plane translational motion of the molecular centres of mass and for the C-C-C bond angle distortion.

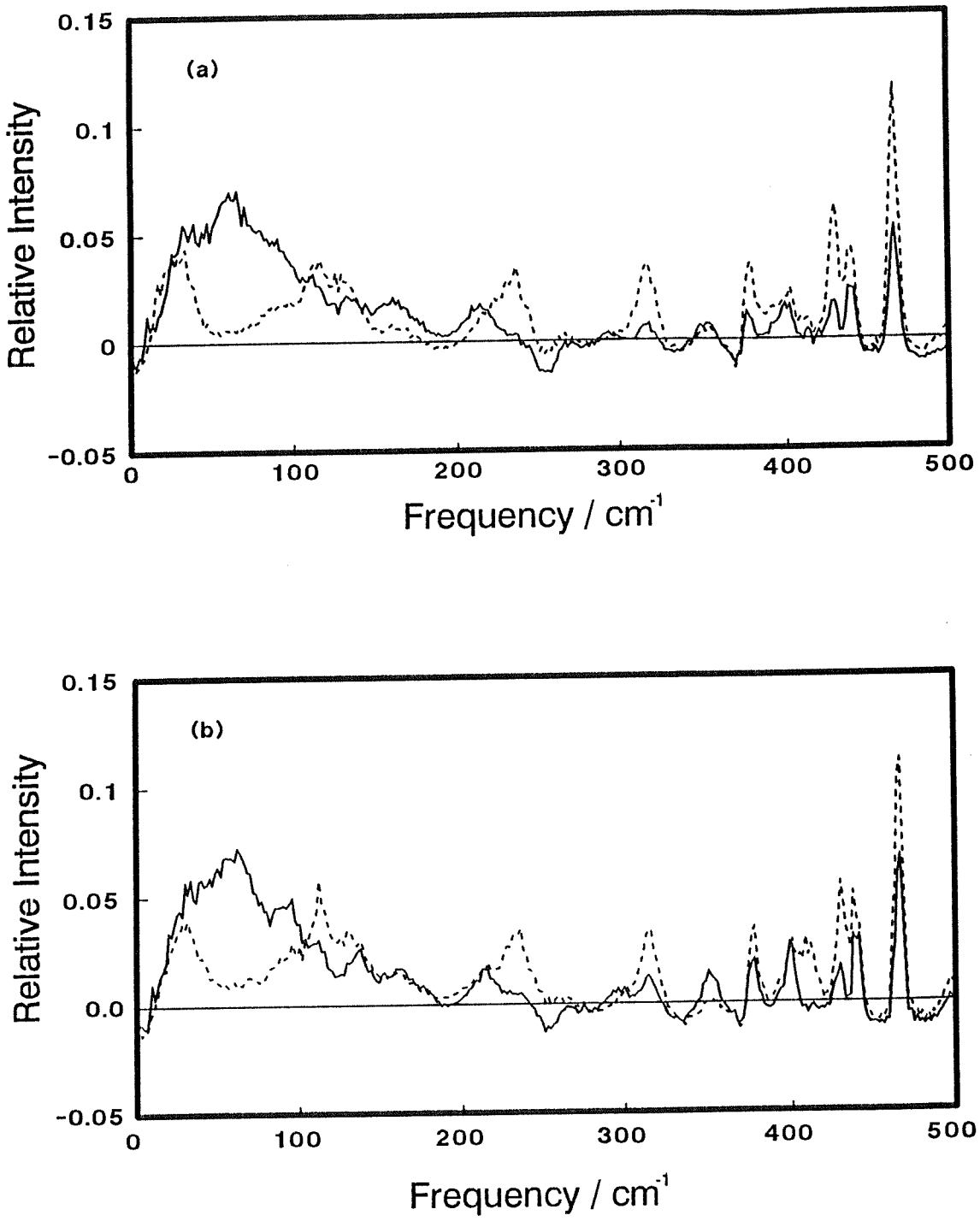

Figure 4.23. Power spectrum of the motion of carbon atom, in-plane(solid line) and out of plane (dashed line) for the layer of (a) A_m = 20.6Å^2 and (b) A_m = 21.2Å^2.

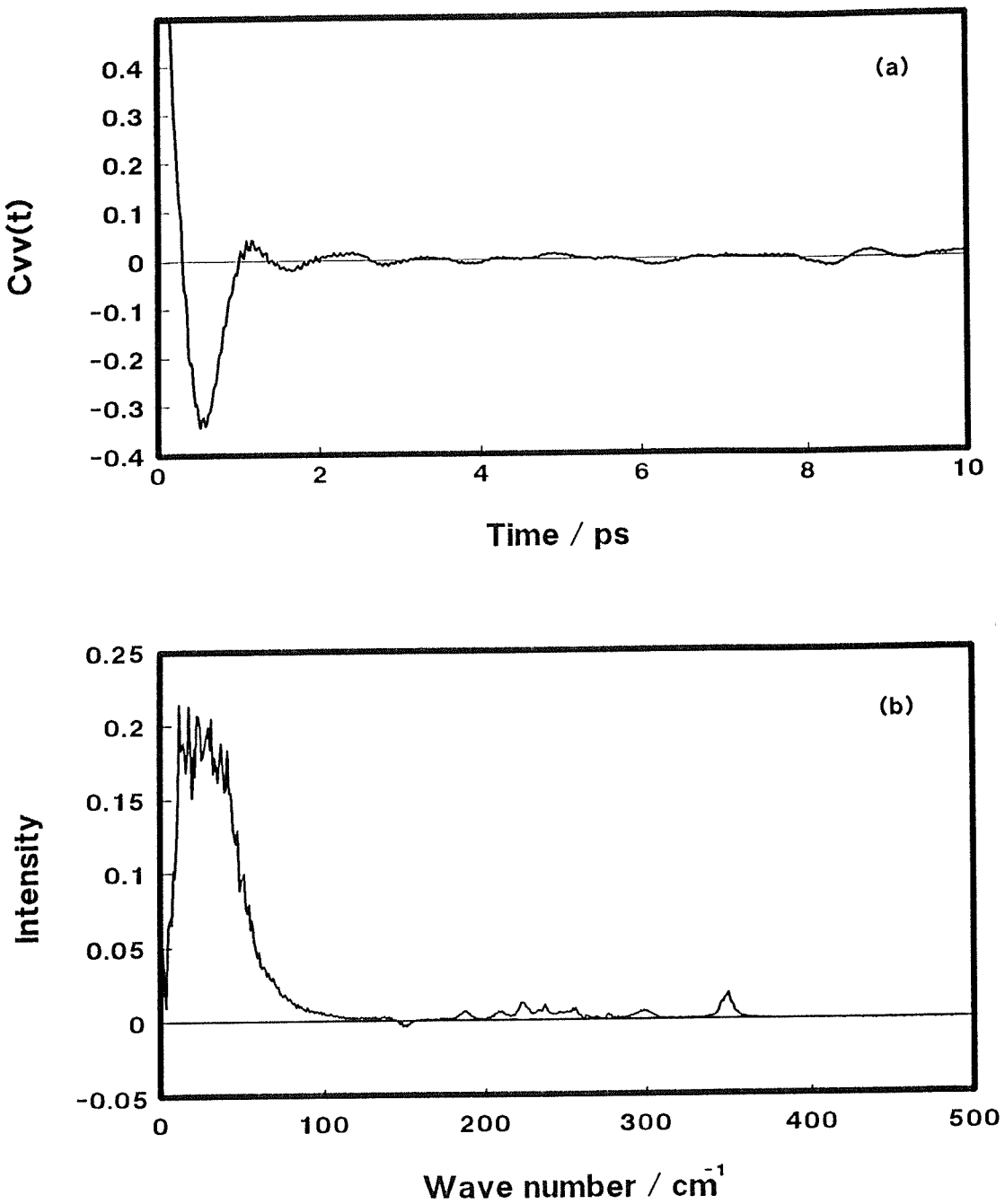

Figure 4.24. The in-plane motion of the molecular centres of mass: (a) Velocity autocorrelation function and (b) power spectrum.

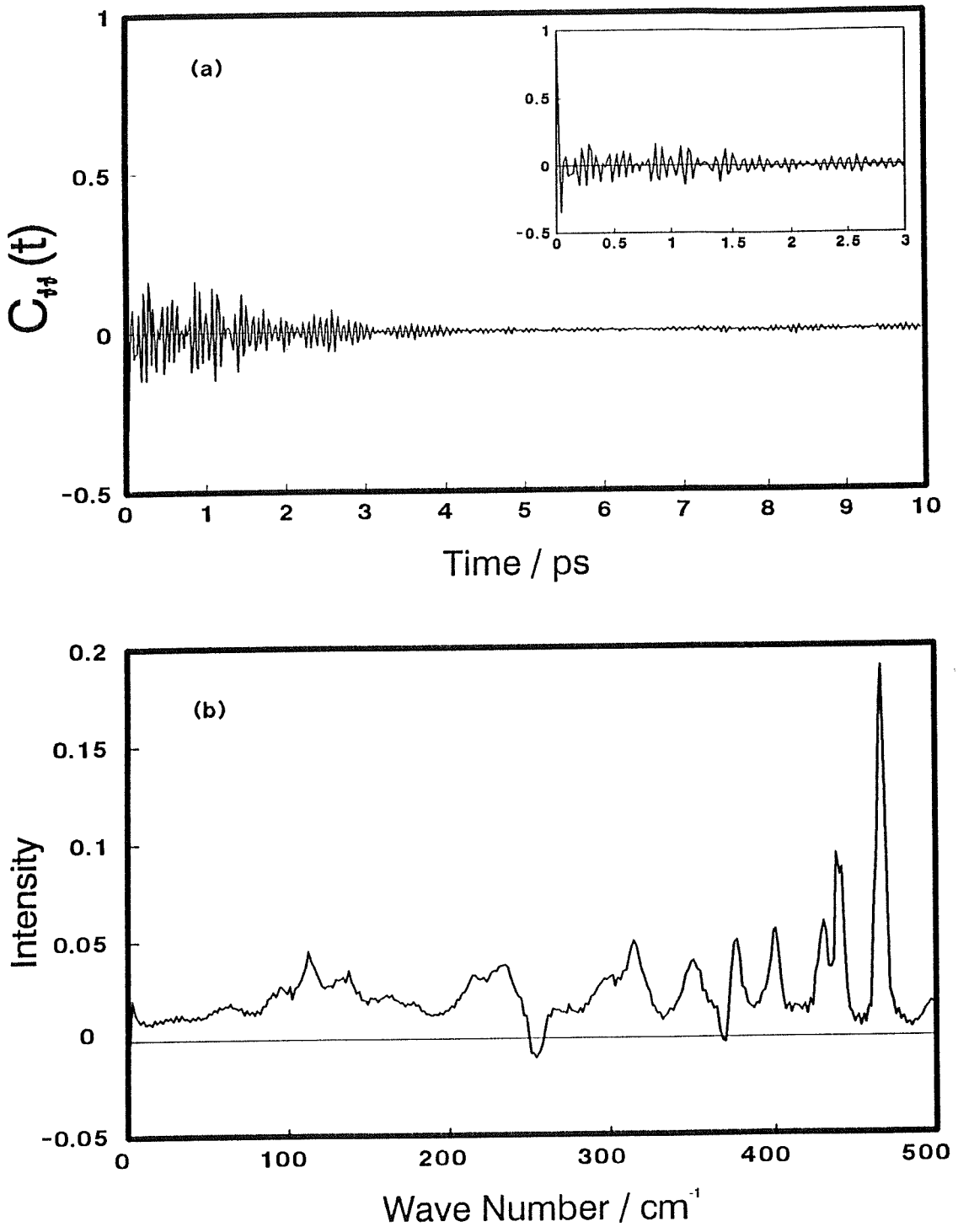

Figure 4.25. The bond-bending motion of the molecular chain in the layer: (a) Autocorrelation function of bond bending motion and (b) power spectrum.

4.5. Conclusions.

The energy minimisation and molecular dynamics simulation using the all-atom model have been carried out to predict the structure and dynamics of the Langmuir-Blodgett film on a structureless surface. In the all-atom model we improved the interaction model between head groups and between head groups and surface by including the partial charge interaction to model the dipolar interactions in the layer. The inclusion of the dipolar interaction did not change the structure of the monolayer significantly at 0K. However, the structure at 300K from molecular dynamics is somewhat different in details to the structure predicted by the explicit-hydrogen model. The all-atom model predicts a conformational distortion (gauche defects) at the bond connecting the carboxylic acid group and the alkyl chain of the molecule like defects in stearic acid crystal B. The overall structure is very similar to that of the monolayer with the explicit-hydrogen model. The distribution of the molecular centres of mass is solid-like, while the distribution of the gauche defects is liquid-like. The molecular tilt of the layer of A_m = 21.2Å^2 is 18.8°, which is more than double the molecular tilt for the layer of the explicit-hydrogen model(9°) and much closer to the tilt angle from the energy minimisation calculation. Interestingly the tilt angle is nearly same as the value predicted by X-ray diffraction[22]. We also found that there is a strong coupling between the rotation of headgroup and the dipolar orientation. The dipolar orientation can also affect the orientation of the chain of the molecule.

References.

[1] J.P. Bareman, G. Cardini and M.L. Klein, Phys. Rev. Letters, **60**, 2152 (1989).

[2] G. Cardini, J.P. Bareman and M.L. Klein, Chem. Phys. Lett., **145**(6), 493 (1988).

[3] J.P. Bareman and M.L. Klein, J. Phys. Chem., **94**, 5202 (1990).

[4] A.J. Kox, J.P.J. Michels and F.W. Wiegel, Nature, **238**, 317 (1980).

[5] P. van der Ploeg and H.J.C. Berendsen, J. Chem. Phys., **76**, 3271 (1982).

[6] J. Harris and S.A. Rice, J. Chem. Phys., **89**, 5898 (1989).

[7] A. Ulman, J.E. Eilers and N. Tilman, Langmuir, **5**, 1147 (1989).

[8] J. Hautman and M.L. Klein, J. Chem. Phys., **91**, 4994 (1989).

[9] E. Egberts and H.J.C. Berendsen, J. Chem. Phys., **89**, 3718 (1988).

[10] J. Hautman, J.P. Bareman, W. Mar, M.L. Klein, J. Chem. Soc. Faraday Trans., **87**,

[11] C.J. Weiner, P.A. Kolleman, D.T. Nguyen, and D.A. Case, J. Comput. Chem., **7**(7), 230 (1986).

[12] R.C. Weast and M.J. Astle, *CRC Handbook of Chemistry and Physics*, 63rd edition, E-56 (1982-1983).

[13] M. Bishop and J.H.R. Clarke, J. Chem. Phys., in press (1991).

[14] M.P. Allen and D.J. Tildesley, *Computer Simulation of Liquids*, Clarendon Press, Oxford (1987).

[15] W.A. Steele, J. Phys. (Paris), **38**, C4-61 (1978).

[16] G.M. Torrie, J.P. Valleau and G.N. Patey, J. Chem. Phys., **76**, 4615 (1982).

[17] N.L. Allinger, J. Am. Chem. Soc., **99**, 8127 (1977).

[18] J.P. Ryckaert and A. Bellemans, Chem. Soc. Faraday Discuss., **66**, 95 (1978).

[19] L. Verlet Phys. Rev., **159**, 98 (1967).

[20] J.-P Ryckaert, Mol. Phys., **55**, 549 (1985).

[21] M. Goto and E. Asada, Bull. Chem. Soc. Jpn., **51**(9), 2456 (1978).

[22] K. Kjaer, J. Als-Nielsen, C.A. Helm, P. Tippman-Krayer and H. Möhwald, J. Phys. Chem., **93**, 3200 (1989).

[23] S. Garoff, H.W. Deckman, J.H. Dunsmuir, M.S. Alvarez and J.M. Bloch, J. Phys. (Paris), **47**, 701 (1986).

CHAPTER FIVE.

A Langmuir-Blodgett Bilayer with the All-Atom Model.

5. A LANGMUIR-BLODGETT BILAYER WITH THE ALL-ATOM MODEL.

5.1. Introduction.

Multi-layer Langmuir-Blodgett films are quite important precursor to fabricate the materials for the various applications such as pyroelectricity of LB film [1] or optical sensors [2]. To understand how a multi-layer LB film behaves in the application, we need to know its structure and to this end, there have been a number of experimental studies to determine the structure of multilayer LB films.

Kimura *et al.*[3] have characterized the orientational properties of the stearic acid multilayer(up to 9 layers) on a germanium plate by FTIR-ATR spectroscopy and concluded that the molecules in the first layer are oriented perpendicular to the surface with an hexagonal or pseudohexagonal subcell packing. However, in the upper layers the hydrocarbon chains tilt at an angle of about 30° with respect to the surface normal. Bonnerot *et al.*[4] also measured the similar phenomena in their studies of multilayers of docosenoic acid (CH_3-$(CH_2)_{20}$-COOH) and ω-tricosenoic acid (CH_2=CH-(CH_2)-COOH) by IR and electron diffraction. In their results the first layer of docosenoic acid and ω-tricosenoic acid are approximately vertical to surface and the layers tilt progressively to 23° for docosenoic acid and 18° for ω-tricosenoic acid as the systems increase towards seven layers.

To our knowledge there has been no computer simulation on the multilayer Langmuir-Blodgett films, although united-atom hydrocarbon chains have been used to model lipid bilayers [5,6,7].

In this chapter we discuss the energy minimisation and molecular dynamics results of the Langmuir-Blodgett bilayer of stearic acid using an all-atom model. For this simulation we need an innovation to allow us to handle the non-bonded potential calculation in order that the calculations are feasible. This idea will be discussed next section , which is one of the important points in this chapter.

5.2. Models.

Our original model for the bilayer is based on the hamiltonian discussed for the all-atom model discussed in chapter 4 with the structure of the headgroup shown in Figure 4.1.

5.2.1. Interaction model for the bilayer.

In chapter 3, we established the importance of including the hydrogen atoms explicitly in the calculations. However, the simulation of 64 molecules of stearic acid required approximately 80 CRAY/XMP-48 hours for 40,000 equilibration steps followed by 50,000 production steps. Since the time for the simulation depends on the n^2, where n is the number of atoms in the system, doubling the number of atoms to simulate a bilayer will put the calculation beyond our resources. To enable us to perform this simulation we combined the inter-molecular potential models for the united-atom model and the explicit-hydrogen model discussed in chapter 3 into a new hybrid model. In the hybrid model the atom in a methylene unit interact with all of the atoms belong to the six nearest-neighbour chains in the same layer. The interaction with all the methylene groups in the beyond nearest-neighbour is through a modified united-atom potential. For the interaction between headgroups and between headgroup and methylene groups the headgroups are always handled in the all-atom representation. The potential parameters for the united-atom representation should be adjusted within reasonable limits to reproduce the layer with the same properties as the all-atom representation. In the explicit-hydrogen model there are 9 interactions between two methylene units while there is only one interaction between two pseudo CH_2 atoms in the united-atom model. Figure 5.1 compares the potentials of these two models for two methylene groups in the relative orientation shown in the inset to the figure. The distances between two nearest neighbour molecules in the system are 4.9Å for the layer with A_m = 20.6Å^2 and 4.94Å for the layer with A_m = 21.2Å^2 respectively. There are significant differences between the

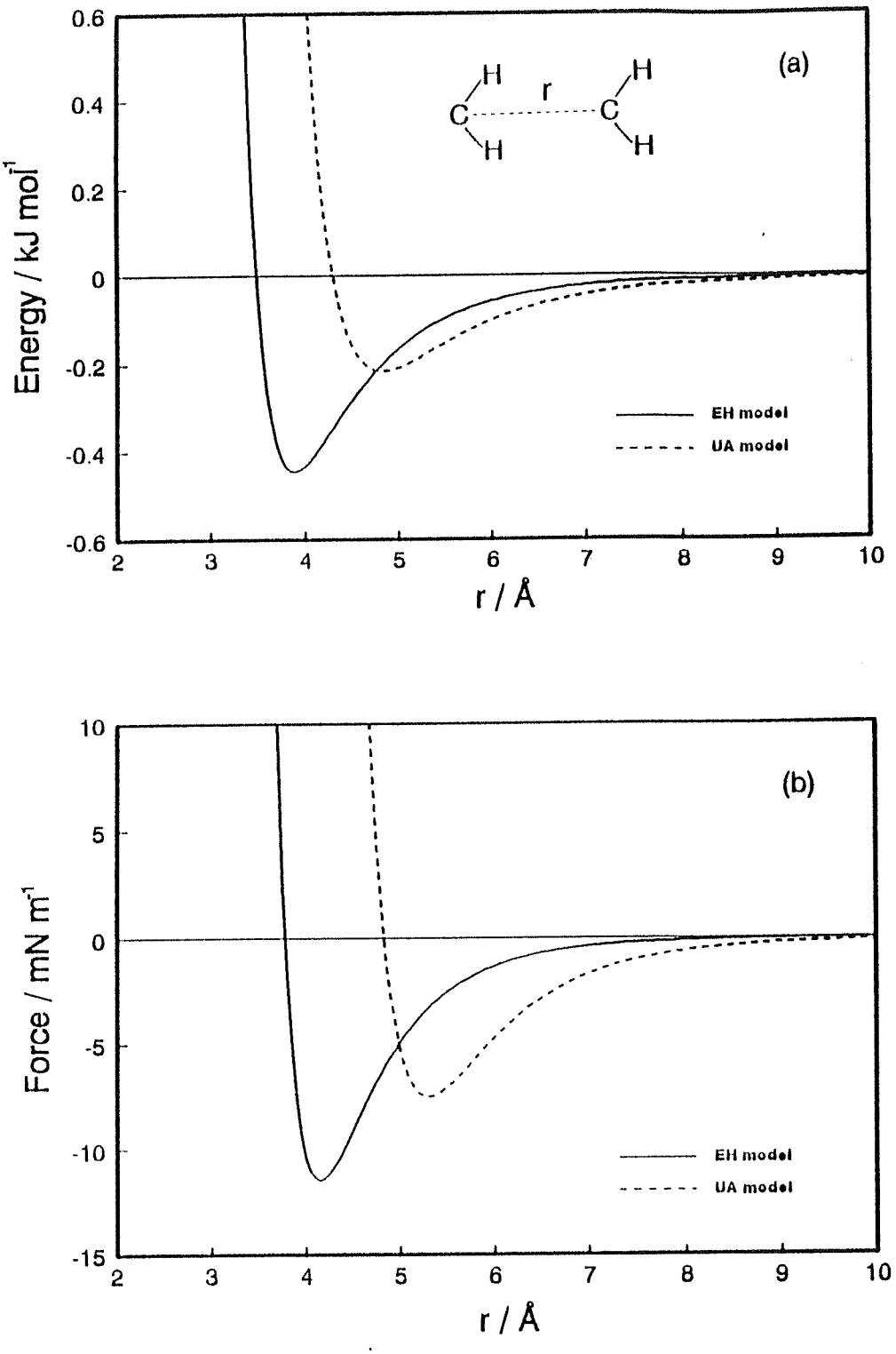

Figure 5.1. (a) The interaction and (b) the force between two methylene units as a function of distance.

potentials for the EH and UA models at this separation which give rise to the difference in the properties discussed in Chapter 3. The next-nearest neighbour separation is 8.5Å and the potentials and forces from the two model are clear at this separation. However we know that the value of σ = 3.973Å and ϵ/k_B = 72.0K are inappropriate from chapter 3 and we can scale these parameters to improve the agreement between the UA and EH models. Bañón *et al.*[8] have already discussed the effect of intermolecular potential parameters of the united-atom model on the equilibrium structure of liquid n-butane. They concluded that the structure is practically unaffected by moderate variations in the Lennard-Jones parameters, but that the configurational equilibrium such as gauche-trans distribution is very sensitive to them. Bareman *et al.*[9] also mentioned that the commonly used potential parameters for the united-atom methylene group underestimate the effective diameter of the alkane chains. We also studied the effect of potential parameters on the tilt behaviour of the monolayer of the united-atom model by energy minimisation to assign suitable parameters to mimic the molecular tilt behaviour of the explicit-hydrogen model monolayer. We have already discussed the effect of size of the united-atom on headgroup area at which tilting begins. A value of σ = 4.3Å for the UA atom was found to reproduce the tilt behaviours. This is very similar to the σ value (4.28Å) used in a recent computer simulation of a polymer system[10]. Several ϵ values have also been used for the alkane chain in the computer simulations, e.g. ϵ/k_B = 70.4K in GROMOS[11] and σ = 59.4Å in the monolayers of hexanol on water [12]. We also scaled the value of ϵ for the methylene group of the united-atom model interaction to match the energy values of hybrid model with that of the all-atom model. To obtain a precise match between the energies of the two models we need to decrease the ϵ/k_B value from 72.0K to 25.0K. This value seems unreasonably small, i.e. smaller than the ϵ/k_B(=49.0K) for the carbon atom of the explicit-hydrogen model. We have also checked the effect of the size of ϵ in the hybrid model on the molecular tilt behaviour. We performed the energy

minimisation with various ϵ/k_B from 72.0K to 25.0K for the UA model but there was little difference in the structure especially in the molecular tilt. From these calculations a value of ϵ/k_B = 52.0K with σ = 4.3Å was found to be suitable for the methylene group of the united-atom interaction in hybrid model. More than 80% of the total energy is in the nearest neighbour interaction in the system using the hybrid model. The potential parameters for the hybrid model are summarized in Table 5.1. The electrostatic interaction was modelled in the same way as discussed for the monolayer simulation discussed in chapter 4. The simulated bilayer was composed of 128 molecules (64 molecules in each layer) with a head-to-head arrangements (Y-type deposition) on hydrophobic surface. The arrangement of the molecules is shown schematically in Figure 5.2. We have not changed the molecule-surface potential significantly. The charges representing the dipole in the headgroup are now approximately 25Å from the surface and the image charge interaction is not important. The hydrophobicity of the surface is built in to the model by placing the molecules in the Y-type deposition mode so that strong headgroup-headgroup interaction is present at the beginning of the calculation. As we discussed in chapter 1, experimentally Y-type deposition is most common deposition mode[13].

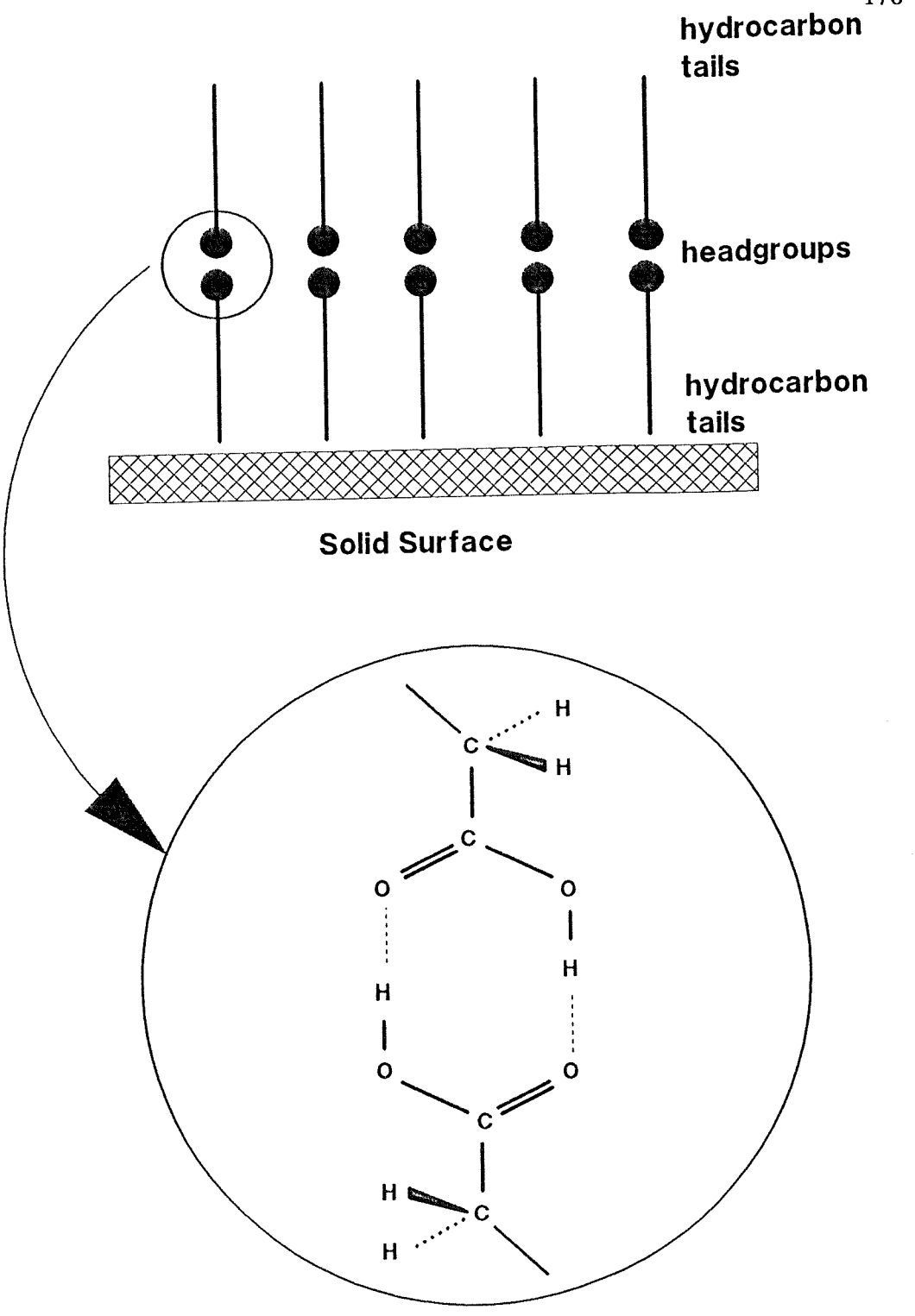

Figure 5.2. Schematic representation of the arrangements of the molecules in the bilayer on surface.

Table 5.1. Potential parameters for the simulation of the bilayer.

atom	ϵ/K	σ/Å	mass/amu	charge/|e|
head[a)]	60.387	3.296	12.011	0.575
carbon	48.784	3.367	12.011	0.0
chain[b)]	52.00	4.30	14.027	0.0
tail	77.25	3.740	15.035	0.0
hydrogen	6.835	2.908	1.008	0.0
oxygen[c)]	75.483	2.940	16.00	-0.350
oxygen[d)]	100.645	2.850	16.00	-0.450
hydrogen[e)]	10.064	1.782	2.016	0.225

a) carbon atom of a carboxylic acid group.

b) CH_2 for the united atom interaction.

c) hydroxyl oxygen of a carboxylic acid group.

d) carbonyl oxygen of a carboxylic acid group.

e) hydrogen atom of a carboxylic acid group.

5.3. Energy minimisation.

We performed the energy minimisation calculations for the stearic acid bilayers using the hybrid model. The bilayer of 128 molecules is set up on the structureless hydrophobic surface in triangular lattice with the configuration shown in Figure 5.2. The total energy, including the intermolecular and the molecule-surface interaction, was calculated as a function of configuration of molecules in the bilayer, i.e. $V = f(\phi_1,\theta_1,\psi_1,\phi_2,\theta_2,\psi_2,d)$, where ϕ_1, θ_1, ψ_1, ϕ_2, θ_2, and ψ_2 are the azimuthal, tilt, and twist angles for lower and upper layer respectively and d is the separation of the two layers defined by a distance between carbon atoms of the headgroups in the lower layer and the upper layer. As before the molecules were fixed in their all-trans conformation. Figure 5.3 shows the minimum energy, E_{min}, and the tilt angle, θ_{min} at E_{min}, as a function of headgroup area A_m. The figure shows that the molecular tilt transition occurs at $A_m = 20.8Å^2$, which is similar result to the results of the energy minimisations using the explicit-hydrogen model and the all-atom model for monolayer. However, E_{min} as a function of A_m is quite different to the curves for the monolayers using the explicit-hydrogen model(Figure 3.2) or the all-atom model (Figure 4.5). The most interesting point is that the molecular tilt of the both layer is nearly same. That indicates that the structure of the bilayer is generally governed by the intermolecular interactions in same layer and the interactions between two layers controls the relative position of two layers at 0K. Therefore there is very small difference in overall structure between monolayer and bilayer in the results of the energy minimisation.

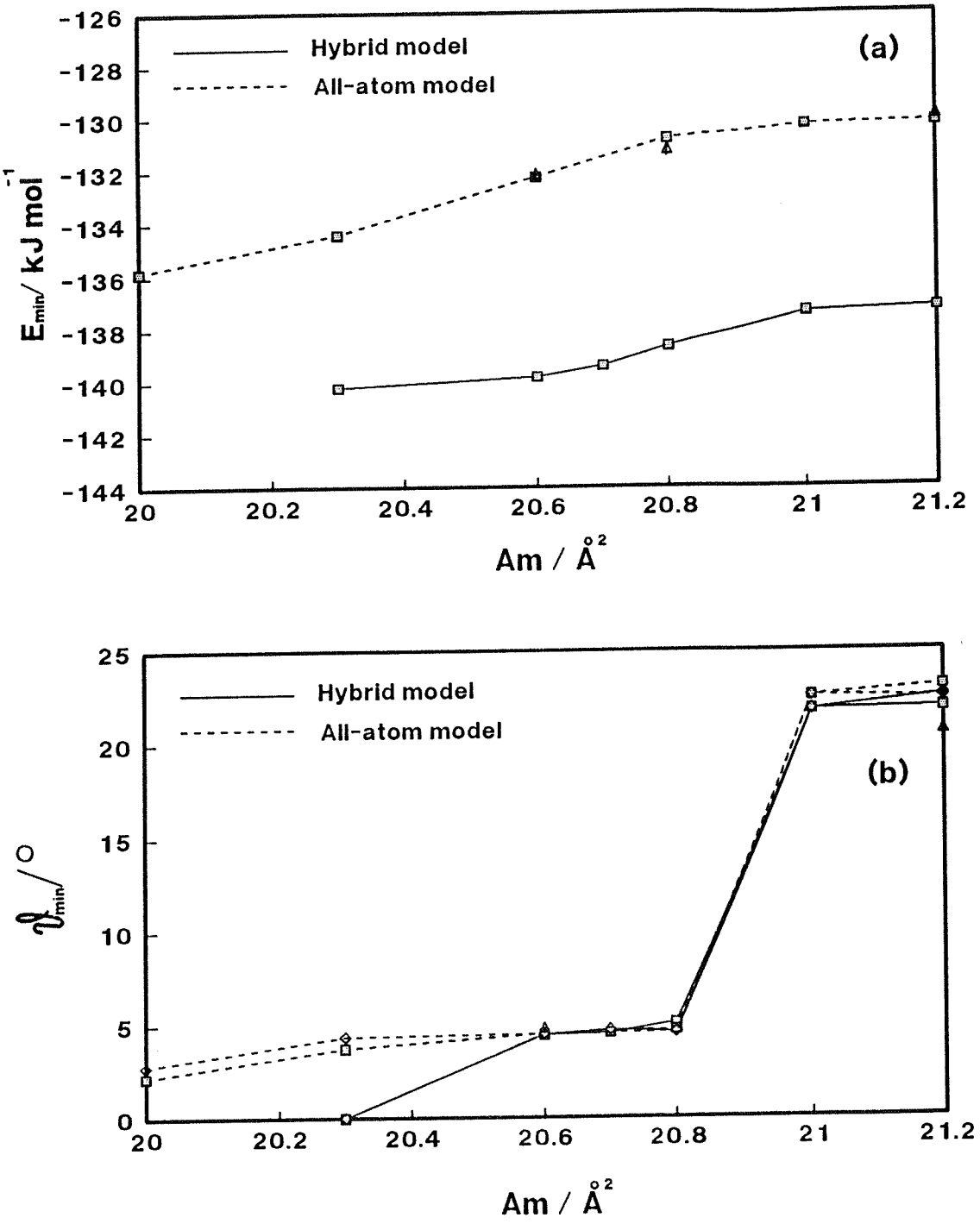

Figure 5.3. The minimum energy E_{min} and molecular tilt at minimum energy θ_{min} of both layer as a function of headgroup area A_m using the hybrid model.

5.4. Molecular dynamics.

Molecular dynamics simulations of a Langmuir-Blodgett bilayer of stearic acid on a structureless hydrophobic surface have been performed using the hybrid model. The system is composed of two monolayers of 64 molecules(8x8) in each layer with the head-to-head arrangement as shown in Figure 5.2. Two molecular dynamics simulations started at 298K from the minimum energy structures at A_m = 20.6Å^2 and A_m = 21.2Å^2 . The two headgroup areas are chosen to be the either side of the transition of molecular tilt as observed in the minimum energy structures discussed in the previous section. The details of molecular dynamics method have been discussed in chapter 3 and chapter 4. We performed the 50,000 steps of equilibration (100 ps) followed by 39,000 steps of production (78 ps) for the system with A_m = 20.6Å^2 and 55,000 steps of equilibration (110 ps) followed by 46,000 steps of production (92 ps) for the system with A_m = 21.2Å^2. This required 130 cpu hours on CRAY/XMP-48. The snapshots of the structure of the bilayers from x- and y-directions at the end of the production phases are shown in Figure 5.4. Both bilayers are well-ordered solid-like structures. However, the most important difference between these structures and those of the monolayer is that the bilayer with A_m = 20.6Å^2 shows significant molecular tilt, while the monolayer at the same density shows only a negligible molecular tilt (see Figure 4.7). Interestingly the minimum energy structure also shows a zero molecular tilt. This structure with molecular tilt is comparable to the structure of stearic acid crystal in the B form[14], which has a similar molecular area (20.7Å^2). The molecular tilt at crystal structure B is approximately 27°.

5.4.1. Orientational properties of the bilayers.

Molecular orientation.

It is clear from Figure 5.4 that an interesting feature of the simulation is the molecular tilt in the bilayer with A_m = 20.6Å^2. To obtain the quantitative result for

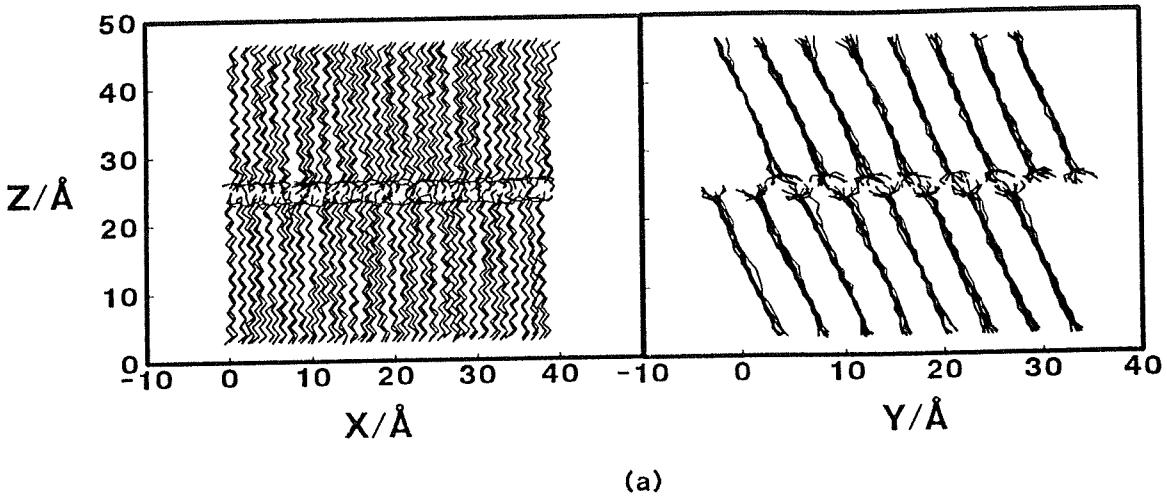

(a)

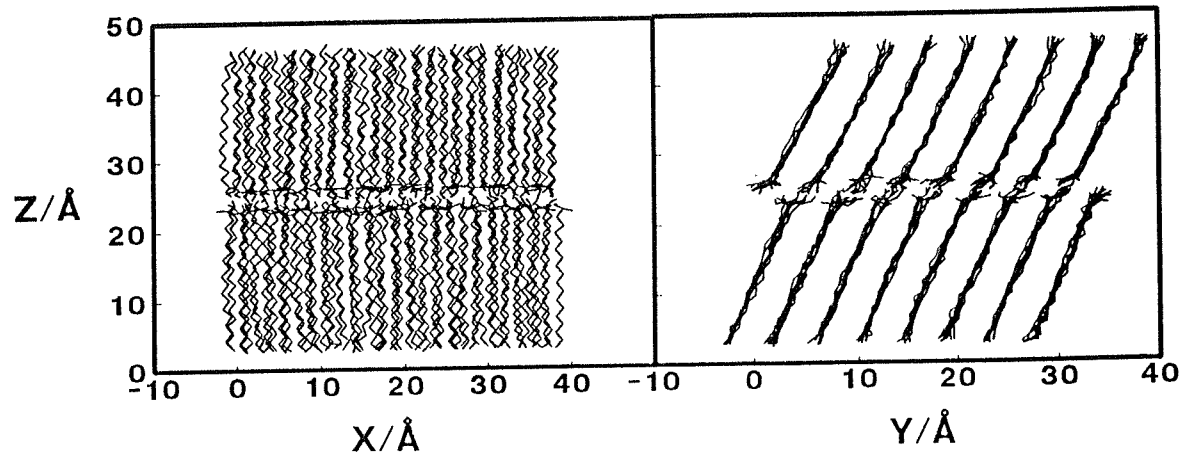

(b)

Figure 5.4. Snapshots of the structure of stearic acid bilayer with (a) A_m = 20.6Å^2 and (b) A_m = 21.2Å^2.

these properties we calculated the distribution of molecular orientations of each of the two layers in the bilayer. The out-of-plane tilt was measured from the angle between molecular long axes and the surface normal. The distribution of molecular tilts, calculated from the inertia tensor of the lower and upper layers are shown in Figure 5.5. The figure confirms that the molecular tilts of the lower and upper layers for both bilayers are very similar. In addition, the molecular tilt of the bilayer with A_m = 20.6Å^2 is similar to that of the bilayer with A_m = 21.2Å^2. The molecular tilts determined from the maximum of g(cos θ) are 17.6° for both the lower and upper layers of the bilayer with A_m = 20.6Å^2 and 18.7° and 17.4° for the lower and upper layers respectively of the bilayer with A_m = 21.2Å^2. As discussed in chapter 4 the monolayer with A_m = 20.6Å^2 shows a negligible molecular tilt of only 2.4°. To try to understand the reason why the molecules tilt in the bilayer at A_m = 20.6Å^2 we performed the short molecular dynamics simulation of a monolayer with A_m = 20.6Å^2 with the headgroup away from the surface for 10,000 steps(20 ps). The molecular tilt distribution of the monolayer is shown in Figure 5.6. Although the distribution is not particularly smooth, due to the short length of the run, the result are very similar to those for the monolayer at same density with headgroup down on the surface(see Figure 4.16). As we shall show later, the head-to-head configuration in the bilayer causes a translational distortion of the in-plane structure which results in the tilting. What this simulation shows is that the molecule-surface interaction is not primarily responsible for the upright structure.

We also analyzed the in-plane molecular orientation in both bilayers. Figure 5.7 shows the distribution of molecular azimuthal angles of the lower and upper layers in both systems. The molecular azimuthal angle is the direction of molecular tilt in the systems which exhibit such a tilt. The maximum in the distributions of molecular azimuthal angles are -87° and 90° for the bilayers with A_m = 20.6Å^2 and A_m = 21.2Å^2 respectively and the molecules are directed to their next-nearest-neighbour in both systems. This behaviour is the same as in the monolayer with A_m = 21.2Å^2, where

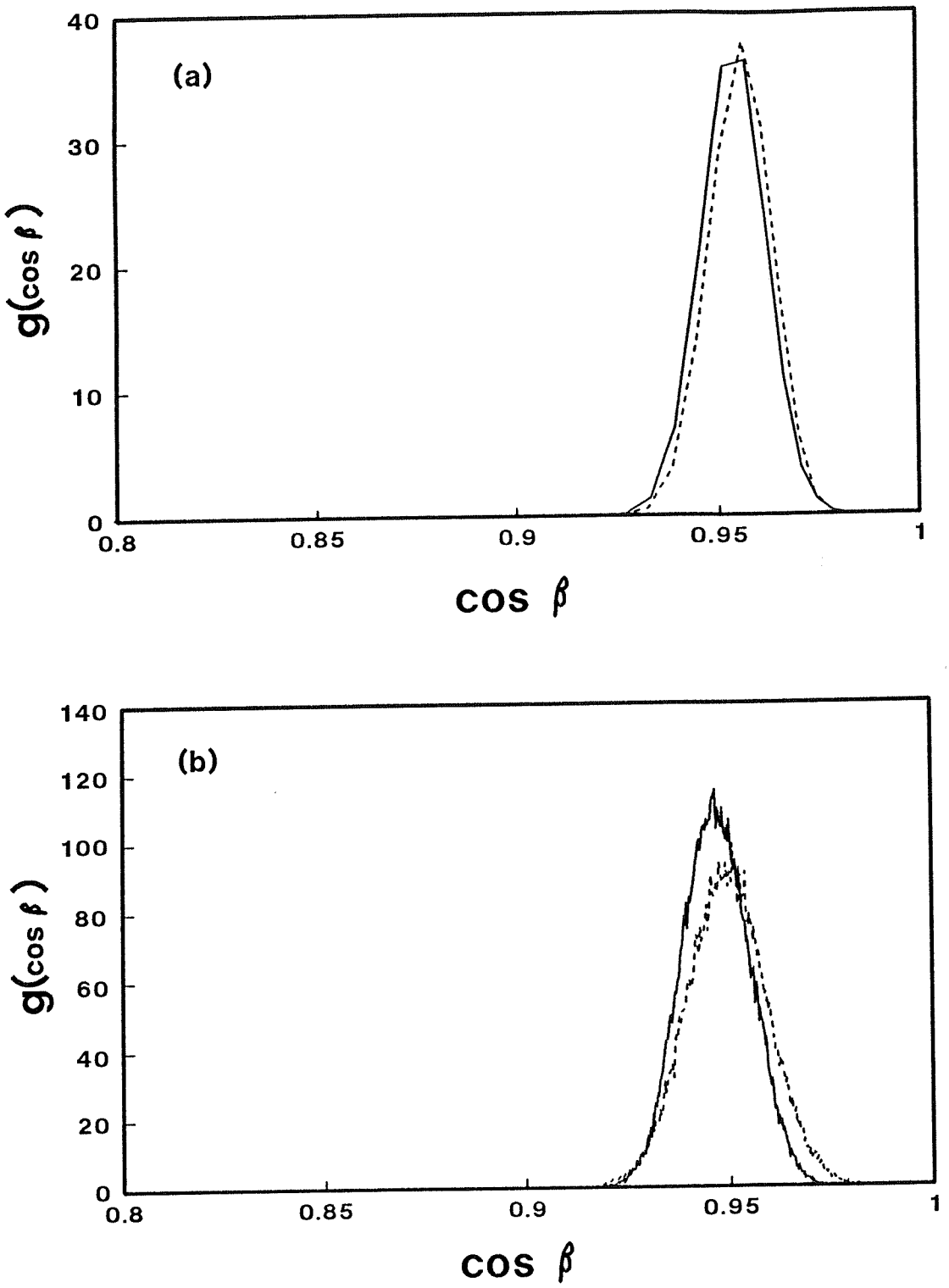

Figure 5.5. The distribution of molecular tilt angle in lower(solid line) and upper(dashed line) layers of the bilayer with (a) $A_m = 20.6Å^2$ and (b) $A_m = 21.2Å^2$.

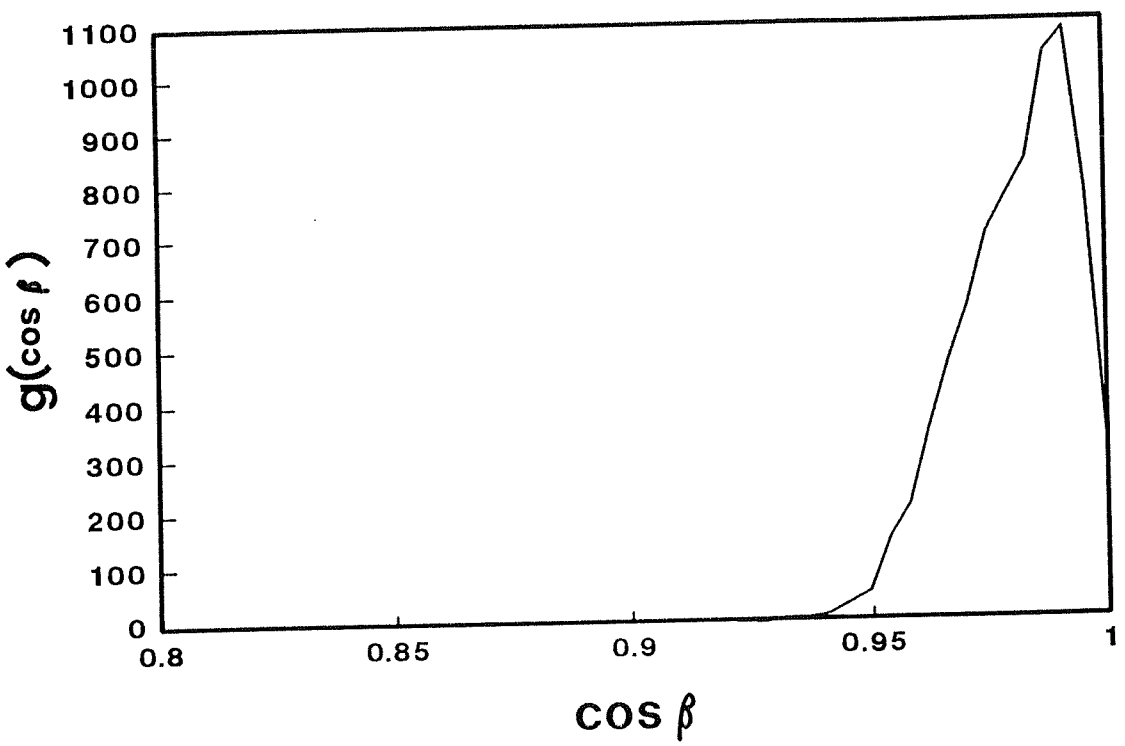

Figure 5.6. The distribution of cosine of the molecular tilt for the monolayer with A_m=20.6Å^2 with head away from the surface.

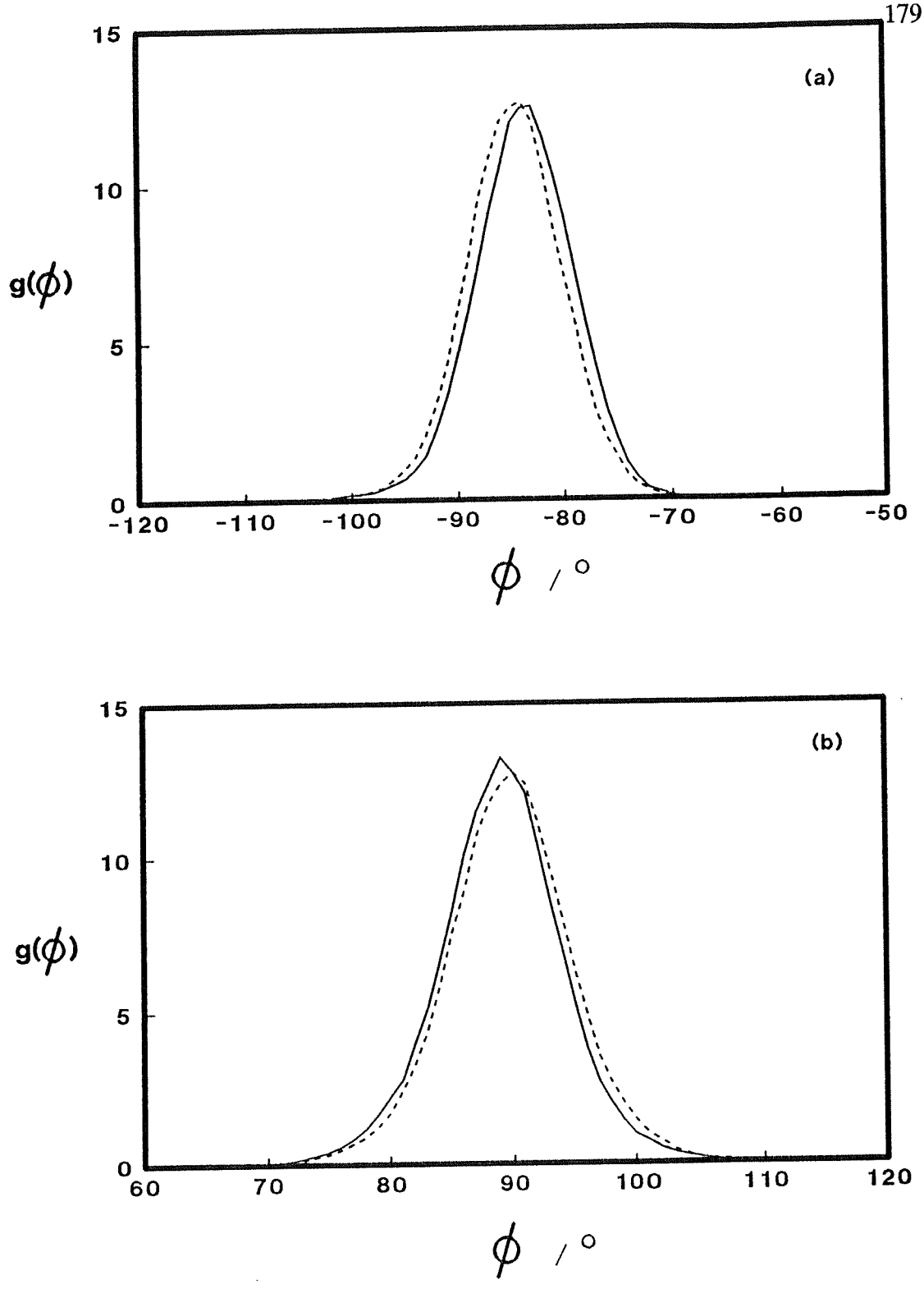

Figure 5.7. The distribution of molecular azimuthal angles of the lower(solid line) and upper(dashed line) layers for the bilayer with (a) A_m = 20.6Å^2 and (b) A_m = 21.2Å^2.

the molecules also tilt to their next-nearest-neighbours (see Figure 4.17). Figure 4.8 shows the distribution of molecular twist angle for the both systems. These distributions describe the in-plane-packing of the molecular chains. The bilayer with A_m = 20.6Å^2 has one molecule per unit cell structure and the molecules in the upper layer and lower layers are anti-parallel. However, the molecules in the bilayer with A_m = 21.2Å^2 are arranged with two molecules per unit cell structure in same layer; two molecules are anti-parallel.

5.4.2. Translational ordering in the bilayers.

Distribution of molecular centres of mass.

The radial distribution functions g(r) of the molecular centres of mass in the lower and upper layers of the both bilayers were calculated to examine the equilibrium translational structures of the bilayers. Figure 5.9 shows the radial distribution functions of the molecular centres of mass for both the bilayer studied. The two diagrams show solid-like distributions of the molecular centres of mass. However, a surprising result is the separation of the first peak to three peaks around r=5Å in the bilayer with A_m = 20.6Å^2. In the monolayer at same density the three peaks were not resolved. This is likely due to the distortion of in-plane arrangement of molecular centres of mass from the triangular structure. We calculated the average position of molecular centres of mass and hexagonal order parameters for both system throughout the simulation. Figure 5.10 shows the hexagonal order parameters for the both bilayer systems throughout the production period. The hexagonal order parameters of lower and upper layer of the bilayer with A_m = 21.2Å^2 are 0.745±0.1 and 0.753±0.1 respectively, which are not much lower value than the hexagonal order parameter (0.8±0.02) of the monolayer at same density. However, the hexagonal order parameters for the bilayer with A_m = 20.6Å^2 are 0.62±0.05 and 0.63±0.05 for the lower and upper layer respectively. These values are significantly

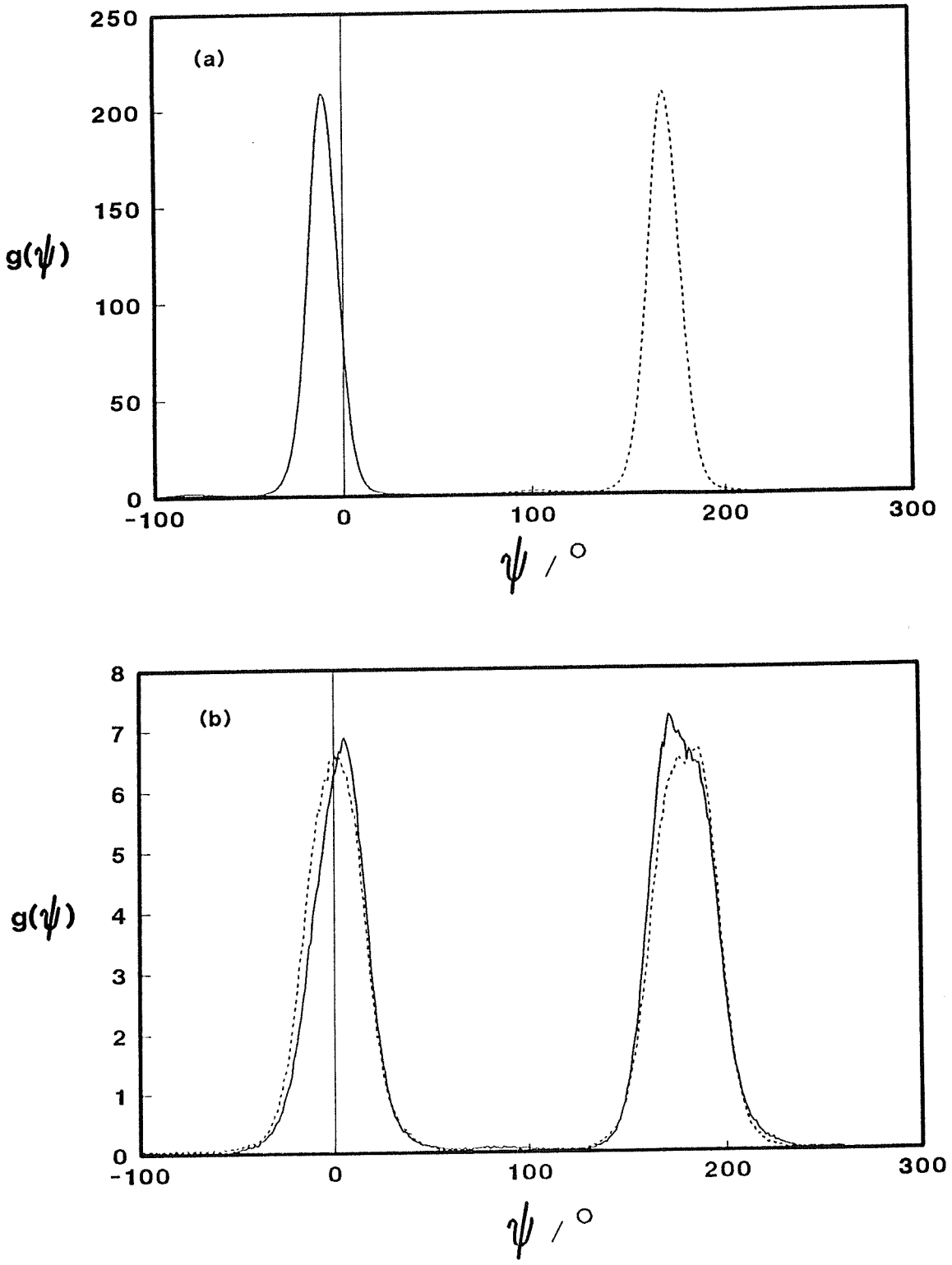

Figure 5.8. The distribution of the molecular twist angles of the lower (solid line) and upper (dashed line) layers for the bilayer with (a) A_m = 20.6Å^2 and (b) A_m = 21.2Å^2.

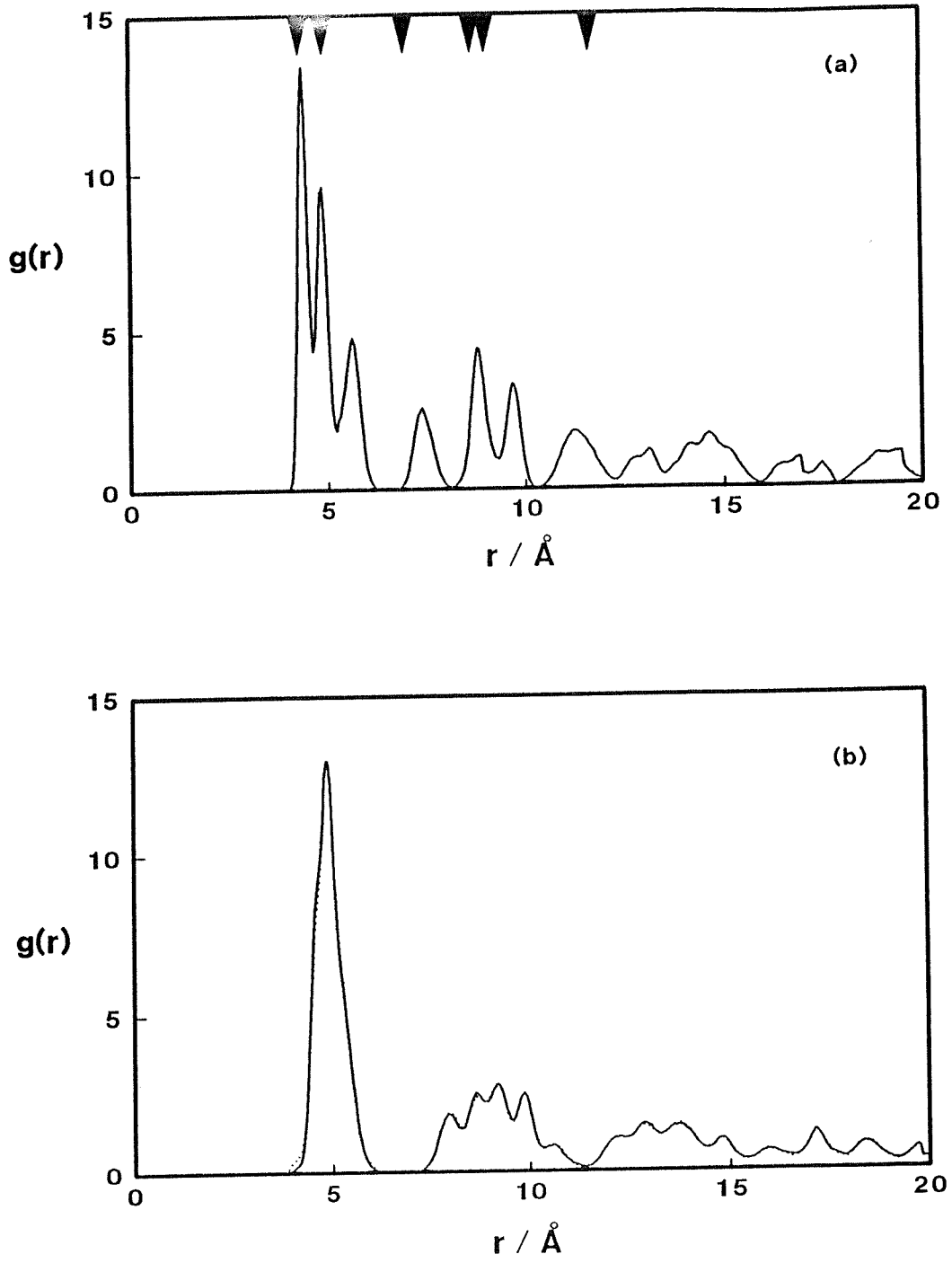

Figure 5.9. The radial distribution functions of the molecular centres of mass for the lower (solid line) and upper (dashed line) layers in the bilayer with (a) $A_m = 20.6Å^2$ and (b) $A_m = 21.2Å^2$.

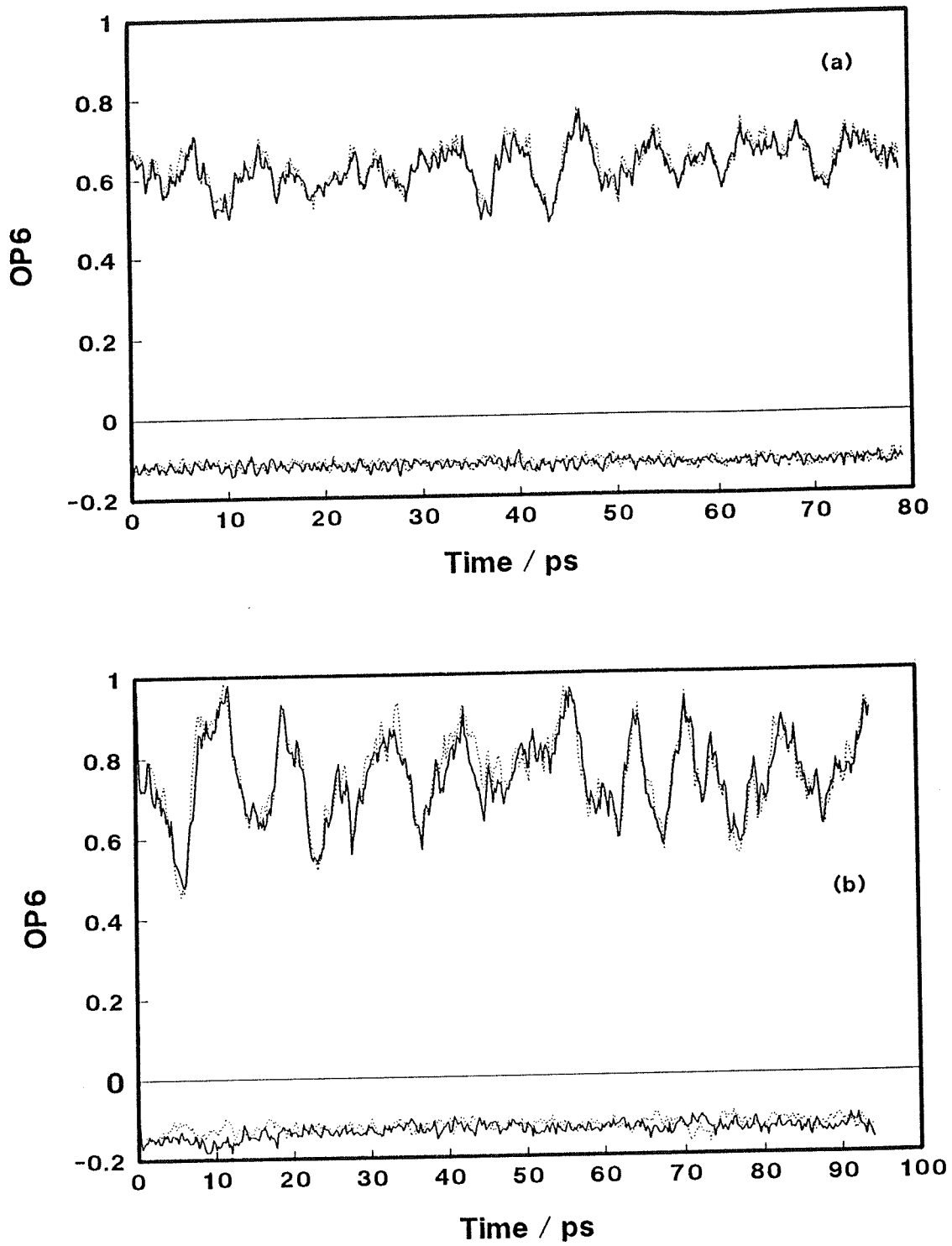

Figure 5.10. Hexagonal order parameters for the lower (solid line) and upper (dashed line) layers in the bilayer with (a) A_m = 20.6Å^2 and (b) A_m = 21.2Å^2.

lower value than that(0.8 ± 0.02) of the monolayer with A_m = 20.6Å^2 and indicate that there is a distortion of in-plane structure of the layer. From the average position of molecular centres of mass shown in Figure 5.11 we found the distortion of in-plane structure of the molecular centres of mass in the bilayer with A_m = 20.6Å^2.

As mentioned by Bareman *et al.*[9] the simulation at constant area with triangular lattice structure using periodic boundary condition can not allow the distortion in the distance between molecules in x- and y- direction. This limit resulted in the angular distortion of in plane arrangement of molecular centres of mass conserving A_m during the simulation. The lattice structure of stearic acid crystal at state B which exhibits the molecular tilt is not triangular[14]. To find out the effect of the lattice structure(distortion) on the structure of the LB layer we performed the molecular dynamics simulation of monolayer at A_m = 20.6Å^2 with configuration perpendicular to the surface. Figure 5.12 shows the distribution of molecular tilt from the molecular dynamics simulation of monolayer. Interestingly the distortion of lattice structure from triangular lattice resulted in the molecular tilt in the monolayer of A_m = 20.6Å^2, at which A_m the monolayer with triangular lattice structure showed very small molecular tilt about 2.4°(see Figure 4.16). Thus the distortion of lattice structure may be the reason why the molecules tilt in the bilayer with A_m = 20.6Å^2.

Conformational defects in the bilayers.

The distribution of carbon atoms and gauche defects g(z) along the surface normal were calculated for both bilayers are shown in Figure 5.13. The distribution of carbon atom in both layers is quite solid-like, and similar to those of monolayer discussed in chapter 4. There is also no significant interpenetration of the lower and upper layers. Gauche defects in a chain are located at the both ends of the molecules especially around the head group. The presence of gauche defects in the middle of the chain resulted in the less solid-like distribution of carbon atom along

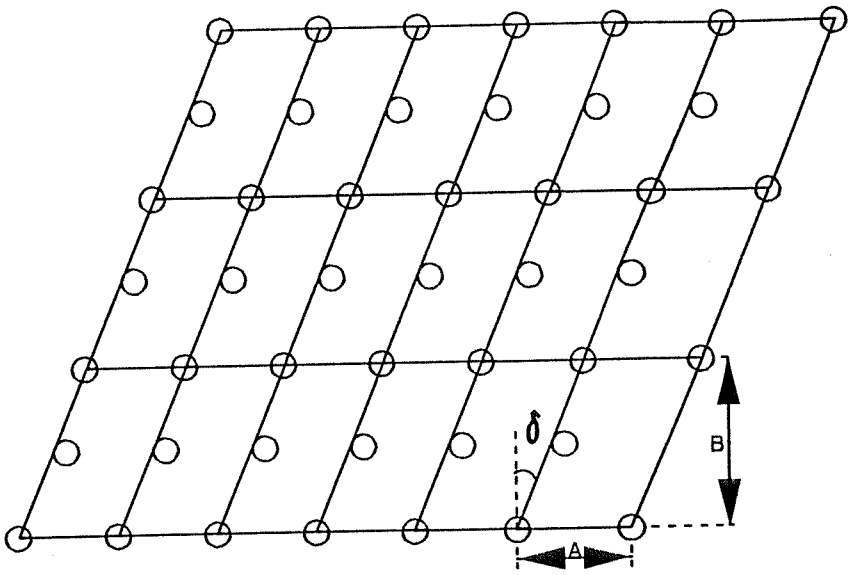

Figure 5.11. The average structure of the molecular centres of mass in the bilayer with A_m = 20.6Å^2.

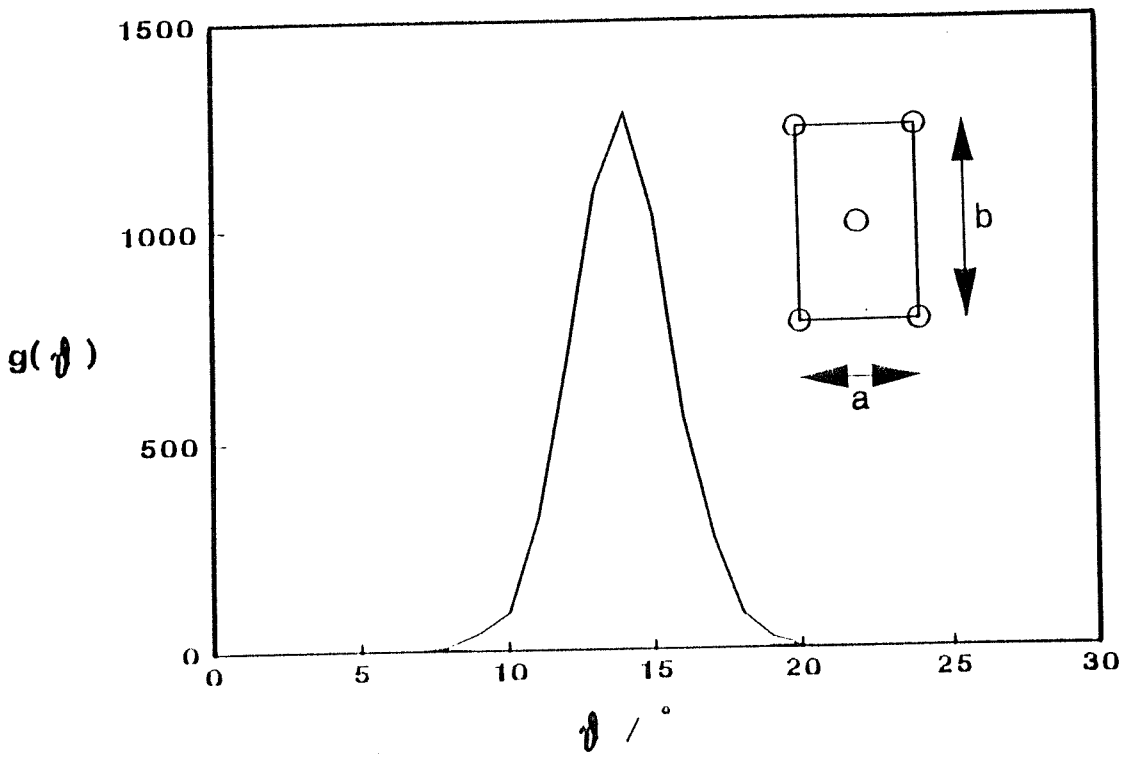

Figure 5.12. The distribution of molecular tilt from molecular dynamics simulation of a layer at A_m = 20.6Å^2 with distorted lattice structure. The inset to the figure shows the unit cell with a = 5.1010Å and b = 8.0756Å.

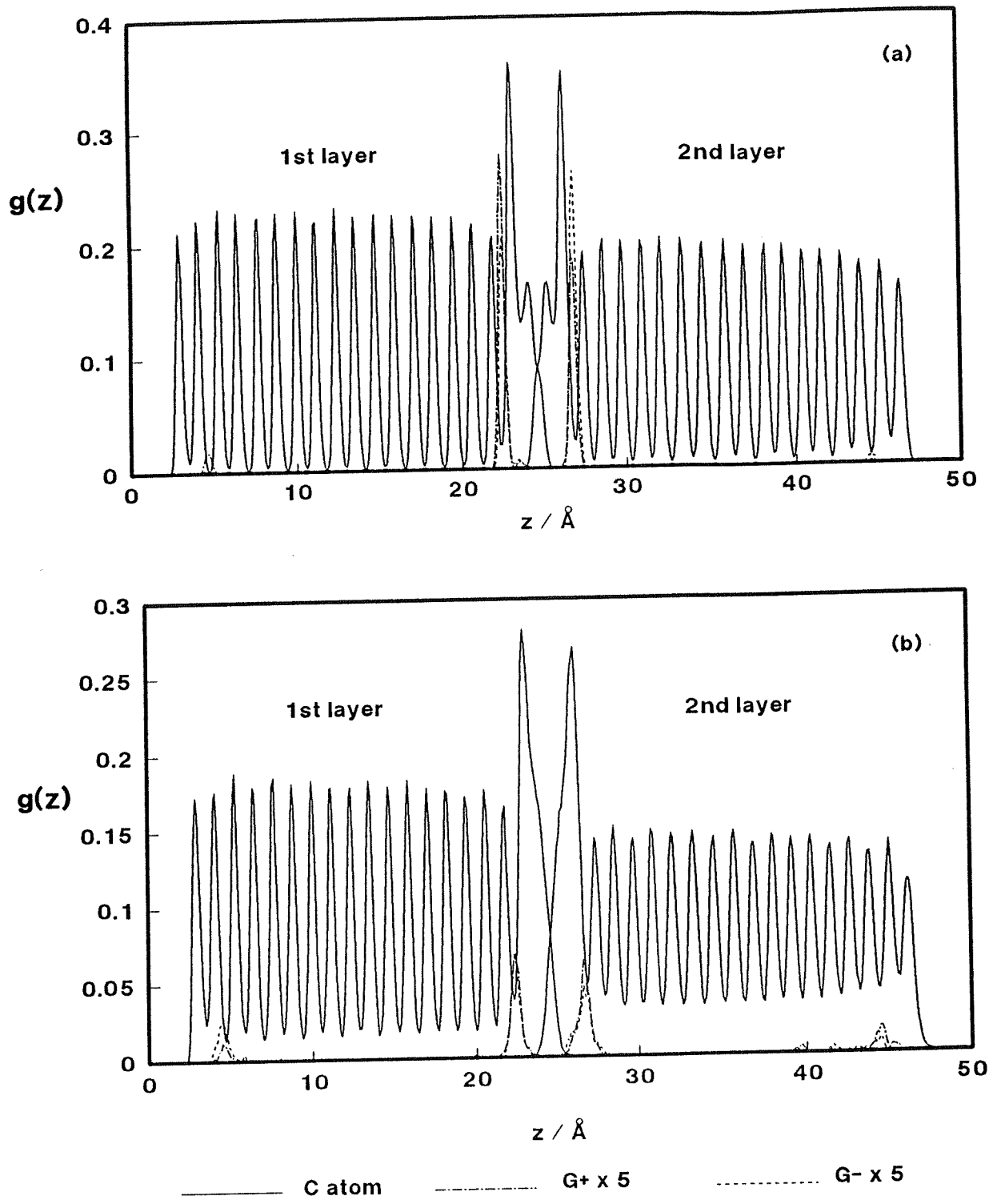

Figure 5.13. The distribution of carbon atoms and gauche defects along the surface normal for the bilayer with (a) $A_m = 20.6Å^2$ and (b) $A_m = 21.2Å^2$.

the surface normal in the bilayer with A_m = 21.2Å^2 than that of the bilayer with A_m = 20.6Å^2(Figure 5.13). The distributions of head and tail groups in the bilayer with A_m = 21.2Å^2 are shown in Figure 5.14. The distribution of head group is more solid-like than that of the tail group because of the gauche defects in the middle of the molecules.

We also examined the effect of gauche defect at the C1-C2 bond on the molecular tilt to find out the reason for molecular tilt in the layer with A_m = 20.6Å^2 by the energy minimisation. The result of energy minimisation showed that the presence of gauche defect at C1-C2 bond does not have any significant effect on the overall structure of the bilayer, especially the molecular tilt, which remains at 0.0°. This means that the gauche defect at C1-C2 bond is not the reason for the molecular tilt in the bilayer with A_m = 20.6Å^2. We also examined the in-plane radial distribution functions of gauche defects for both bilayers. Figure 5.15 shows the radial distribution functions of gauche defects in both systems. The radial distribution functions of gauche defects are less solid-like than those of the molecular centres of mass, while there is strong peak around r = 5Å.

5.4.3. Dipolar orientation in the bilayers.

The dipolar interaction shows the effect on the orientation of the molecules in the bilayers. We examined the distributions of in-plane and out-of-plane orientation of the dipoles in the bilayers. Figure 5.16 shows the distributions of the dipolar tilt(θ_μ) angles of the bilayers. The dipoles in both bilayers are nearly parallel to the surface and the dipoles in lower and upper in a bilayer are parallel to each other. The small peaks around 20° and 160° for lower and upper layers respectively are due to the gauche defects around the C1-C2 bond. The distribution of dipolar tilt angles of bilayers is very similar to that of the monolayer(see Figure 4.21). Figure 5.17 shows the azimuthal angle(ϕ_μ) distribution of dipoles in the bilayers. The in-plane dipolar orientation between the lower and upper layers is always anti-parallel each

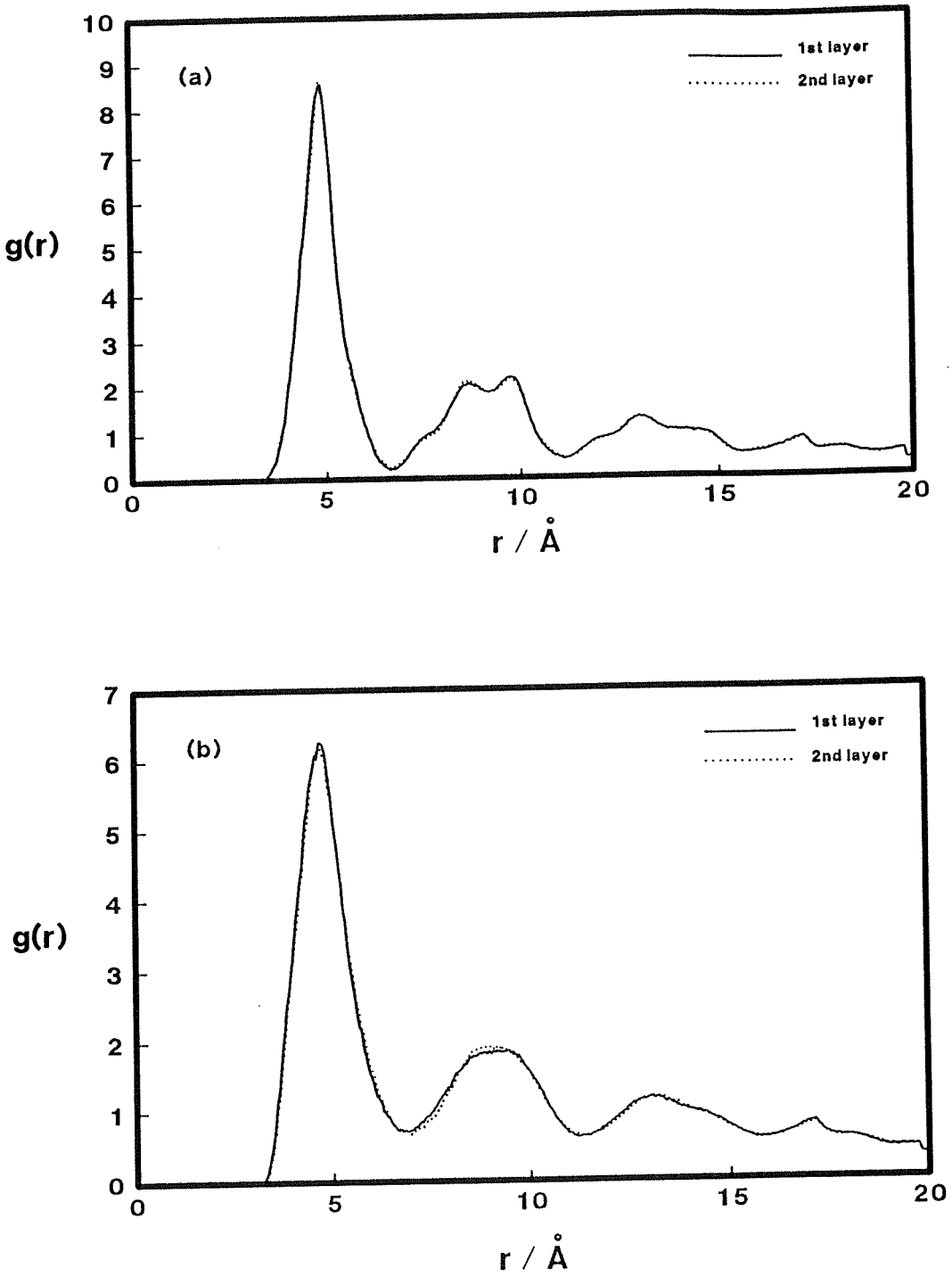

Figure 5.14. The radial distribution function for (a) the headgroup and (b) the tail group in the bilayer with A_m = 21.2Å^2.

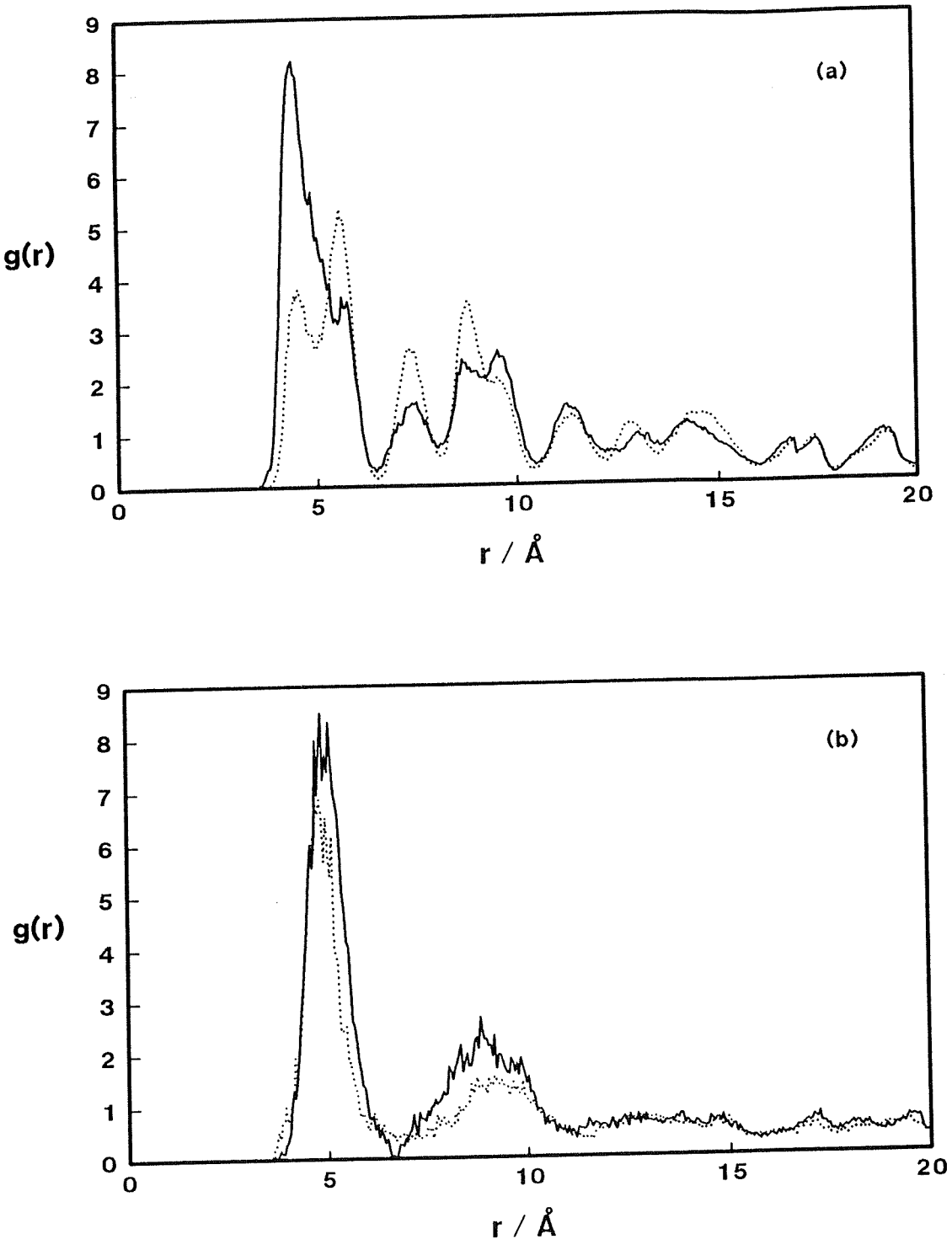

Figure 5.15. The radial distribution function of gauche defects of the lower(solid line) and upper(dashed line) layers in the bilayer with (a) A_m = 20.6Å^2 and (b) A_m = 21.2Å^2.

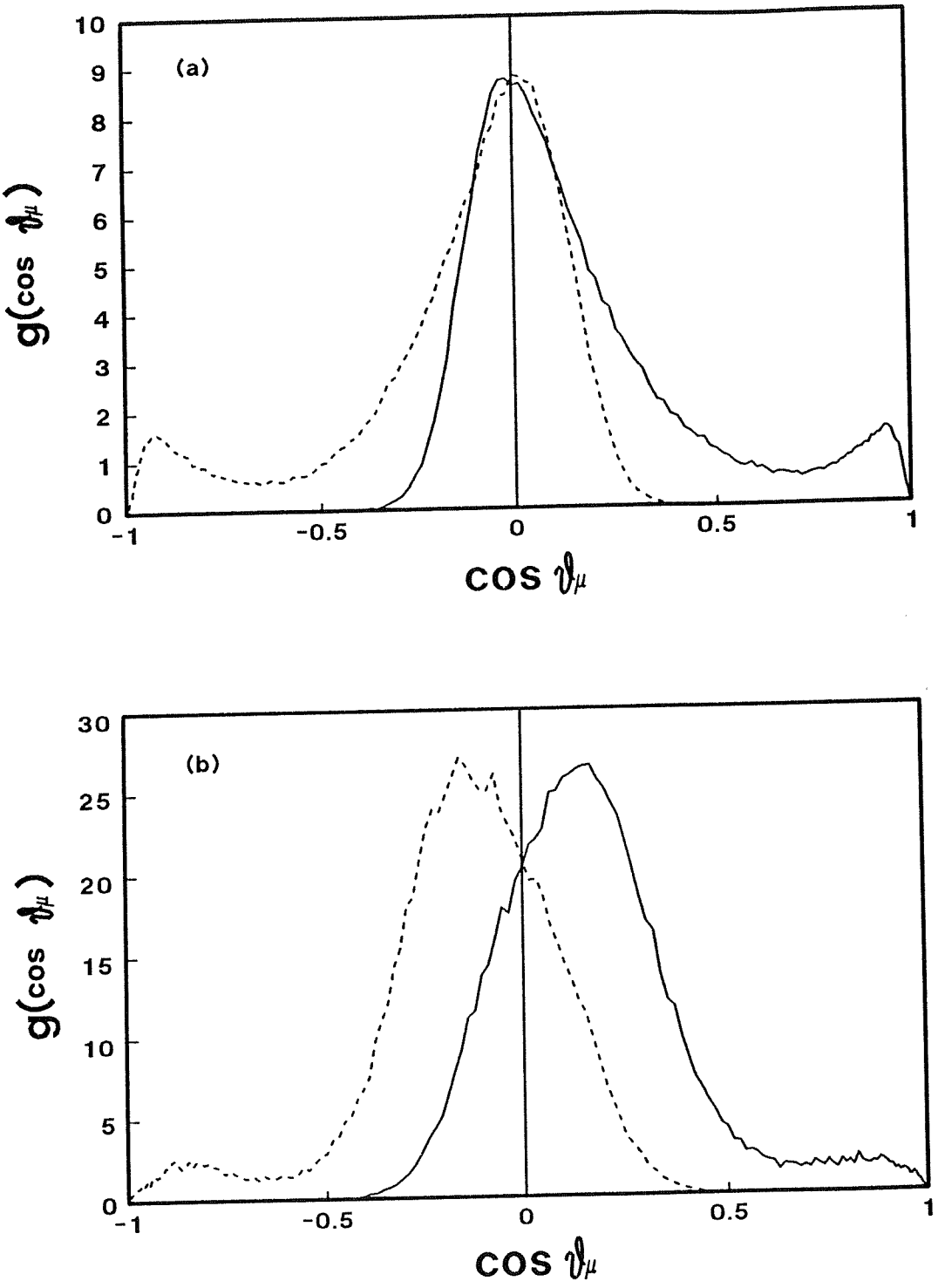

Figure 5.16. The distribution of dipolar tilt angles of the lower layer (solid line) and upper layer (dashed line) in the bilayer with (a) A_m = 20.6Å^2 and (b) A_m = 21.2Å^2.

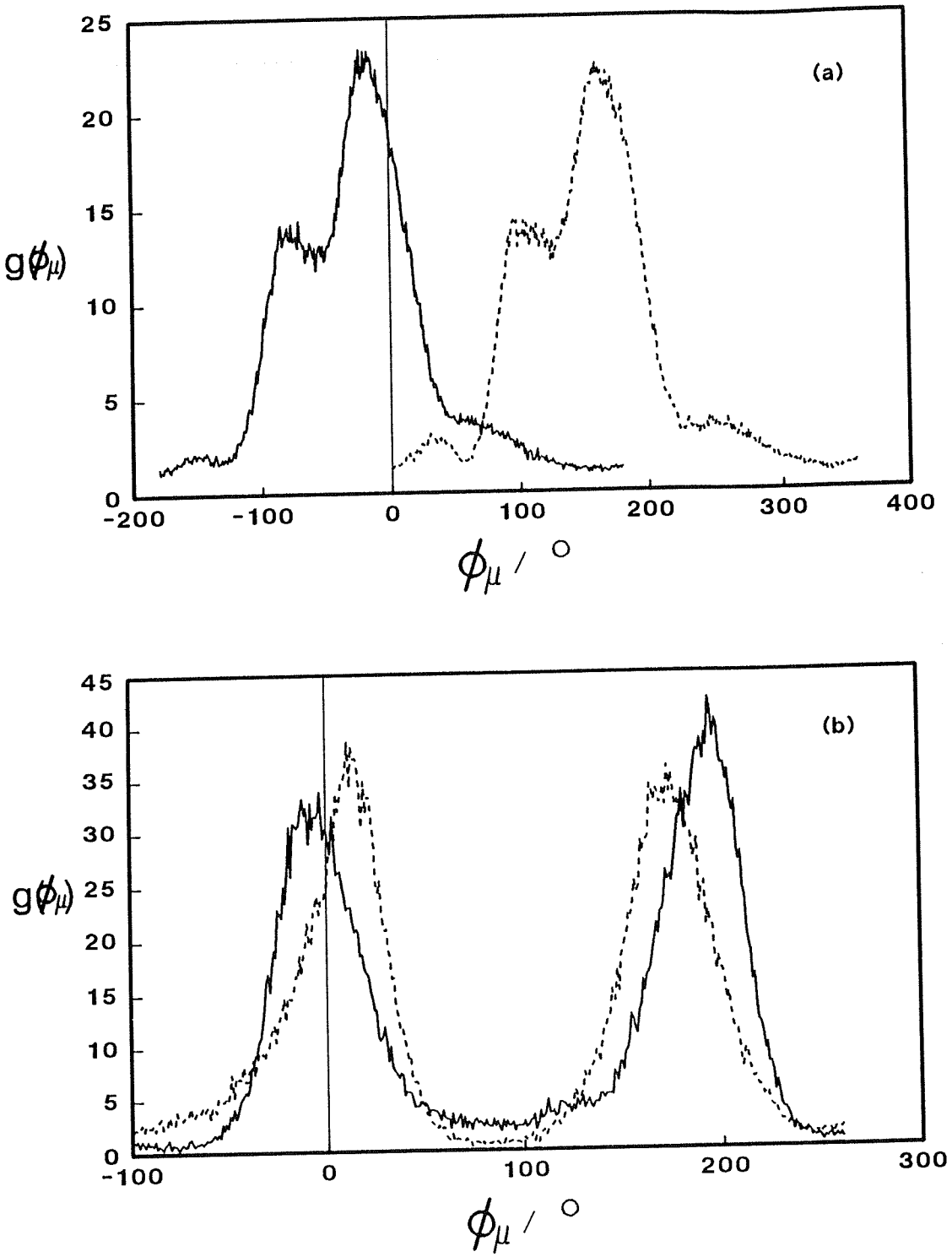

Figure 5.17. The distribution of dipolar azimuthal angles of the lower layer (solid line) and upper layer (dashed line) in the bilayer with (a) A_m = 20.6Å^2 and (b) A_m = 21.2Å^2.

other in both bilayers. The dipoles in the bilayer with A_m = 20.6Å^2 have a one dipole per unit cell in-plane structure while the dipoles in the bilayer with A_m = 21.2Å^2 exhibit a two dipoles per unit cell structure with anti-parallel orientations. This in-plane dipolar-structures are approximately as the distribution of the short axes of the hydrocarbon backbones of the molecules. The small peaks around ϕ = -90° and ϕ = 100° for the lower and upper layers respectively are due to the gauche defects around the C1-C2 bond. The precise dipolar azimuthal orientation is strongly correlated to the dihedral rotation around the C1-C2 bond. In Figure 5.17(a) the peak around ϕ = -90° for the lower layer is due to the gauche minus defect at C1-C2 bond and corresponding to the peak at ϕ = 100° for the upper layer which is due to the gauche plus defect at C1-C2 bond in the upper layer. From this analysis we found the strong correlation of the dipolar orientation which is due to the electrostatic interaction between the lower and upper layers. The dipolar azimuthal distribution of the bilayer with A_m = 21.2Å^2 is similar to that of the monolayer with A_m = 21.2Å^2 but the dipolar azimuthal distribution of the bilayer with A_m = 20.6Å^2 is quite different with those of the monolayer with A_m = 20.6Å^2(see Figure 4.22). In the monolayer there is only weak electrostatic interactions between partial charges in head groups and image charges in the surface but in the bilayer the electrostatic interaction between headgroups in the lower and upper layers are strong enough to control the orientation of the dipoles. Figure 5.18 shows the distribution of the dihedral angle around the C1-C2 bond of the lower and upper layers in the both bilayers. The figure shows that the dihedral rotations in the lower and upper layers are strongly correlated with each other. In the bilayer with A_m = 21.2Å^2 the gauche minus defects for the dihedral angle of around -80° in the lower layer is corresponding to the gauche plus defects for the angle of around 80° in the upper layer. In the monolayer with A_m = 20.6Å^2 the distribution of the dihedral angles of the C1-C2 bond is symmetric but that of the bilayer is not symmetric at same headgroup area. The electrostatic interaction between layer and surface in the monolayer is the interaction

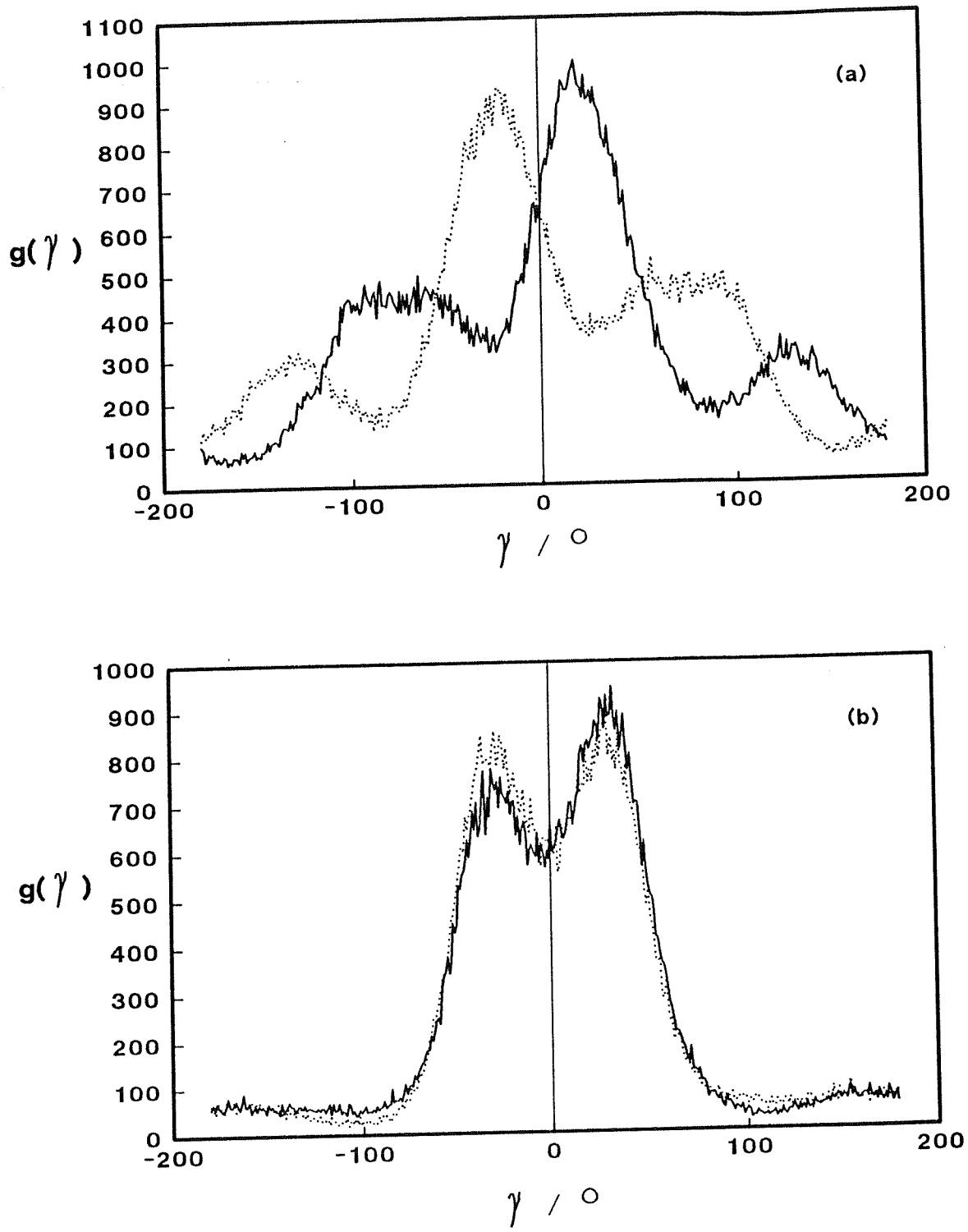

Figure 5.18. The distributions of dihedral angle of the bond C1-C2 of the lower layer(solid line) and upper layer(dashed line) in the bilayer with (a) A_m = 20.6Å^2 and (b) A_m = 21.2Å^2.

between charges in head groups and their image charges in the surface so there is little barrier to move image charges. However, in order to change the orientation of the dipole in the bilayer the rotation of the bond around the headgroup,especially the C1-C2 bond, is required(see Figure 5.19). The dihedral rotation of the bond has an energy barrier to overcome.

5.4.4. Dynamics of the bilayers.

The dynamics of the bilayer of A_m = 21.2Å^2 have also been examined through the velocity auto-correlation functions and their Fourier transforms using Eq.(4.16) and Eq.(4.17). Figure 5.20(a) shows the velocity auto-correlation of the molecular centres of mass and the autocorrelation function of the C-C-C bond angle of the chain. Figure 5.20(b) shows the Fourier transform of the velocity of carbon atoms including atoms in the headgroup. This diagram shows that the dynamics in the bilayer are the combination of various motion with different time scales like monolayers discussed in chapters 3 and 4. The overall dynamics is similar to those of the monolayers. The peaks at wave numbers of $0<\omega<150$ cm^{-1} are due to the translational and tilting motion of stearic acid molecules. The motiom of molecular centres of mass in the bilayer is slower than that in the monolayer and has a broad range of frequency. The peaks in the range of $200<\omega<500$ cm^{-1} are mainly due to the bond angle deformation motion in the chains. The peak around $\omega=230$ cm^{-1} is due to the bond deformation motion of the headgroup. This result indicates that the dynamics of the headgroup in the bilayer is restricted by the strong electrostatic interaction (supposed to be hydrogen bond) between headgroups in the upper and lower layer.

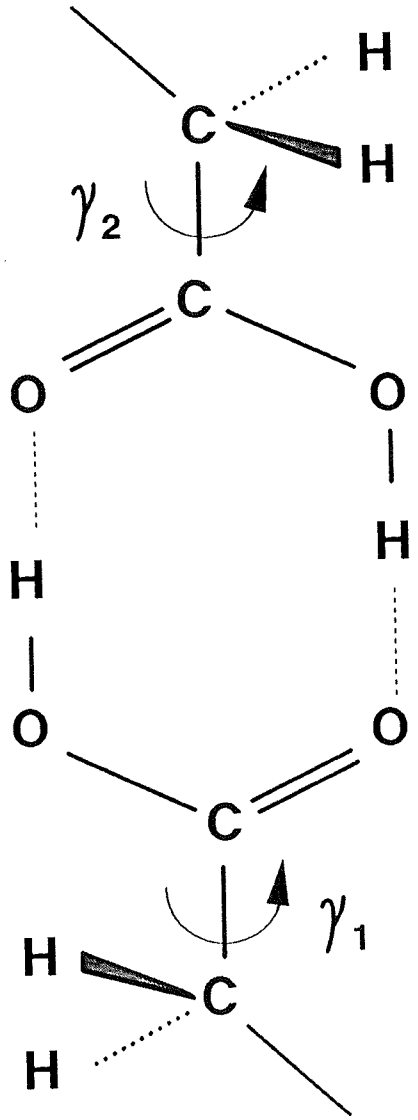

Figure 5.19. Schematic representation of the coupled dihedral rotation around head groups between lower and upper layers in the bilayer.

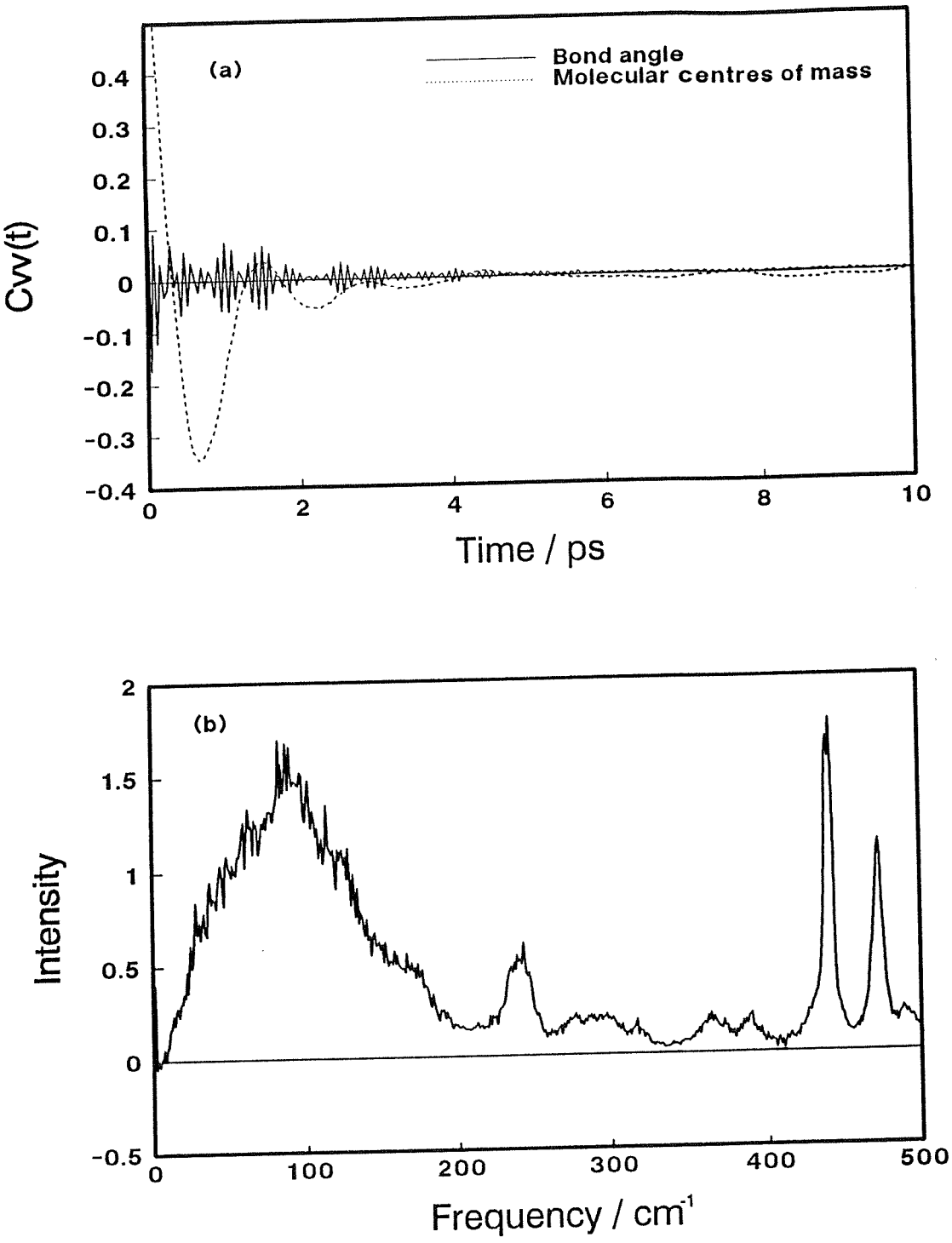

Figure 5.20. (a) Auto-correlation functions and (b) power spectrum of the carbon atom motion in the bilayer with A_m = 21.2Å^2.

5.5. Conclusions.

The structure of Langmuir-Blodgett bilayers of stearic acid on structureless hydrophobic surface have been examined by the energy minimisation calculation and molecular dynamics. The structures of bilayers at 0K from the energy minimisation has no significant difference with those of the monolayers at 0K. The lower and upper layers show the similar orientational properties e.g. the molecular tilt and azimuthal behaviours. The bilayers at 300 K from molecular dynamics calculation show similar in-plane structure to those of the monolayers at same density. The distributions of molecular centres of mass are solid-like while the head and tail group show the liquid-like structure due to the gauche defects at the ends of the molecules. The orientation of dipoles is strongly correlated by the strong electrostatic interaction between lower and upper layers and resulted in the strongly coupled dihedral rotation of C1-C2 bonds, which dominate the head group orientation of a molecule.

The out-of-plane structure, molecular tilt, of the bilayer with A_m = 20.6Å^2 shows significant difference with that of the monolayer at same A_m. The bilayer shows significant molecular tilt about 18° while monolayer oriented vertically to the surface at A_m = 20.6Å^2. This structural change was due to the distortion of the lattice structure in the bilayer. The molecules in the bilayers tilted to their next nearest neighbours. The dynamics of the bilayer is very similar to that of the monolayer. However, the dynamics of the headgroup is restricted by the electrostatic interaction between the two layers.

References.

[1] P. Christie, C.A. Jones, M.C. Petty and G.G. Roberts, J. Chem. Phys. D, **19**, L167 (1986).

[2] C.A. Brown, F.C. Burns, W. Knoll, J.D. Swalen and A. Fisher, J. Phys. Chem., **87**, 3616 (1983).

[3] F. Kimura, J. Umemura and T. Takenaka, Langmuir, **2**, 96 (1986).

[4] A. Bonnerot, P.A. Chollet, H. Frisby and M. Hoclet, Chem. Phys., **97**, 365 (1985).

[5] P. van der Ploeg and H.J.C. Berendsen, J. Chem. Phys., **76**(6), 3271 (1982).

[6] P. van der Ploeg and H.J.C. Berendsen, Mol. Phys., **49**, 233 (1983).

[7] E. Egberts and H.J.C. Berendsen, J. Chem. Phys., **89**, 3718 (1988).

[8] A. Bañón, F. Serrano Adán, and J. Santamaría, J. Chem. Phys., **83**, 297 (1985).

[9] J.P. Bareman and M.L. Klein, J. Phys. Chem., **94**, 5202 (1990).

[10] J.H. Clarke and D. Brown, Mol. Simul., **3**, 27 (1989).

[11] J. Hermans, H.J.C. Berendsen, W.F. van Gunsteren, and J.P.M. Postma, Biopolymers, **23**, 1513 (1984).

[12] W.L. Jorgensen, J.D. Madura, C.J. Swenson, J. Am. Chem. Soc., **106**, 6638 (1984).

[13] M.C. Petty and W.A. Barrow, *Langmuir-Blodgett films*, Chapter 2 edited by G. Roberts (1990).

[14] M. Goto and E. Asada, Bull. Chem. Soc. Jpn., **51**, 2456 (1978).

CHAPTER SIX.

Conclusions.

6. CONCLUSIONS.

In chapter 1 we discussed the quasi-two-dimensional phase transitions in a monolayer of stearic acid on water. The monolayer shows a liquid-solid transition at the molecular area of around 21Å^2. This is close to the density at which the films are transferred to solid surfaces to make Langmuir-Blodgett films. In order to understand the structure and dynamics of the stearic acid molecules in these Langmuir-Blodgett films we have performed molecular dynamics simulations of a monolayer on a hydrophillic surface and a bilayer on a hydrophobic surface. The surface was treated as a smooth continuum and we consider three models for the adsorbate-adsorbate interaction: the united-atom model, the explicit-hydrogen model and the all-atom model.

In order to understand the minimum energy structure of the layers we performed energy minimisation calculations at various headgroup areas(A_m). The energy minimisation calculations reveal that compressing the adsorbed layer causes a change in the molecular tilt. The united-atom model did not reproduce the phase transition at a reasonable headgroup area per molecule which is observed in the surface pressure-area isotherm. The united-atom model with σ = 3.923Å and ϵ/k_B = 72.0K which were used in the studies of liquid alkane, lipid bilayer and the molecular dynamics simulation of a Langmuir-Blodgett film predicted the molecular tilt at A_m = 17.6Å^2 which is larger than the normal solid densities of all forms of crystalline stearic acid. As we discussed in chapter 3 it is possible to reproduce the molecular tilt behaviour of the explicit-hydrogen model using the united-atom model with a rescaled value for the σ of the methylene group(σ=4.3Å). The explicit-hydrogen model predicted the phase transition observed in the surface pressure-area isotherm at the molecular area of around 21Å^2. The monolayer has a molecular tilt of about 30° with respect to the surface normal at A_m > 21 Å^2. By further compression the layer changes its molecular tilt from 30° to 0° within a very small

range of molecular area(A_m). The united-atom model and the explicit-hydrogen model showed a similar sharp tilt transition but showed different minimum energy behaviours. These differences are due to the packing of the hydrogen atoms of the methylene unit in the explicit-hydrogen model and relative difference in the effective size of methylene unit in the chain. The inclusion of the electrostatic interactions between the headgroups in the all-atom model did not have a big influence on the minimum energy structure since the configurational energy of the film is dominated by the intermolecular Van der Waals interactions which account for more than 90% of the total energy. The minimisation calculation using the all-atom model showed a molecular tilt transition at A_m = 20.7Å^2. The energy minimisation of the bilayer with a head-to-head structure showed that there is a very strong correlation in the translational and orientational structure of the two layers. The structure of each layer was quite similar to the minimum energy structure of the monolayer at the same density.

We also performed the molecular dynamics simulations of the monolayers at A_m = 20.79Å^2 and A_m = 21.2Å^2 to predict the structure and dynamics of the layer at 300K using the explicit-hydrogen model. This simulation also predicted a change in the molecular tilt at a molecular area of around A_m = 21Å^2. The layer showed a molecular tilt 0° at A_m = 20.79Å^2 and approximately 9° at A_m = 21.2Å^2 with the molecules pointing to their next-nearest-neighbours. The molecular tilt of 9° at A_m = 21.2Å^2 is much smaller than the value of 32° obtained from the energy minimisation. The difference in the molecular tilt is predominantly due to the increase in the effective density of the layer caused by the lateral thermal vibrations of the molecules in the plane of the surface. The radial distribution function of the centres of masses of the molecules is solid-like while the densities at which we performed the simulation are normally labelled as a liquid regime in the surface pressure-area isotherm of the Langmuir monolayer of stearic acid[1]. The layers also

showed a hexagonally, well-ordered structure (hexagonal order parameter ≈ 0.77) throughout the production phase of the simulation. The stearic acid molecules in the layer exhibit conformational defects at 300K. The defects are distributed mainly at the top and bottom of the layer and exhibit significant intermolecular and intramolecular correlations. The layer also showed long lived co-operative motions involving simultaneous changes in the molecular tilt and the azimuthal orientation, which arise because of the relatively small molecular tilt in the layer.

In chapter 4 we discussed the results of molecular dynamics simulations using the all-atom model including electrostatic interactions between the headgroups and between the headgroup and the surface. The layers exhibit well-ordered structures with similar orientational properties to those obtained from the monolayer using the explicit-hydrogen model. The radial distribution functions of the centres of masses of molecules are solid-like and the centres of masses of molecules have well-ordered in-plane hexagonal structure(order parameters = 0.8 ± 0.02). The layers show significant conformational disorder at the C-C bond connecting the carboxylic acid group and alkyl tail group even in the layer with $A_m = 20.6Å^2$. Such a gauche defect is found in the stearic acid crystal form B, which has a headgroup area of $20.7Å^2$. The layer with $A_m = 20.6Å^2$ has a negligible molecular tilt of 2.4° but the layer with $A_m = 21.2Å^2$ has a molecular tilt of 18.8°, which is more than twice the molecular tilt obtained using the explicit-hydrogen model at the same density. The structure factor S(**k**) for the monolayer is dependent on the molecular tilt and molecular rotation along the long axes and especially the direction of molecular tilt in the layer. The structure factor for the layer with $A_m = 20.6Å^2$ showed two strong and four weak peaks while the structure factor for the layer with $A_m = 21.2Å^2$ showed four strong and two weak peaks due to the molecules tilting towards the next-nearest-neighbour in the layer. The dipolar interactions in the layer have an effect on the precise orientation of the molecules although the overall orientation of the layer is controlled

by the inter-chain non-bonded interactions. Due to the head-to-head alignment of dipoles the molecular planes are parallel to each other.
A study of the dynamics of the layer showed that the broad peak in the density of states in the region of $0<\omega<150$ cm^{-1} is due to the translational motion of the molecules and that sharp peaks in the range 200 cm^{-1} to 500 cm^{-1} are mainly due to bond angle distortion.

In chapter 5 we reported the results of the molecular dynamics simulation of a bilayer Langmuir-Blodgett film of stearic acid. The most important feature of the bilayer is the very strong correlation of molecular distribution and dynamics because of the strong electrostatic interactions between the two layers. As in the monolayer the radial distribution of the centres of molecular masses was solid-like while the distributions of head and tail groups were liquid-like, because of the gauche defects at the top and bottom of the molecule. The orientation of the dipole is strongly correlated to the dihedral rotation of the C1-C2 bond connecting the headgroup and the alkyl tail of the molecule. The dynamic property of the bilayer is similar to that of the monolayer. However, due to the strong electrostatic interactions between the two layers the dynamics of the headgroup is restricted.

In summary the computer simulation predicts a molecular tilt of the Langmuir-Blodgett film at a headgroup areas of around 21$Å^2$. The structure of the layer is solid-like in terms of radial distribution function of the molecular centres of mass. The molecules in the layer have a significant number of gauche defects at the tops and bottoms of the molecules. The molecular tilt from molecular dynamics simulation is much smaller than that from energy minimisation because of the decrease in the effective separation between molecules by the lateral thermal vibration motion and the conformational defects in the molecules. The molecules in the layers tilt to their next-nearest-neighbours.

References.

[1] R.A. Hann, *Langmuir-Blodgett Films*, Edited by G. Roberts, 1990 Plenum Press, New York.